Variable Grid Finite-difference Modeling Including Surface Topography

By

Koichi Hayashi

B.S., Earth Sciences (1990)
Chiba University

Submitted to Department of Earth, Atmospheric, and Planetary Sciences
in the partial fulfillment of the requirements
for the degree of Master of Sciences

at the
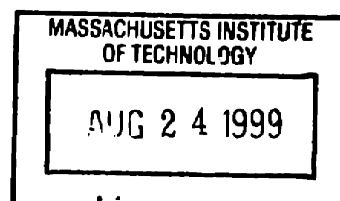
MASSACHUSETTS INSTITUTE OF TECHNOLOGY

August 6, 1999

[September 1999]

Signature of Author ....
Department of Earth, Atmospheric, and Planetary Sciences
August 6, 1999

Certified by ....
M. Nafi Toksöz
Professor of Geophysics
Thesis advisor

Accepted by ....
Ronald G. Prinn
Chairman
Department of Earth, Atmospheric, and Planetary Sciences

Variable Grid Finite-difference Modeling Including Surface Topography

By

Koichi Hayashi

Submitted to Department of Earth, Atmospheric, and Planetary Sciences
on August 6, 1999, in partial fulfillment of the requirements
for the degree of Master of Sciences

Abstract

We have developed a two-dimensional viscoelastic finite-difference modeling method for highly complex surface topography and subsurface structures. Realistic modeling of seismic wave propagation in the near surface region is complicated by many factors, such as strong heterogeneity, topographic relief and large attenuation. In order to account for these complications, we use a velocity-stress staggered grid and employ an O(2,4) accurate viscoelastic finite-difference scheme. The implementation includes an irregular free surface condition for topographic relief and a variable grid technique in the shallow parts of the model.

Several methods of free surface condition are bench marked, and an accurate and simple condition is proposed. In the proposed free surface condition, stresses are calculated so that the shear and normal stresses perpendicular to the boundary are zero. The calculation of particle velocities does not involve any specific calculations, and the particle velocities are set to zero above the free surface. A stable variable grid method is introduced, where we use a three times finer grid in the near surface or low velocity region compared to the rest of the model. In order to reduce instability, we apply averaging or weighting to the replacement of the coarse grid components within the fine grid. The method allows us to avoid any limitation of the shape of the grid size boundary. Numerical tests indicate that approximately ten grid-points per shortest wavelength with the variable grid method results in accurate calculations. The method requires a stair-shaped discretization of a free surface. We investigated the stair-shaped structures, and found that the cause of the dispersion from irregular free surface is mainly a numerical error due to the large grid sizes rather than the Rayleigh waves scattering due to the stair-shaped boundary.

The finite-difference modeling is applied to the investigation of near surface wave propagation. Several numerical simulations are performed to show the characters of wave propagation in the near surface region. The simulations show that the low velocity thin layers just below the surface and anelastic attenuation have significant effect on surface seismic record. The 2-D modeling of near surface structure beneath a 2-D refraction survey line is carried out. The comparison of the observed data with theoretical waveforms is performed. The characters in the observed data can be explained by a subsurface model constructed by P-wave traveltime tomography.

Thesis Supervisor: M. Nafi Toksöz
Title: Professor of Geophysics

Acknowledgments

Contents

Chapter 1

Introduction

Surface seismic methods have been widely used for civil engineering investigations and environmental problems. However, there are increasing demand for investigations of more complex geological features. The shallow seismic method will play an important role in such investigations, but requires accurate and reliable data, interpolation and modeling (Steeples, 1998). In order to improve the shallow seismic methods, accurate and efficient numerical modeling methods are needed. The finite-difference method is one such technique that can be used for complex structures, because it can account for factors that complicate seismic wave propagation, such as large velocity contrasts, strong heterogeneity, topographic relief, and attenuation. The modeling of irregular free surface topography and the inclusion of attenuation are two factors that are particularly important in modeling.

The real earth is not perfectly elastic, and propagating waves attenuate with time due to various energy-loss mechanisms. The effect of attenuation on wave propagation is generally very large in near surface, and therefore should be considered in the studies of near surface wave propagation. Anelastic attenuation can be described using a viscoelastic model (Lay and Wallace, 1995). Numerical modeling of linear viscoelastic seismic responses in the time domain has recently become practical through algorithms based on the superposition of relaxation mechanisms. The standard linear solid (SLS) is a simple viscoelastic model consisting of a spring in parallel with a dashpot in a series (Pipkin, 1986). Day and Minster (1984) described a method to connect several SLSs in parallel to yield an excellent approximation to a constant Q in a predefined frequency band. Blanch (1995) showed that several SLSs connected in parallel can be tuned through a single parameter to yield a constant Q approximation. Robertsson et al. (1994) presented a viscoelastic finite-difference method using memory variables to eliminate the convolution terms of viscoelastic equations. These algorithms enable us to calculate attenuation

efficiently.

Generally, the solid earth's surface is not flat. Since sources and receivers are usually placed on the ground surface, topography may have a significant influence on recorded data. For finite-difference modeling of irregular free surfaces, several computational methods have been presented. These methods can be classified into two main groups. The first is the method in which the finite-difference grid is deformed to match exactly the free surface relief (Hestholm and Ruud, 1994). It is effective for relatively smooth topography, but has limitations for steep topography. The second method employs a rectangular grid and generalizes the free surface condition (Robertsson, 1996). Unlike the first method, the second method has no limitations on the shape of topographic relief. However, its drawback is that it requires very fine gridding, requiring at least 15 grid-points per wavelength (Robertsson,1996).

An efficient solution to the above dilemma is to use a finer sampling of grid in the vicinity of the irregular free surface compared to the deeper parts of the model. The method is called a multi-grid or variable grid method. Several seismological studies describing the variable grid approach have been reported. McLaughlin and Day (1994) employed a variable grid scheme to seismic wave simulations using a 3-D elastic velocity-displacement finite-difference method. Falk et al. (1995) used a varying grid spacing technique to model tube waves. De Lilla (1997) proposed a variable grid finite-difference method that can handle any integer number for a grid size ratio. Robertsson and Holliger (1997) applied the variable grid method to rough topography. This approach enables us to handle rough topography efficiently.

In this thesis, I will show that the generalized free surface condition, combined with the variable grid approach, enables us to apply a two-dimensional, viscoelastic, finite-difference modeling to steep and complex structures. In Chapter 2, I derive velocity-stress elastic wave equations and extend them to the viscoelastic case. Then, I show its finite-

7

difference approximation and fundamental benchmark tests to demonstrate the accuracy and reliability of the finite-difference code. In Chapter 3, I present an accurate and stable free surface condition that can handle irregular free surface, perform benchmark tests, and present criteria for accuracy are presented. In chapter 4, I present a stable variable grid method, perform several numerical tests, and combine the method with the irregular free surface condition. In Chapter 5, I apply finite-difference modeling to the investigation of near surface wave propagation, with numerical simulations, and carry out calculations to match the observed waveform data obtained by a 2-D seismic field experiment.

Chapter 2

Viscoelastic Finite-difference Method

Seismologists began using finite-difference methods to solve wave propagation problems some 30 years ago. Most of the early works regarding the application of finite-difference methods to seismic wave propagation were based on the second-order elastic wave equation in which the displacement of media was directly solved. Alterman and Kornfeld (1968), Alterman and Karal (1968) developed the algorithm for homogeneous media. Boore (1972) and Kelly et al. (1976) developed the algorithm for heterogeneous media. Virieux (1986) proposed a alternative method in which the second-order wave equation was reformulated to first-order hyperbolic equations using the velocity-stresses staggered grid scheme for the P-SV problem. Levander (1988) extended the staggered grid scheme to a fourth-order finite-difference method. Carcione (1993), Robertsson et al. (1994), and Xu and McMechan (1998) presented viscoelastic finite-difference method based on the fourth-order staggered grid scheme. Jih et al. (1988), Tessmer et al. (1992), Hestholm and Ruud (1994), Graves (1996), and Robertsson (1996) developed the algorithm for irregular topography.

In this chapter, I derive velocity-stress elastic wave equations in the first section. In the second section, I extend it to the viscoelastic case and show its finite-difference implementation. Finally, I show some fundamental benchmark tests to demonstrate the accuracy and the reliability of a finite-difference code that I developed.

2.1 Velocity-stress Elastic Wave Equations

Although my finite-difference modeling is based on the viscoelastic wave equation, the method has been extended from elastic velocity-stress finite-difference modeling. The

derivation of the velocity-stress elastic wave equations gives the fundamental idea and mathematical foundation of the wave equation. The relationship between forces and deformation in infinitesimal strain theory is largely empirically based and given by a constitutive law called Hook's law. The deformation is a function of material properties of the body such as density, rigidity (resistance to shear), and incompressibility (resistance to change in volume). The material properties are known as elastic moduli. When stress varies with time, strain varies similarly, and the balance between stress and strain results in seismic waves. These waves travel at velocities that depend on the elastic moduli and are governed by equations of motion.

In the following description of the elastic wave equations, I will employ Cartesian coordinate (x_1, x_2, x_3). At first, I show a general three-dimensional relationships between nine strain components and three displacement components (u_1, u_2, u_3). Normal strain can be defined by

$$\varepsilon_{11} = \frac{\partial u_1}{\partial x_1} \qquad \varepsilon_{22} = \frac{\partial u_2}{\partial x_2} \qquad \varepsilon_{33} = \frac{\partial u_3}{\partial x_3}, \qquad (2.1.1)$$

here, x_2, x_2, x_3 are the coordinate axes. The first subscript indicates the orientation of the line segment, and second indicates the direction of length change. Shear strains are defined by

$$\varepsilon_{12} = \frac{1}{2}\left(\frac{\partial u_1}{\partial x_2} + \frac{\partial u_2}{\partial x_1} \right) \qquad \varepsilon_{21} = \frac{1}{2}\left(\frac{\partial u_2}{\partial x_1} + \frac{\partial u_1}{\partial x_2} \right)$$

$$\varepsilon_{13} = \frac{1}{2}\left(\frac{\partial u_1}{\partial x_3} + \frac{\partial u_3}{\partial x_1} \right) \qquad \varepsilon_{31} = \frac{1}{2}\left(\frac{\partial u_3}{\partial x_1} + \frac{\partial u_1}{\partial x_3} \right) . \qquad (2.1.2)$$

$$\varepsilon_{23} = \frac{1}{2}\left(\frac{\partial u_2}{\partial x_3} + \frac{\partial u_3}{\partial x_2} \right) \qquad \varepsilon_{32} = \frac{1}{2}\left(\frac{\partial u_3}{\partial x_2} + \frac{\partial u_2}{\partial x_3} \right)$$

These nine terms constitute the infinitesimal strain tensor, a symmetric tensor with six independent quantities that can be ordered as

$$\varepsilon_{ij} = \begin{pmatrix} \dfrac{\partial u_1}{\partial x_1} & \dfrac{1}{2}\left(\dfrac{\partial u_2}{\partial x_1}+\dfrac{\partial u_1}{\partial x_2}\right) & \dfrac{1}{2}\left(\dfrac{\partial u_3}{\partial x_1}+\dfrac{\partial u_1}{\partial x_3}\right) \\[3mm] \dfrac{1}{2}\left(\dfrac{\partial u_2}{\partial x_1}+\dfrac{\partial u_1}{\partial x_2}\right) & \dfrac{\partial u_2}{\partial x_2} & \dfrac{1}{2}\left(\dfrac{\partial u_3}{\partial x_2}+\dfrac{\partial u_2}{\partial x_3}\right) \\[3mm] \dfrac{1}{2}\left(\dfrac{\partial u_3}{\partial x_1}+\dfrac{\partial u_1}{\partial x_3}\right) & \dfrac{1}{2}\left(\dfrac{\partial u_3}{\partial x_2}+\dfrac{\partial u_2}{\partial x_3}\right) & \dfrac{\partial u_3}{\partial x_3} \end{pmatrix}. \qquad (2.1.3)$$

We can represent all nine strain terms of (2.1.3) with compact indicial notation,

$$\varepsilon_{ij} = \frac{1}{2}\left(\frac{\partial u_i}{\partial x_j} + \frac{\partial u_j}{\partial x_i}\right). \qquad (2.1.4)$$

The trace of the strain tensor is called the cubic dilatation, θ ,

$$\theta = \varepsilon_{ii} = \frac{\partial u_1}{\partial x_1} + \frac{\partial u_2}{\partial x_2} + \frac{\partial u_3}{\partial x_3} = \nabla \cdot u . \qquad (2.1.5)$$

Second, I define a stress tensor. Here, we subdivide the area of fictitious plane into area elements with surface area, ΔA. A small force, ΔF, acts on each elements. The stress components acting on the plane (x_1 face) that has a normal in the x_1 direction are defined by

$$\sigma_{11} = \lim_{\Delta A_1 \to 0} \frac{\Delta F_1}{\Delta A_1}$$

$$\sigma_{12} = \lim_{\Delta A_1 \to 0} \frac{\Delta F_2}{\Delta A_1}, \qquad (2.1.6)$$

$$\sigma_{13} = \lim_{\Delta A_1 \to 0} \frac{\Delta F_3}{\Delta A_1}$$

The first index of σ_{ij} in (2.1.6) corresponds to the direction of the normal to the plane being acted on by the force, and the second index indicates the direction of the force. For two other planes, we define six additional stress components,

$\sigma_{21}, \quad \sigma_{22}, \quad \sigma_{23}$ acting on the x_2 face,

$\sigma_{31}, \quad \sigma_{32}, \quad \sigma_{33}$ acting on the x_3 face.

All of these are implicitly functions of space and time. A three dimensional stress tensor is defined as

$$\sigma_{ij} = \begin{pmatrix} \sigma_{11} & \sigma_{12} & \sigma_{13} \\ \sigma_{21} & \sigma_{22} & \sigma_{23} \\ \sigma_{31} & \sigma_{32} & \sigma_{33} \end{pmatrix}.$$ (2.1.7)

The diagonal terms are called normal stresses, and the off-diagonal terms are called shear stresses.

Third, I consider a force balance on a cubic element in a continuum that is under going internal motions. Applying Newton's second law to the medium gives

$$\rho \frac{\partial^2 u_i}{\partial t^2} = f_i + \frac{\partial \sigma_{ij}}{\partial x_j}.$$ (2.1.8)

where f_i represents body forces. This set of three equation is called the equation of motion for a continuum. For example, u_1 (x_1 component of displacement) can be written as

$$\rho \frac{\partial^2 u_1}{\partial t^2} = \frac{\partial \sigma_{11}}{\partial x_1} + \frac{\partial \sigma_{12}}{\partial x_2} + \frac{\partial \sigma_{13}}{\partial x_3},$$ (2.1.9)

with no body forces.

Fourth, I show the relationship between stress and displacement. There are provided by constitutive laws that relate stress to strain. The most general form of constitutive law for linear elasticity is Hooke's law

$$\sigma_{ij} = c_{ijkl} \cdot \varepsilon_{kl}.$$ (2.1.10)

The constants of proportionality, C_{ijkl} are known as elastic moduli and define the material properties of the medium. In its general form, C_{ijkl} is a third-order tersor with 81 terms relating the nine elements of the strain tensor to nine elements of the stress tensor by linear sum. In the case of an isotropic elastic substance, the elastic moduli can reduce to two independent moduli called Lame constants, λ and μ. These are related to C_{ijkl} by

$$C_{ijkl} = \lambda \delta_{ij} \delta_{kl} + \mu \left(\delta_{ik} \delta_{jl} + \delta_{il} \delta_{jk} \right).$$ (2.1.11)

where the Kronecker dekta function is used. Inserting this into (2.1.10) gives,

$$\sigma_{ij} = \left(\lambda\delta_{ij}\delta_{kl} + \mu\left(\delta_{ik}\delta_{jl} + \delta_{il}\delta_{jk}\right)\right)\varepsilon_{kl},$$

(2.1.12)

which reduces to

$$\sigma_{ij} = \lambda\varepsilon_{kk}\delta_{ij} + 2\mu\varepsilon_{ij}.$$

(2.1.13)

Using the equation (2.1.5), (2.1.13) can be written as,

$$\sigma_{ij} = \lambda\theta\delta_{ij} + 2\mu\varepsilon_{ij}.$$

(2.1.14)

Thus, the stress-strain relationship is written as,

$$\sigma_{ij} = \begin{pmatrix} \lambda\theta+2\mu\varepsilon_{11} & 2\mu\varepsilon_{12} & 2\mu\varepsilon_{13} \\ 2\mu\varepsilon_{21} & \lambda\theta+2\mu\varepsilon_{22} & 2\mu\varepsilon_{23} \\ 2\mu\varepsilon_{31} & 2\mu\varepsilon_{32} & \lambda\theta+2\mu\varepsilon_{33} \end{pmatrix}.$$

(2.1.15)

Substituting the equations (2.1.3) and (2.1.5) into (2.1.15), the stress-strain relationship can be expressed as the stress-displacement relationship as follows (only i=1 terms are shown),

$$\sigma_{11} = \lambda\theta + 2\mu\varepsilon_{11} = \lambda\left(\frac{\partial u_1}{\partial x_1} + \frac{\partial u_2}{\partial x_2} + \frac{\partial u_3}{\partial x_3}\right) + 2\mu\frac{\partial u_1}{\partial x_1}$$

$$\sigma_{12} = 2\mu\varepsilon_{12} = \mu\left(\frac{\partial u_1}{\partial x_2} + \frac{\partial u_2}{\partial x_1}\right)$$

(2.1.16)

$$\sigma_{13} = 2\mu\varepsilon_{13} = \mu\left(\frac{\partial u_1}{\partial x_3} + \frac{\partial u_3}{\partial x_1}\right)$$

Now, I derive velocity-stress relationship in a two-dimensional case. In the following description, I use the x, z coordinate system in which x and z means x_1 axis and x_3 axis respectively. In a two-dimensional elastic case, the equation (2.1.8) reduces to following two equations.

$$\rho\frac{\partial^2 u_x}{\partial t^2} = \frac{\partial\sigma_{xx}}{\partial x} + \frac{\partial\sigma_{xz}}{\partial z}$$

(2.1.17)

$$\rho\frac{\partial^2 u_z}{\partial t^2} = \frac{\partial\sigma_{xz}}{\partial x} + \frac{\partial\sigma_{zz}}{\partial z}$$

And, substituting the equations (2.1.3) and (2.1.5) into (2.1.15) yields the following three equations.

$$\sigma_{xx} = \lambda\theta + 2\mu\varepsilon_{xx} = \lambda\left(\frac{\partial u_x}{\partial x} + \frac{\partial u_z}{\partial z}\right) + 2\mu\frac{\partial u_x}{\partial x} = (\lambda + 2\mu)\frac{\partial u_x}{\partial x} + \lambda\frac{\partial u_z}{\partial z}$$

$$\sigma_{zz} = \lambda\theta + 2\mu\varepsilon_{zz} = \lambda\left(\frac{\partial u_x}{\partial x} + \frac{\partial u_z}{\partial z}\right) + 2\mu\frac{\partial u_z}{\partial z} = (\lambda + 2\mu)\frac{\partial u_z}{\partial z} + \lambda\frac{\partial u_x}{\partial x} . \qquad (2.1.18)$$

$$\sigma_{xz} = 2\mu\varepsilon_{xz} = \mu\left(\frac{\partial u_x}{\partial z} + \frac{\partial u_z}{\partial x}\right)$$

The equations (2.1.17) and (2.1.18) can be transformed into the following first order hyperbolic system,

$$\frac{\partial v_x}{\partial t} = b\left(\frac{\partial\sigma_{xx}}{\partial x} + \frac{\partial\sigma_{xz}}{\partial z}\right)$$

$$\frac{\partial v_z}{\partial t} = b\left(\frac{\partial\sigma_{xz}}{\partial x} + \frac{\partial\sigma_{zz}}{\partial z}\right)$$

$$\frac{\partial\sigma_{xx}}{\partial t} = (\lambda + 2\mu)\frac{\partial v_x}{\partial x} + \lambda\frac{\partial v_z}{\partial z} , \qquad (2.1.19)$$

$$\frac{\partial\sigma_{zz}}{\partial t} = (\lambda + 2\mu)\frac{\partial v_z}{\partial z} + \lambda\frac{\partial v_x}{\partial x}$$

$$\frac{\partial\sigma_{xz}}{\partial t} = \mu\left(\frac{\partial v_x}{\partial z} + \frac{\partial v_z}{\partial x}\right)$$

where, $b = 1/\rho$, ρ is a density, v_x and v_z are particle velocities, σ_{xx} and σ_{zz} are normal stresses, σ_{xz} is a shear stress, and λ and μ are Lame's constants. This system is a fundamental equations for a velocity-stress staggered grid finite difference method that is widely used in exploration seismology and that my finite-difference method is based on.

14

2.2 Viscoelastic Formulation Using Standard Linear Solid

In the previous section, I was concerned with an elastic case. The real Earth is, however, not perfectly elastic and propagating waves attenuate with time due to various energy-loss mechanisms. The objective of this study is the application of finite-difference modeling to near surface seismic methods. The effect of attenuation on wave propagation is generally very large in a near surface region. The attenuation should be considered in a study about near surface wave propagation. For this reason, the following discussion of the free surface condition and the variable grid method will be concerned with the viscoelastic case. The anelastic behavior can be described by a viscoelastic model. Blanch et al. (1995) presented efficient viscoelastic modeling based on the Standard Linear Solids (SLS) in which a spring and dashpot in series, in parallel with a spring. In this method, the stress and strain relaxation times can be calculated by the least square method. Robertsson et al. (1994) presented a finite-difference scheme based on the second-order accurate time, fourth-order accurate space, O(2,4), velocity-stress staggered grid (Levander, 1988) for viscoelastic modeling. We employ this method because the additional computer memory requirement to that of elastic case is small compared with elastic case.

2.2.1 Viscoelastic Modeling Using τ

In this section, I describe a theoretical anelastic model based on viscoelastic theory, a phenomenological way to describe combined elastic and viscous behavior of materials. The basic hypothesis is that the current value of the stress tensor depends on the history of the strain tensor. The viscoelastic hypothesis can be described as

$$\sigma_{ij} = G_{ijkl} * \dot{\varepsilon}_{kl} = \dot{G}_{ijkl} * \varepsilon_{kl} ,\tag{2.2.1}$$

(Christensen, 1982) where * denotes time convolution, dot denotes derivative in time. The convolution transform each strain history, $\varepsilon_{ij}(t)$, into a corresponding stress history, $\sigma_{ij}(t)$.

15

G is a fourth-order tensor-valued function called the relaxation function. The relaxation function G determines the behavior of a material. For one-dimensional or in the special case of a simple shear in an isotropic homogeneous material, the equation (2.2.1) reduces to

$$\sigma = G * \dot{\varepsilon} = \dot{G} * \varepsilon .$$
(2.2.2)

The Standard Linear Solid (SLS) has been shown to be a general mechanical viscoelastic model. An array of SLS has the stress relaxation function,

$$G(t) = M_R \left(1 - \sum_{l=1}^{L} \left(1 - \frac{\tau_{\varepsilon l}}{\tau_{\sigma l}} \right) e^{\frac{-t}{\tau_{\sigma l}}} \right) \theta(t)$$
(2.2.3)

(Blanch et al., 1993) where, θ (t) is the Heaviside function, M_R is the relaxed stress modulus corresponding to G(t), and $\tau_{\sigma l}$ and $\tau_{\varepsilon l}$ are the stress and strain relaxation times for the lth SLS. M_R is related to the elastic modulus M_U (Liu et al.,1976).

$$M_U = M_R \left/ \left(1 - \sum_{l=1}^{L} \left(\frac{\tau_{\varepsilon l} - \tau_{\sigma l}}{\tau_{\varepsilon l}} \right) \right) \right. .$$
(2.2.4)

$M_U = \mu$ for transverse waves, and $M_U = \lambda + 2\mu$ for longitudinal waves (Aki and Richards, 1980). The complex stress modulus $M_C(\omega)$ is defined as the Fourier transform of the stress relaxation function. The quality factor Q is defined as

$$Q(\omega) = \frac{\text{Re}\left(Mc\left(\omega\right)\right)}{\text{Im}\left(Mc\left(\omega\right)\right)} ,$$
(2.2.5)

this equation defines Q as the number of wavelengths a pulse may propagate before its amplitude drops by a factor of $e^{-\pi}$. Thus, Q is a function of frequency. For an array of Standard Linear Solids, the equation (2.2.3) and (2.2.5) yield,

$$Q(\omega) = \frac{1 - L + \sum_{l=1}^{L} \frac{1 + \omega^2 \tau_{\varepsilon l} \tau_{\sigma l}}{1 + \omega^2 \tau_{\sigma l}^2}}{\sum_{l=1}^{L} \frac{\omega\left(\tau_{\varepsilon l} - \tau_{\sigma l}\right)}{1 + \omega^2 \tau_{\sigma l}^2}} ,$$
(2.2.6)

Blanch et al. (1995) proposed the τ -method for the viscoelastic modeling. The τ method is based on the simple observation that the level of attenuation caused by a SLS can

16

be determined by a dimensionless (frequency scale independent) variable τ . If we defined τ as

$$\tau = \frac{\tau_{\varepsilon l}}{\tau_{\sigma l}} - 1 = \frac{\tau_{\varepsilon l} - \tau_{\sigma l}}{\tau_{\sigma l}} , \qquad (2.2.7)$$

the inverse of Q and the velocity c(ω) for one SLS can be written as,

$$Q^{-1} = \frac{\omega \tau_{\varepsilon l} \tau}{1 + \omega^2 \tau_{\sigma l}^2 (1 + \tau)} , \qquad (2.2.8)$$

$$(c(\omega))^2 = \frac{M_U}{\rho} \left(1 + \left(\frac{M_U}{M_R} - 1 \right) \frac{1}{1 + \omega^2 \tau_{\varepsilon l}^2} \right)^{-1} . \qquad (2.2.9)$$

Using the parameter τ to tune an array of SLSs, and assuming that τ is small (i.e. $1 + \tau \approx 1$), equation (2.2.6) yields

$$Q^{-1} = \sum_{l=1}^{L} \frac{\omega \tau_{\varepsilon l} \tau}{1 + \omega^2 \tau_{\sigma l}^2} . \qquad (2.2.10)$$

In this expression Q^{-1} is linear in τ . Therefore, we can easily find the best approximation in the least square sense over a predefined frequency range to any Q_0 by minimizing over τ the expression,

$$J = \int_{\omega_a}^{\omega_b} (Q^{-1}(\omega, \tau, \tau_l) - Q_0^{-1})^2 d\omega , \qquad (2.2.11)$$

to zero and solve for τ . To find the minimum, we set the derivative of J with respect to τ to zero and solve for τ .

$$\frac{dJ}{d\tau} = 2 \int_{\omega_a}^{\omega_b} (Q^{-1}(\omega, \tau, \tau_l) - Q_0^{-1}) \times \frac{dQ^{-1}(\omega, \tau_{\sigma l}, \tau)}{d\tau} d\omega = 0 . \qquad (2.2.12)$$

The final formula for τ is

17

$$\tau = \frac{1}{Q_0} \cdot \frac{\displaystyle\sum_{l=1}^{L} I_{0l}}{\displaystyle\sum_{l=1}^{L} I_{1l} + 2\sum_{l=1}^{L-1}\sum_{k=l+1}^{L} I_{2kl}}$$
(2.2.13)

where,

$$I_{0l} = \frac{1}{2\tau_{\sigma l}}\left[\log\left(1 + \omega^2\tau_{\sigma l}^2\right)\right]_{\omega_a}^{\omega_b}$$
(2.2.14)

$$I_{1l} = \frac{1}{2\tau_{\sigma l}}\left[\arctan\left(\omega\tau_{\sigma l}\right) - \frac{\omega\tau_{\sigma l}}{1 + \omega^2\tau_{\sigma l}^2}\right]_{\omega_a}^{\omega_b}$$
(2.2.15)

$$I_{2lk} = \frac{\tau_{\sigma l}\tau_{\sigma k}}{\tau_{\sigma k}^2 - \tau_{\sigma l}^2}\left[\frac{\arctan\left(\omega\tau_{\sigma l}\right)}{\tau_{\sigma l}} - \frac{\arctan\left(\omega\tau_{\sigma k}\right)}{\tau_{\sigma k}}\right]_{\omega_a}^{\omega_b}$$
(2.2.16)

$$\tau_{\sigma l} = \frac{1}{\omega_l},$$
(2.2.17)

where, ω_1 is the frequency of interest. Figures 2.1 and 2.2 shows the example of Q(ω) and c(ω) defined by one SLS mechanism in which following parameters are used,

Q=10

τ_r=0.003848

τ_σ=0.003183

density : ρ=2000kg/m^3

velocity :c(ω=∞)=2000m/sec (M.=8GPa)

ω_1=50Hz$\times$2π,

where τ_σ is given by equation (2.2.17), τ is given by equations (2.2.13) to (2.2.16), and τ_r is given by equation (2.2.7). The Q shown in Figure 2.1 is given by equation (2.2.8), and the velocity shown in Figure 2.2 is given by equation (2.2.9).

2.2.2 Viscoelastic Staggered Grid Finite-difference Method

Robertsson et al. (1994) proposed the viscoelastic finite-difference modeling based on the τ method mentioned above. For simplicity, I will derive the equations for a one-dimensional case, where the viscoelastic equations are the same as the viscoacoustic. From the definition of pressure and dilatation,

$$\sigma = -p ,\tag{2.2.18}$$

and

$$-\dot{\varepsilon} = \upsilon_x ,\tag{2.2.19}$$

where v is the particle velocity, and subscript x means spatial derivative. Taking the time derivative of equation (2.2.2) and using equations (2.2.18) and (2.2.19) leads to,

$$-\dot{p} = \dot{G} * \upsilon_x .\tag{2.2.20}$$

Substituting equation (2.2.3) into (2.2.20) yields,

$$-\dot{p} = M_R\left(1 - \sum_{l=1}^{L}\left(1 - \frac{\tau_{\varepsilon l}}{\tau_{\sigma l}}\right)\right)\upsilon_x + M_R\left(\sum_{l=1}^{L}\frac{1}{\tau_{\sigma l}}\left(1 - \frac{\tau_{\varepsilon l}}{\tau_{\sigma l}}\right)e^{\frac{-t}{\tau_{\sigma l}}}\right)\theta(t) * \upsilon_x .\tag{2.2.21}$$

The convolution terms in the equation (2.2.21) can be eliminated by introducing so-called memory variables, which will be denoted r_l (Carcione et al., 1988). Then, equation (2.2.21) reduces to,

$$-\dot{p} = M_R\left(1 - \sum_{l=1}^{L}\left(1 - \frac{\tau_{\varepsilon l}}{\tau_{\sigma l}}\right)\right)\upsilon_x + \sum_{l=1}^{L} r_l ,\tag{2.2.22}$$

where

$$r_l = M_R\left(\frac{1}{\tau_{\sigma l}}\left(1 - \frac{\tau_{\varepsilon l}}{\tau_{\sigma l}}\right)e^{\frac{-t}{\tau_{\sigma l}}}\right)\theta(t) * \upsilon_x . \quad 1 \leq l \leq L .\tag{2.2.23}$$

From the equation (2.2.23), we see that r_l is governed by convolutions of v_x with exponential functions. A set of first-order linear differential equations can be obtained instead of the convolution as follows. First, by taking the time derivative of equation (2.2.23), we obtain,

$$\dot{r}_l = -\frac{1}{\tau_{\sigma l}} M_R \left(\frac{1}{\tau_{\sigma l}} \left(1 - \frac{\tau_{\varepsilon l}}{\tau_{\sigma l}} \right) e^{\frac{-t}{\tau_{\sigma l}}} \right) \theta(t) * \upsilon_x + M_R \left(\frac{1}{\tau_{\sigma l}} \left(1 - \frac{\tau_{\varepsilon l}}{\tau_{\sigma l}} \right) e^{\frac{-t}{\tau_{\sigma l}}} \right) \delta(t) * \upsilon_x.$$

$$1 \le l \le L \qquad (2.2.24)$$

From equation (2.2.23) we notice that equation (2.2.24) reduces to

$$\dot{r}_l = -\frac{1}{\tau_{\sigma l}} r_l + M_R \left(\frac{1}{\tau_{\sigma l}} \left(1 - \frac{\tau_{\varepsilon l}}{\tau_{\sigma l}} \right) e^{\frac{-t}{\tau_{\sigma l}}} \right) \upsilon_x, \quad 1 \le l \le L. \qquad (2.2.25)$$

We have derived a set of first-order linear differential equations for the memory variables. Newton's second law completes the full description of wave propagation in a viscoelastic medium. That is,

$$\rho \dot{\upsilon} = -p_x, \qquad (2.2.26)$$

where ρ is the density. From equations (2.2.22), (2.2.25) and (2.2.26), we can derive staggered grid finite-difference equations (second-order accurate in time, fourth-order accurate in space) as follows,

$$p_j^{n+1/2} = p_j^{n-1/2} - M_R \frac{\tau_{\varepsilon l}}{\tau_{\sigma l}} \frac{\Delta t}{\Delta h} \left(c_1 \left(\upsilon_{j+3/2}^n - \upsilon_{j-3/2}^n \right) + c_2 \left(\upsilon_{j+1/2}^n - \upsilon_{j-1/2}^n \right) \right)$$

$$- \frac{\Delta t}{2} \left(r_j^{n+1/2} + r_j^{n-1/2} \right) \qquad (2.2.27)$$

$$r_j^{n+1/2} = \frac{1}{1 + \frac{\Delta t}{2\tau_{\sigma l}}} \left(r_j^{n-1/2} \left(1 - \frac{\Delta t}{2\tau_{\sigma l}} \right) - M_R \frac{1}{\tau_{\sigma l}} \left(\frac{\tau_{\varepsilon l}}{\tau_{\sigma l}} - 1 \right) \right.$$

$$\left. \times \frac{\Delta t}{\Delta h} \left(c_1 \left(\upsilon_{j+3/2}^n - \upsilon_{j-3/2}^n \right) + c_2 \left(\upsilon_{j+1/2}^n - \upsilon_{j-1/2}^n \right) \right) \right] \qquad (2.2.28)$$

$$\upsilon_j^{n+1/2} = \upsilon_j^{n-1/2} - \frac{\Delta t}{\Delta h \rho} \left(c_1 \left(p_{j+3/2}^n - p_{j-3/2}^n \right) + c_2 \left(p_{j+1/2}^n - p_{j-1/2}^n \right) \right) \quad (2.2.29)$$

$$c_1 = -\frac{1}{24}, \quad c_2 = \frac{9}{8} \qquad (2.2.30)$$

where Δt is the time step and Δh is the spatial step. Indices n and j correspond to time and

20

space coordinates respectively ($p_j^n = p(n\Delta t, j\Delta h)$). In the equation (2.2.28), Crank-Nicolson scheme (Strang, 1986) is employed to ensure a stable solution. Figure 2.3 shows the one-dimensional staggered finite-difference grid.

The results from the one-dimensional case described above are easily generalized to higher dimensions (Appendix A). In two-dimensional viscoelastic staggered grid finite-difference modeling, the following three sets of equations are solved.

Equations governing stress:

$$\frac{\partial \sigma_{xx}}{\partial t} = \pi \frac{\tau_\varepsilon^p}{\tau_\sigma} \left(\frac{\partial \upsilon_x}{\partial x} + \frac{\partial \upsilon_z}{\partial z} \right) - 2\mu \frac{\tau_\varepsilon^s}{\tau_\sigma} \frac{\partial \upsilon_z}{\partial z} + r_{xx} \qquad (2.2.31)$$

$$\frac{\partial \sigma_{zz}}{\partial t} = \pi \frac{\tau_\varepsilon^p}{\tau_\sigma} \left(\frac{\partial \upsilon_x}{\partial x} + \frac{\partial \upsilon_z}{\partial z} \right) - 2\mu \frac{\tau_\varepsilon^s}{\tau_\sigma} \frac{\partial \upsilon_x}{\partial x} + r_{zz} \qquad (2.2.32)$$

$$\frac{\partial \sigma_{xz}}{\partial t} = \mu \frac{\tau_\varepsilon^s}{\tau_\sigma} \left(\frac{\partial \upsilon_x}{\partial z} + \frac{\partial \upsilon_z}{\partial x} \right) + r_{xz} \qquad (2.2.33)$$

Equations governing particle velocities:

$$\frac{\partial \upsilon_x}{\partial t} = \frac{1}{\rho} \left(\frac{\partial \sigma_{xx}}{\partial x} + \frac{\partial \sigma_{xz}}{\partial z} \right) \qquad (2.2.34)$$

$$\frac{\partial \upsilon_z}{\partial t} = \frac{1}{\rho} \left(\frac{\partial \sigma_{xz}}{\partial x} + \frac{\partial \sigma_{zz}}{\partial z} \right) \qquad (2.2.35)$$

Equations governing the so called memory variables, which are introduced to eliminate the numerically inconvenient convolution arising in the viscoelastic constitutive relation:

$$\frac{\partial r_{xx}}{\partial t} = -\frac{1}{\tau_\sigma} \left(r_{xx} + \pi \left(\frac{\tau_\varepsilon^p}{\tau_\sigma} - 1 \right) \left(\frac{\partial \upsilon_x}{\partial x} + \frac{\partial \upsilon_z}{\partial z} \right) - 2\mu \left(\frac{\tau_\varepsilon^s}{\tau_\sigma} - 1 \right) \frac{\partial \upsilon_z}{\partial z} \right) \quad (2.2.36)$$

$$\frac{\partial r_{zz}}{\partial t} = -\frac{1}{\tau_\sigma}\left(r_{zz} + \pi\left(\frac{\tau_\varepsilon^p}{\tau_\sigma} - 1\right)\left(\frac{\partial v_x}{\partial x} + \frac{\partial v_z}{\partial z}\right) - 2\mu\left(\frac{\tau_\varepsilon^s}{\tau_\sigma} - 1\right)\frac{\partial v_x}{\partial x}\right) \quad (2.2.37)$$

$$\frac{\partial r_{xz}}{\partial t} = -\frac{1}{\tau_\sigma}\left(r_{xz} + \mu\left(\frac{\tau_\varepsilon^s}{\tau_\sigma} - 1\right)\left(\frac{\partial v_x}{\partial z} + \frac{\partial v_z}{\partial x}\right)\right) \quad (2.2.38)$$

σ_{ij} : the ijth component of the symmetric stress tensor.

v_i : the ith component of the particle velocity.

r_{ij} : the memory variables.

τ_ε^p 、 τ_ε^s : the viscoelastic strain relaxation times for P- and SV-waves, respectively.

τ_σ :the viscoelastic stress relaxation time for both the P- and SV waves.

μ : the relaxation modulus corresponding to SV-waves, which is analogous to Lame constant μ in the elastic case.

π : the relaxation modulus corresponding to P-wave, which is analogous to $\lambda + 2\mu$ in the elastic case.

ρ : the density.

Equation (2.2.31) to (2.2.35) corresponds to equations (2.1.19) in the elastic case. In order to calculate equations (2.2.31) to (2.2.38), I employed second-order accurate in time and forth-order accurate in space O(2,4) scheme as I showed for the one-dimensional case. The differential equations are given in Appendix B. In this implementation, the finite-difference grid is staggered in space as shown in Figures 2.4 to 2.6.

In the two-dimensional case, the viscoelastic horizontal free-surface satisfies the following conditions:

$$\sigma_{iz} = 0 \qquad i=x,z \qquad (2.2.39)$$

$$r_{iz} = 0 \qquad i=x,z \qquad (2.2.40)$$

22

these conditions lead the following equations by using equations (2.2.31) to (2.2.33):

$$\frac{\partial v_x}{\partial z} = -\frac{\partial v_z}{\partial x}$$ (2.2.41)

$$\frac{\partial v_z}{\partial z} = -\left(1 - 2\frac{\tau_\varepsilon^s}{\tau_\varepsilon^p}\frac{\mu}{\pi}\right)\frac{\partial v_x}{\partial x}.$$ (2.2.42)

Vertical free-surface boundary can be implemented in the same way.

The stability criteria for the conditionally stable schemes are similar to elastic schemes (Levander, 1988). The Courant number ($c\Delta t/\Delta x$, where c is the velocity) for viscoelastic schemes has to be adjusted to the highest phase velocity, which is found at infinite frequency c_{max} as follows :

$$c_{max} = \sqrt{\tau_\varepsilon M_R \Big/ \tau_\sigma \rho}.$$ (2.2.43)

In order to minimize artificial reflections from the boundaries of a model, Higdon's (1986, 1987, 1990) absorbing boundary condition is used in the calculation.

2.3 Basic Test of the Accuracy of the Viscoelastic Finite-difference Method

In the next chapter, I will discuss the accuracy of finite-difference calculation in the presence of irregular free surface. To clarify the discussion about irregular free surface and show the reliability of the finite-difference code that I developed, I will show several fundamental benchmark tests in homogeneous case.

2.3.1 1-D Acoustic Case

First, I will show the accuracy of the forth-order approximation in space by comparison

with the second-order approximation in space in a one-dimensional case. An acoustic homogeneous model with velocity of 2000m/s, a density of 1500kg/m³ is used for this comparative study. The source is a point explosion represented with a 100 Hz Ricker wavelet. Nominal wavelength is 20m. The waveforms were collected at a 100m source receiver offset. The grid size is varied from 0.5m to 10m. Table 2.1 shows the results of the simulations as a function of grid size.

Table 2.1 Grid sizes and numerical dispersion in 1D simulation

Grid size (m)	Wavelength/grid size	Dispersion	
		2nd order (Figure 2.7)	4th order (Figure 2.8)
0.5	40	No	No
1	20	No	No
2	10	Small	No
2.5	8	Medium	Small
4	5	Large	Medium
5	4	Large	Large
10	2	Large	Large

In Figure 2.7 and Figure 2.8, particle velocities from the simulation with various grid sizes are plotted together with the analytical solution. The results of the simulation can be summarized as follows.

For the grid size of 0.5m and 1m (approximately 40 and 20 grid-points per wave length), the simulation yields sufficiently accurate results. However, for the grid size of 2m (approximately 10 grid-points per wave length), we can see obvious numerical dispersion in the calculation of second-order approximation. On the contrary, we can see that the fourth-order approximation has no numerical dispersion. Furthermore, in the case of the grid size of 2.5m (approximately 8 grid-points per wave length), the numerical dispersion is little in fourth-order approximation. These results confirm that the second-order approximation requires 20 grid-points per wave length and fourth-order approximation requires 10 grid-points per wave length in the case of a one-dimensional simulation.

2.3.2 2-D Elastic Case

In 2-D elastic medium, we have P- and S- waves which propagate with different velocity and wavelength. We also have surface waves in the presence of the free surface. Here, I will show the numerical dispersion due to the variation of grid sizes for these three waves. The model is an infinite elastic solid with P- and S-velocities of 2000 and 1000m/s, respectively, and a density of 1800kg/m^3. The source is a point explosion for P-wave, and a vertical force for S-wave with a 50 Hz Ricker wavelet . Thus, the approximate P- and S-wave wavelength are 40 and 20m respectively. The waveforms were collected at the right side of the source (x direction). The source receiver offset is 100m. The grid sizes were varied from 0.5m to 10m. Table 2.2 shows the list of the grid sizes as well as the results of the simulation.

Table 2.2   Grid sizes and numerical dispersion in 2D simulation

Grid size (m)	P-wave			S-wave	
	Wavelength/ grid size	Dispersion		Wavelength/ grid size	Dispersion
		2nd order (Figure 2.9)	4th order (Figure 2.10)		4th order (Figure 2.11)
0.5	80	No	No	40	No
1	40	No	No	20	No
2	20	No	No	10	No
2.5	16	No	No	8	Small
4	10	Small	No	5	Large
5	8	Large	Small	4	Large
10	4	Large	Large	2	Large

In Figure 2.9 to Figure 2.11, pressure from the simulation for the P-wave, and the vertical component of particle velocity for the S-wave with various grid sizes are plotted. In Figure 2.9 and Figure 2.10, analytical solutions are plotted together with the finite-difference solutions. In the case of the P-waves, for the grid size of 0.5m to 2.5m (approximately 80 to 16 grid-points per wave length), the simulation yields sufficiently accurate results. However, for the grid size of 4m (approximately 10 grid-points per wave length), we can see obvious numerical dispersion in the calculation of second-order approximation. On the contrary, we can see that the fourth-order approximation has no numerical dispersion.

25

Furthermore, in the case of the grid size of 5m (approximately 8 grid-points per wave length), the numerical dispersion is small in the fourth-order approximation. For S-waves in the grid size of 0.5m and 1m (approximately 40 and 20 grid-points per wave length), the simulation yield sufficiently accurate results. There is little dispersion in the grid size of 2m (approximately 10 grid-points per wave length), and obvious dispersion in the grid size of 2.5m (approximately 8 grid-points per wave length).

A flat semi-infinite elastic medium was used for the simulation of surface waves (Rayleigh waves). The model is a Poisson solid with P- and S-velocities of 3000 and 1730m/s, respectively, and a density of 2500kg/m³. A source and a receiver were placed on the surface. The source is a 15Hz Ricker wavelet that generates vertical component of particle velocity at a point on the free surface. The wavelength of Rayleigh waves is approximately 100m. The waveforms were collected at the 1000m source receiver offset. The grid sizes were varied from 5m to 25m. Table 2.3 shows the list of the grid sizes as well as the results of the simulation.

Table 2.3 Grid sizes and numerical dispersion for the simulation of Rayleigh waves (Figure 2.12)

Grid size (m)	Wavelength/grid size	Dispersion
		4th order
5	20	No
10	10	No
12.5	8	Small
20	5	Large
25	4	Large

In Figure 2.12, the vertical component of particle velocities from the simulation with various grid sizes are plotted. For the grid size of 5m and 10m (approximately 20 and 10 grid-points per wave length), the simulation yields sufficiently accurate results. There is little dispersion in the grid size of 12.5m (approximately 8 grid-points per wave length), and obvious dispersion in the grid size of 20m (approximately 5 grid-points per wave length).

The results of the simulation for two-dimensional elastic case can be summarized as follows. The second-order approximation requires 20 grid-points per wavelength and fourth-order approximation requires 10 grid-points per wavelength. It should be noted that we have to consider the wavelength of S-waves and surface waves with respect to S-velocity.

2.3.3 Viscoelastic Model

In this section, I will show three basic benchmark tests of viscoelastic modeling by comparison with analytical solutions.

The first example is a one-dimensional model that is an infinite viscoacoustic medium with velocity of 2000m/s and a density of 2000kg/m^3. I will show three calculations in which a quality factor Q is 20, 50, 100 respectively. The receivers are located 0m to 190m from the source at 10m distance interval. For a source wavelet, 50Hz Ricker wavelet is employed. An analytical solution can be calculated in frequency domain by the use of complex velocity c(ω) given by the following equation (Lay and Wallace, 1995),

$$c(\omega) = c(\omega_{ref})\left(1 + \frac{1}{\pi Q(\omega)}\ln\left(\frac{\omega}{\omega_{ref}}\right) + \frac{i}{2Q(\omega)}\right) , \qquad (2.2.44)$$

where, Q(ω) is a quality factor, ω_{ref} is some reference frequency, c(ω_{ref}) is a velocity at the reference frequency. In this example, ω_{ref} of 50Hz, and elastic modulus M_U of 8Gpa ($2000^2 \times 2000$) were used. c(ω_{ref}) were calculated by equation (2.2.9). Table 2.4 shows the relaxation times for three Q models which were optimized by the least square method mentioned in the previous section and c(ω_{ref}). These relaxation times are calculated for the τ_σ of 0.003183 that is obtained from equation (2.2.17), and optimized for a frequency range from 25 to 75Hz.

27

Table 2.4   Relaxation times (sec) and a velocity (m/sec) at the reference frequency for three different Q model.

	τ_σ	τ_t	$c(\omega_{ref})$.
Q=10	0.003183	0.003848	1920
Q=20	0.003183	0.003515	1954
Q=50	0.003183	0.003316	1980

In Figure 2.13 to 2.15, the particle velocity from the simulation and an analytical solution are plotted. We can see that the finite-difference solutions closely agree with analytical solutions without the slight difference in the phase velocity. I will comment about this difference later. In order to investigate the accuracy of the simulation, I compare the maximum amplitude of the finite-difference solution with theoretical amplitude. In Figure 2.16, the maximum amplitude of the finite-difference solution is plotted together with the theoretical amplitude A(x) obtained from the following equation;

$$A(x) = A_0 \exp\left(- \frac{f\pi x}{cQ} \right),$$

(2.2.45)

Here, A_0 is the amplitude at the source, x is the distance between the source and a receiver, c is the velocity (2000m/sec), f is the frequency (50Hz). In Figure 2.16, we can see that the amplitude of the finite-difference solution agrees with the theoretical one very well. I also calculated a quality factor $Q(\omega)$ and phase velocity $c(\omega)$ from the finite-difference solution in the frequency domain using the amplitude ratio of two traces. Two traces used in the calculation are 90m and 190m. Figure 2.17 shows the amplitude ratio of two traces obtained by Fourier transform as well as the theoretical Q obtained from the equation (2.2.8). Figure 2.18 shows the phase velocity obtained by Fourier transform as well as the theoretical velocity $c(\omega)$ obtained from the equation (2.2.9). In Figure 2.17 and Figure 2.18, we can see that the finite-difference solution $Q(\omega)$ and $c(\omega)$ is very close to the analytical $Q(\omega)$ and $c(\omega)$.

The second example is the two-dimensional case. The model is an infinite viscoelastic solid with P- and S- wave velocities of 2000 and 1000 respectively, density of 1800kg/m³ and Q

28

of 20 (both Q_p and Q_s). The source is a point explosion with a 50Hz Ricker wavelet.   The relaxation times optimized by the least square method are listed in Table 2.7. These relaxation times are calculated for the τ_σ of 0.003183 that is obtained from equation (2.2.21), and optimized for frequency range from 25 to 75Hz. Same relaxation times are used for both Q_p and Q_s.

Table 2.7   Relaxation times for two-dimensional example

	τ_σ	τ_ϵ
Q=20	0.003183	0.003515

The receivers are located at the right side of the shot (positive x direction) from 10m to 163m from the source at 9m distance interval. In figure 2.19, the pressure from the simulation is plotted together with the elastic case (Q = infinity). The dispersion due to the viscoelastic attenuation looks to be a correct tendency. The maximum amplitude of viscoelastic and elastic calculations are plotted in Figure 2.20, together with the theoretical amplitude. In a two dimensional case, the theoretical amplitude of body waves can be calculated by following equation,

$$A(x) = A_0 \exp\left(-\frac{f\pi(x - x_0)}{cQ}\right) \times \sqrt{\frac{x_0}{x}}, \qquad (2.2.46)$$

here A_0 is the amplitude at the some reference receiver, x_0 is the location of the reference receiver, x is the location of each receiver, c is the velocity (2000m/sec), f is the frequency (50Hz). The amplitude of both the finite-difference and theoretical solutions closely agrees.

These numerical examples prove the accuracy and reliability of this viscoelastic modeling as well as my finite-difference code. The results also implies that the few pairs of relaxation mechanism can yield sufficiently accurate results for practical purposes.
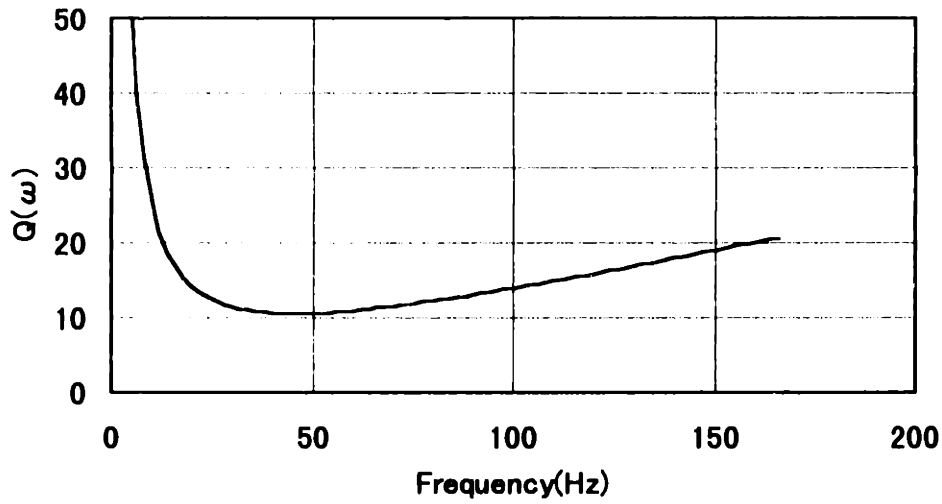
Figure 2.1:   Approximation to a constant Q of 10 by one SLS mechanism
using the equation (2.2.8). τ_ε=0.003848, τ_σ=0.003183. density : ρ =2000kg/m³,
velocity :c(ω =∞)=2000m/sec, (M_U=8GPa), ω_1=50Hz×2 π .
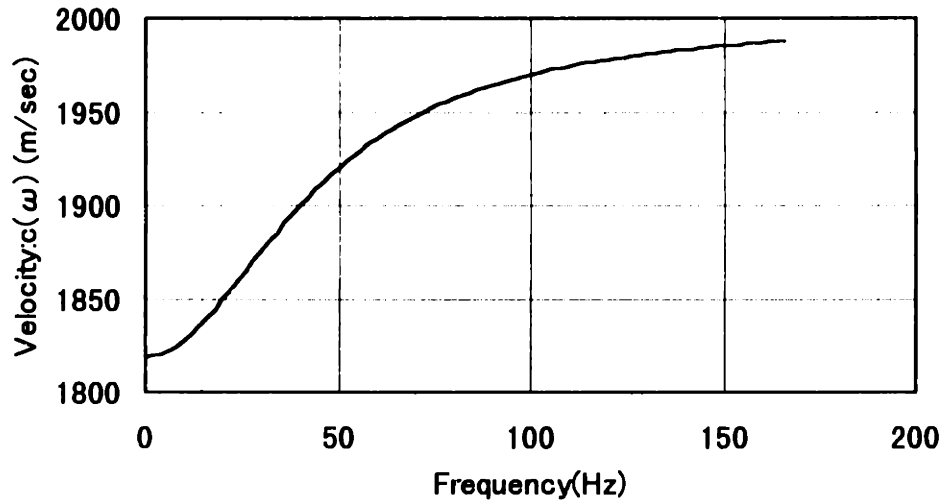
Figure 2.2:   Velocity defined by one SLS mechanism using the equation (2.2.9).
τ_ε=0.003848, τ_σ=0.003183. density : ρ =2000kg/m³,
velocity :c(ω =∞)=2000m/sec, (M_U=8GPa), ω_1=50Hz×2 π .

a) Discretization of the medium on a 1-D staggered grid.

b) A second-order spatial stencil for the stress update.

c) A second-order spatial stencil for the velocity update.

d) A fourth-order spatial stencil for the stress update.

e) A fourth-order spatial stencil for the velocity update.
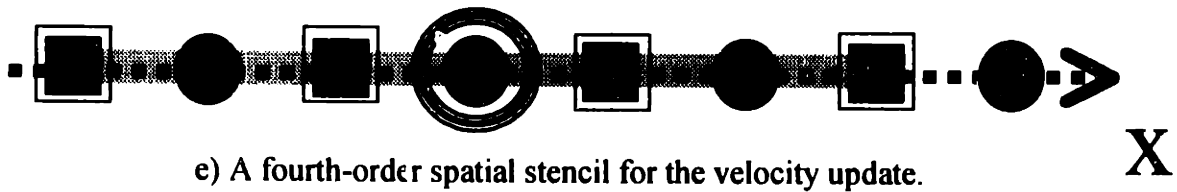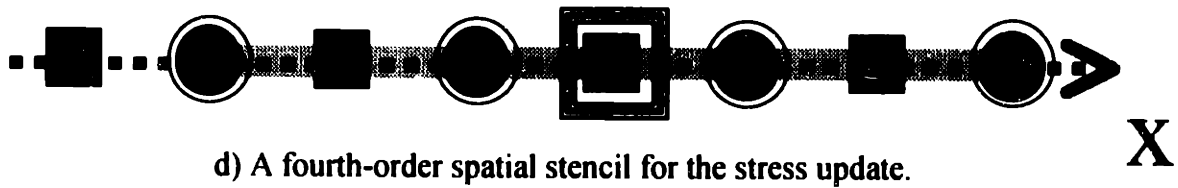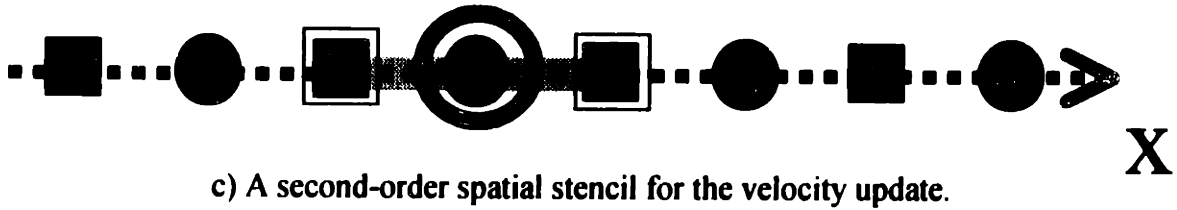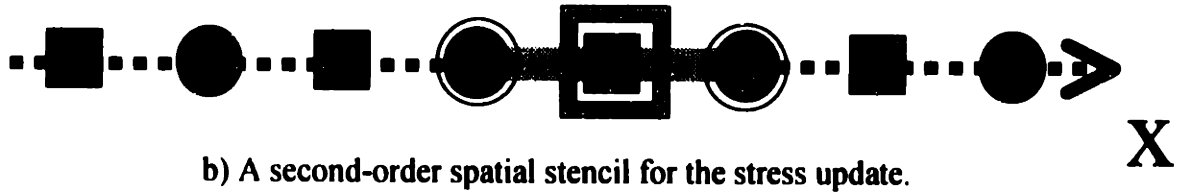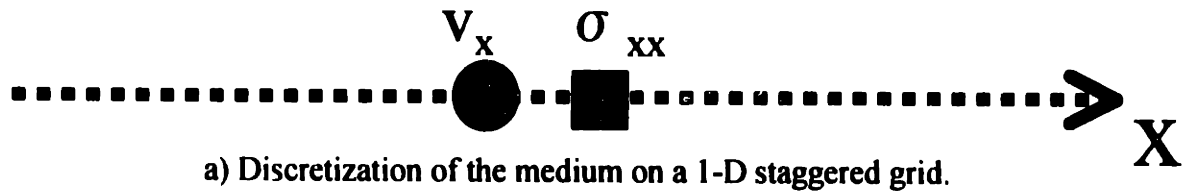
Figure 2.3: The one dimensional staggered finite-difference grid. σ_{xx} is a normal stress, and v_x is a velocity in x-direction.
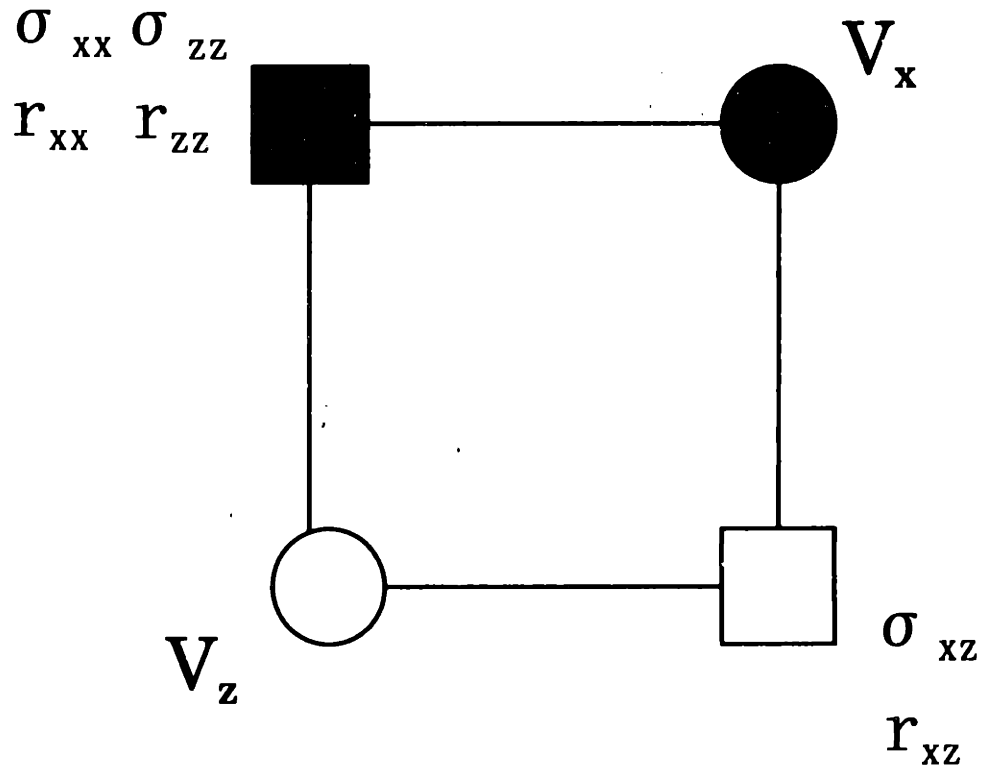
Figure 2.4: The two dimensional staggered finite-difference grid. σ_{xx} and σ_{zz} are normal stresses, v_x and v_z are particle velocities. r_{xx}, r_{zz} and r_{xz} are memory variables.
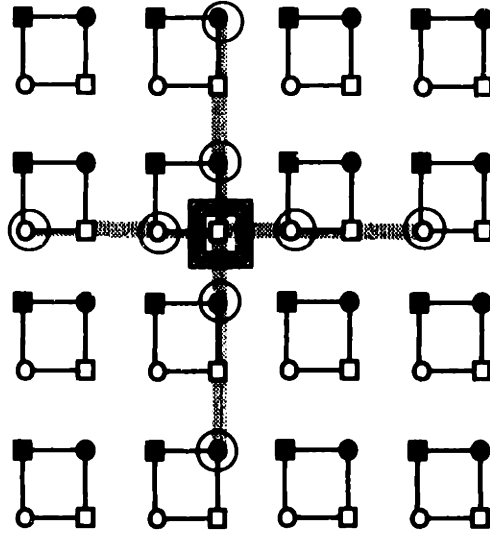
a) A stencil for a shear stress, σ_{xz}, and a memory variable r_{xz}.
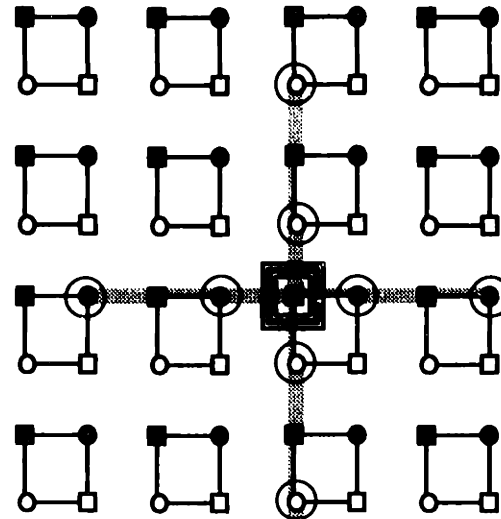
b) A stencil for normal stresses, σ_{xx} and σ_{zz}, and memory variables r_{xx} and r_{zz}.

Figure 2.5: Fourth-order spatial stencils for stress update. Within the grid-cells, the solid squares represent the σ_{xx}, σ_{zz}, r_{xx}, r_{zz}, components, the light squares the σ_{xz}, r_{xz} components, the solid circles the v_x components, the light circles represent the v_z components(σ : stress, r: memory variable, v: velocity).
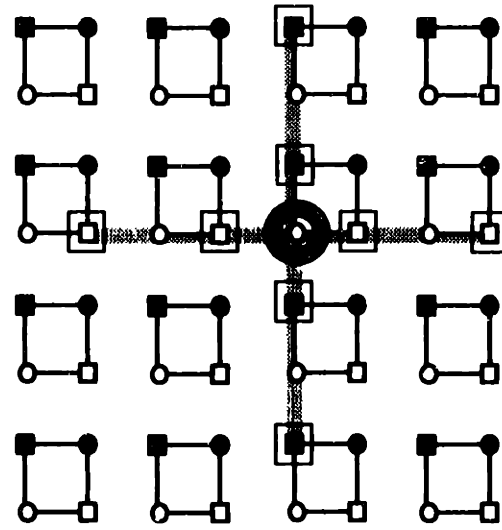
a) A stencil for a particle velocity, v_z.
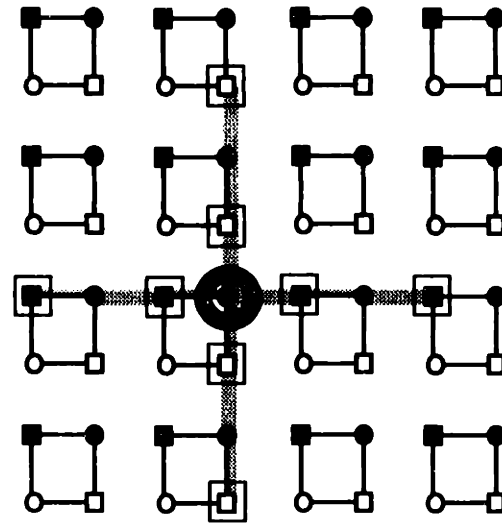
b) A stencil for a particle velocity, v_x.

Figure 2.6: Fourth-order spatial stencils for velocity update. Within the grid-cells, the solid squares represent the σ_{xx}, σ_{zz}, r_{xx}, r_{zz}, components, the light squares the σ_{xz}, r_{xz} components, the solid circles the v_x components, the light circles represent the v_z components(σ : stress, r: memory variable, v: velocity).

T i m e (msec)

0	10	20	30	40	50	60	70	80	90	100	110	

Analytical solution.

Source wavelet.

Δx=0.5m
λ/Δx=40

Δx=1.0m
λ/Δx=20

Δx=2.0m
λ/Δx=10

Δx=2.5m
λ/Δx=8

Δx=4.0m
λ/Δx=5

Δx=5.0m
λ/Δx=4

Δx=10.0m
λ/Δx=2
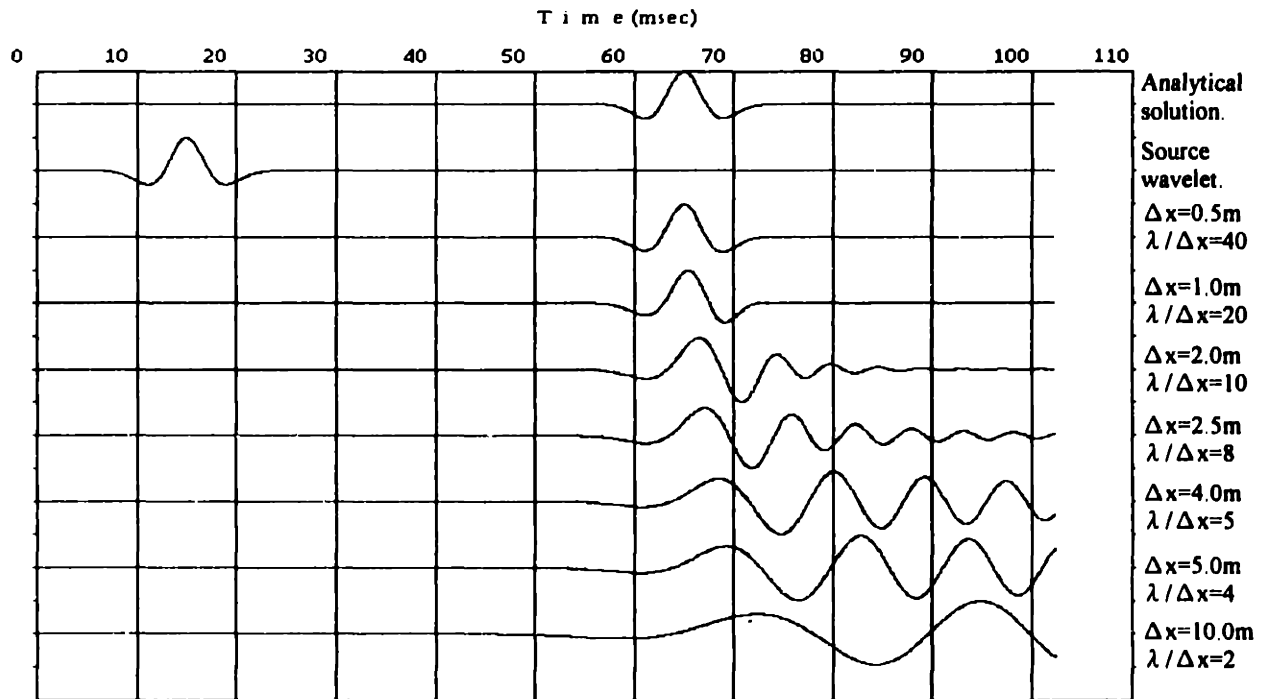
Figure 2.7: Particle velocities from the second-order approximation with various grid sizes (one-dimensional). Δx means grid size and λ/Δx means wavelength per grid size.

T i m e (msec)

0	10	20	30	40	50	60	70	80	90	100	110	

Analytical solution.

Source wavelet.

Δx=0.5m
λ/Δx=40

Δx=1.0m
λ/Δx=20

Δx=2.0m
λ/Δx=10

Δx=2.5m
λ/Δx=8

Δx=4.0m
λ/Δx=5

Δx=5.0m
λ/Δx=4

Δx=10.0m
λ/Δx=2
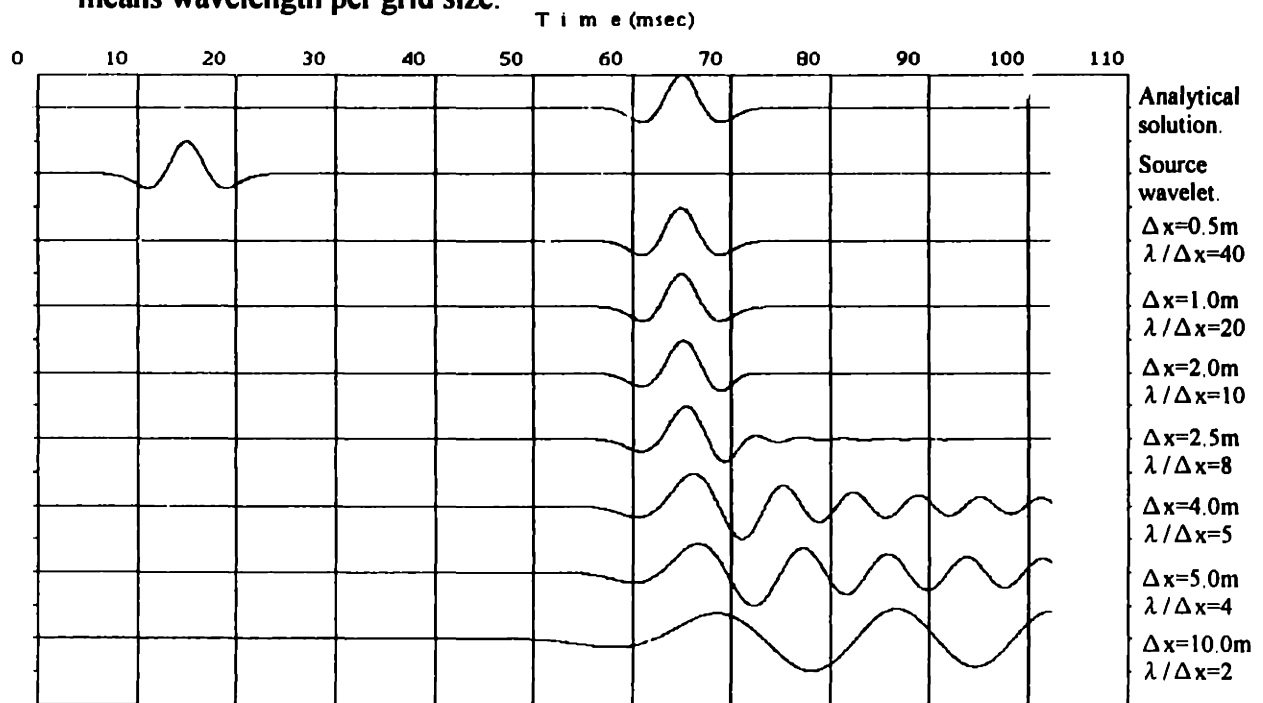
Figure 2.8: Particle velocities from the fourth-order approximation with various grid sizes (one-dimensional). Δx means grid size and λ/Δx means wavelength per grid size.
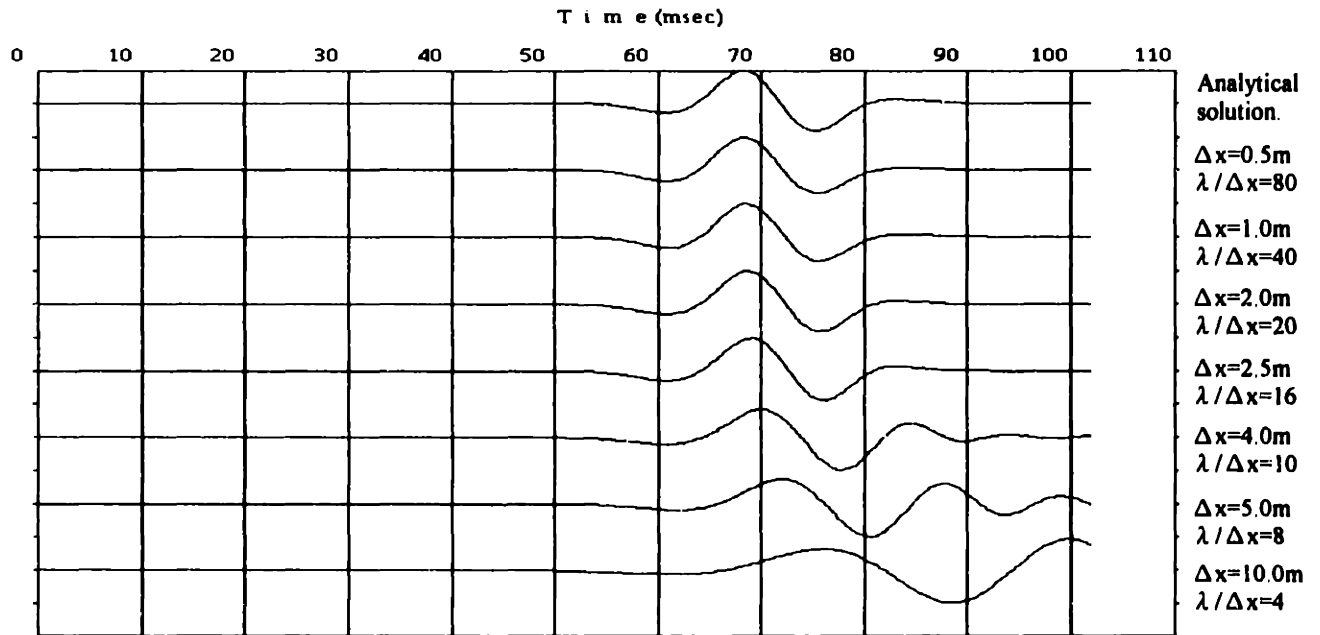
Figure 2.9: P-waves (pressure) from the second-order approximation with various grid sizes (two-dimensional). Δx means grid size and λ / Δx means wavelength per grid size.
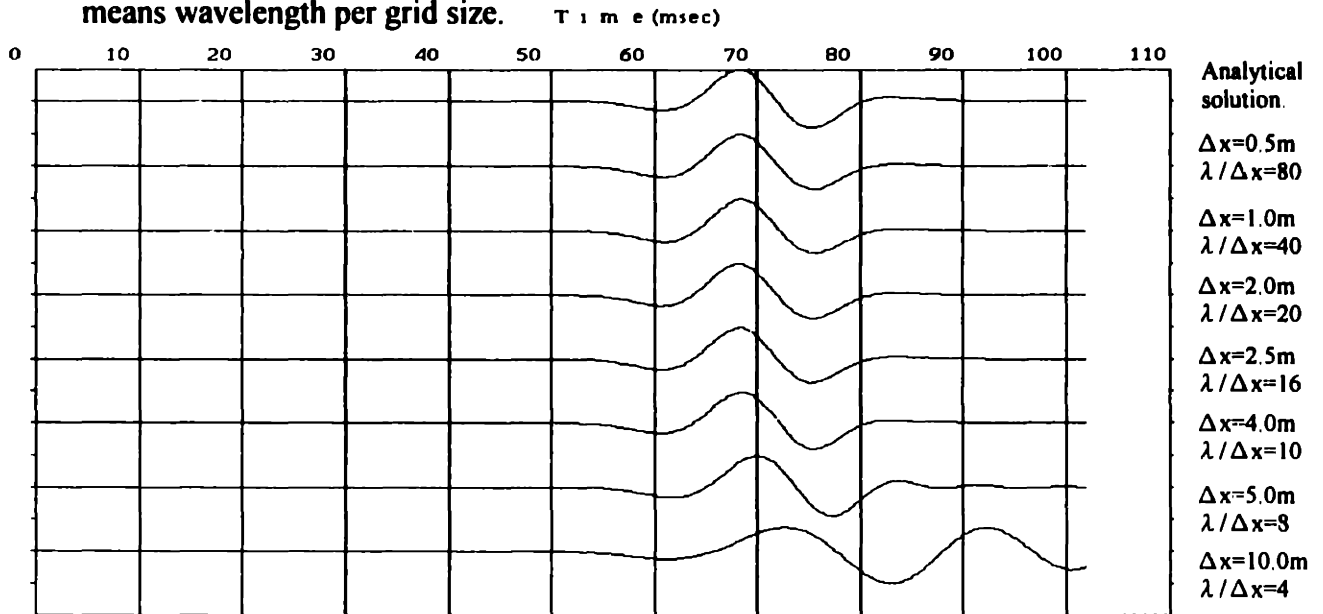
Figure 2.10: P-waves (pressure) from the fourth-order approximation with various grid sizes (two-dimensional). Δx means grid size and λ / Δx means wavelength per grid size.

T i m e (msec)

0   20   40   60   80   100   120   140   160   180   200   220

Δx=0.5m
λ/Δx=40

Δx=1.0m
λ/Δx=20

Δx=2.0m
λ/Δx=10

Δx=2.5m
λ/Δx=8

Δx=4.0m
λ/Δx=5

Δx=5.0m
λ/Δx=4

Δx=10.0m
λ/Δx=2
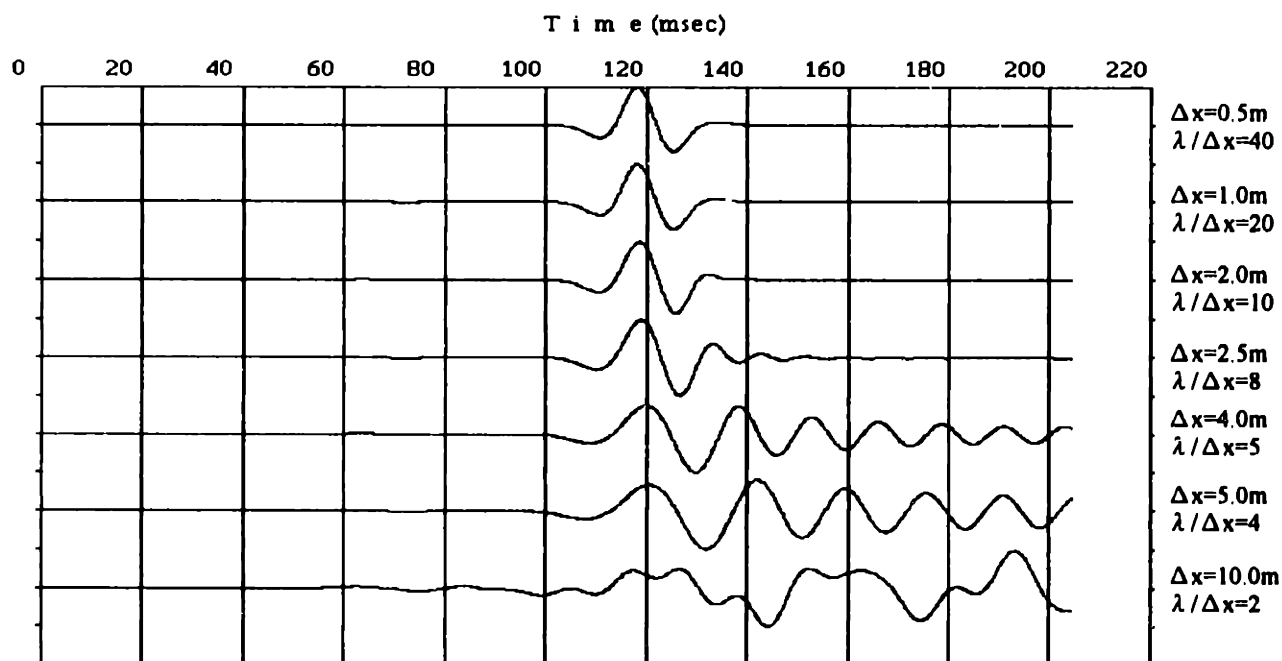
Figure 2.11: S-waves (particle velocity) from the fourth-order approximation with various grid sizes (two-dimensional). Δx means grid size and $\lambda/\Delta x$ means wavelength per grid size.

T i m e (msec)

0   100   200   300   400   500   600   700   800   900   1000   1100

Δx=5m
λ/Δx=20

Δx=10m
λ/Δx=10

Δx=12.5m
λ/Δx=8

Δx=20.0m
λ/Δx=5

Δx=25m
λ/Δx=4
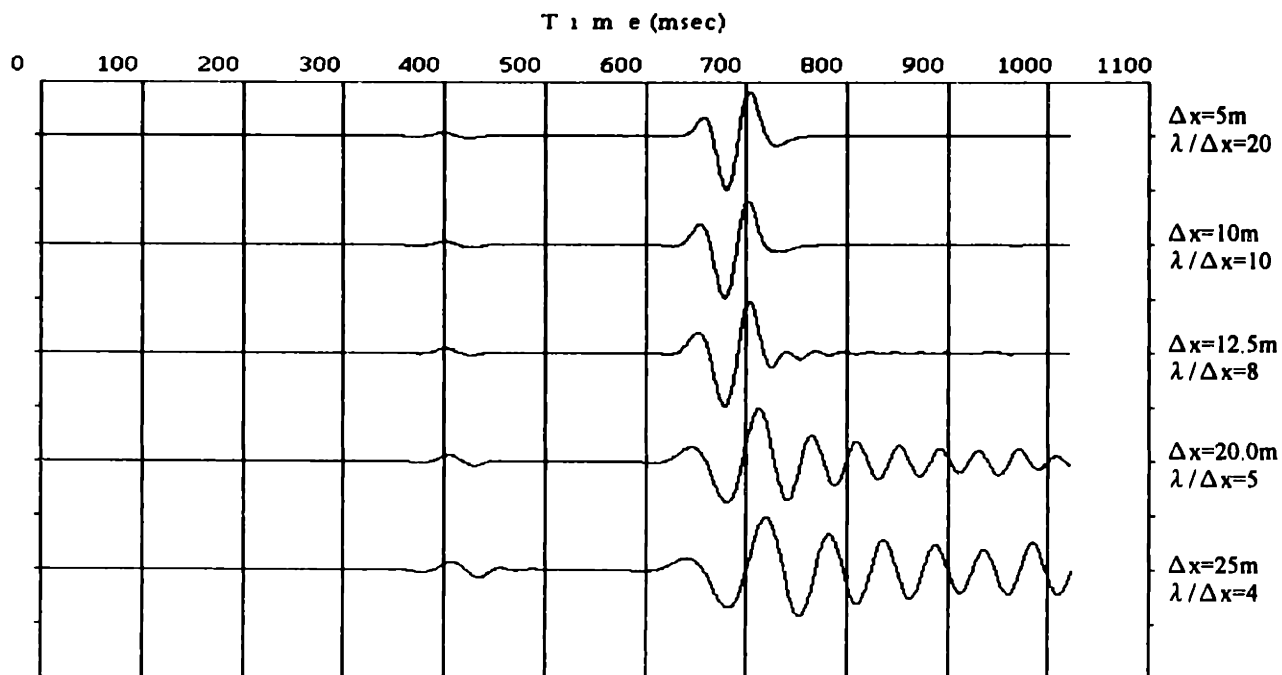
Figure 2.12: Rayleigh-waves (vertical component of particle velocity) from the fourth-order approximation with various grid sizes (two-dimensional). Δx means grid size and $\lambda/\Delta x$ means wavelength per grid size.

37
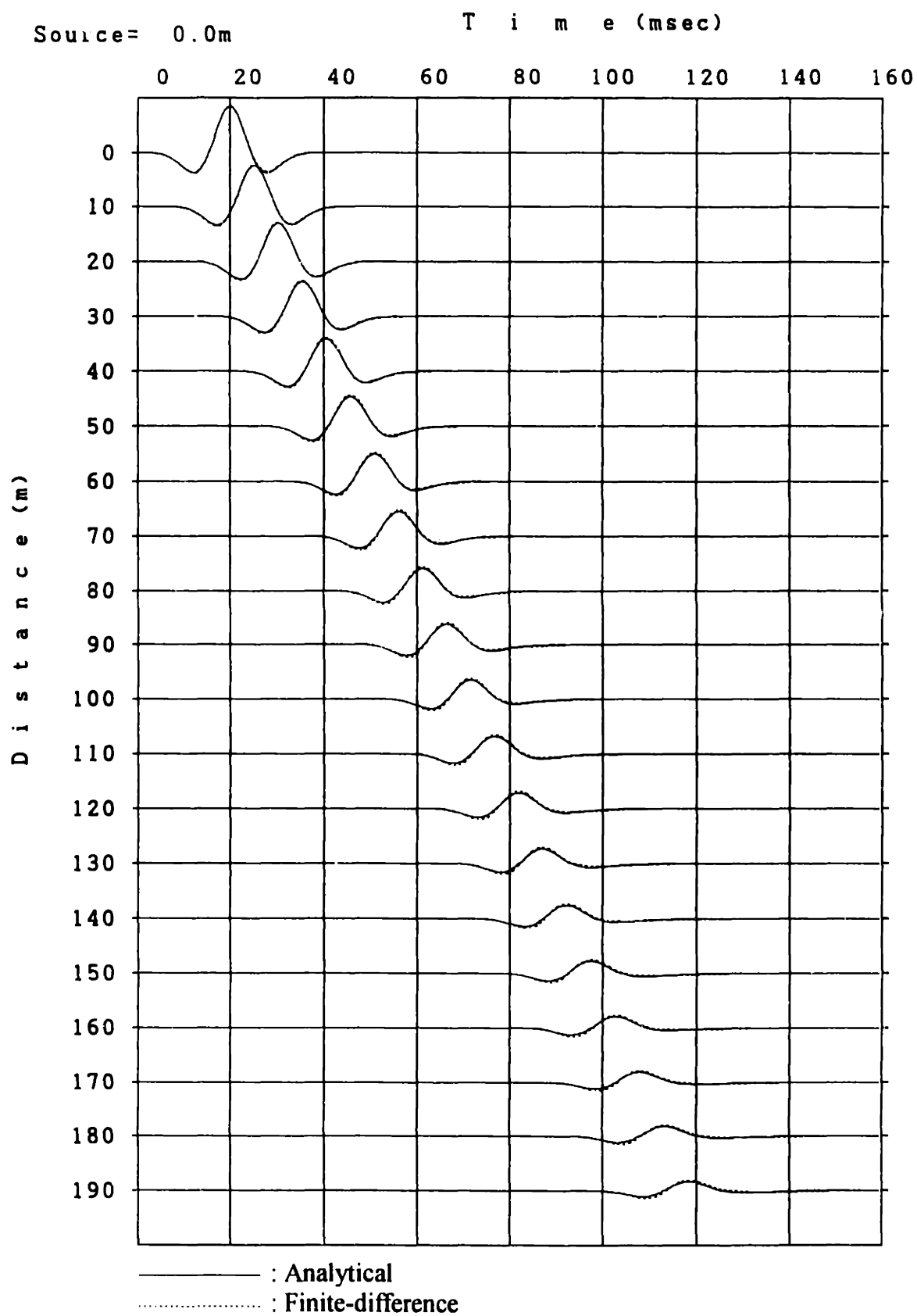
Figure 2.13: Comparison of a finite-difference solution with a analytical solution. Q=10.
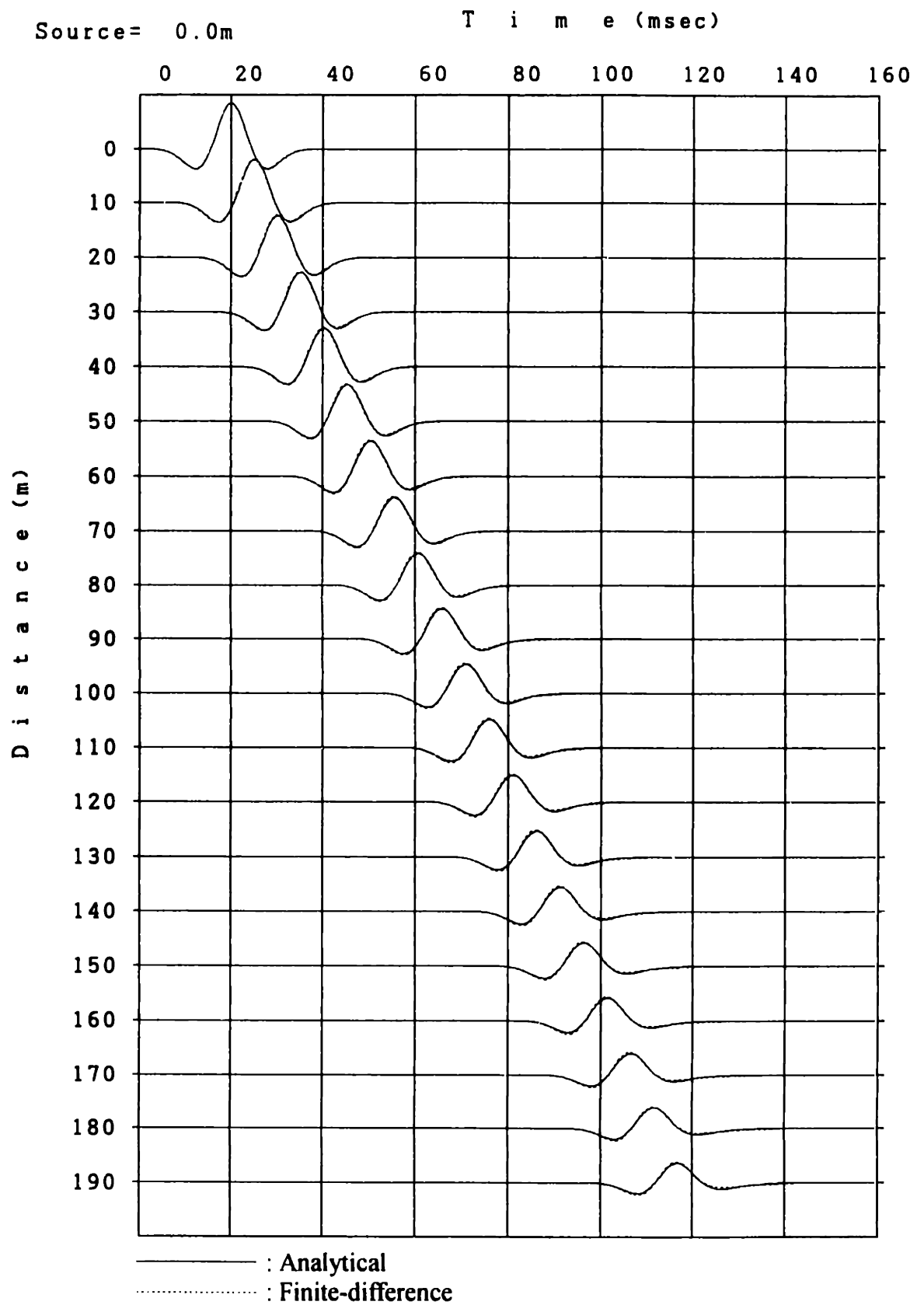
Figure 2.14: Comparison of a finite-difference solution with a analytical solution. Q=20.

Source= 0.0m

T i m e (msec)
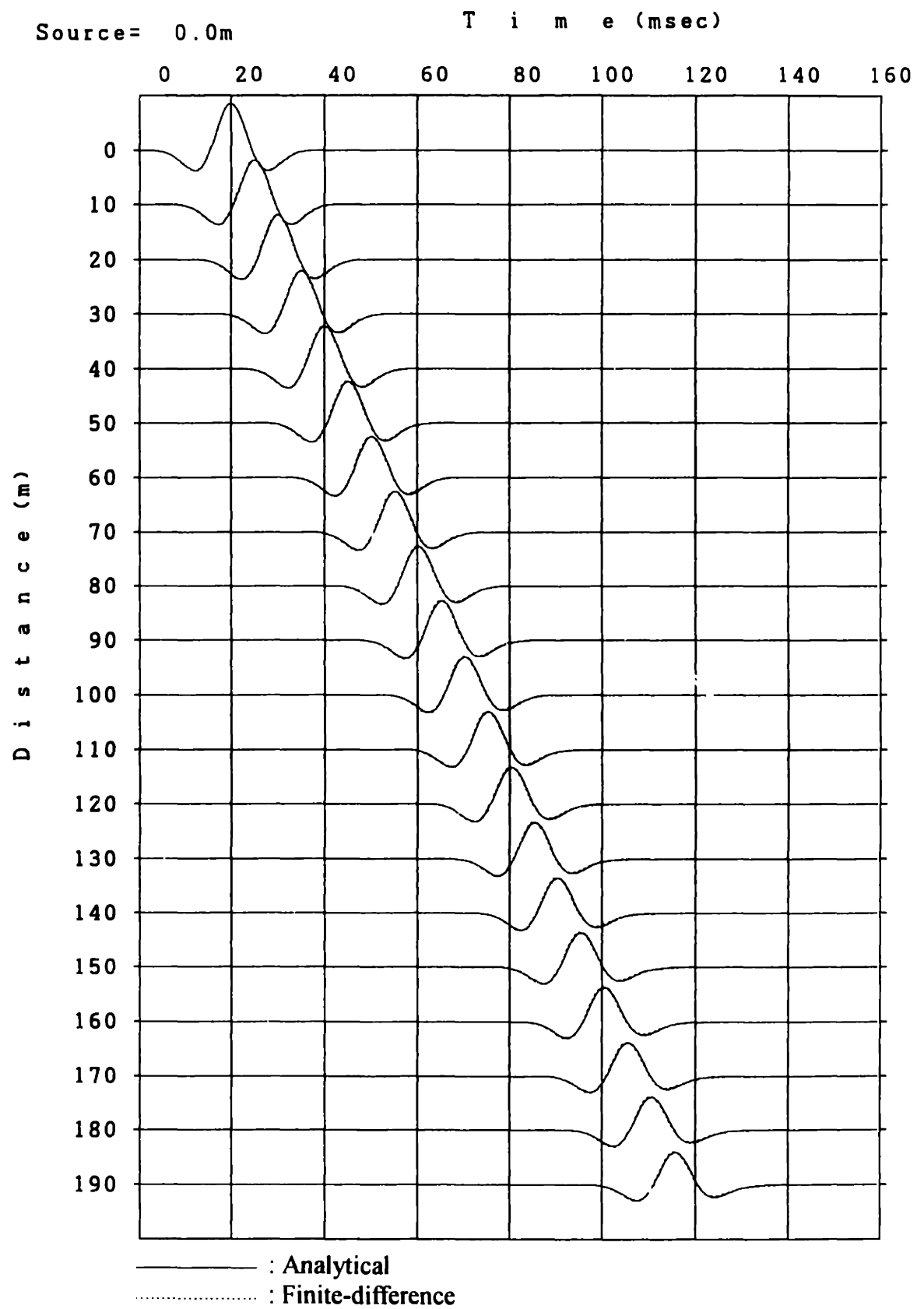
Figure 2.15: Comparison of a finite-difference solution with a analytical solution. Q=50.

————— : Analytical

.... : Finite-difference

40
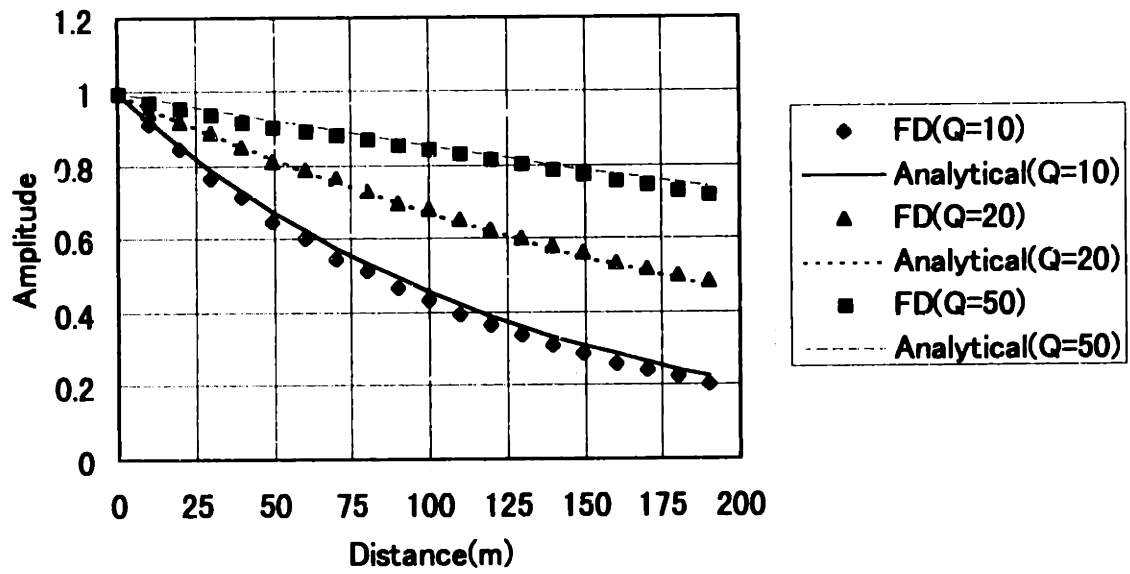
Figure 2.16: Maximum amplitude of finite-difference solutions (Figure 2.13 to 2.15) in comparison to analytical solutions.
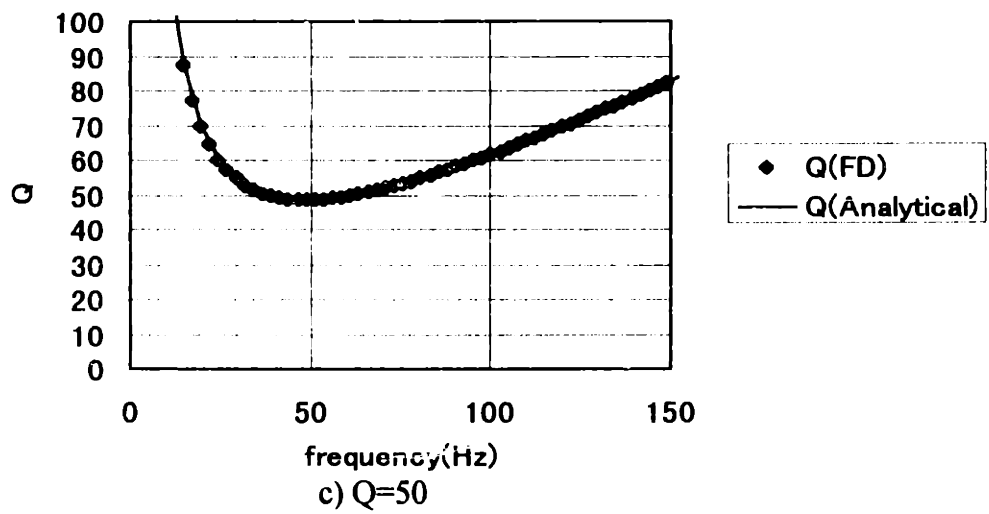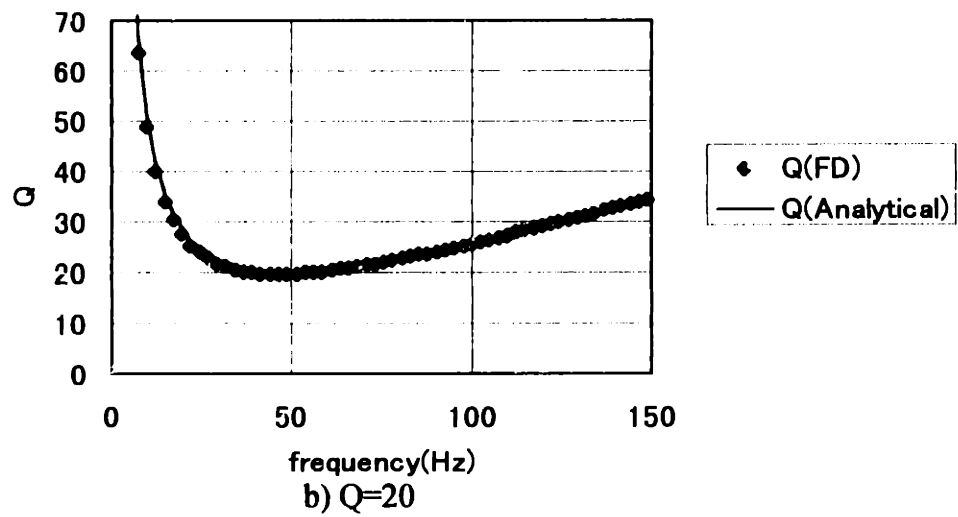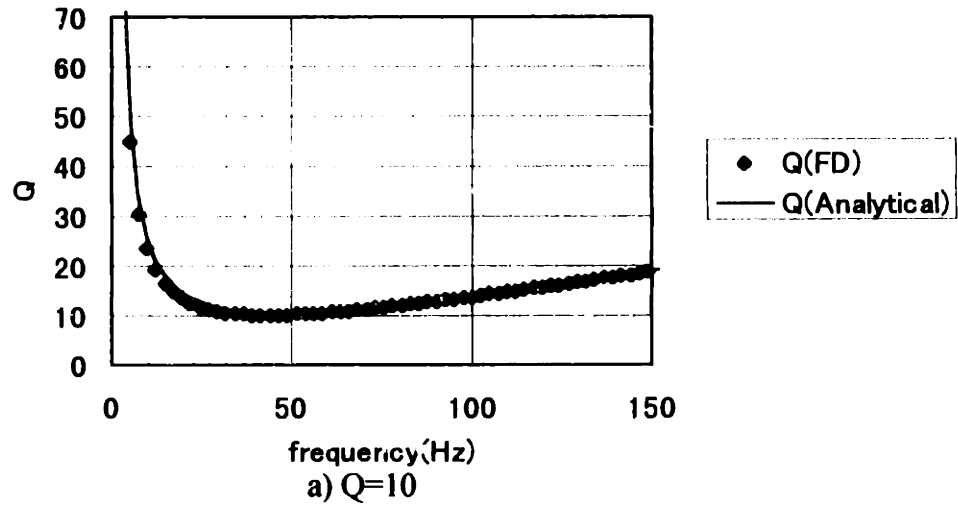
a) Q=10

b) Q=20

c) Q=50

Figure 2.17:   Q(ω) obtained from finite-difference solution in comparison to a analytical solution.
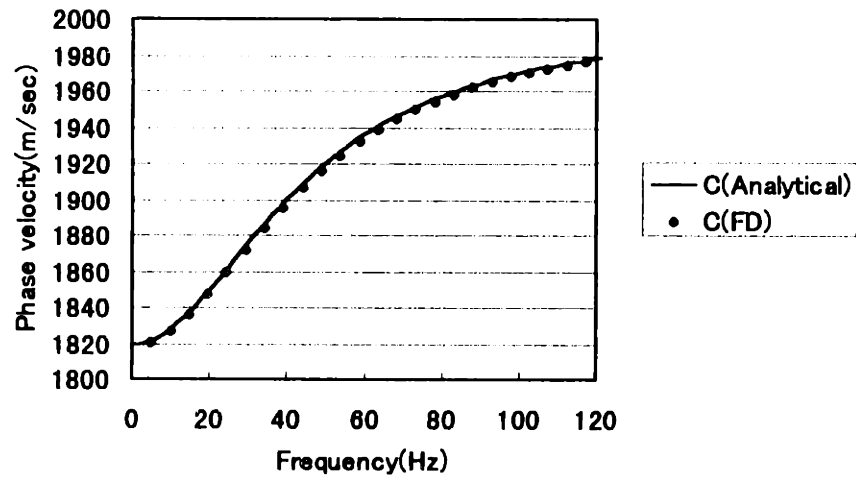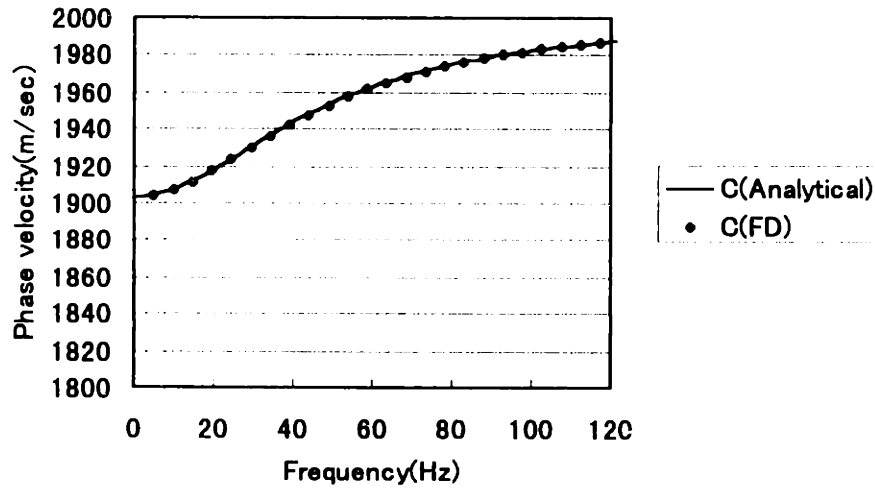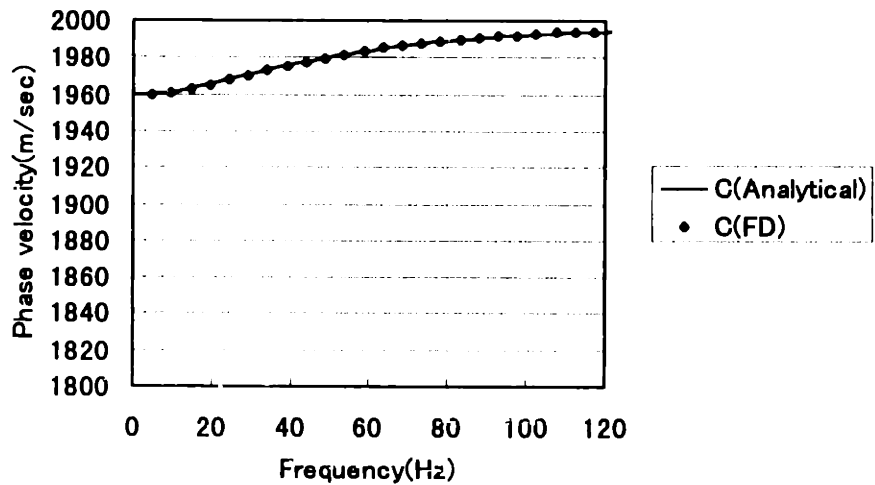
Figure 2.18: Phase velocity $c(\omega)$ obtained from finite-difference solution in comparison to a analytical solution.
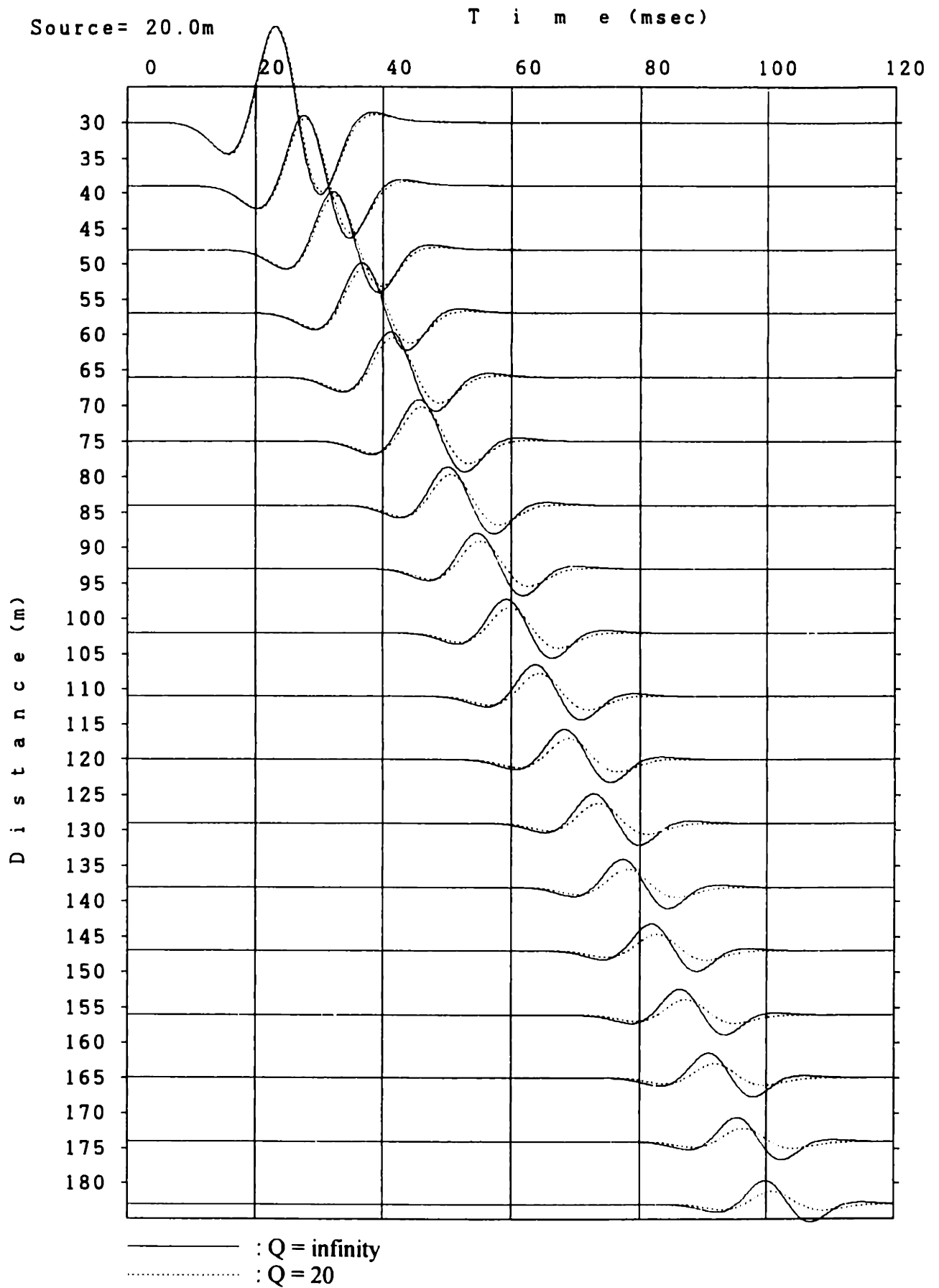
Figure 2.19: Comparison of viscoelastic model (Q=20) with elastic model (Q=infinity).
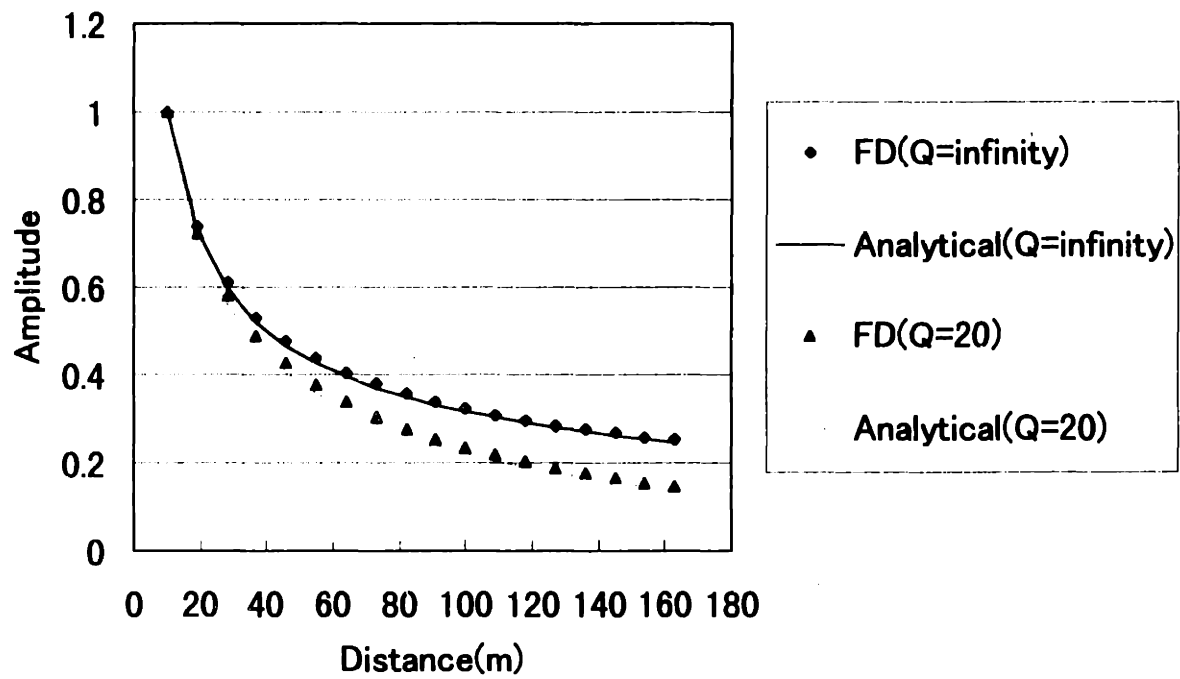
Figure 2.20:   Maximum amplitude of finite-difference solutions (Figure 2.19) in comparison to analytical solutions.

Chapter 3

A Free Surface Approximation in the Presence of Topography

3.1 Introduction

Robertsson (1996) proposed a generalized image method for the free surface condition in which stress-tensor components are imaged and the irregular free surface boundary condition is enforced to ensure that the shear and normal stresses perpendicular to the boundary are zero. This method is based on a robust theoretical derivation and the criteria for stability and accuracy are well established. An alternative method to model surface topography is to let Vp,Vs$\rightarrow$0 in the region above the free surface (the density in the region above the free surface is not 0 to avoid numerical instability). This method is called the vacuum formulation (Graves, 1996). This approach is attractive because it can be implemented with the same difference equations used in the interior of the model, and thus, the effects of surface topography are modeled in the same manner as internal media interfaces. However, the method is unstable and could be inaccurate.

In order to combine the simplicity of the vacuum method as well as the accuracy of the generalized image method, I propose an approach based on a combination of these mehotds.

3.2 Finite-difference Approximation

In the proposed method, stresses are calculated so that the shear and normal stresses

perpendicular to the boundary are zero, just as in Robertsson's generalized image method. However, the calculation of particle velocities does not involve any specific boundary calculation. Table 1 shows the comparison of the three differentmethods for dealing with free surface conditions.

Table 3.1 Three methods of free-surface approximation

	Calculation of particle velocities	Calculation of stresses
Generalized image method	Imaging stresses.	Free surface condition (the shear and normal stresses perpendicular to the boundary are zero). Set particle velocities to zero above the free surface.
Vacuum formulation	No specific calculation.	No specific calculation. Set P and S wave velocities to zero above the free surface.
Proposed method	No specific calculation.	Free surface condition (the shear and normal stresses perpendicular to the boundary are zero). Set particle velocities to zero above the free surface.

The implementation of three approximation methods can be summarized as follows.

3.2.1 Generalized Image Method

In this method, the free surface is located exactly through the upper part of the staggered grid points $z=0$, (in the case of horizontal surface) as shown in Figure 3.1. Then, the normal stresses σ_{xx}, σ_{zz}, the memory variables (see the Chapter 2) r_{xx}, r_{zz}, and the particle velocity v_x are located on the free surface. At $z=0$, the σ_{zz} and the r_{zz} are equal to zero. To honor the free surface condition, the σ_{xx} and r_{xx} are updated using only horizontal derivatives of the velocities through equations (2.2.41) and (2.2.42). If we employ fourth-order approximation in space, further consideration is required. To calculate the shear stress σ_{xz} and the memory variable r_{xz} at $z=0$, and stresses and memory variables at $z=1$, the particle velocities are set to zero on all rows above the free surface. To calculate particle velocities, stresses above the free surface are set to the anti-symmetric value of under the free surface (imaging), so that the shear and normal stresses perpendicular to the boundary on the free surface are zero.

47

Figure 3.2 shows the staggered finite-difference grid in the vicinity of the free surface used in the generalized image method. In order to account for the irregular surface, the following calculation is performed at vicinities of the corners. The normal stresses σ_{xx}, σ_{zz}, and the memory variables r_{xx}, r_{zz} are set to zero at the inner and outer corner. The shear stresses σ_{xz}, and the memory variables r_{xz} are set to zero at the outer corner. Imaging is performed in both directions to respect the vertical and horizontal derivatives of the stress components. The updating of velocities is calculated separately for the vertical and horizontal derivatives.

3.2.2 Vacuum Method

The vacuum method does not involve any specific boundary calculation. Free surface condition is implicitly calculated by P- and S-wave velocities which are set to zero in the region above the free surface. To avoid numerical instability, the density in the region above the free surface is not zero (usually, the same density as the interior of the model is used).

In order to assure the symmetry of the left and right sides of the vertical boundary, the following special consideration is needed. On the vertical boundary whose right side is air, P- and S-wave velocities are set to zero only for the calculation of the shear stress (Figure 3.3).

3.2.3 Proposed Method

The proposed method is a combination of the image method and the vacuum method. In the proposed method, stresses are calculated so that the shear and normal stresses perpendicular to the boundary are zero, just as in the generalized image method. However, the calculation of particle velocities is similar to the vacuum method and does not involve any specific boundary calculation. Figure 3.4 shows the staggered finite-difference grid in the vicinity of

the free surface used in the proposed method.

In the calculation of stresses for the irregular surface, there is a difference between the generalized image method and the proposed method. In the generalized image method, the σ_{xx}, σ_{zz} and r_{xx}, r_{zz} are set to zero at the inner and outer corner, and the σ_{xz}, and r_{xz} are set to zero at the outer corner. However, in the proposed method, the grid on the inner corner and the σ_{xz}, and r_{xz} on the outer corner are calculated in the same manner as the interior of the model. Thus, only the σ_{xx}, σ_{zz} and r_{xx}, r_{zz} of the grid on the outer corner are set to zero. The calculation of particle velocities does not involve any specific calculation even if the surface topography is not flat.

3.3 Comparison of Accuracy

To examine the validity of the method, I have carried out a large number of numerical tests to compare the three methods (Generalized image method, Vacuum formulation, Proposed method). Figure 3.5 shows the example of the computations including irregular surface. Here, I show two examples of the results of numerical tests.

3.3.1 Flat Surface with Various Slopes

A flat, semi-infinite, elastic medium was chosen to be the first numerical test for the free surface with topography. This model is similar to the model presented by Robertsson (1996). The model is a Poisson solid with P- and S-velocities of 3000 and 1730m/s, respectively, and a density of 2500kg/m^3. In this test, the slope of the free surface was varied. If wave propagation is modeled accurately, independent of the slope of the surface, then the algorithm should also allow for accurate modeling of free surfaces with more general shapes. To avoid problems due to the uncertainty of the exact location of the source, a P-wave source (15Hz Ricker wavelet) located 30 m below the surface was employed. The

slope of the free surface was varied from -90° to 90° at 15° intervals, and the waveforms were collected at 1000m source receiver offset in a direction parallel to the free surface. The receivers were located 50 m below the surface. The recorded particle velocities were rotated to the coordinate system of the 0° case, so that all waveforms can be compared to each other directly. The solution for the 0° slope can be regarded as the exact solution. Figure 3.6 and 3.7 show the examples of particle velocity wavefields (parallel to the free surface).

Before showing slope results, I show some basic comparison of different methods. Figure 3.8 shows the particle velocities from the 0° case with various offsets. The first arrival is body waves (P-waves) and the second arrival is surface waves (Rayleigh waves). We can see horizontal component of particle velocity component dominates P-waves and vertical velocity dominates Rayleigh waves. Figure 3.9 shows the comparison of three methods in the 0° case against a solution of a discrete wave-number integral method that can be considered as an exact solution. In this calculation, grid size was set to 2m (approximately 50 grid points per wavelength) which is sufficiently small, and we can assume there is no numerical error due to the grid size. In Figure 3.9, there is a phase shift of Rayleigh waves in the proposed method compared with the boundary element method. However, the difference is so small that it may be neglected if we are mainly concerned with body waves. Furthermore, other numerical tests showed this difference of phase velocity only appears when the source and receivers are placed at very shallow depth below the surface compared with the wave lengths. For most applications, I consider this difference not to be significant.

In Figures 3.10 to 3.12, particle velocity from the simulations with various slopes and the methods are plotted, for the grid sizes of 2m and 5m. For the grid size of 2m (approximately 50 grid points per wavelength), all methods yield sufficiently accurate results. However, for the grid size of 5m (approximately 20 grid points per wavelength), we can see a significant numerical dispersion in the image method and the vacuum method. On

the contrary, the dispersion of the proposed method is relatively small.

3.3.2 Presence of Irregular Surface

In this example, three methods of free surface approximation were compared with a finite-difference method (generalized image method) using Dr. Johan O. Robertsson's code. Figure 3.13 shows the model used in the second numerical test. The model is a elastic Poisson solid with P- and S-velocities of 2000 and 1155m/s, respectively, and a density of 1000kg/m^3. A P-wave source (110Hz Ricker wavelet) located at a distance of 30m and 5m below the surface was employed.

At first, I will compare three methods of free surface approximation with the various grid sizes. In Figure 3.14, the particle velocity (vertical component) from the simulations with the various grid sizes is plotted. The receivers were located at a distance of 120m and 4m below the surface. All methods yield sufficiently accurate results when using a large number of grid-points per wavelength (40 or 80). However, in the case of a smaller number of grid points (10 or 20), we can see that the proposed method is most accurate.

Next, I compared the following four methods using the same model.

Table 3.2   Benchmark test

Method	Developer
FD (Image method)	Hayashi, K.
FD (Proposed method)	Hayashi, K.
FD (Vacuum method)	Hayashi, K.
FD (Image method)	Robertsson, J. O.

The receivers were placed on two lines shown in Figure 3.15. The grid size of 0.25m (approximately 40 grid points per wavelength) is used in my three calculations. Figures 3.16 to 3.19 show the particle velocities from the simulations. Figure 3.16 and 3.17 show the waveforms collected at the receivers located before the ramp. We can consider that these waveforms have little effect from irregular surface. Before the ramp, five calculations

show excellent agreement, and it means that four methods yield the same result if the surface is flat. Figure 3.18 and 3.19 show the waveforms collected at the receivers located behind the ramp. I plotted the waveforms at the shallowest receiver (distance of 120m and 4m below the surface) in Figure 3.20 with a large scale. We can see that the four finite-difference solutions agree sufficiently. This result proves the reliability of the finite-difference code that I developed, even if the surface is irregular.

The results of the above two numerical examples imply that the proposed method is most accurate, when using at least 20 to 40 grid-points per wavelength. Therefore, I will use the propose method as free surface approximation in the following discussion.

3.4 Investigation about Stair-shaped Boundary

Robertsson (1996) mentioned that the generalized free surface condition that we employed yields a good representation of a "staircase-shaped" function, whereas a smooth boundary must be discretized in terms of such steps. Fuyuki and Matsumoto (1980) found that the scattering of Rayleigh waves can be substantial from relatively small steps compared to the wavelength. This scattering from the stair-shaped boundary should be avoided when we model a smooth boundary. In addition to that, our free surface numerical tests did not reveal whether the observed Rayleigh wave dispersion was an actual wave phenomenon or a numerical error. Thus, I performed the following tests to reveal the effect of a stair-shaped discretization on a smooth free surface.

Figure 3.21 shows the $45°$ slope model used in the numerical test. The model is an elastic solid with P- and S-velocities of 5082 and 3000m/s, respectively, and a density of 2000kg/m^3. A P-wave source (200Hz Ricker wavelet) located at a distance of 25m and 6m below the surface was employed. In this test, not only the grid size but also the step size of the slope was varied. The step size and the grid size are defined in Figure 3.22. In Figure 3.23, particle velocity (vertical component) from the simulations with the various grids and

step sizes are plotted. The receivers were located 4m below the surface and at 6m distance intervals. Table 3.3 shows the list of the grid and step sizes as well as the results of the computation.

Table 3.3 Grid and step sizes and the resulting dispersion

Model	Grid size (m)	Step size (m)	Wavelength/ grid size	Wavelength/ step size	Dispersion	Figure
A	0.5	0.5	30	30	No	Figure9 (a)
B	0.5	1.0	30	15	No	(b)
C	1.0	1.0	15	15	No	(c)
D	0.5	1.5	30	10	No	(d)
E	1.5	1.5	10	10	Small	(e)
F	0.5	2.0	30	7.5	Small	(f)
G	2.0	2.0	7.5	7.5	Medium	(g)
H	0.5	3.0	30	5	Medium	(h)
I	3.0	3.0	5	5	Large	(i)

The waveforms are also ordered as a matrix in Figure 3.24. The results of the computation can be summarized as follows. The results from model A to C (Figure3.23 (a) to (c)) have no large difference and no dispersion; we can consider these waveforms to be accurate. The model D (Figure 3.23 (d)) and the model E (Figure 3.23 (e)) are the same step size, however, the dispersion of the model E is larger than the one of the model D. We can see a similar tendency in the models F, G (Figure 3.23 (f) and (g)) and the models H, I (Figure 3.23 (h) and (i)) in which the step sizes are equivalent. This result implies that the numerical errors due to large grid sizes are larger than the Rayleigh wave scattering due to the stair-shaped boundary.

The above numerical tests were performed on a model with a constant slope of $45°$. However, we can expect that the constant slope is accurate compared to the surface with arbitrary slope. To confirm that the accuracy does not depend on the curvature of the free surface boundary, I performed other numerical tests using the model shown in Figure 3.25 (model A) and Figure 3.26 (model B). In these tests, the free surface boundary is curved smoothly. The model A has a relatively gentle slope, and the model B has a steep one. The

models are elastic solids with P- and S-velocities of 6000 and 3000m/s, respectively, and a density of 1800kg/m³. A P-wave source (100Hz Ricker wavelet) located at a distance of 24m and 12m below the surface was employed. In this test, the grid sizes were set to 0.5m, 1.0m, 2.0m and 3.0m, and the shortest wavelength is approximately 30m (corresponding to grid-points per wavelength of 60, 30, 15 and 10 respectively). The grid size and step size are equivalent in this test. In Figure 3.27 (model A) and Figure 3.28 (model B), particle velocity (vertical component) from the simulations with the various grid sizes are plotted. The waveforms were obtained at receivers located 12m below the surface and at 12m distance intervals. With 60 grid-points per wave length (Figure 3.27 (a) and Figure 3.28 (a)), there is no dispersion and it can be considered as accurate. As the grid size increases, the dispersion due to the stair-shaped surface boundary increases. However, we can see from Figure 3.27 that the dispersion is mainly generated at the distance between 200 and 250m where the slope of surface is relatively gentle. To compare this result with constant 45° case mentioned before, we can see that the dispersion of the latter is larger than the former.

3.5 Conclusions

The results of numerical tests imply that the proposed method requires at least 30 grid-points per wavelength. In particular, relatively gentle slopes require a large number of grid points per wavelength. The cause of the dispersion is mainly a numerical error due to the large grid sizes rather than the actual Rayleigh wave scattering due to the stair-shaped free surface boundary.
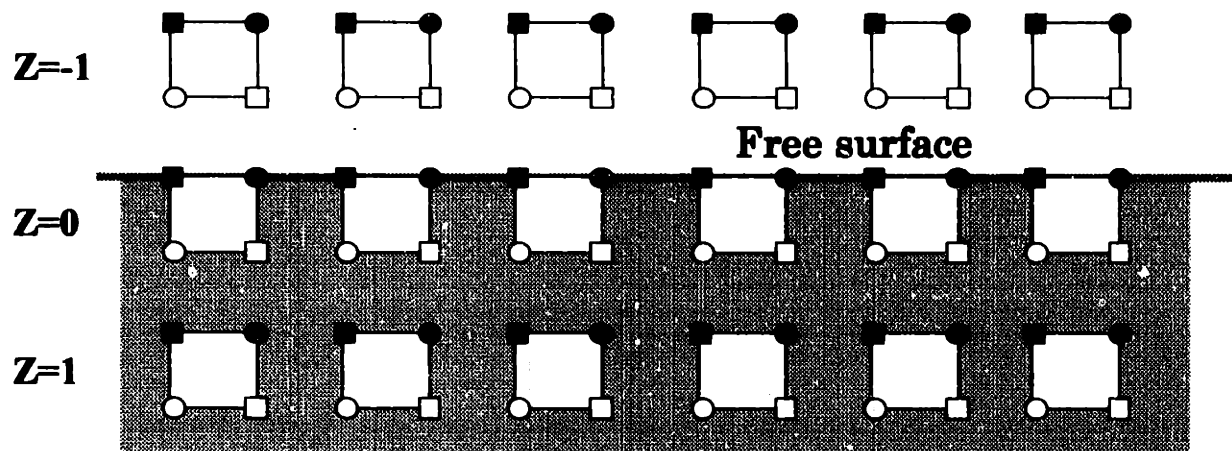
Figure 3.1: Staggered finite-difference grid in the vicinity of the horizontal free-surface boundary (image method). Within the grid-cells, the solid squares represent the σ_{xx}, σ_{zz}, r_{xx}, r_{zz}, components, the light squares the σ_{xz}, r_{xz} components, the solid circles the v_x components, the light circles represent the v_z components(σ : stress, r: memory variable, v: velocity).
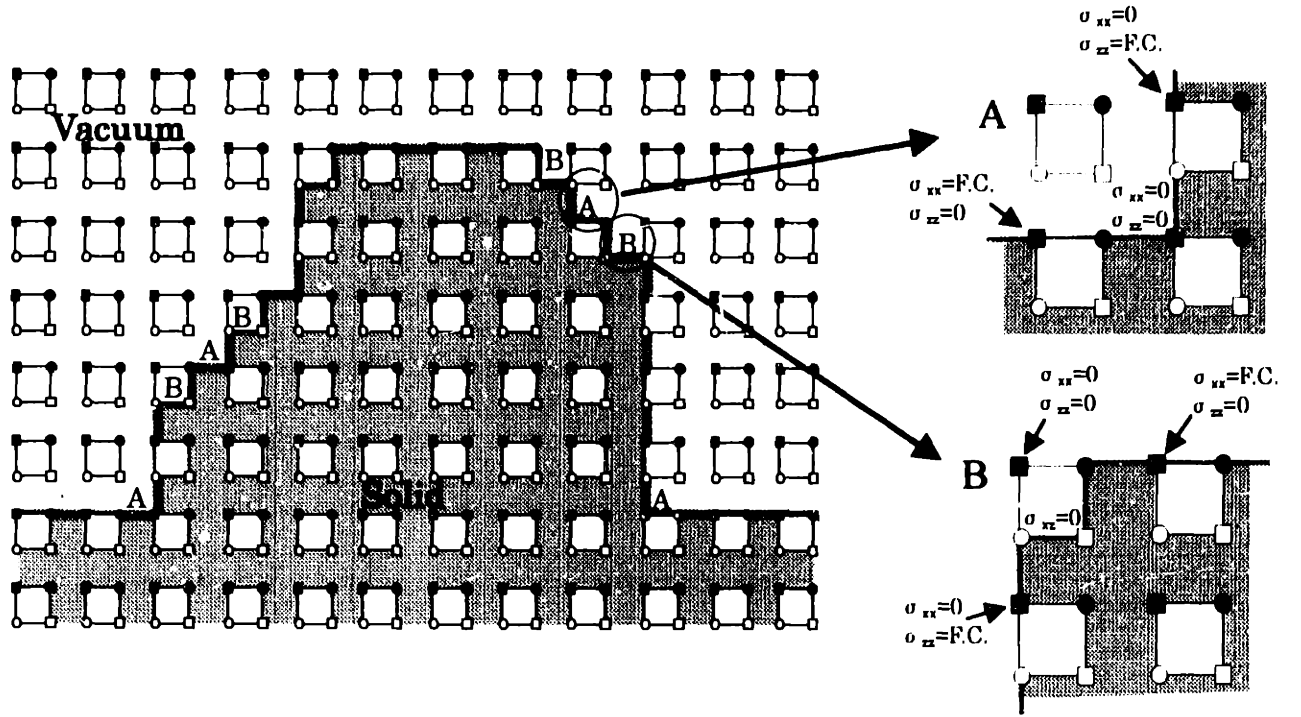
Figure 3.2: Staggered finite-difference grid of generalized image method (Robertosson, 1996) in the vicinity of free surface boundary. On the boundary, free surface condition(F.C.) is that the normal and shear stresses perpendicular to the boundary are zero. Within the grid-cells, the solid squares represent the σ_{xx}, σ_{zz}, r_{xx}, r_{zz}, components, the light squares the σ_{xz}, r_{xz} components, the solid circles the v_x components, the light circles represent the v_z components(σ : stress, r: memory variable, v: velocity).
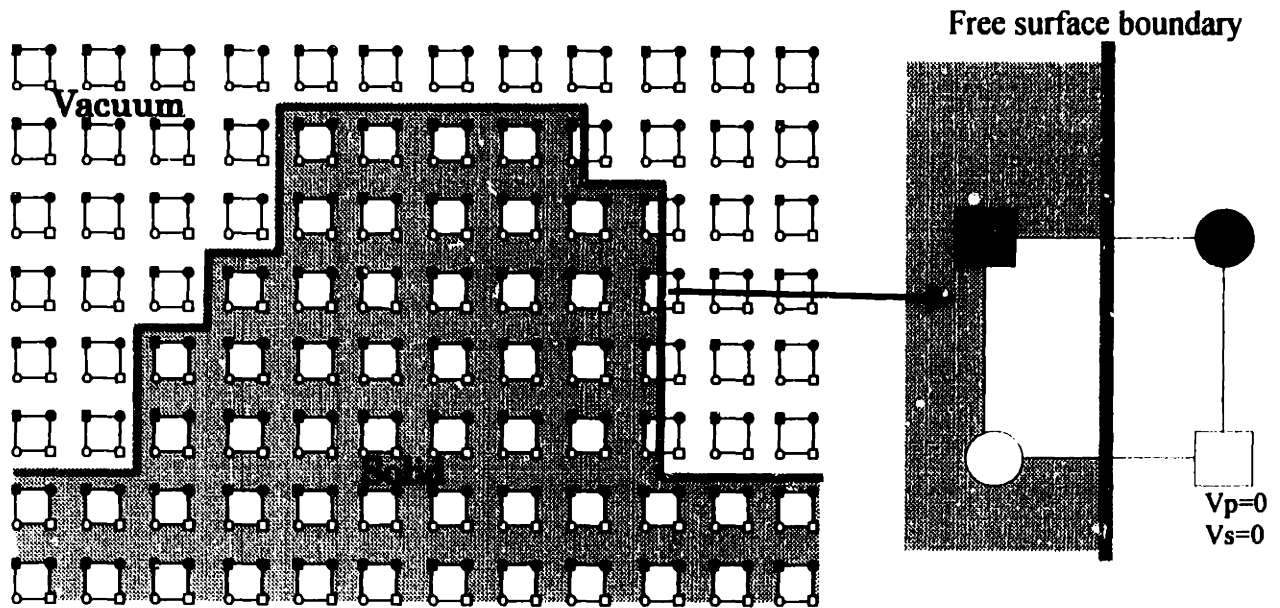
Figure 3.3: Staggered finite-difference grid of the vacuum method in the vicinity of free surface boundary. On the boundary, free surface condition(F.C.) is that the normal and shear stresses perpendicular to the boundary are zero. Within the grid-cells, the solid squares represent the σ_{xx}, σ_{zz}, r_{xx}, r_{zz}, components, the light squares the σ_{xz}, r_{xz} components, the solid circles the v_x components, the light circles represent the v_z components(σ : stress, r: memory variable, v: velocity).
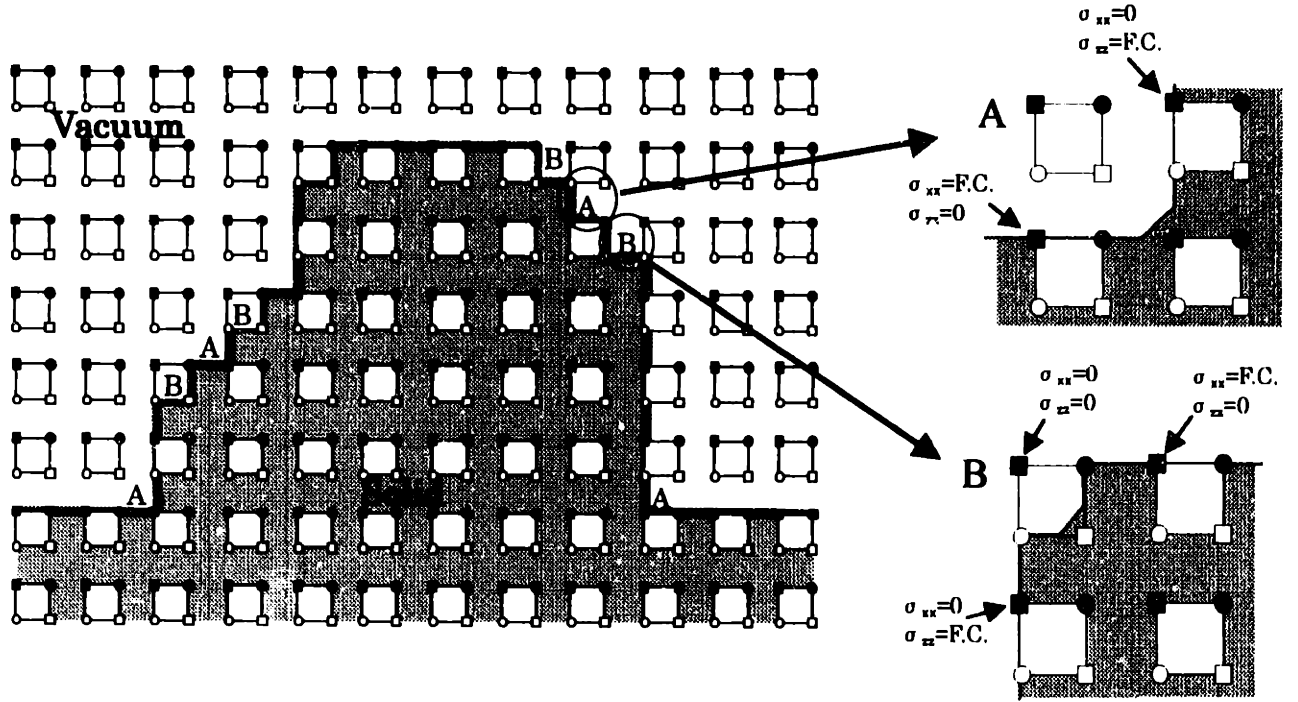
Figure 3.4: Staggered finite-difference grid of the proposed method in the vicinity of free surface boundary. On the boundary, free surface condition(F.C.) is that the normal and shear stresses perpendicular to the boundary are zero. Within the grid-cells, the solid squares represent the σ_{xx}, σ_{zz}, r_{xx}, r_{zz}, components, the light squares the σ_{xz}, r_{xz} components, the solid circles the v_x components, the light circles represent the v_z components(σ : stress, r: memory variable, v: velocity).
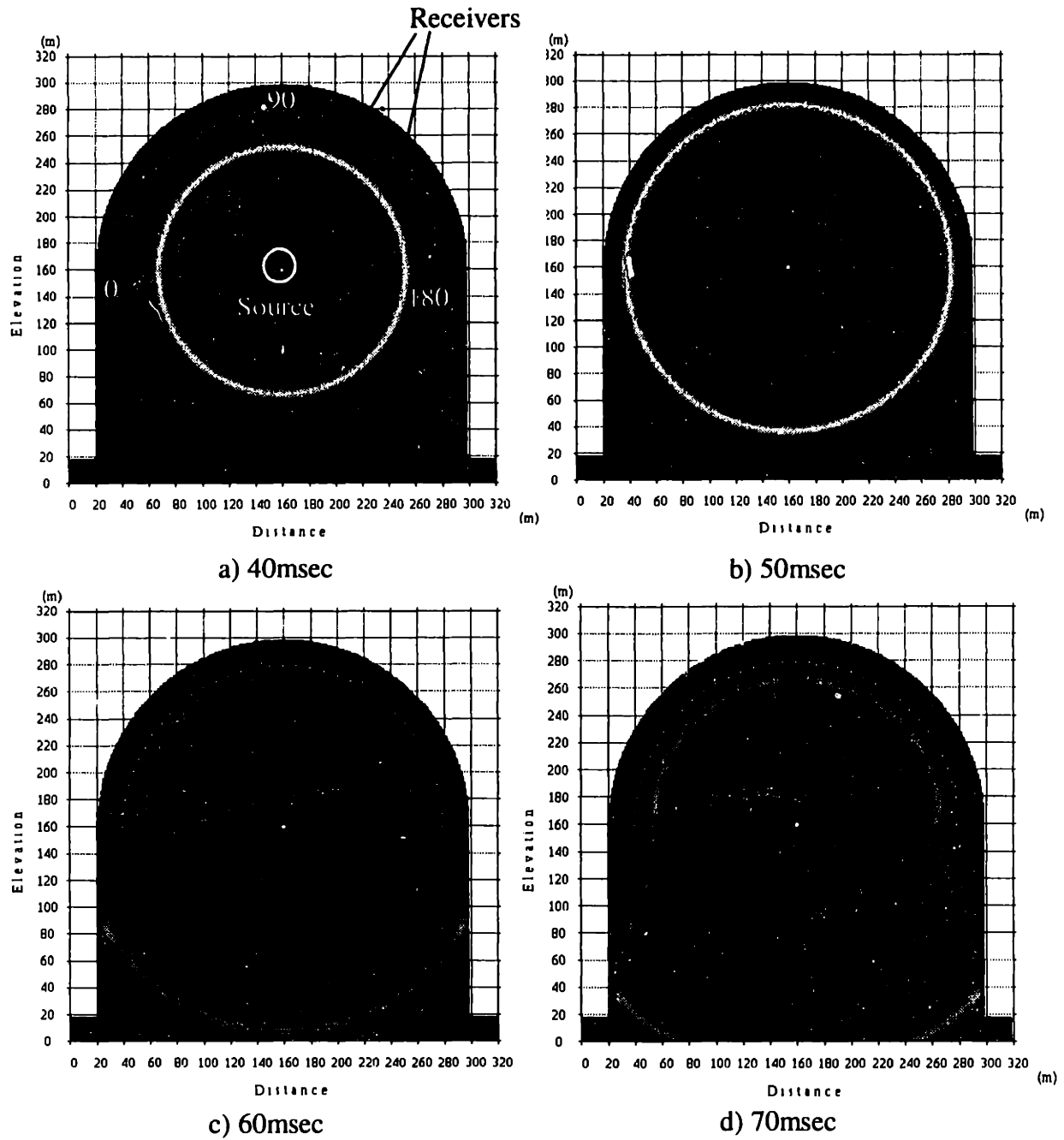
Figure 3.5: Example of the computation including irregular free surface (proposed method). a) to d) : wave field of pressure. e) : pressure collected at receivers. A model is a homogeneous elastic solid with P- and S-velocities of 3000 and 1500m/sec, respectively, and a density of 1800kg/m³. A source is a P-wave source with 100Hz Ricker wavelet.

59
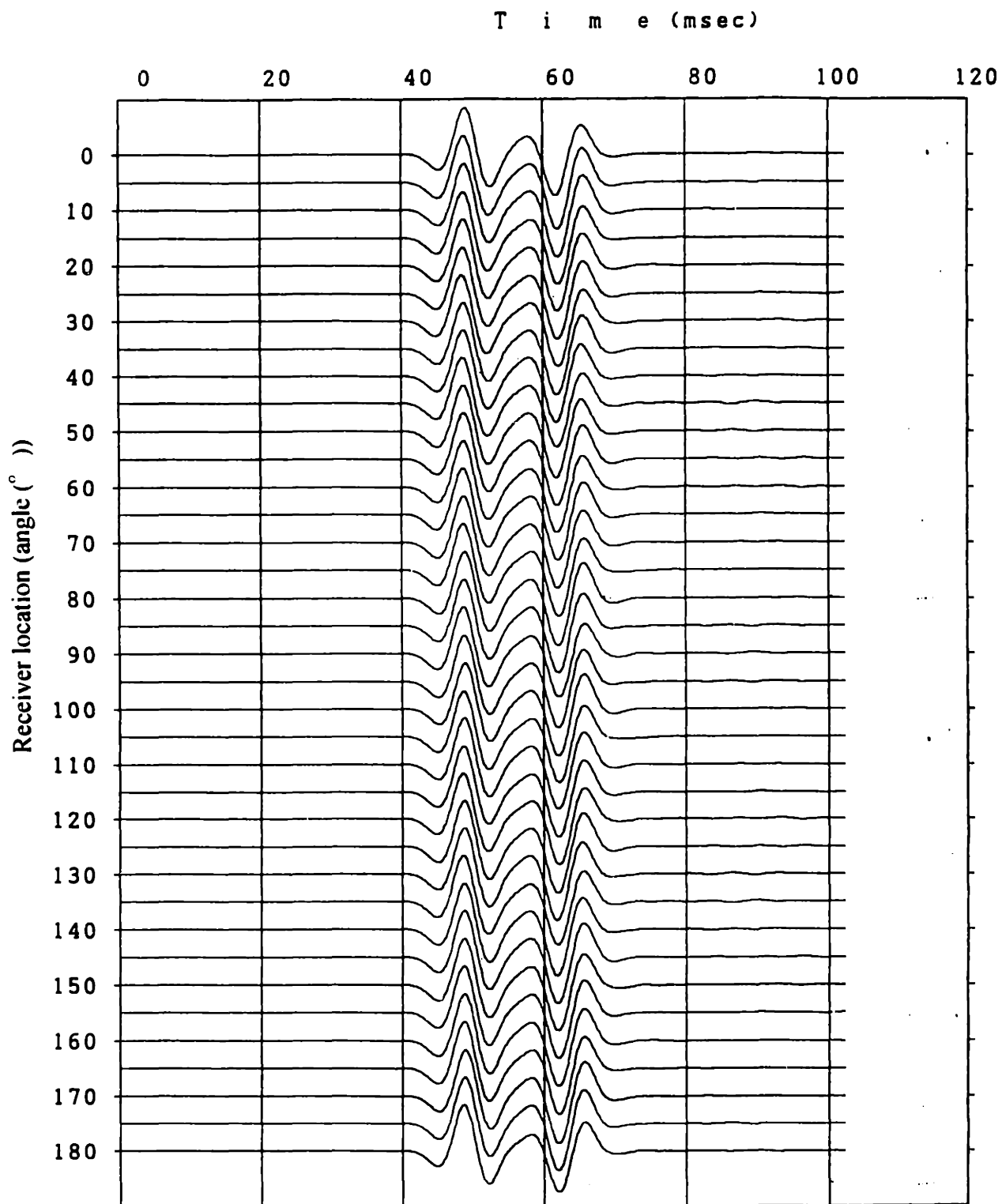
Figure 3.5, continued: e) pressure collected at receivers. $0°$ corresponds to the leftmost receiver, and $180°$ corresponds to the rightmost receiver.
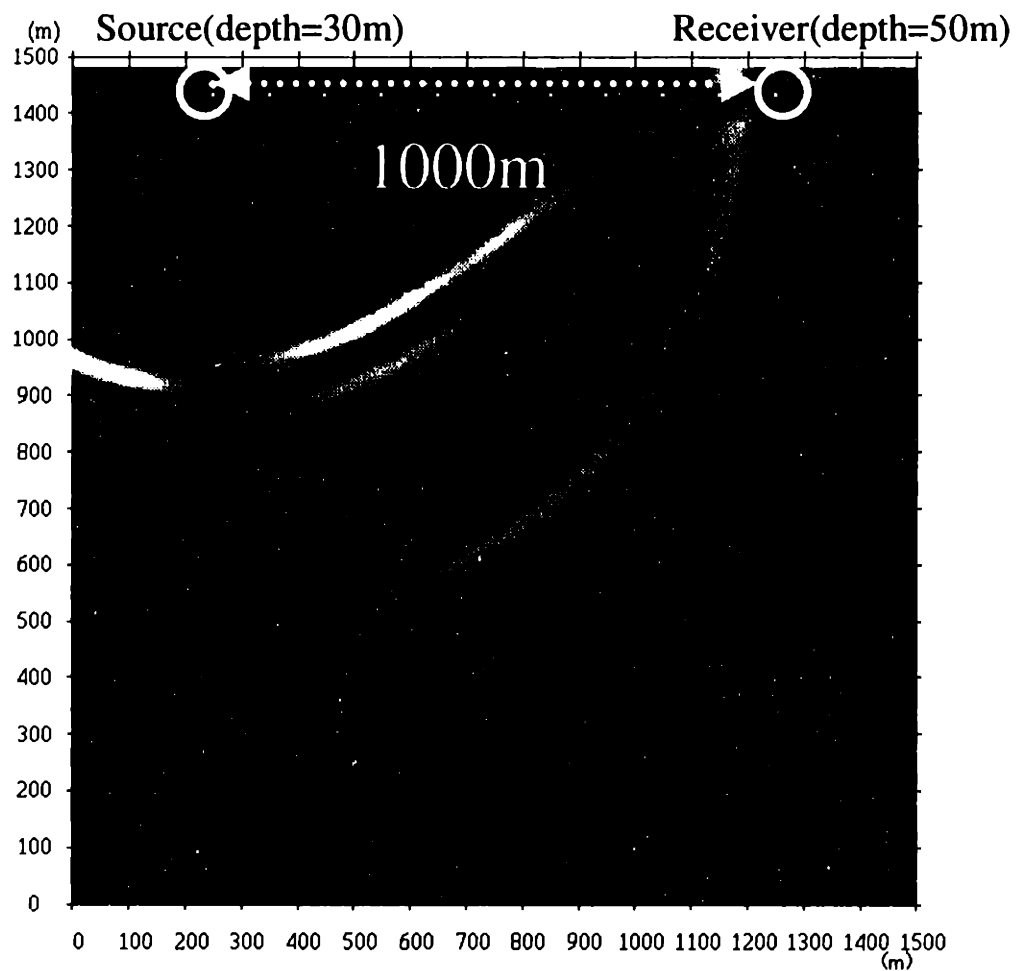
Figure 3.6: Example of particle velocity wavefield (parallel to the free surface) at time 400msec. $0°$ case.
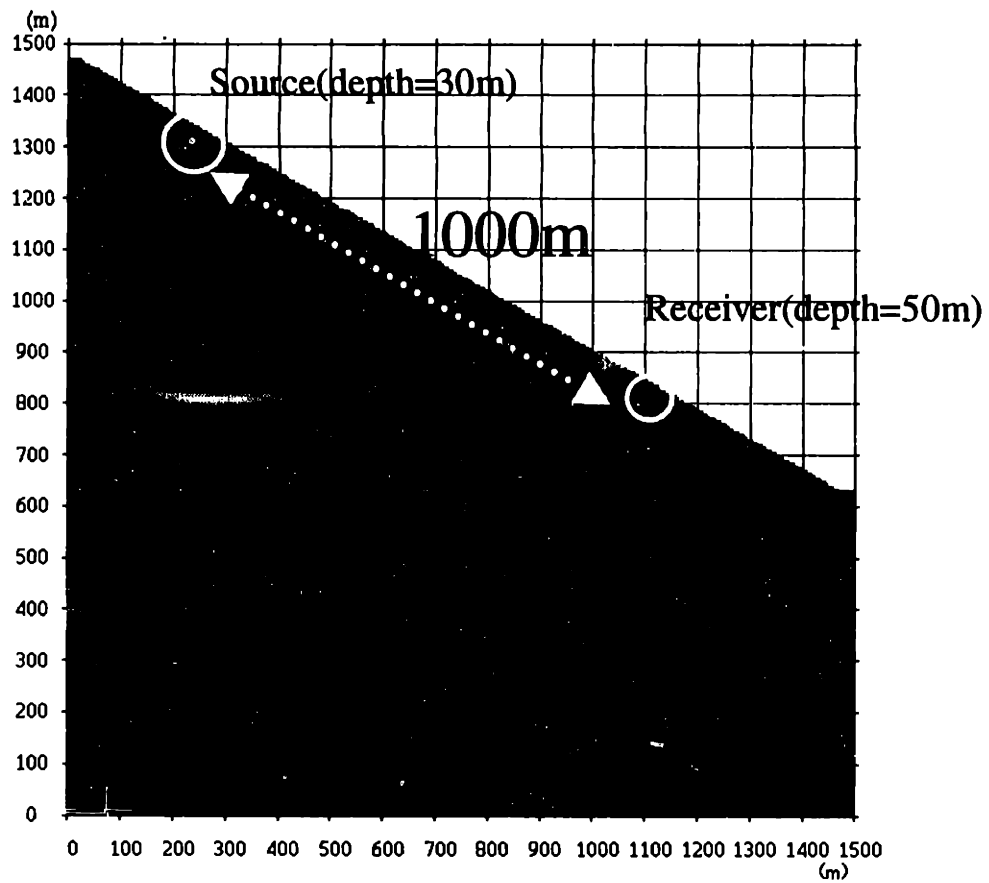
Figure 3.7: Example of particle velocity wavefield (parallel to the free surface) at time 400msec. 30° case.

T i m e (msec)

a) Horizontal component of particle velocity.

T i m e (msec)
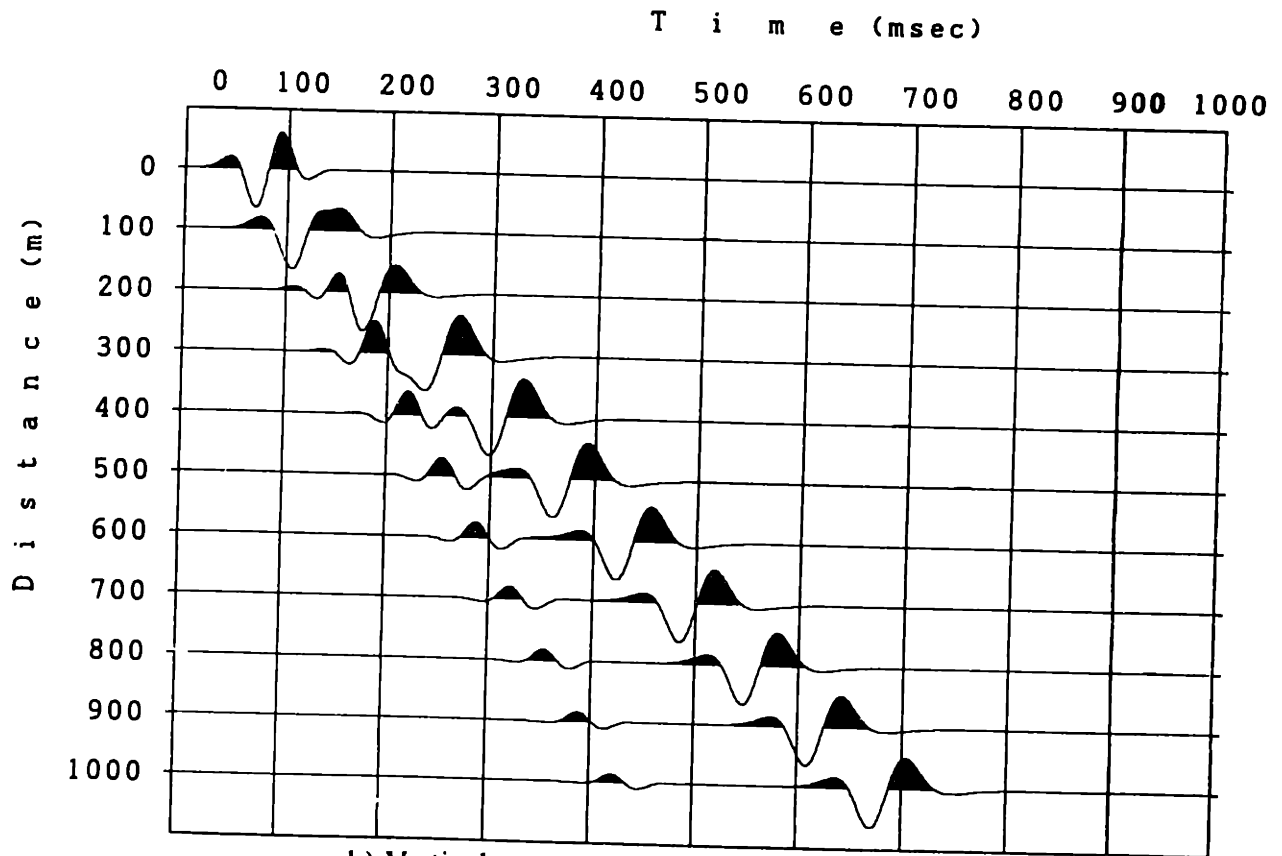
b) Vertical component of particle velocity.

Figure 3.8: Particle velocities from the 0° case with various offset. Waveforms are normalized by each trace. a) Horizontal component of particle velocity. b) Vertical component of particle velocity.
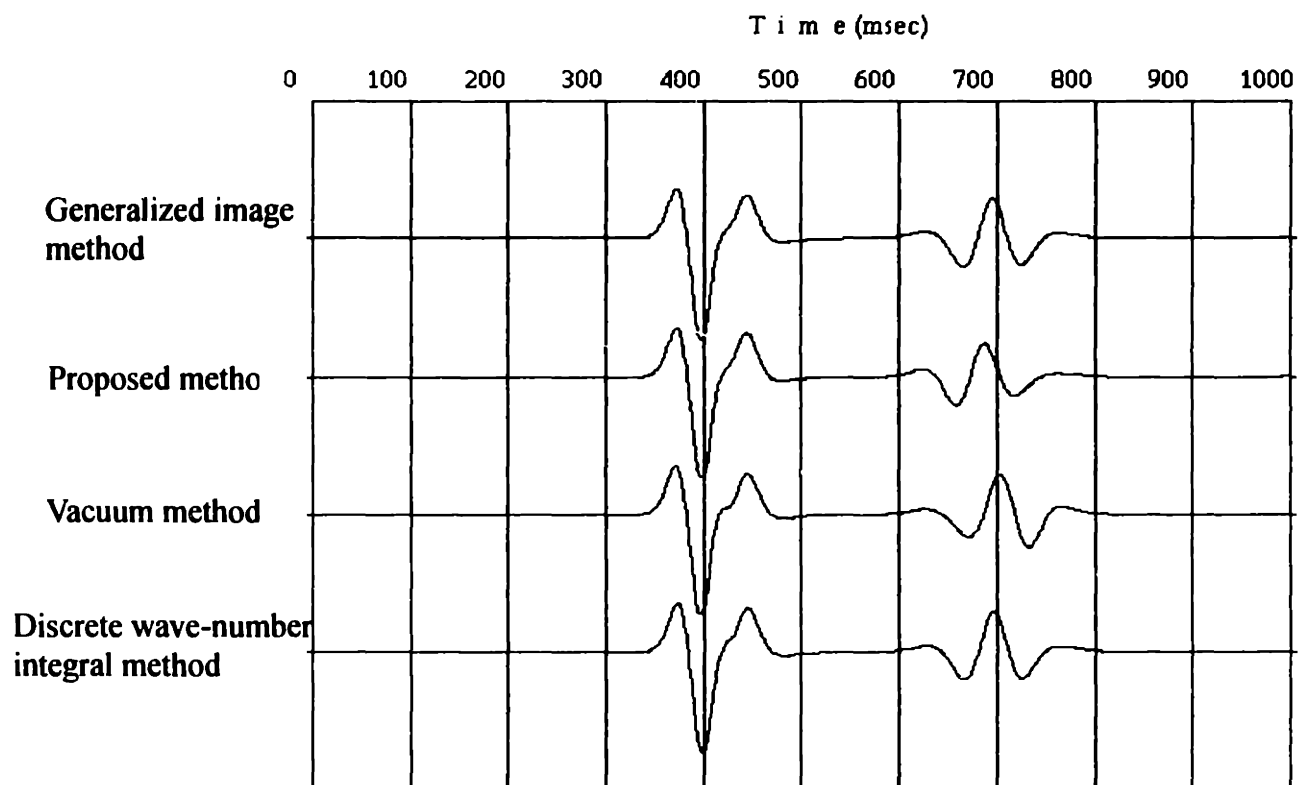
Figure 3.9: Comparison of a three methods in the 0° case against a solution of a discrete wave-number integral method. Grid size is 2m. Particle velocity parallel to the surface is plotted.

T i m e (msec)
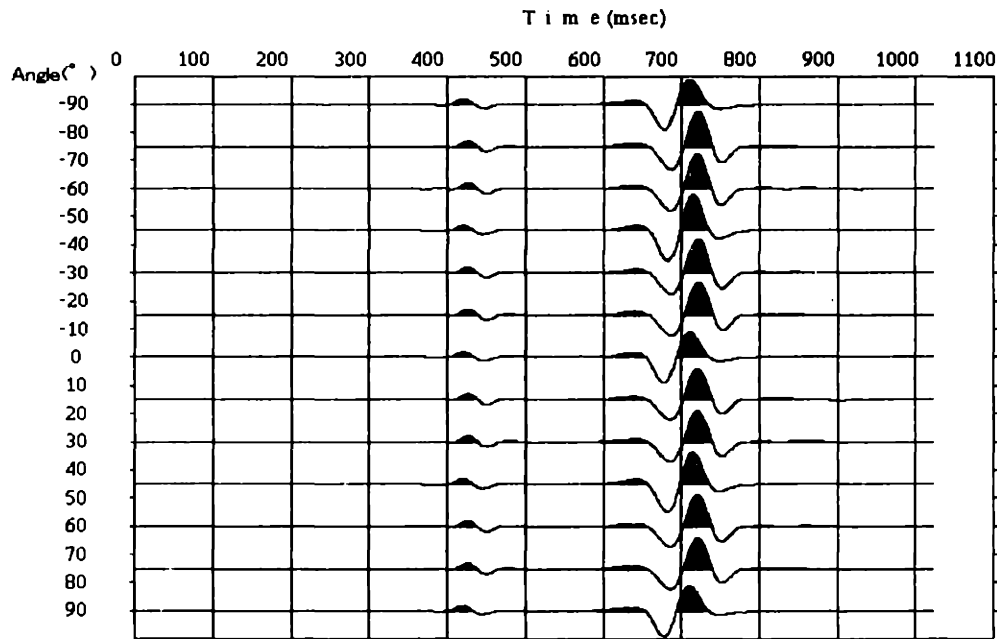
a) Generalized image method. Grid size = 2 m ($\lambda / \Delta x$ = 50).

T i m e (msec)
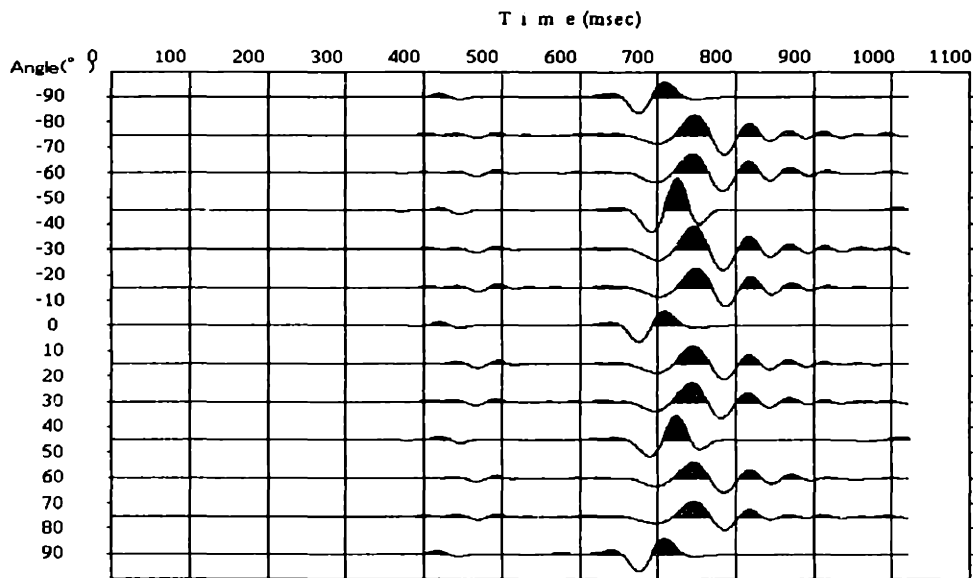
b) Generalized image method. Grid size = 5 m ($\lambda / \Delta x$ = 20).

Figure 3.10: Generalized image method. Time series collected at 50m below the free surface and 1000m source-receiver offset. Particle velocity perpendicular to the free surface is plotted. The angles correspond to the dip of the flat free surface ($0°$ is horizontal).
a) Grid size = 2 m (λ (wavelength)/ Δx(grid size) = 50).   b) Grid size = 5 m ($\lambda / \Delta x$ = 20).

T i m e (msec)
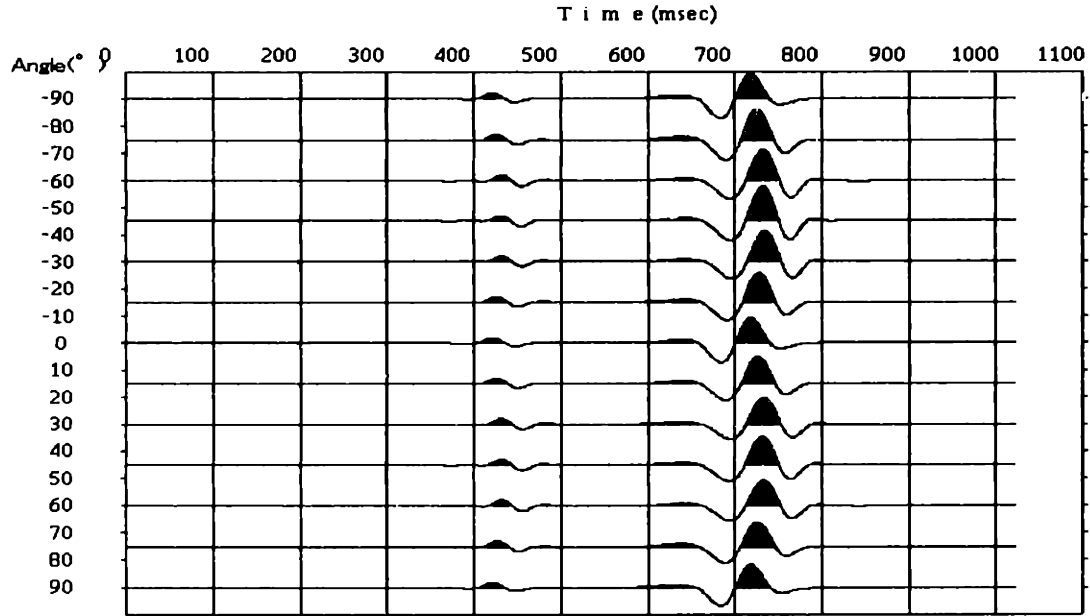
a) Vacuum method. Grid size = 2 m ($\lambda / \Delta x = 50$).

T i m e (msec)
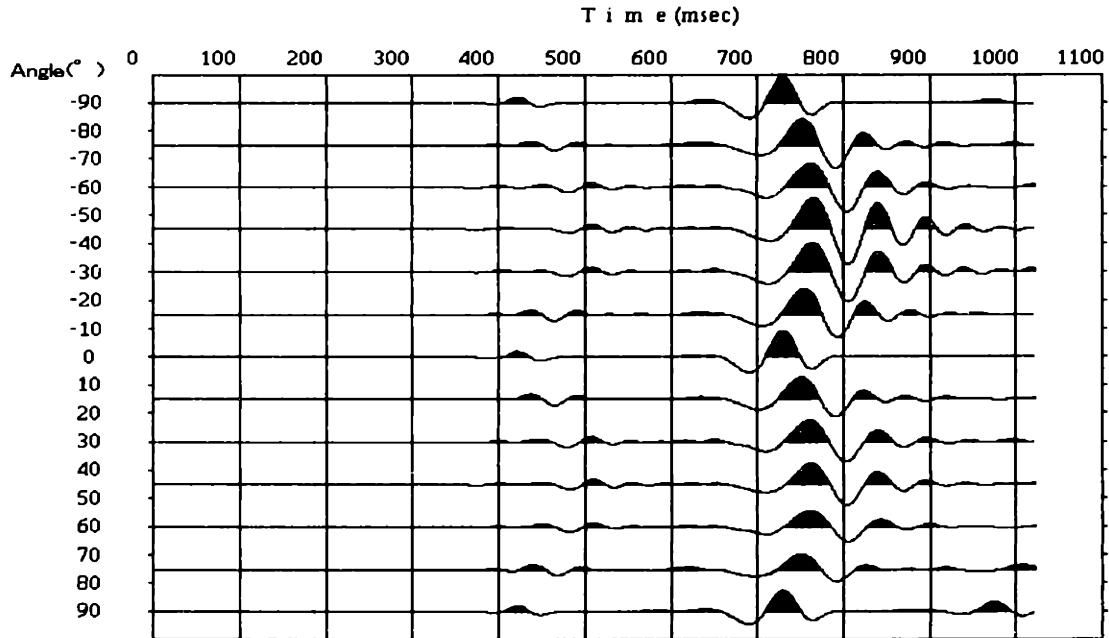
b) Vacuum method. Grid size = 5 m ($\lambda / \Delta x = 20$).

Figure 3.11: Vacuum method. Time series collected at 50m below the free surface and 1000m source-receiver offset. Particle velocity perpendicular to the free surface is plotted. The angles correspond to the dip of the flat free surface (0° is horizontal).

a) Grid size = 2 m ($\lambda / \Delta x = 50$).   b) Grid size = 5 m ($\lambda / \Delta x = 20$).

T i m e (msec)

Angle(°) 0   100   200   300   400   500   600   700   800   900   1000   1100
-90
-80
-70
-60
-50
-40
-30
-20
-10
0
10
20
30
40
50
60
70
80
90

a) Proposed method. Grid size = 2 m ($\lambda / \Delta x$ = 50).

T i m e (msec)
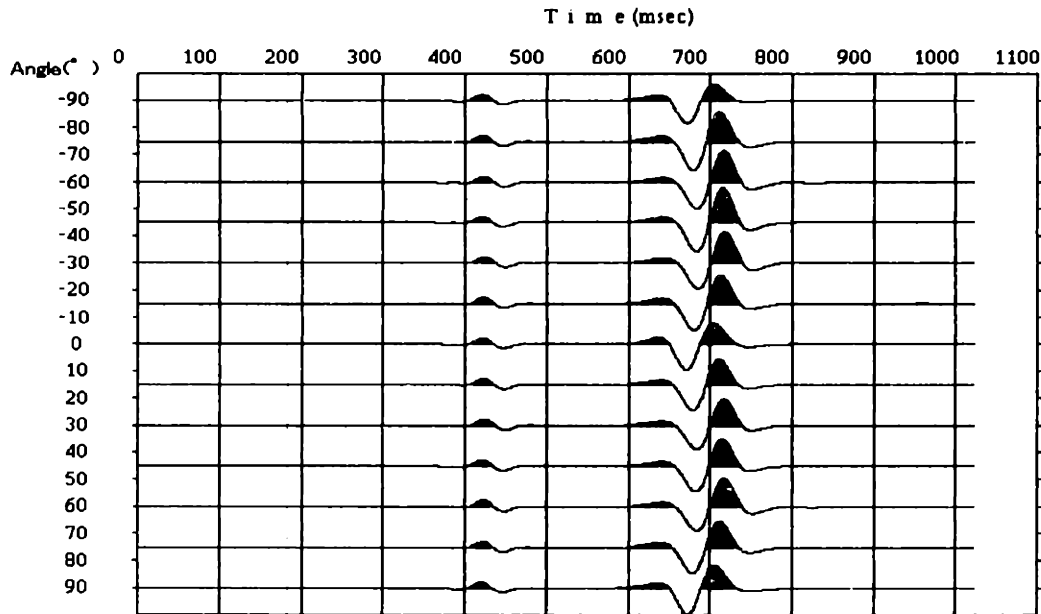
Angle(°) 0   100   200   300   400   500   600   700   800   900   1000   1100
-90
-80
-70
-60
-50
-40
-30
-20
-10
0
10
20
30
40
50
60
70
80
90
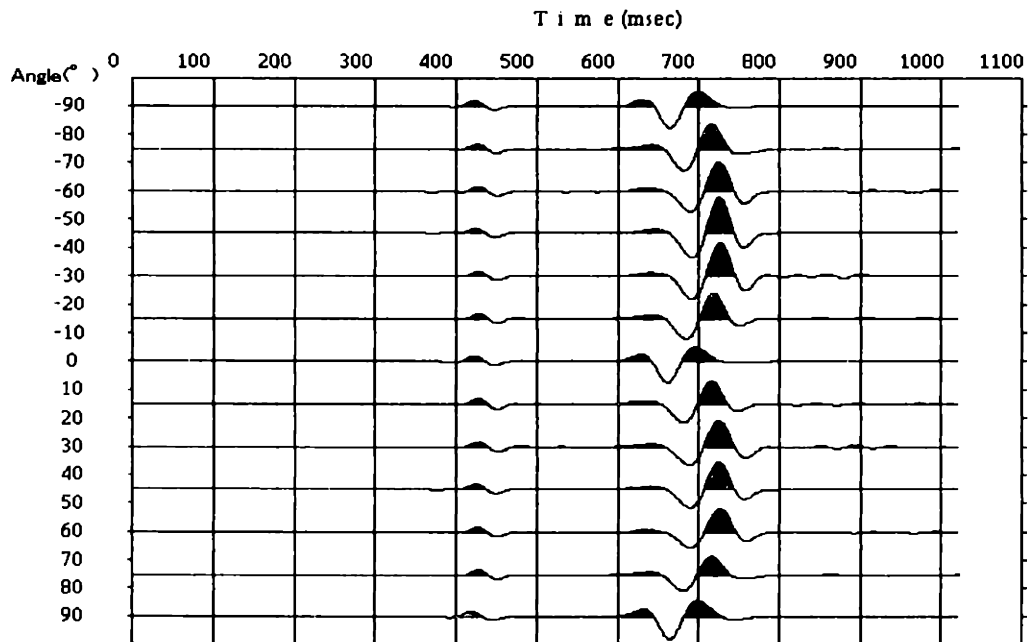
b) Proposed method. Grid size = 5 m ($\lambda / \Delta x$ = 20).

Figure 3.12: Proposed method. Time series collected at 50m below the free surface and 1000m source-receiver offset. Particle velocity perpendicular to the free surface is plotted. The angles correspond to the dip of the flat free surface ($0°$ is horizontal).
a) Grid size = 2 m ($\lambda / \Delta x$ = 50).   b) Grid size = 5 m ($\lambda / \Delta x$ = 20).
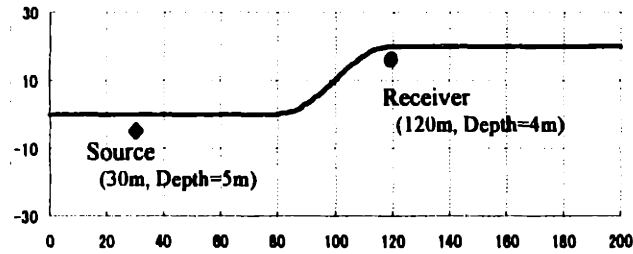
Figure 3.13: The model used in the second numerical test.
P-velocity=2000m/s, S-velocity=1155m/s,
Dencity=1000kg/m³, Qp=10000, Qs=10000,
Source=Ricker wavelet (110Hz)
Minimum wavelength (S-wave) is approximately 10m.
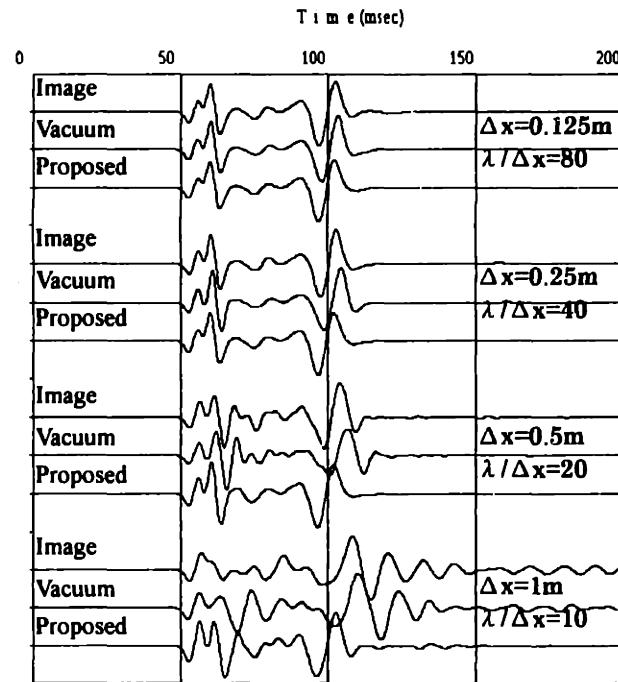
Figure 3.14: Time series of particle velocity perpendicular to the free surface with various grid sizes for the model given in Figure 5. Δx : grid size. λ : minimum wave length (approximately 10m) . Image : Generalized image method. Vacuum : Vacuum formulation. Proposed : Proposed method.

68
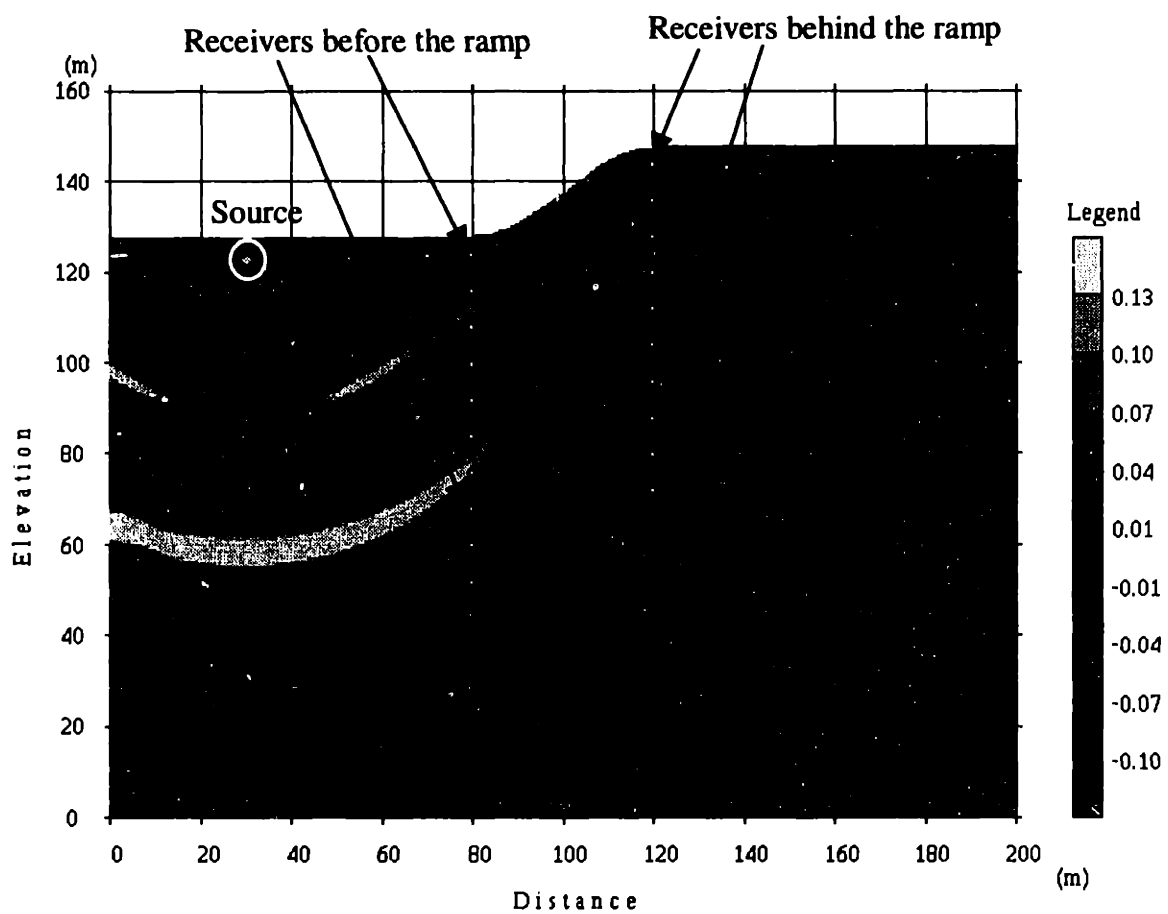
Figure 3.15: Receiver locations with a wave field of particle velocity (vertical component) at tome 45msec.
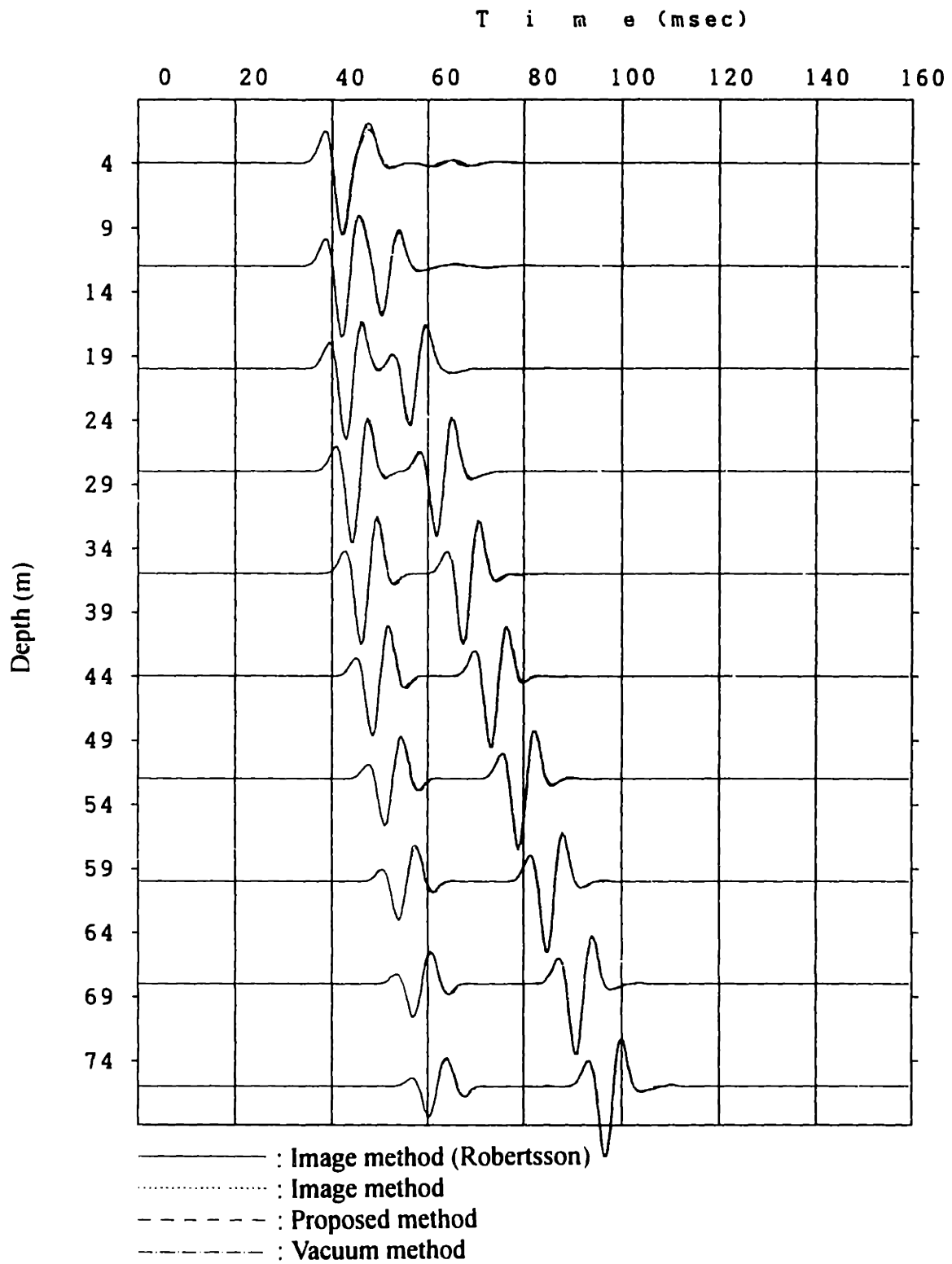
Figure 3.16: Particle velocity (horizontal component) collected at the receivers located before the ramp.
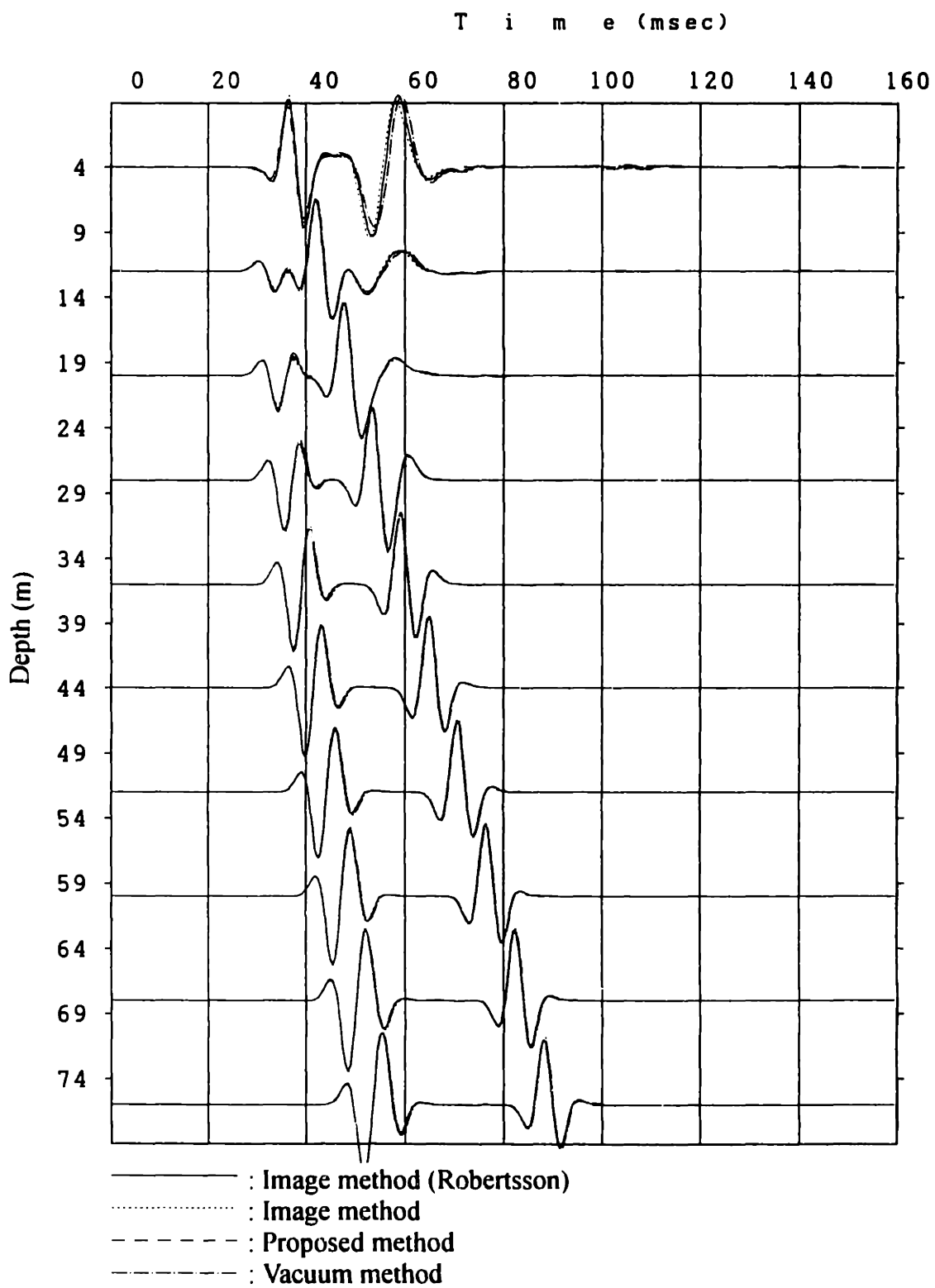
Figure 3.17: Particle velocity (vertical component) collected at the receivers located before the ramp.
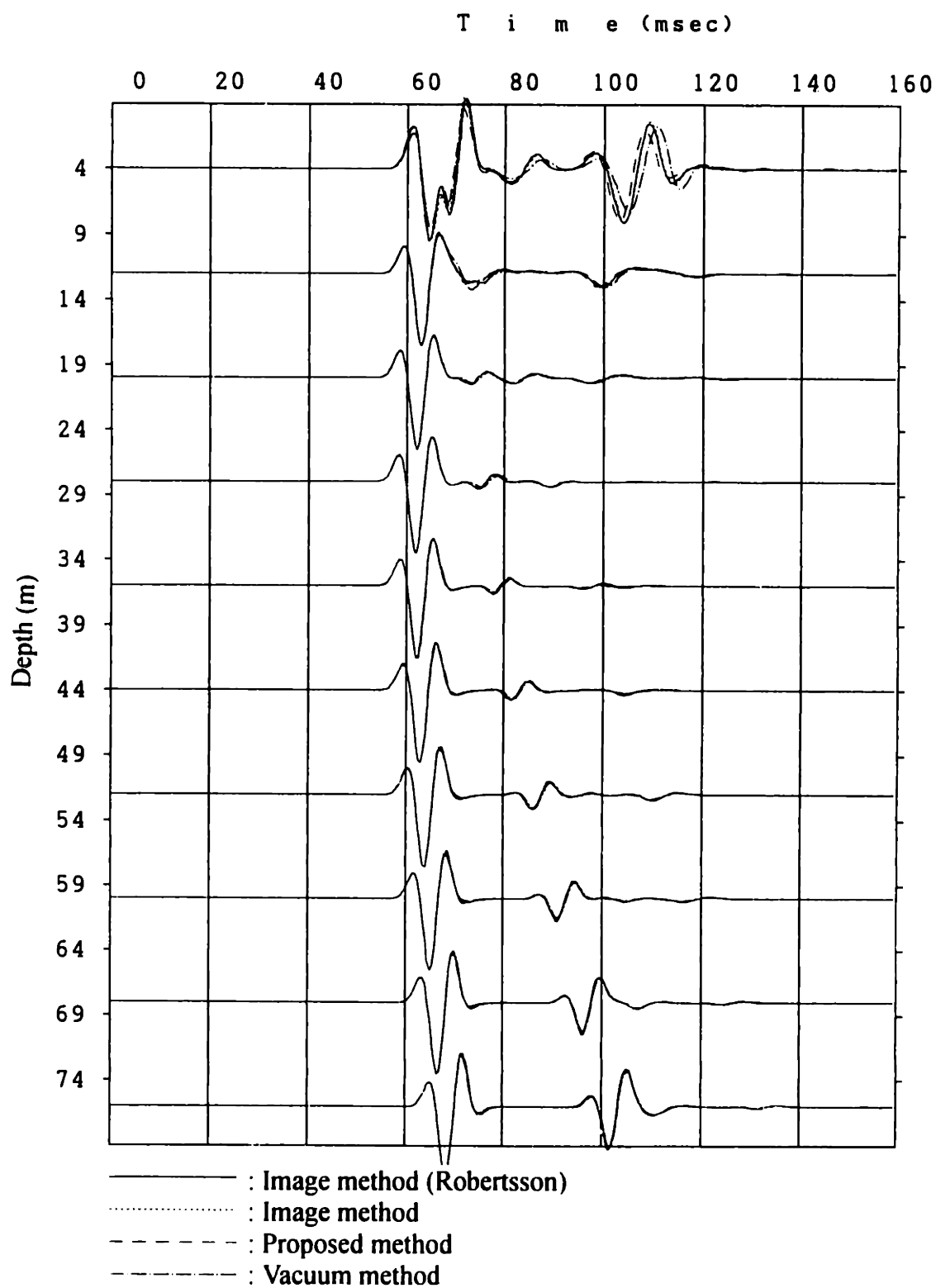
Figure 3.18: Particle velocity (horizontal component) collected at the receivers located behind the ramp.
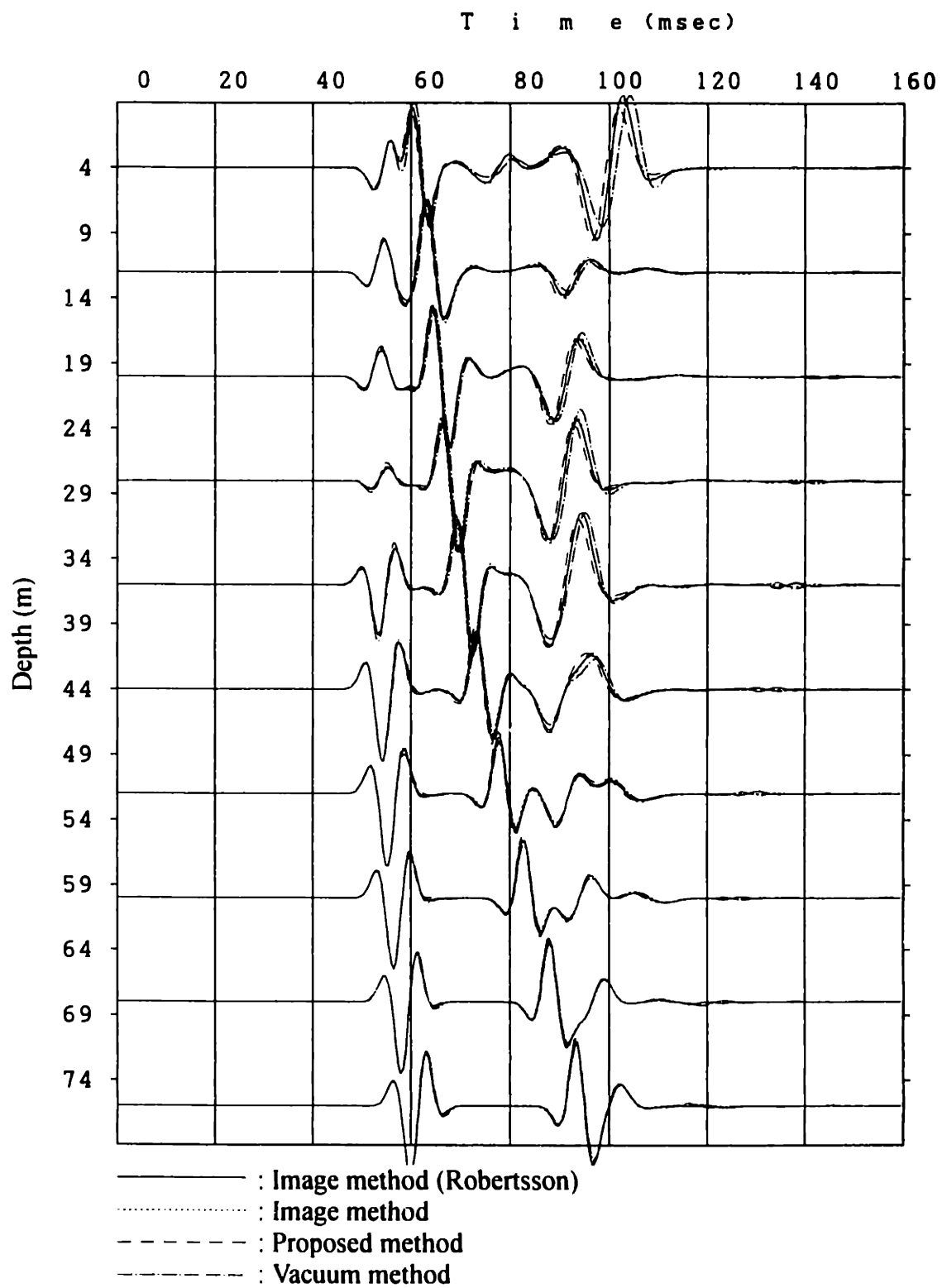
Figure 3.19: Particle velocity (vertical component) collected at the receivers located behind the ramp.
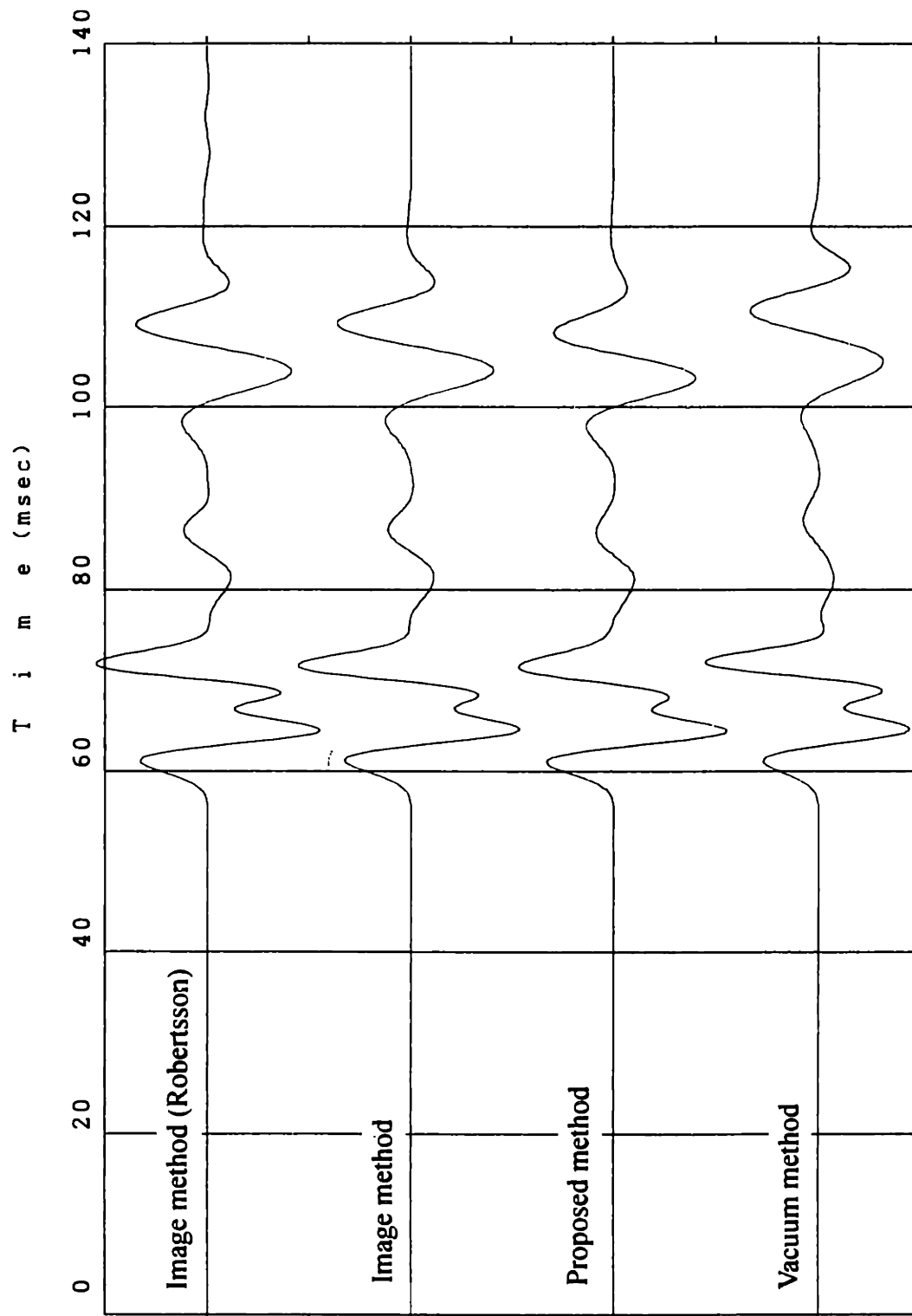
Figure 3.20: Particle velocity (horizontal component) collected at the shallowest receiver located behind the ramp.

Time= 25 0

a) Model A. Grid size = 0.5m, Step size = 0.5m.
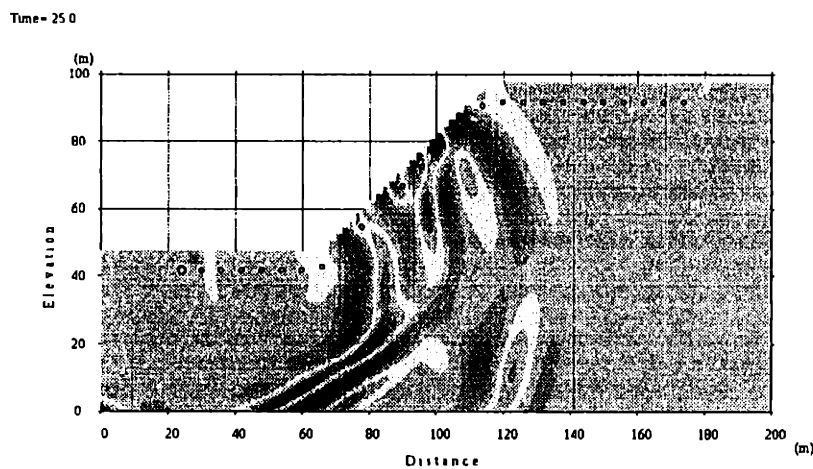
Time= 25 0

b) Model F. Grid size = 0.5m, Step size = 2.0m.

Figure 3.21: Two models from table 2 used in the numerical test, with a wavefield of particle velocity (vertical component) at time 25msec.
P-velocity=5082m/s, S-velocity=3000m/s,Density=2000kg/m^3
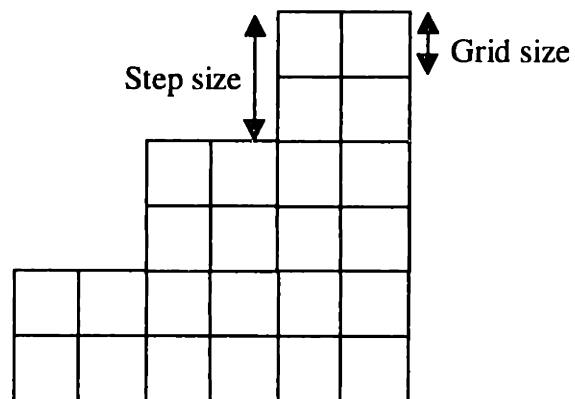
Figure 3.22: The definition of the grid size and the step size.
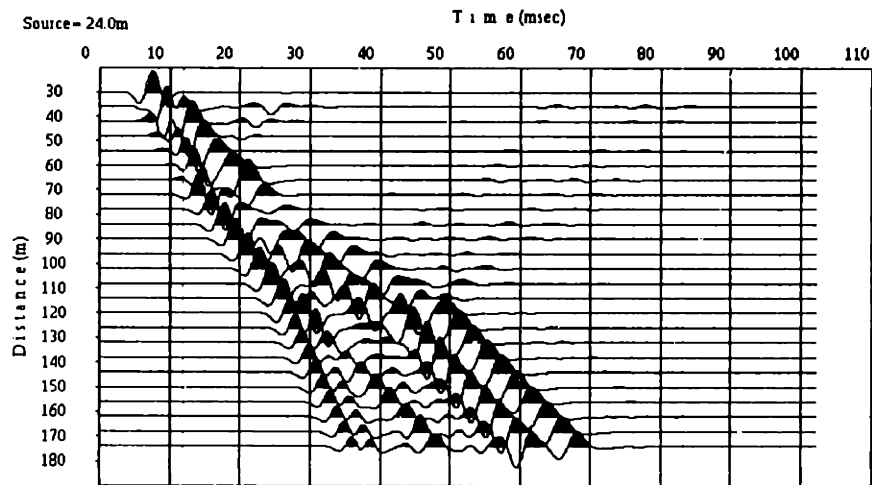
a) Model A. Grid size = 0.5m, Stepsize=0.5m.
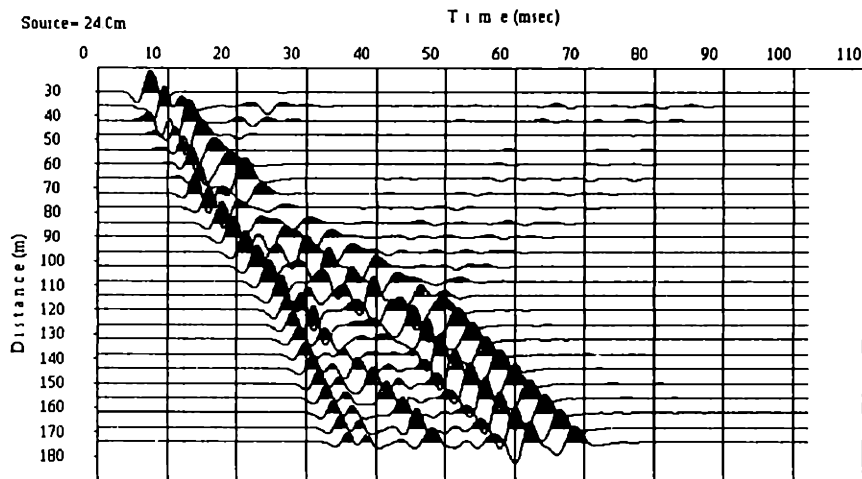
b) Model B. Grid size = 0.5m, Step size = 1m.
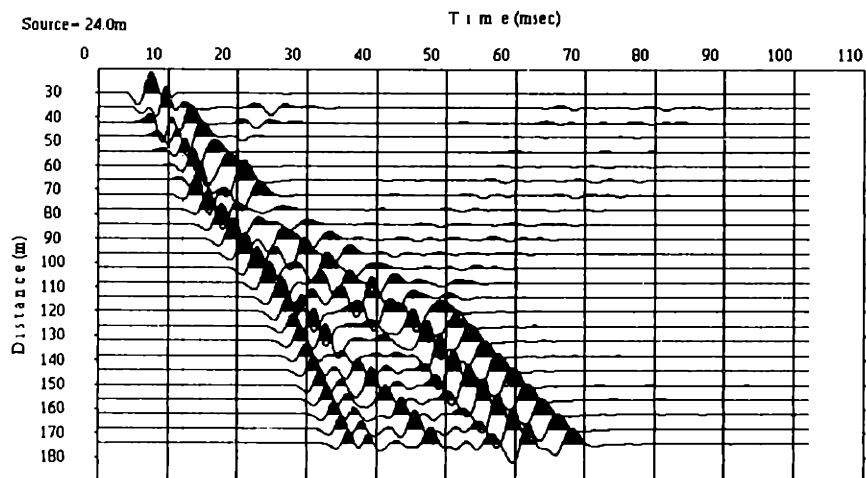
c) Model C. Grid size = 1.0m, Step size = 1.0m.

Figure 3.23: The Particle velocity (vertical component) from the simulation with the various grid and step sizes for the models given in Table 3.3.

76

Source= 24.0m
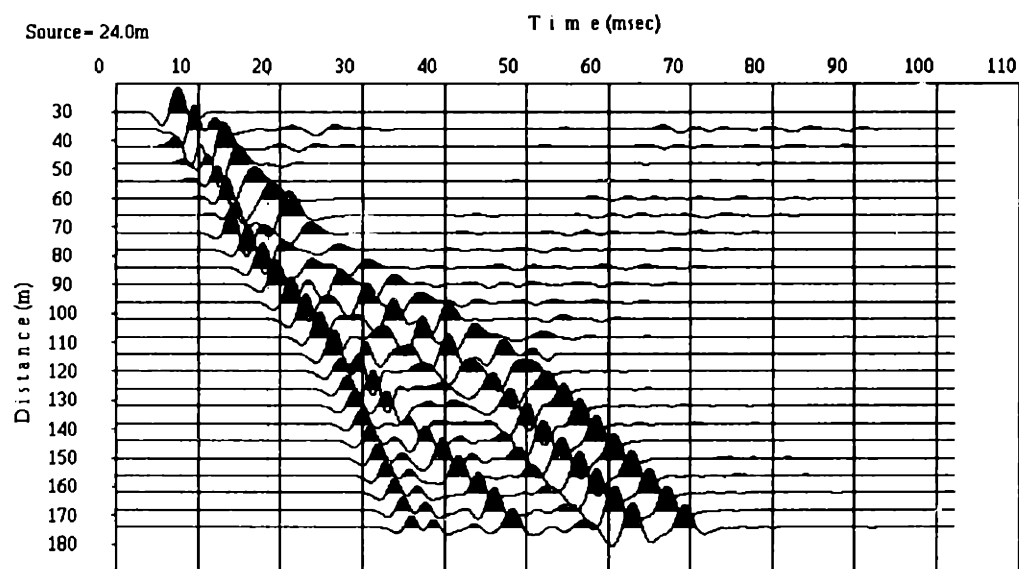
d) Model D. Grid size = 0.5m, Step size =1.5m.

Source= 24.0m
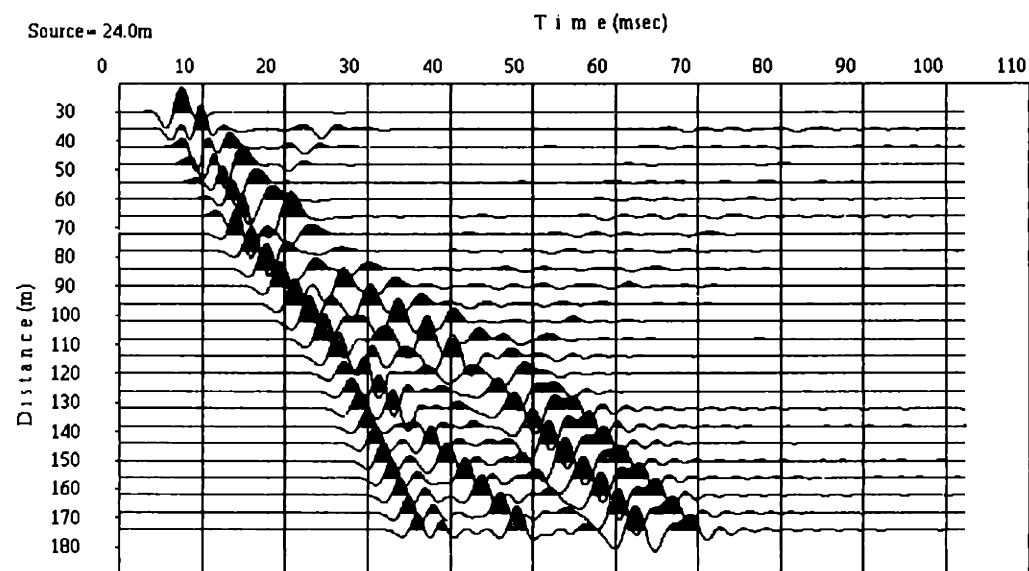
e) Model E. Grid size = 1.5m, Step size = 1.5m.

Figure 3.23, continued:
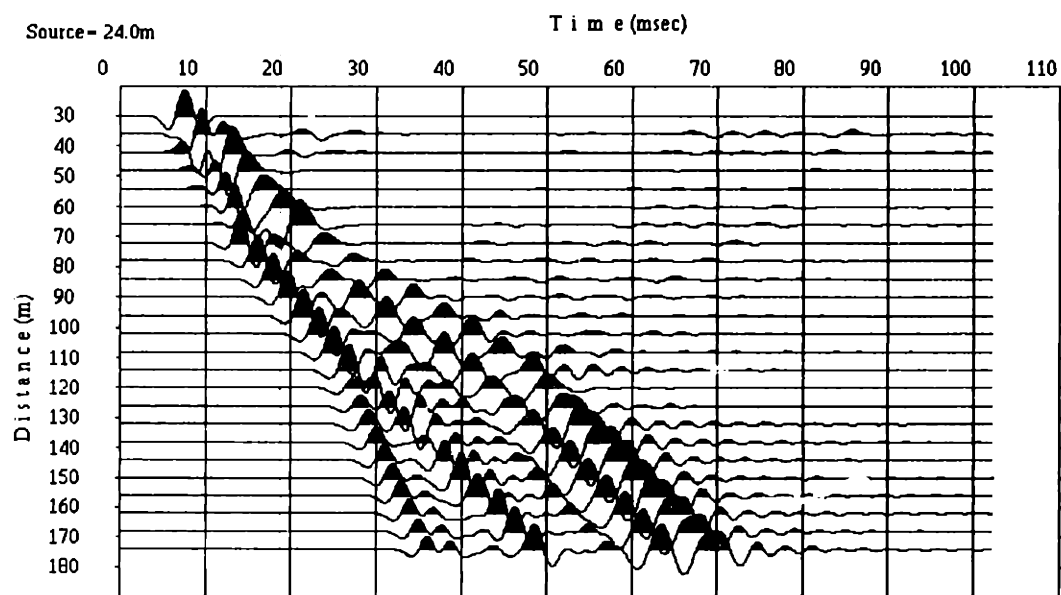
f) Model F. Grid size = 0.5m, Step size = 2.0m.
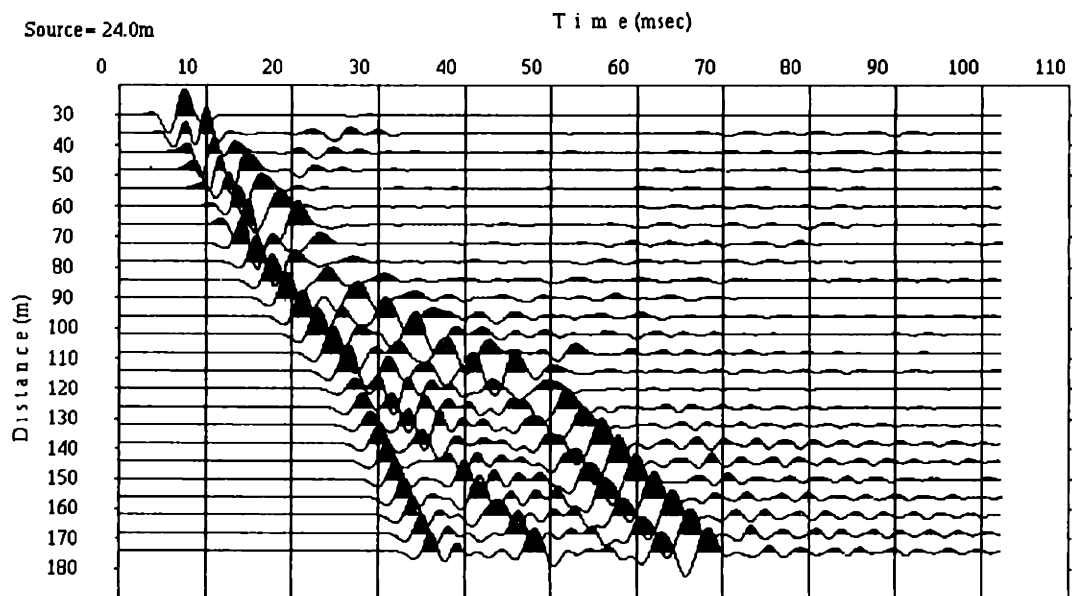
g) Model G. Grid size = 2.0m, Step size = 2.0m.

Figure 3.23, continued:
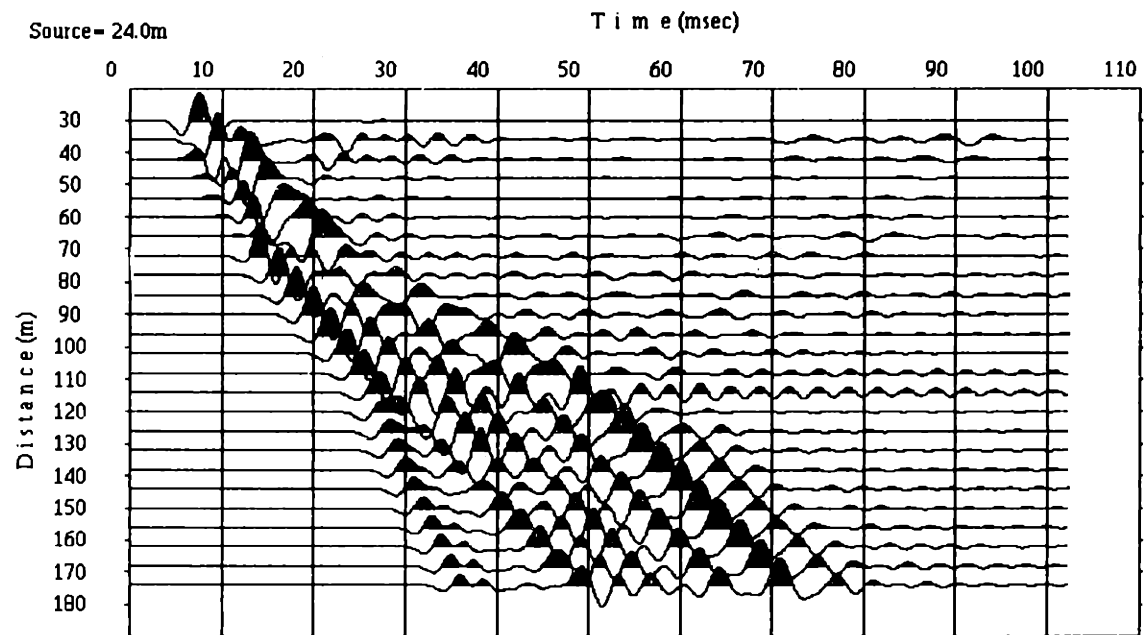
h) Model H. Grid size = 0.5m, Step size = 3.0m.
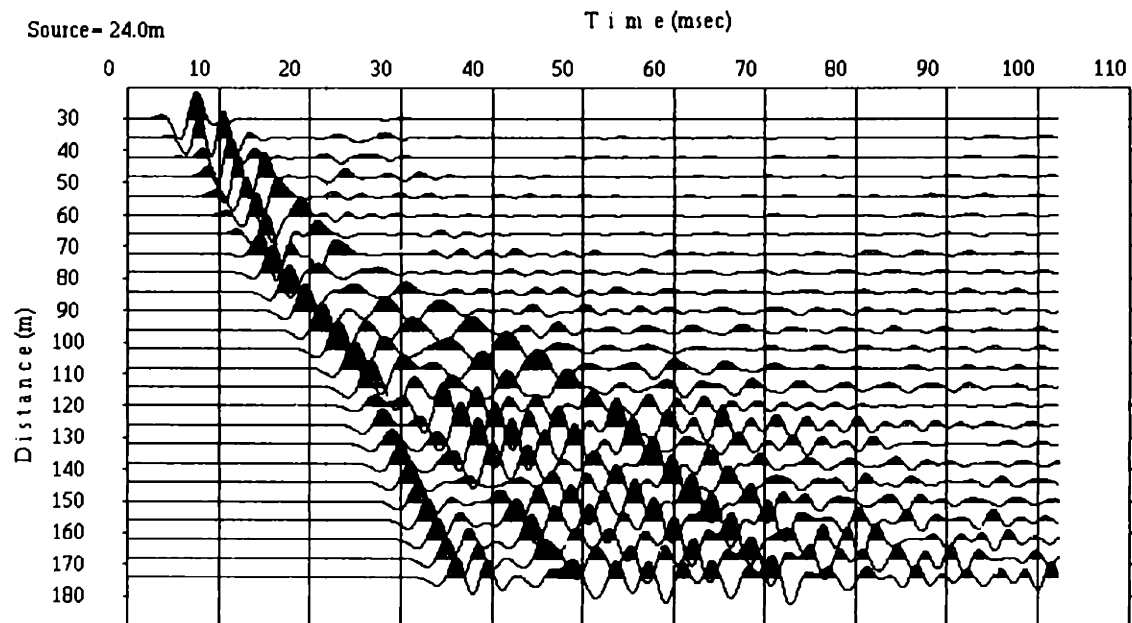
i) Model I. Grid size = 3.0m, Step size = 3.0m.

Figure 3.23, continued:

79

Grid size

	0.5m	1.0m	1.5m	2.0m	3.0m
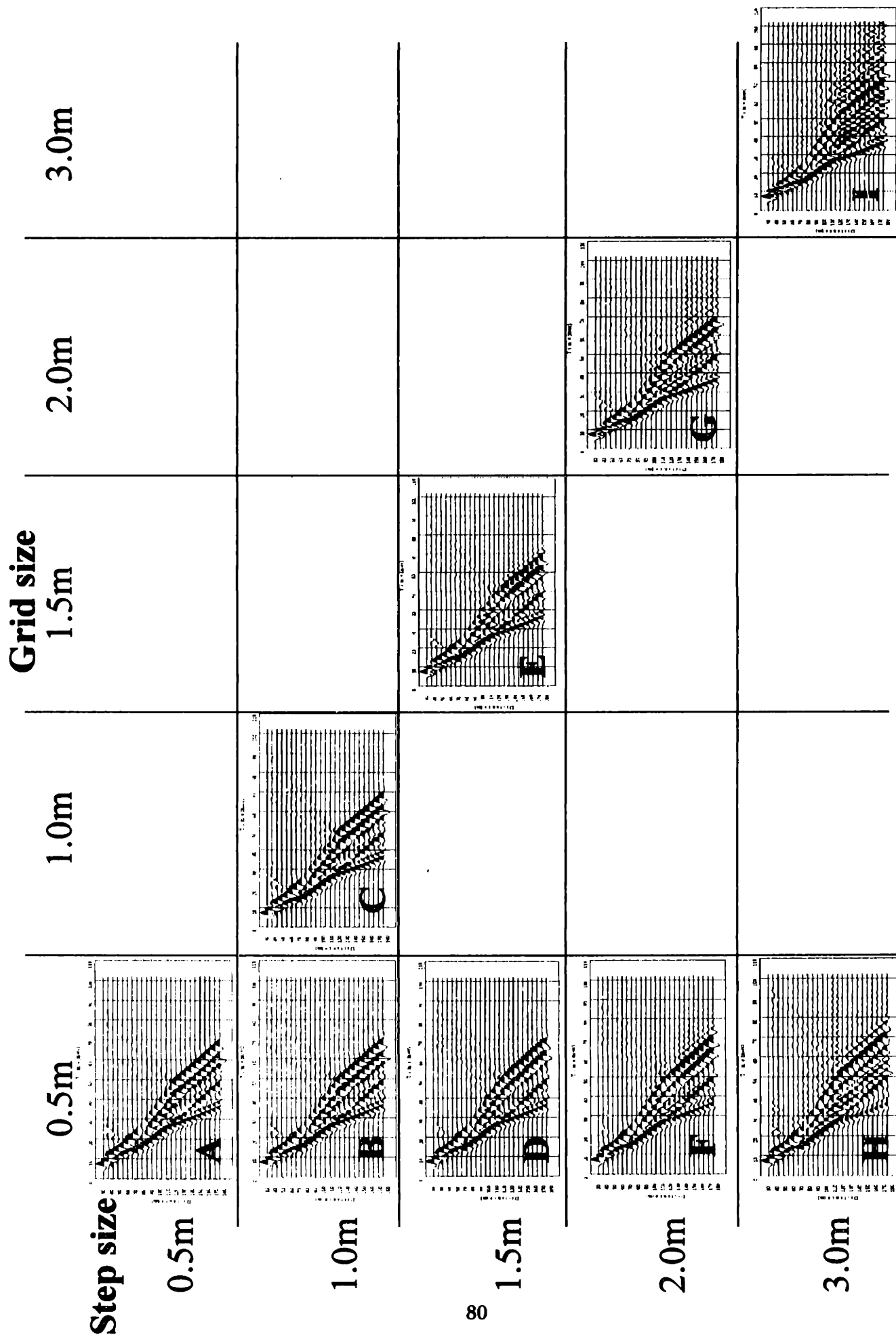
Figure 3.24: The Particle velocity (vertical component) from the simulation with the various grid and step sizes for the models given in Table 3.3.

Step size

0.5m

1.0m

1.5m

2.0m

3.0m
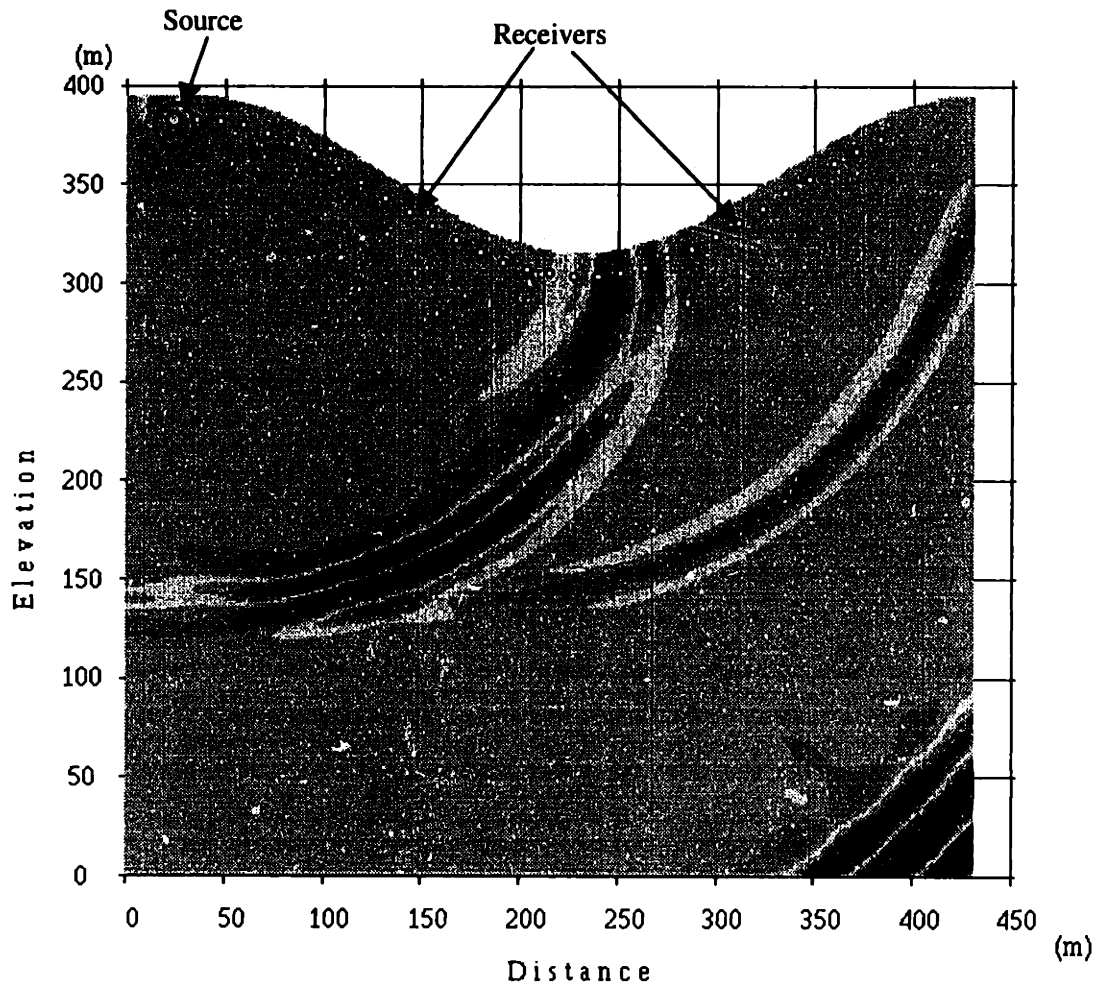
Model A

Time= 100.0

Figure 3.25: The model (A) used in the numerical test, with a wavefield of particle velocity (vertical component) at time 100msec.
P-velocity=6000m/s, S-velocity=3000m/s,Density=1800kg/m^3.

Model B
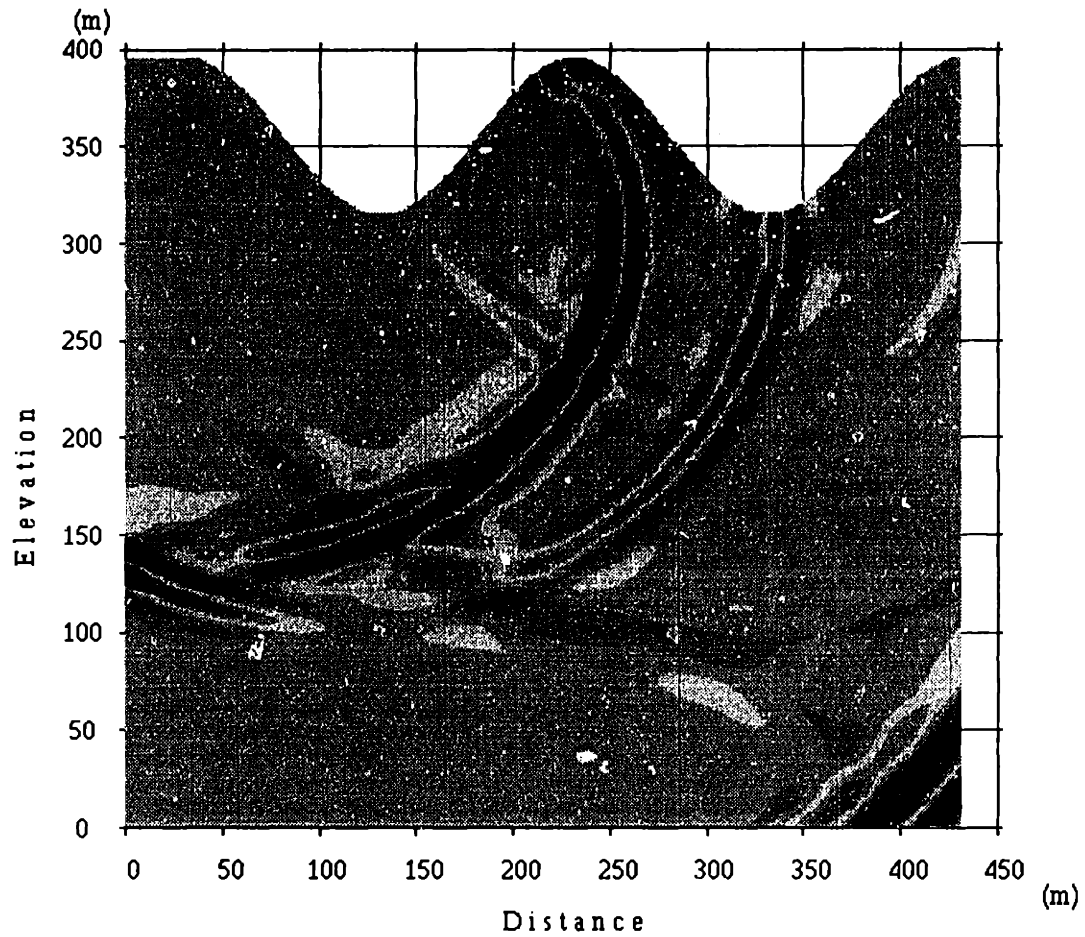
Figure 3.26: The model (B) used in the numerical test, with a wavefield of particle velocity (vertical component) at time 100msec.
P-velocity=6000m/s, S-velocity=3000m/s,Density=1800kg/m^3.

Source= 24.0m   T i m e (msec)

a) Grid size = 0.5m ($\lambda / \Delta x = 60$).

Source= 24.0m   T i m e (msec)
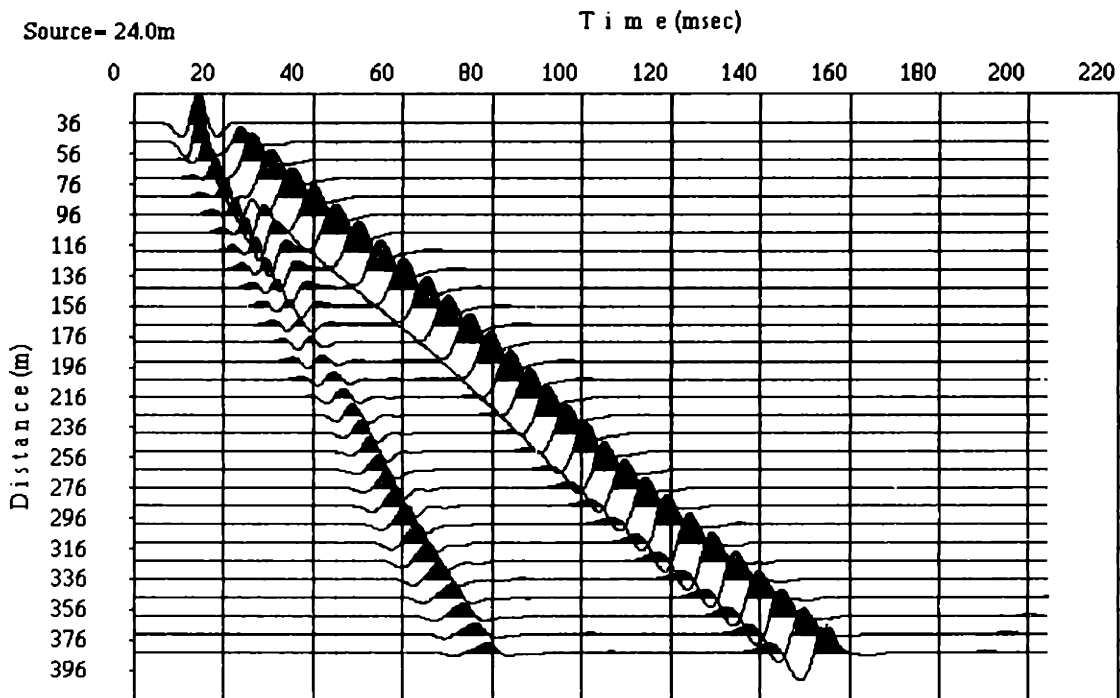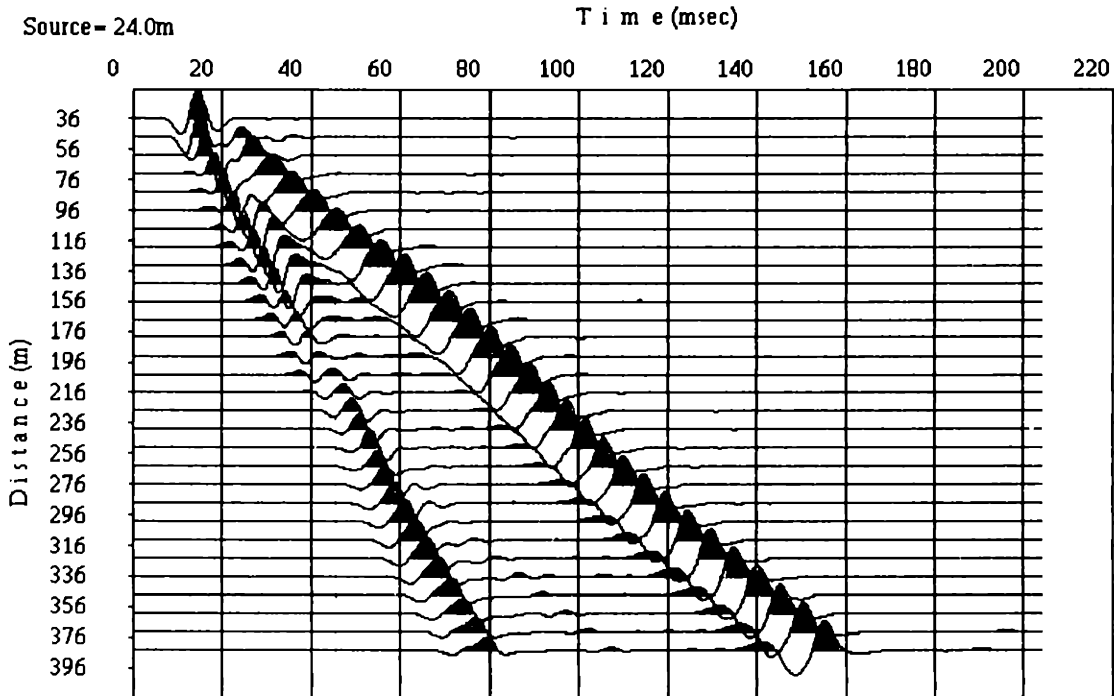
b) Grid size = 1.0m ($\lambda / \Delta x = 30$).

Figure 3.27: The Particle velocity (vertical component) from the simulation with the various grid sizes for the model (A) in Figure 3.25.

83

Source= 24.0m

T i m e (msec)

c) Grid size = 2.0m ($\lambda / \Delta x = 15$).

Source= 24.0m

T i m e (msec)
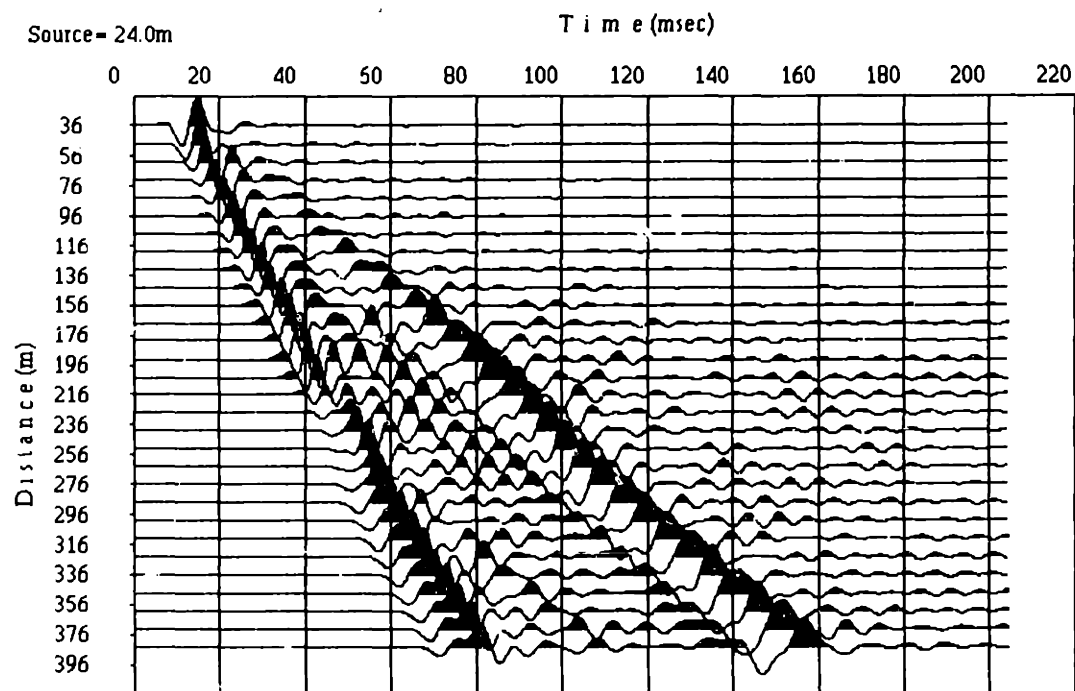
d) Grid size = 3.0m ($\lambda / \Delta x = 10$).

Figure 3.27, continued:

84

a) Grid size = 0.5m ($\lambda / \Delta x = 60$).

Source= 24.0m

b) Grid size = 1.0m ($\lambda / \Delta x = 30$).
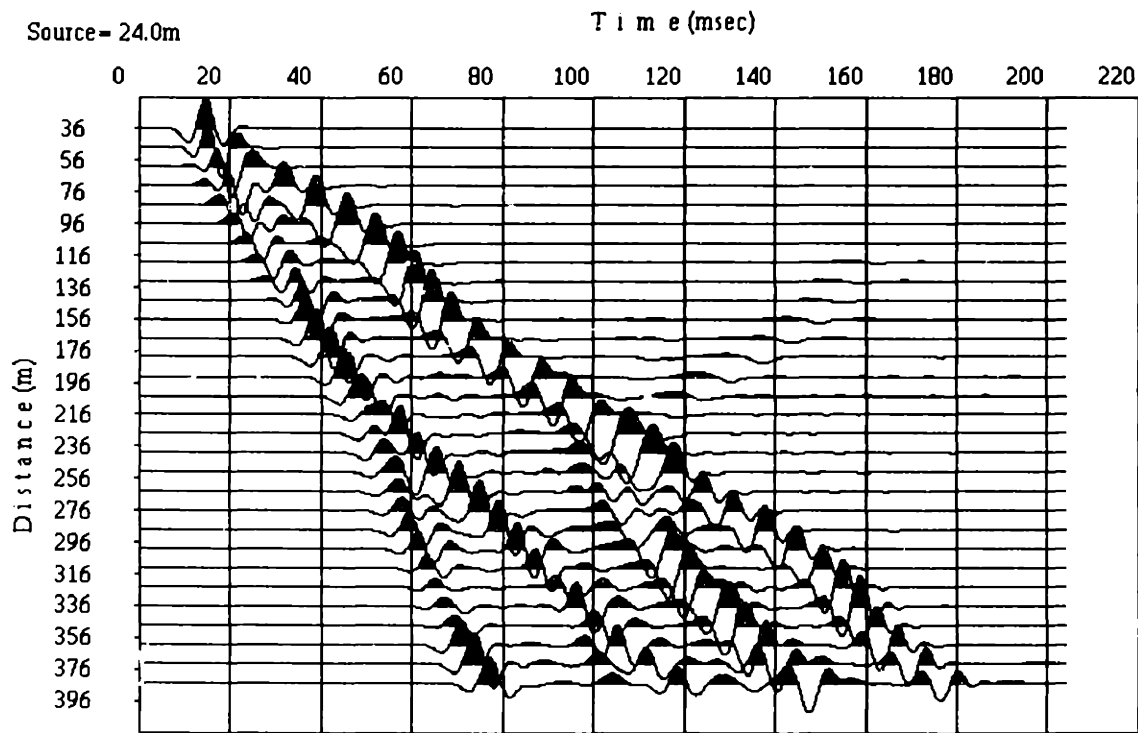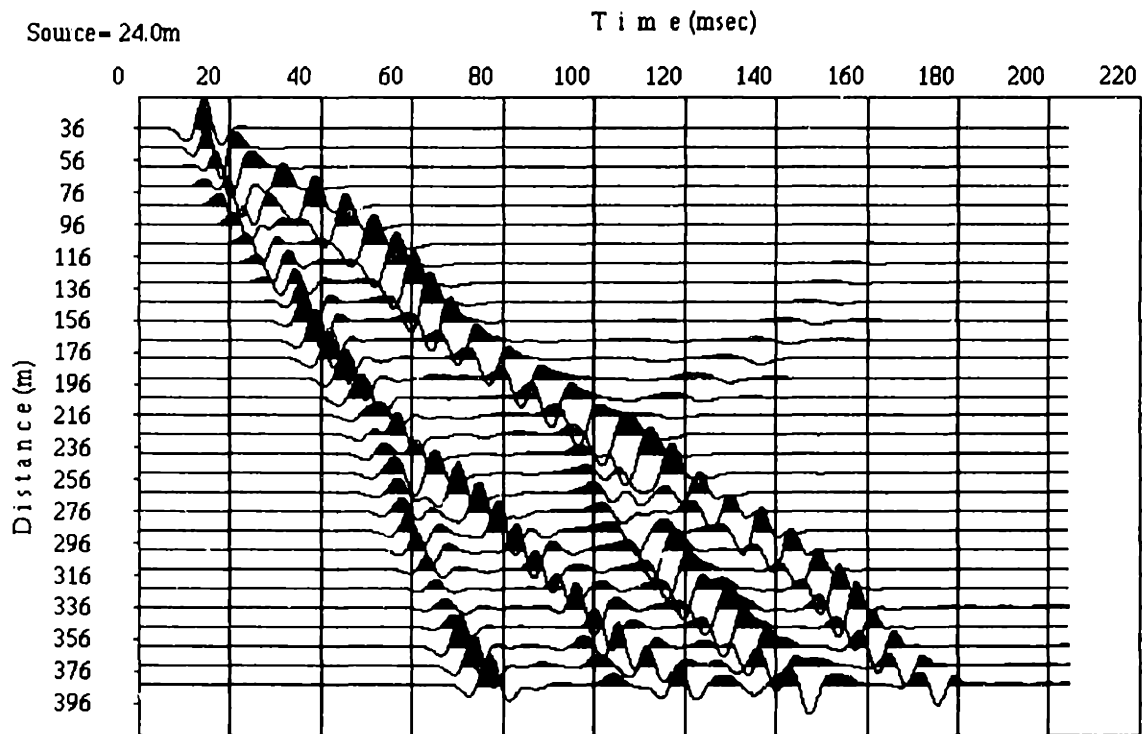
Figure 3.28: The Particle velocity (vertical component) from the simulation with the various grid sizes for the model (B) in Figure 3.26.
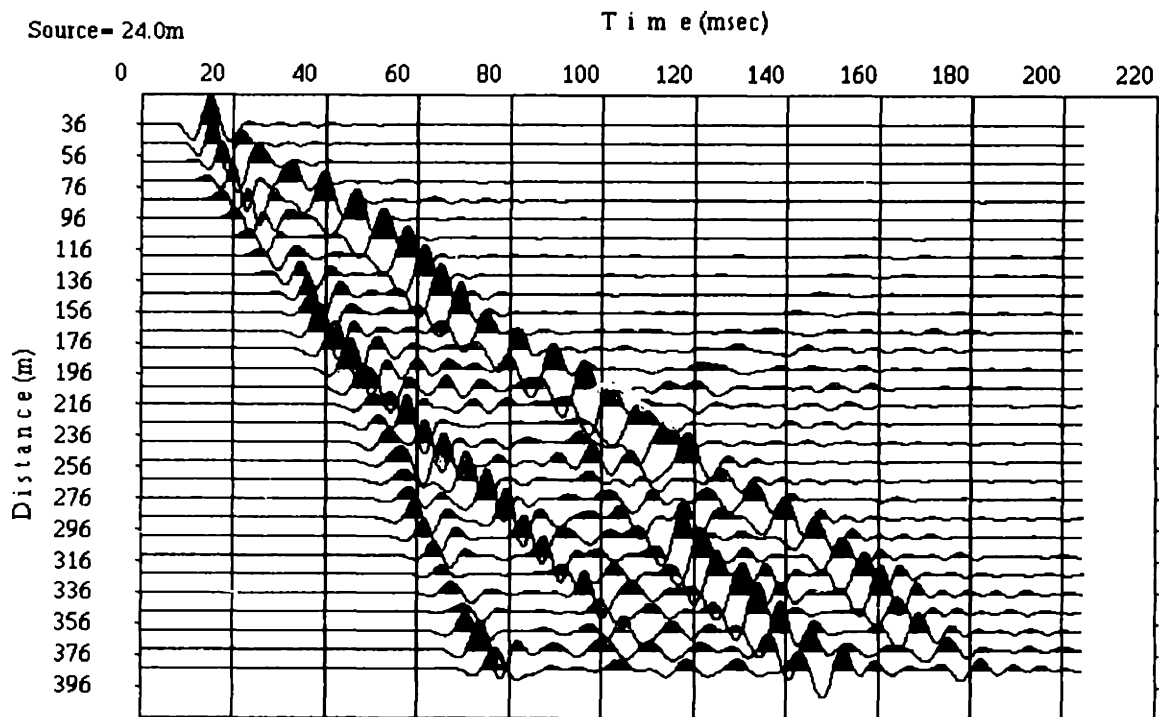
c) Grid size = 2.0m ($\lambda / \Delta x = 15$).
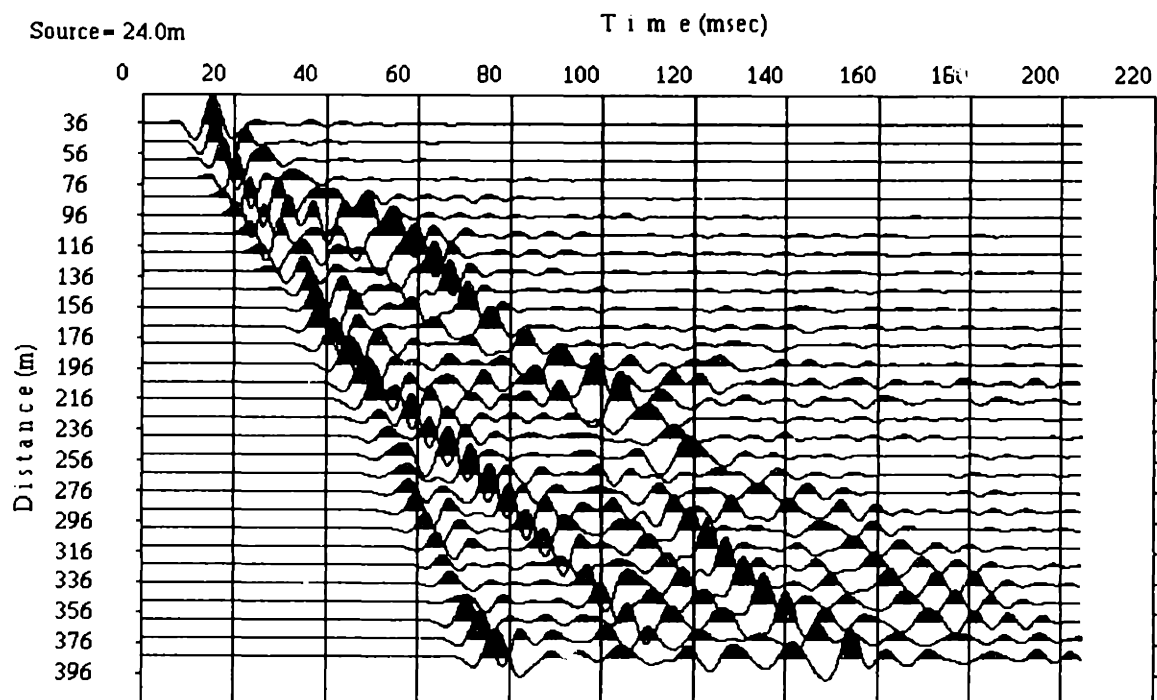
d) Grid size = 3.0m ($\lambda / \Delta x = 10$).

Figure 3.28, continued:

86

Chapter4

Variable Grid Finite-difference Method

4.1 Introduction

A uniformly spaced grid used to a model an irregular surface and low velocities in the shallow subsurface require large portions of the model to be over sampled. The resulting memory requirements would severely limit the size of the models. An obvious solution to this dilemma is to use a finer grid in the vicinity of the free surface compared to the deeper parts of the model. The variable grid approach allows us to vary the discretization of the model and the wavefield as required by the velocity structure. Compared to a standard uniform finite-difference grid approach, this method saves a considerable amount of memory and computations. Therefore, we combined the variable grid method with our irregular free-surface modeling.

In the variable grid method, one has to decide a particular size ratio of fine grids to coarse grids (grid ratio). The selection of the appropriate grid ratio is important. The large grid ratio can improve the efficiency of the computation. However, as the grid ratio increases, the numerical inaccuracy due to the change of the grid sizes may increase (De Lilla, 1997). In this study, I employ the grid ratio of three for the following reasons: First, the smaller grid ratio is better for the stability and accuracy. Second, the previous chapter has revealed that the calculation of irregular surface required at least 30 grid-points per wavelength for sufficiently accurate result. Thus, if we use a three times finer grid in the near surface region, other region can be calculated by using ten grid-points per wavelength that is the optimum number of O(2,4) staggered grid scheme (see the Chapter 2). Finally, an odd value for grid ratio is preferable, as it will be shown later.

4.2 One-dimensional Variable Grid Method

4.2.1 Computation Procedure

At first, I will describe an one-dimensional case for the sake of simplicity. Figure 4.1 shows the one-dimensional staggered grid and a computation procedure. If we choose an odd number for the grid ratio, the particle velocities and the stresses on both coarse and fine grids can be placed in exactly the same place. This character of the odd grid ratio can significantly reduce the complication of the computation. Therefore, we can say that the odd grid ratio is preferable for the velocity-stress staggered grid. The computation procedure is the following (Figure 4.1).

1. Update the stresses on the coarse grid.
2. At the boundary on the fine grid (Figure 4.1 A), replace the stresses on the fine grid by the stresses on the coarse grid, calculated in the first step.
3. Update the stresses on the fine grid without a boundary. At the next boundary (Figure 4.1 B), a fourth-order stencil cannot be used. Therefore, we use a second-order approximation there.
4. Replace coarse grid stresses within the fine grid region by the fine grid. Subsequently, the same procedure is applied to the velocity fields, and the second step can be omitted.

4.2.2 Numerical Example

I will show two, one-dimensional, numerical examples to demonstrate the accuracy and efficiency of this variable grid method. The first model is an acoustic homogeneous model with velocity of 2000m/s and a density of 2000kg/ m^3. The source is a point explosion with a 100 Hz Ricker wavelet. Then, the approximate wavelength is 20m. The receivers are

located 0m to 190m from the source at 10m distance interval. The three times finer grids were placed at the distance between 100m and 145m. The grid size was 1m in the coarse grid region and 1/3m in the fine grid region. Figure 4.2 shows the particle velocity from the simulation. Waveforms seem not to be affected by the change of the grid sizes. Figure 4.3 shows the same waveforms with large gain. In Figure 4.3, we can see reflection from the boundary between the two grid sizes. However, the amplitude of the reflection is sufficiently small. Figure 4.4 shows the maximum amplitude of waveforms. From Figure 4.4, we can see that the effect of the change of grid sizes on the amplitude is less than 0.03%. Table 4.1 shows the amplitude of the direct and the reflected waves at the distance of 50m. The amplitudes of the reflected waves from the boundary between different grid sizes are less than 0.01% of the incident waves. The amplitude ratio cf the reflected waves to the incident waves is sufficiently small compared with the reflection from the absorbing boundary (Peng and Toksöz, 1995). Therefore, I consider that these numerical reflection can be neglected in the practical simulation.

Table 4.1 The amplitude of the direct and the reflected waves at the distance of 50m.

	Amplitude	Amplitude ratio
Direct wave (40msec)	2.500231	100
First reflection (90msec)	0.000197	0.00788
Second reflection (130msec)	0.000117	0.00468

The second model is an heterogeneous acoustic model. P-velocities and densities are shown in Table 4.2. The source is a point explosion with a 100 Hz Ricker wavelet. The approximate wavelength in each velocity region is also shown in Table 4.2.

Table 4.2   Velocity model and corresponding wave length

Distance	Velocity(m/sec)	Density(kg/m^3)	Wavelength(m)	Wavelength/grid size	
				Coarse(1m)	Fine(1/3m)
~105m	2000	1000	20	20	60
105~140m	500	1000	5	5	15
140m~	4000	2000	40	40	120

The receivers are located 10m to 190m from the source at 10m distance intervals. Two

simulations were performed. The first simulation employed the uniform grid of 1m and second model employed the variable grid in which the coarse grid of 1m and the fine grid of 1/3m were used. In the variable grid model, three times finer grids were placed at the distance between 100m to 145m. Figure 4.5 and Figure 4.6 shows the particle velocity from the simulations. From the simulation of the uniform grid (Figure 4.5), we can see obvious numerical dispersion due to the small grid-points per wavelength in the low velocity zone (105 to 140m). We can also see that the result of the variable grid calculation (Figure 4.6) has no numerical dispersion and yields accurate waveforms.

4.3 Two-dimensional Variable Grid Method

4.3.1 Computation Procedure

Figure 4.7 shows the two-dimensional, staggered, finite-difference grid in the vicinity of the boundary between different grid sizes. We use a three times finer grid (both horizontally and vertically) in the near surface or low velocity region compared to the rest of the model. Figure 4.8 shows the computation procedure of the proposed variable grid method. The computation procedure can be summarized as follows:

1. Update the stresses on the coarse grid.

2. At the fine grid boundary, interpolate the stresses on the coarse grid calculated in the first step. Use a simple linear interpolation.

3. Update the stresses on the fine grid without the boundary. Next to the boundary, a fourth-order stencil can not be used. Therefore, a second-order approximation is used.

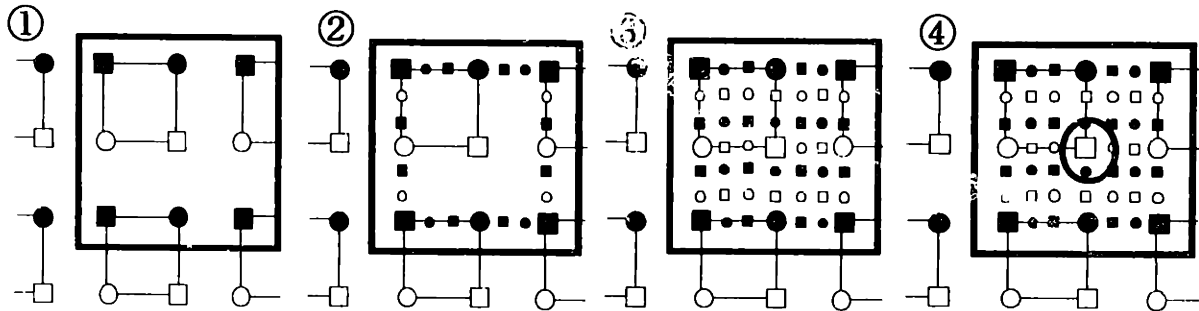4. Coarse grid stresses within the fine grid region by the fine grid values. Apply the same procedure to the velocity fields. For the viscoelastic case, memory variables can be updated with the stress field simultaneously. Only the velocity field needs to be updated separately.

4.3.2 Improvement of Stability

The simple implementation of this variable grid method is not stable if we perform a large number of time steps. Figure 4.9 shows an example of the instability due to the variable grid computation. In order to reduce the instability of the computation, I applied averaging or weighting to the replacement of the coarse grid components within the fine grid (fourth step in Figure 4.8). Figure 4.10 shows several methods of averaging or weighting applied to the replacement components. Figure 4.11 shows the energy of the waveforms (shown in Figure 4.9) integrated over time for various methods. As a result of this comparison, I conclude that 5 point averaging or 9 point weighting is most stable. This result implies that the weight of the center node of the stencil is crucial for a stable computation.

4.3.3 Numerical Example

I will show several two-dimensional numerical examples to demonstrate the accuracy and efficiency of the variable grid method. The first model is an elastic Poisson solid with P- and S-velocities of 3000 and 1730m/sec respectively, and a density of 1800kg/m^3. Figure 4.12 shows the location of the source and receivers, and the fine grid region. A vertical line source (z direction) is placed at the distance of 20m with the horizontal component (x-direction) of velocity. Thus the source generates a plane wave propagating in x direction. A 50 Hz Ricker wavelet is used as a source wavelet. The receivers were located at the right side of the source, 10 to 190m offset at 10m distance interval. The area of fine grid is located between distance of 100 and 150m as shown in Figure 4.12. The grid size is 3m in the coarse grid region and 1m in the fine grid region. Figure 4.13 shows the pressure (the sum of normal stresses: $\sigma_{xx} + \sigma_{zz}$) from the simulation. Waveforms seem not to be affected by the change of the grid sizes. I performed the simulation for the same velocity model but using the uniform grid of 3m. Figure 4.14 shows the difference between the variable grid and the uniform grid. We can see clear numerical reflection from the boundary between

different grid sizes. However, the amplitude ratio of the reflected waves to the incident waves is less than 0.3%. This ratio is larger than the one-dimensional case, but still sufficiently small compared with the reflection from the absorbing boundary (Peng and Toksöz, 1995). Figure 4.15 shows the comparison of maximum amplitude of the variable grid simulation with the uniform grid simulation. The increase of amplitude in large offset (source-receiver distance) may be due to the reflection from absorbing boundary. This figure implies that the effect of the change of grid sizes is much less than the effect of the reflected waves from the absorbing boundary. Therefore, I assume that these numerical reflection can be neglected in practical simulations.

In order to investigate the stability and accuracy in more complex structure, I performed two more numerical tests. The second model has a fine grid area that is square as shown in Figure 4.16. The model is an elastic solid with P- and S-velocities of 3000 and 1500m/sec respectively and density of 1800kg/m^3. Two simulations with different source locations were performed. The location of the source and receivers are shown in Figure 4.16. The source is a point explosion with a 200Hz Ricker wavelet. The grid size was 1m in the coarse grid region and 1/3m in the fine grid region. Figure 4.17 and Figure 4.18 show the pressure collected at the receivers, together with the simulations in which the uniform grid of 1m was used. We can see the difference between the variable grid calculation and uniform grid calculation is sufficiently small wherever the source is placed.

The third model has the low velocity area which is covered by the fine grid. The velocity model and the location of a source and receivers are shown in Figure 4.19. The source is a P-wave source with a 50Hz Ricker wavelet. Velocities, densities and corresponding wave lengths are listed in Table 4.3.

Table 4.3   Velocities, density and corresponding wavelength for third model

	P-velocity (m/sec)	S-velocity (m/sec)	Density (kg/m³)	Shortest wavelength (m)	Wavelength/grid size Coarse (3m)	Fine(1m)
Background	3000	1500	1800	30	10	30
Low velocity area	1000	500	1500	10	3.333	10

Three calculations (uniform grid of 3m, uniform grid of 1m, variable grid of 3m in coarse grid and 1m in fine grid) were performed. Figure 4.20 shows the discretization of the velocity model at the vicinity of a velocity boundary. I would like to mention that the uniform grid of 1m and the variable grid use the different discretization of the velocity models. An example of the snapshots are shown in Figure 4.21. The snapshots of the uniform grid (3m) computation shows clear numerical dispersion due to the low velocity area (see the snapshot of 200msec). However, one of the variable grid computation yields an accurate result compared with the uniform grid of 1m. Furthermore, the boundary numerical reflections from different grid sizes are small in the variable grid computation. In the snapshots of variable grid computation, we can see a slight scattering that cannot be seen in the uniform grid of 1m. This scattering may be due to the difference of the discretization of the velocity model shown in Figure 4.20.

Figure 4.22 shows the pressure collected at the receivers. We can see the clear numerical dispersion in the waveforms from the uniform grid of 3m. However, the waveforms from the uniform grid of 1m and the variable grid (3m in coarse grid and 1m in fine grid) yield sufficiently accurate results. This example shows the efficiency of the variable grid method. There is a slight difference between the uniform grid of 1m and the variable grid. This difference may be due to the difference of discretization of velocity model.

4.4 The Calculation of the Irregular Free Surface Combined with Variable Grid Method

I applied the variable grid method to the calculation of irregular topography mentioned in

93

the Section 3.3. The first model is the flat surface with a slope. The area of the fine grid is shown in Figure 4.23. Here, I will show the case of $45°$. Figure 4.24 shows the comparison of the uniform grid of 10m with the variable grid in which the coarse grid of 10m and the fine grid of 10/3m are used. Plotted waveforms are particle velocity parallel to the surface. We can see the waveforms in the variable grid have no numerical dispersion that can be seen in the waveforms of the uniform grid of 10m. Figure 4.25 shows the waveforms collected at 1000m source receiver offset with the various grid sizes. The result shows that a coarse grid size of 10 m combined with a fine grid size of 10/3m gives a more accurate solution than using a uniform grid of 5m.

The second model has the irregular surface. The area of the fine grid is shown in Figure 4.26. The calculated waveforms with the various grid sizes are shown in Figure 4.27. The result shows that the waveforms of a coarse grid size of 1 m combined with a fine grid size of 1/3m are as accurate as the solution using a uniform grid of 0.5m.

These two results suggest that approximately ten grid-points per wavelength, combined with the variable grid method, will give an accurate solution to a model with an irregular surface.

1-D Variable grid
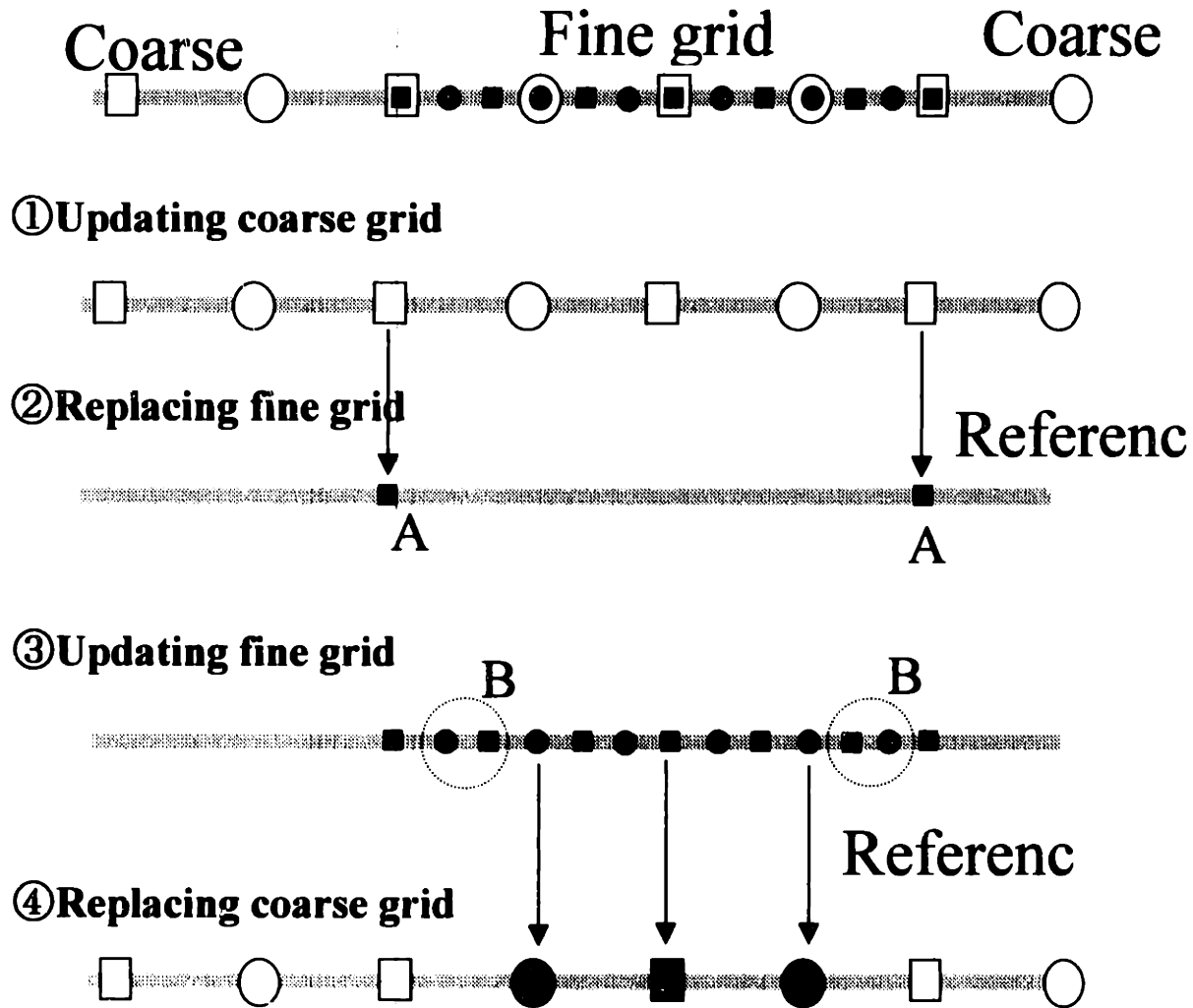
Figure 4.1: The one-dimensional staggered grid and a computation procedure.

① Updating the stresses on the coarse grid.

② At the boundary on the fine grid (A), the stresses on the fine grid are replaced by the stresses on the coarse grid calculated in the first step.

③ Updating the stresses on the fine grid without a boundary. At the next boundary (B), a fourth-order stencil can not be used. Therefore, a second-order approximation is used at there.

④ Coarse grid stresses within the fine grid region are replaced by the fine grid. Subsequently, the same procedure is applied to the velocity fields, and the second step can be omitted.
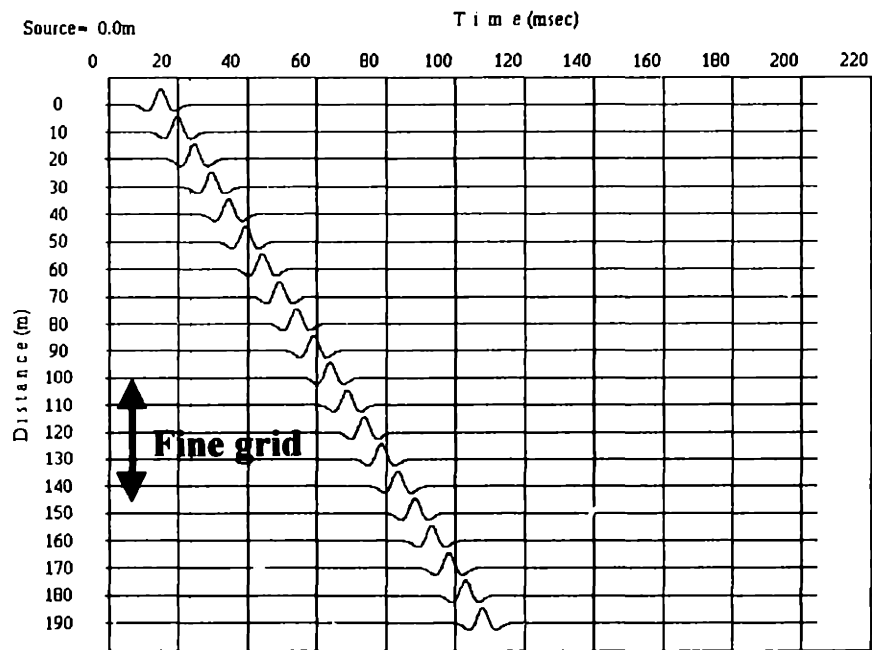
Figure 4.2: Time series of particle velocity from the 1-D simulation. A model is an acoustic homogeneous model. with velocity of 2000m/sec and a density of 2000kg/m³. The three times finer grids are placed between 100m and 145m.
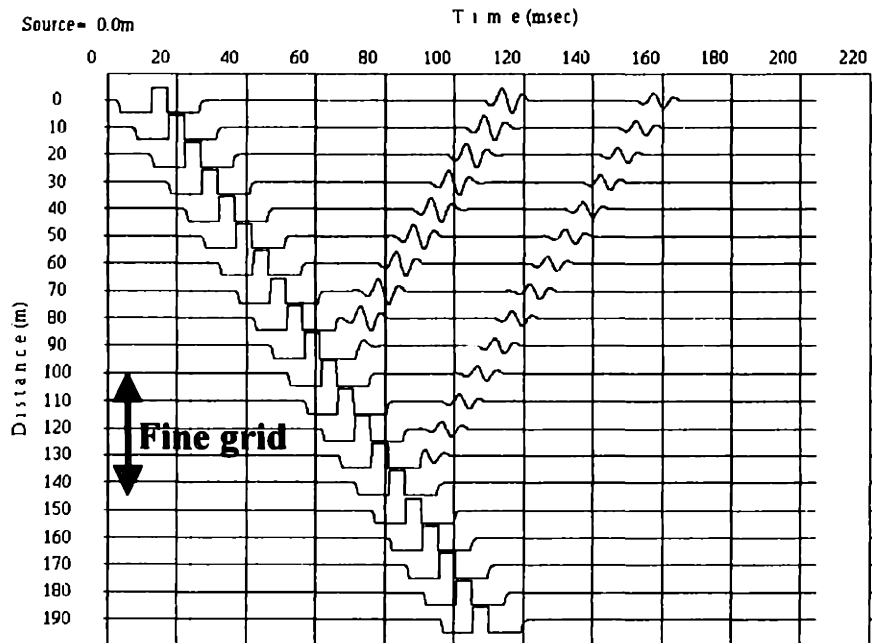
Figure 4.3: The same waveforms as Figure 4.2 with large gain.

96
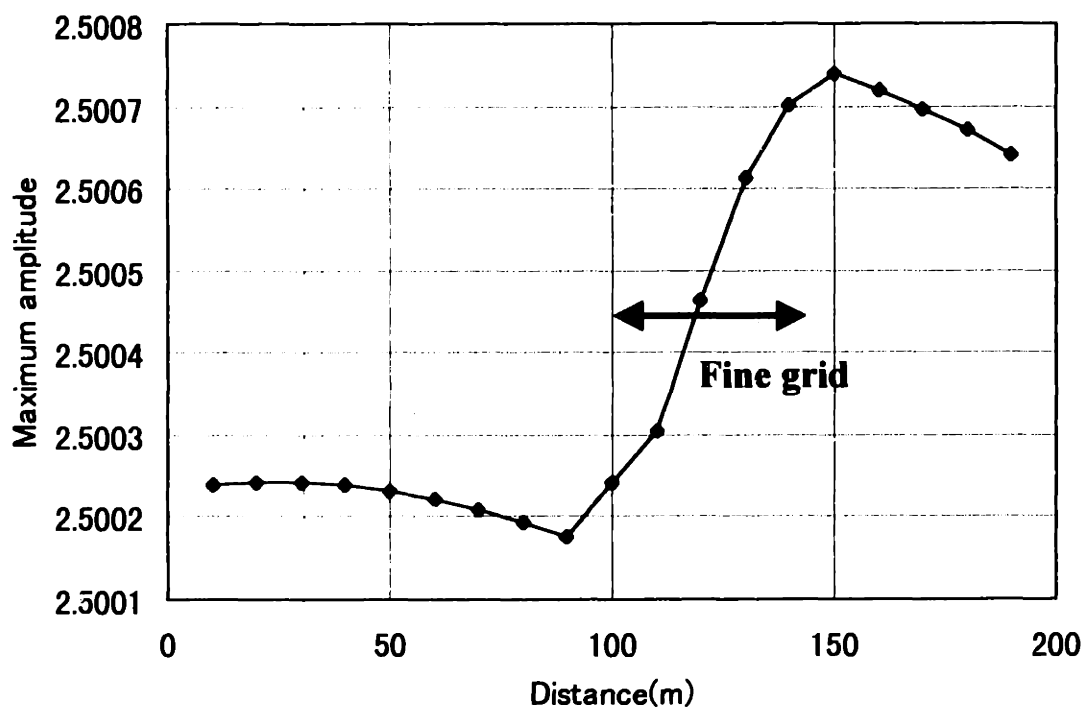
Figure 4.4: The maximum amplitude of waveforms shown in Figure 4.2 and 4.3. Theoretically, the amplitude should be constant. The effect of the change of grid sizes on the amplitude is less than 0.03%.
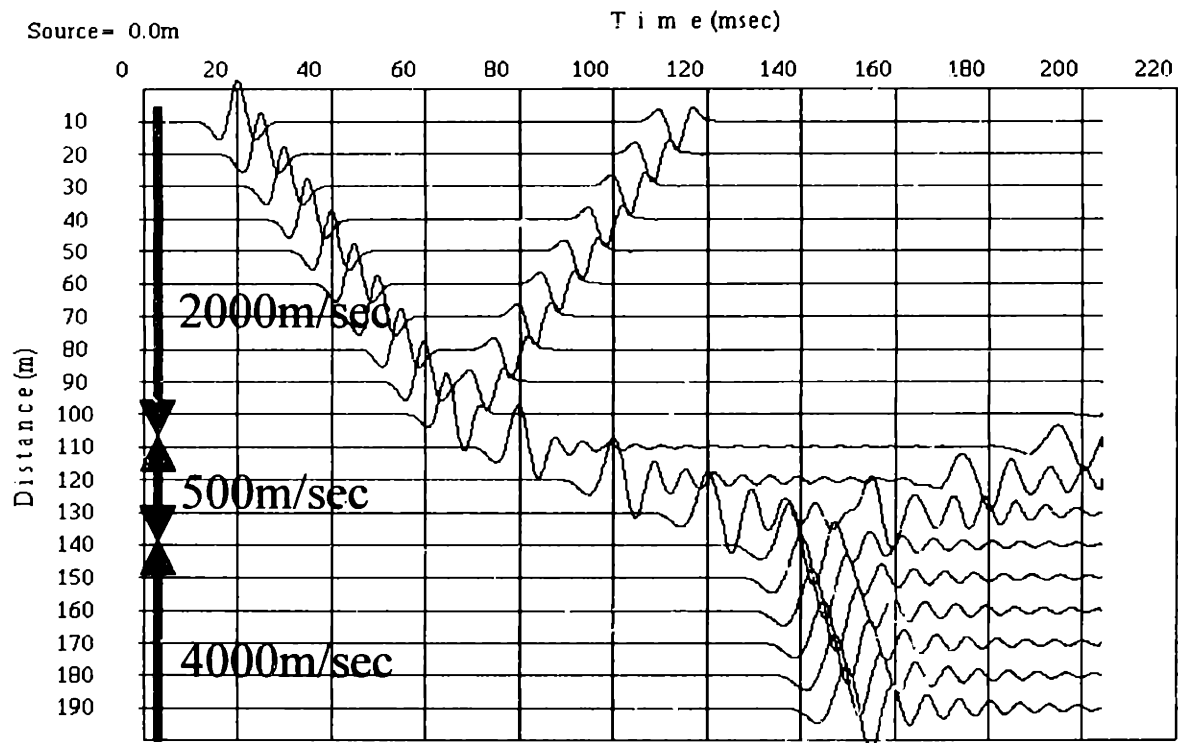
Figure 4.5: The particle velocity from the simulation with the uniform grid of 1m.
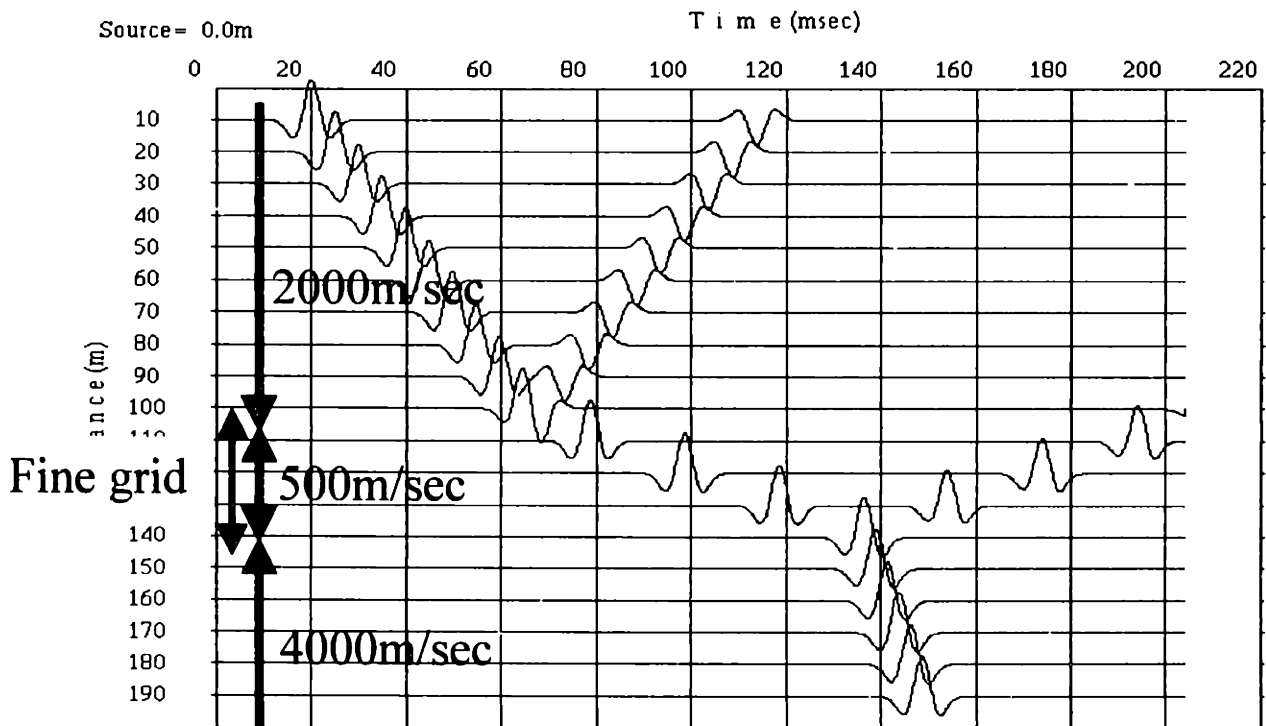
Figure 4.6: The particle velocity from the simulation with the variable grid in which the coarse grid of 1m and the fine grid of 1/3m. Three times finer grids are placed at the distance between 100m to 145m.

98
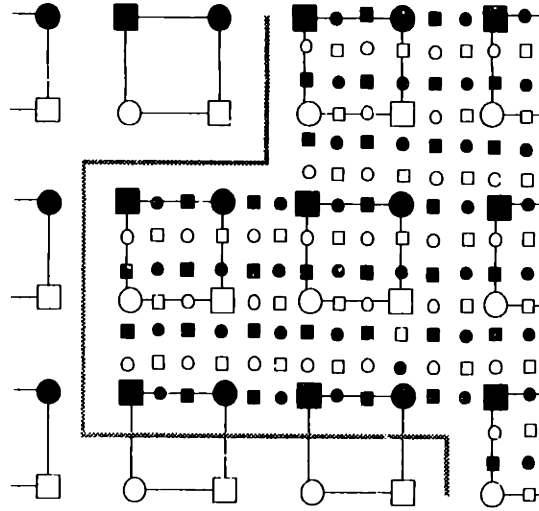
Figure 4.7: The two-dimensional staggered finite-difference grid in the vicinity of the boundary between different grid sizes.

Figure 4.8: The computation procedure for the variable grid method.

① Updating the stresses on the coarse grid.

② At the fine grid boundary, the stresses are interpolated by the stresses on the coarse grid calculated in the first step. Simple linear interpolation is used.

③ Updating the stresses on the fine grid without the boundary. Next to the boundary, a fourth-order stencil can not be used. Therefore, a second-order approximation is used.

④ Coarse grid stresses within the fine grid region are replaced by the fine grid. Subsequently, the same procedure is applied to the velocity fields. For the viscoelastic case, memory variables can be updated with the stress field simultaneously. Only the velocity field is updated separately.
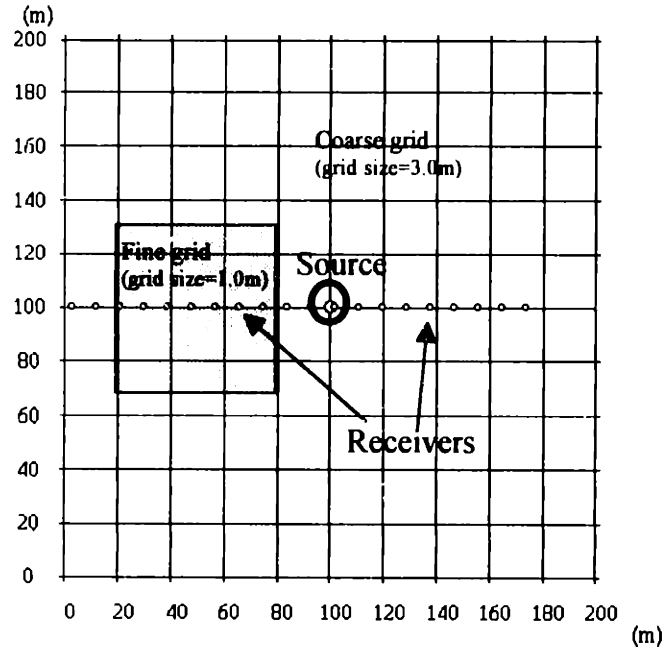
a) A source and receivers locations, and the fine grid region. A model is a homogeneous elastic solid with P- and S-velocities of 3000 and 1500m/sec, respectively, and a density of 1800kg/m³.
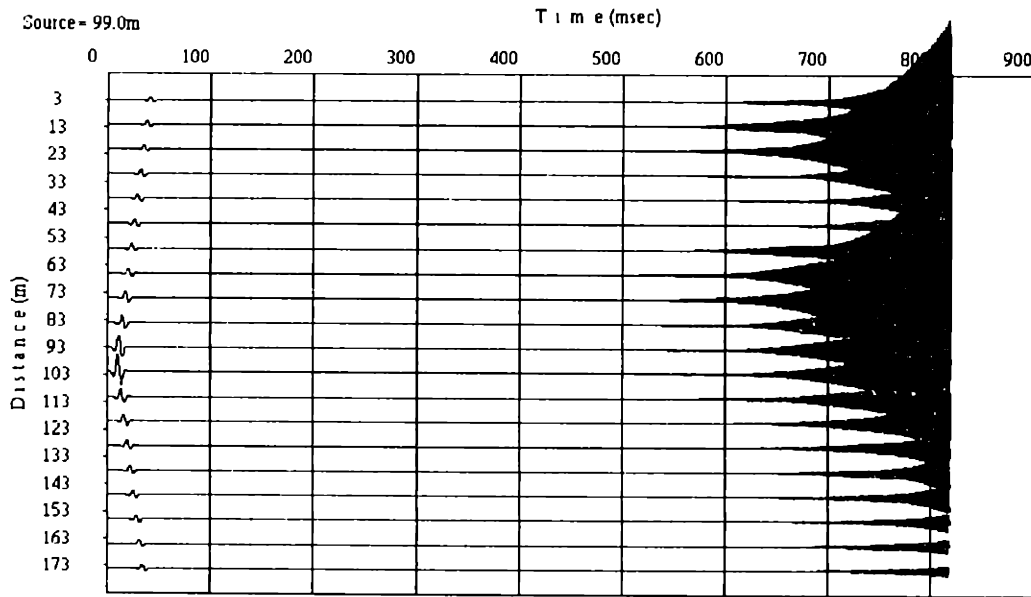
b) Pressure collected at the receivers.

Figure 4.9: Instability due to the variable grid implementation. a) A model used in the simulation. b) Pressure collected at the receivers. A source is a P-wave source with 100Hz Ricker wavelet. Δt (time step) is 0.05msec. 16384 time steps are performed.

A:No weighting or averaging   B:5 point averaging   C:9 point averaging

D:5 point weighting   E:9 point weighting
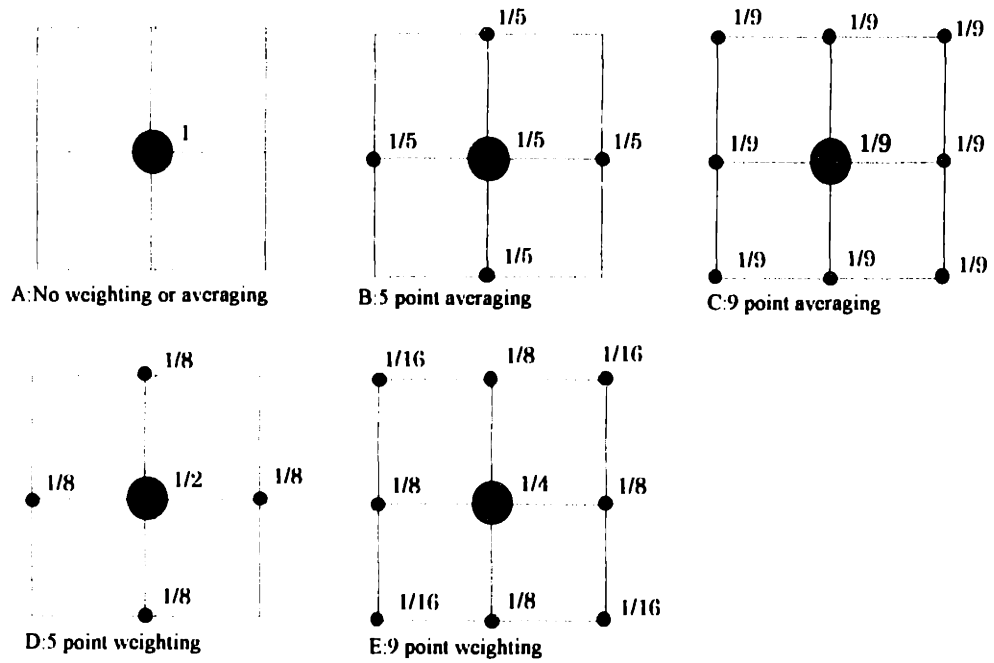
Figure 4.10: The method of averaging and weighting applied to the replacement of the coarse grid components within the fine grid (Figure 4.8. Step④).
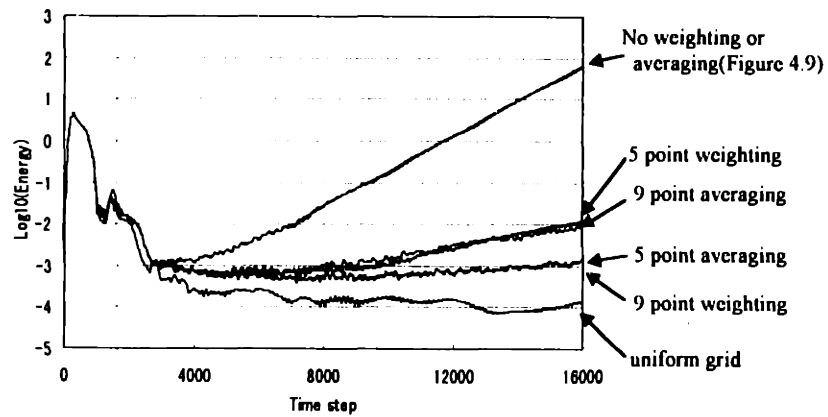
Figure 4.11: The energy of waveforms shown in Figure 4.9 with various weighting methods.

101
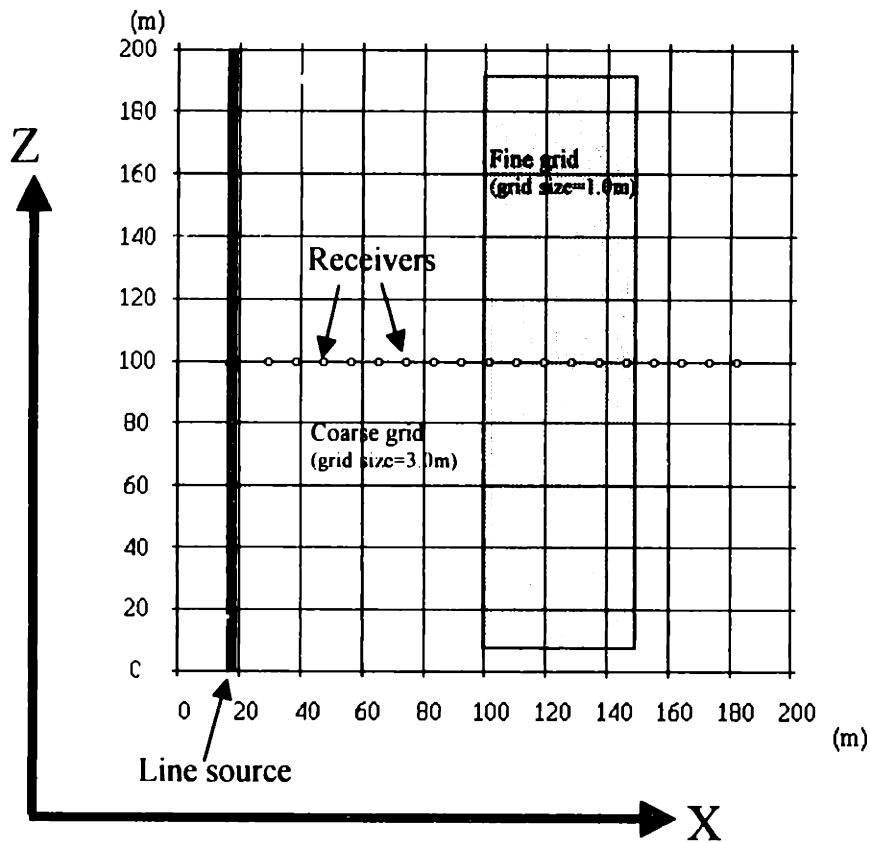
Figure 4.12: A source and receivers locations, and the fine grid region. A model is a homogeneous elastic solid with P- and S-velocities of 3000 and 1730m/sec, respectively, and a density of 1800kg/m³. The area of fine grid is located between distance of 100 and 150m. The grid size is 3m in the coarse grid region, and 1m in the fine grid region.
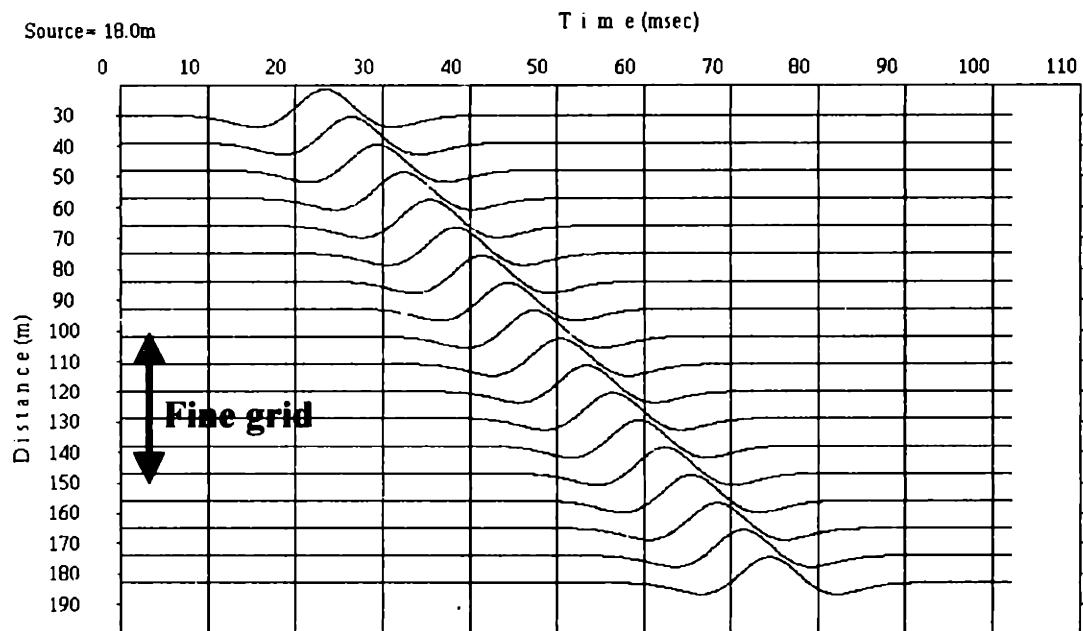
Figure 4.13: Pressure from the simulation. A 50 Hz Ricker wavelet is used as a source wavelet.
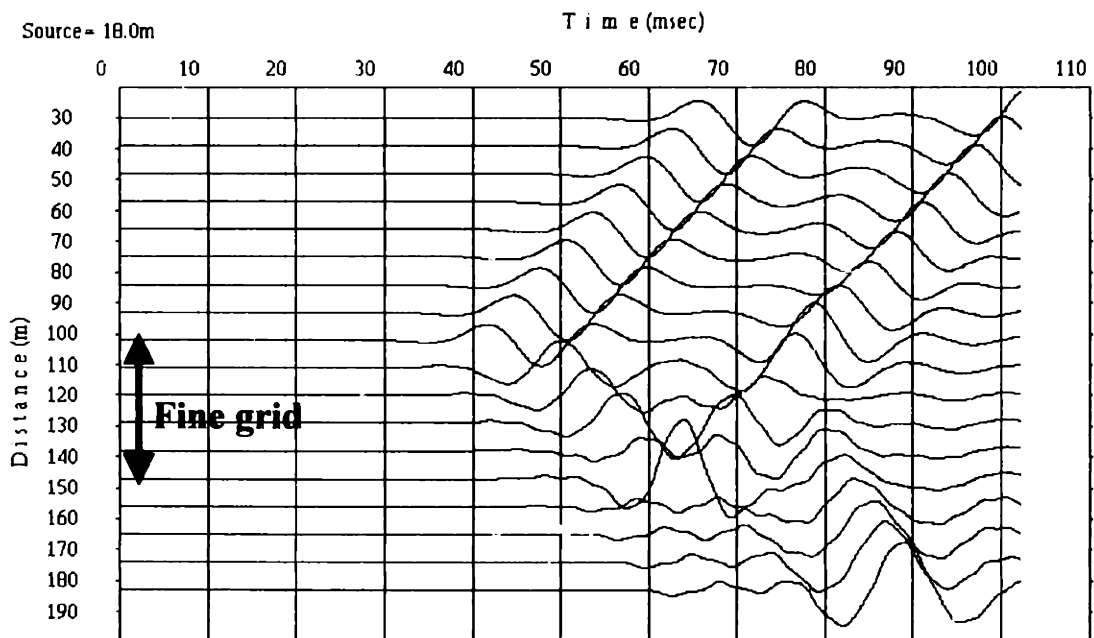
Figure 4.14: Difference between the variable grid and the uniform grid of 3m.
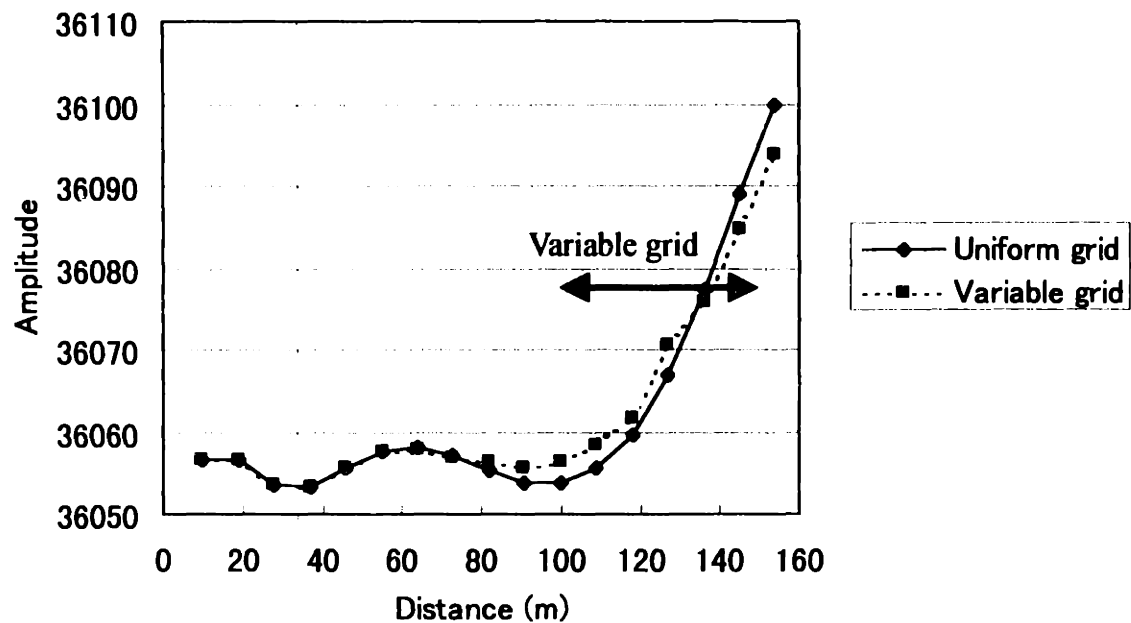
Figure 4.15: The maximum amplitude of waveforms shown in Figure 4.13 in comparison to the uniform grid of 3m. Theoretically, the amplitude should be constant. The effect of the change of grid sizes on the amplitude is less than 0.02%.
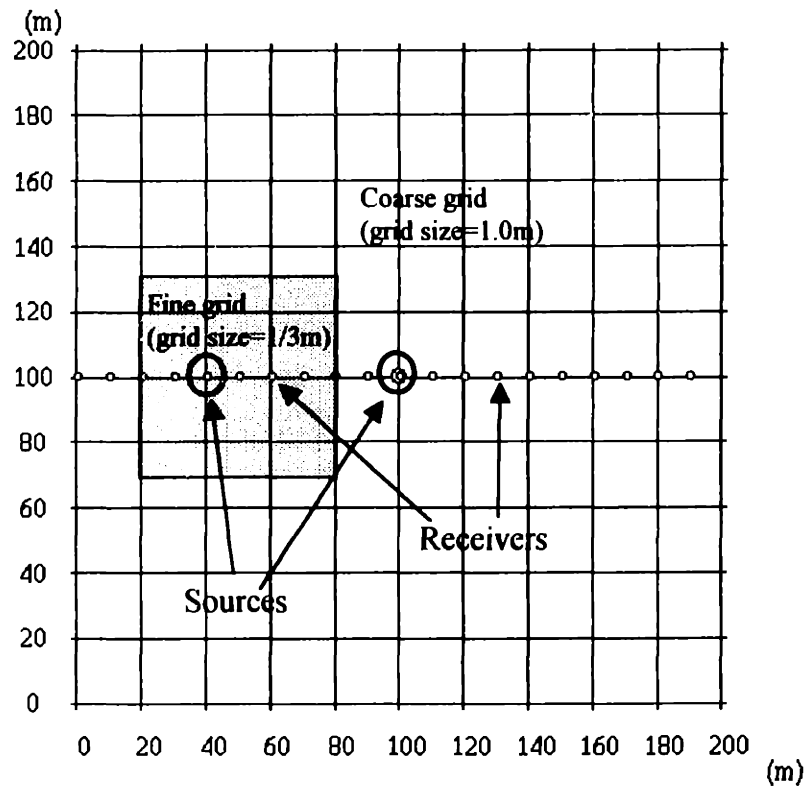
Figure 4.16: Sources and receivers locations, and the fine grid region. A model is a homogeneous elastic solid with P- and S-velocities of 3000 and 1500m/sec, respectively, and a density of 1800kg/m³. The source is a point explosion with a 200Hz Ricker wavelet. The grid size was 1m in the coarse grid region and 1/3m in the fine grid region.
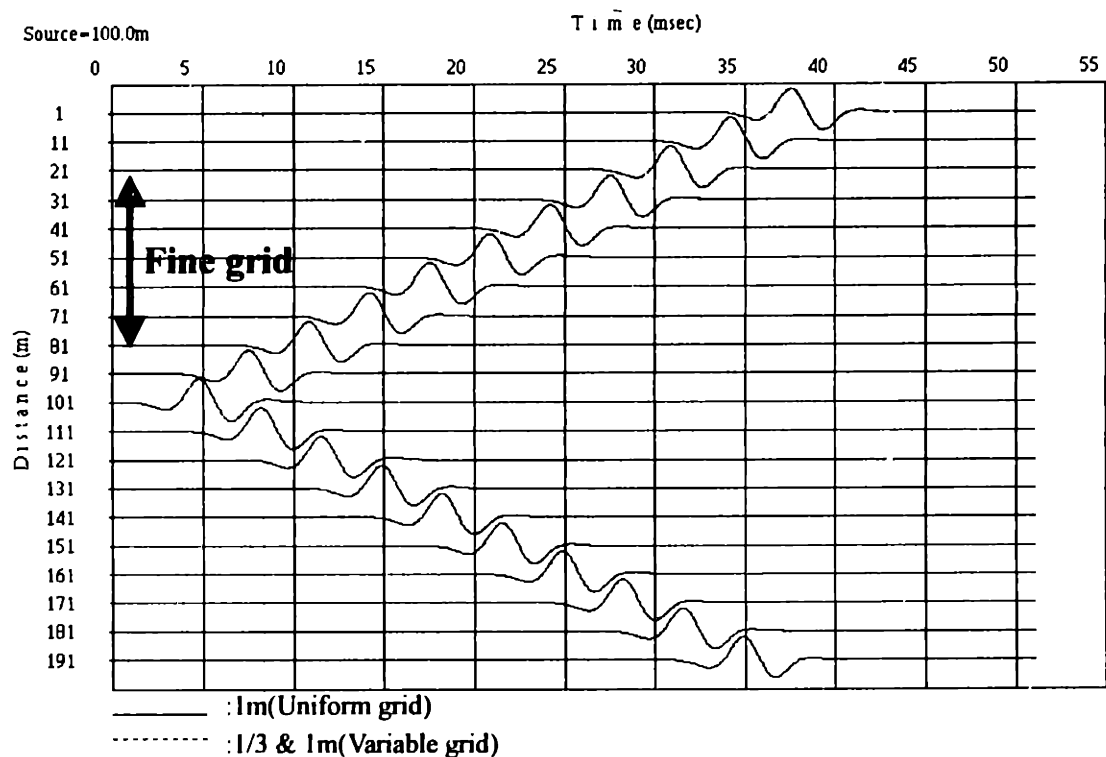
a) small gain.
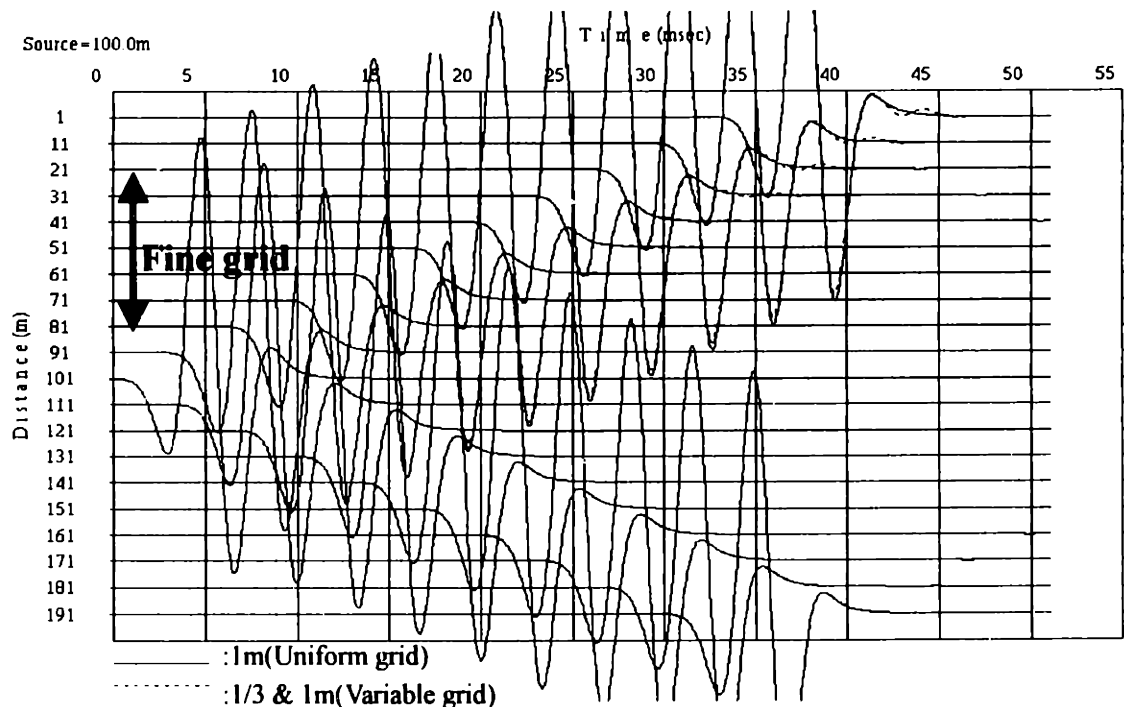
b) large gain.

Figure 4.17: Simulation with the source of 100m. Pressure collected at the receivers is plotted. a) small gain. b) large gain. Solid line: uniform grid of 1m. Dashed line: variable grid of 1/3 and 1m.
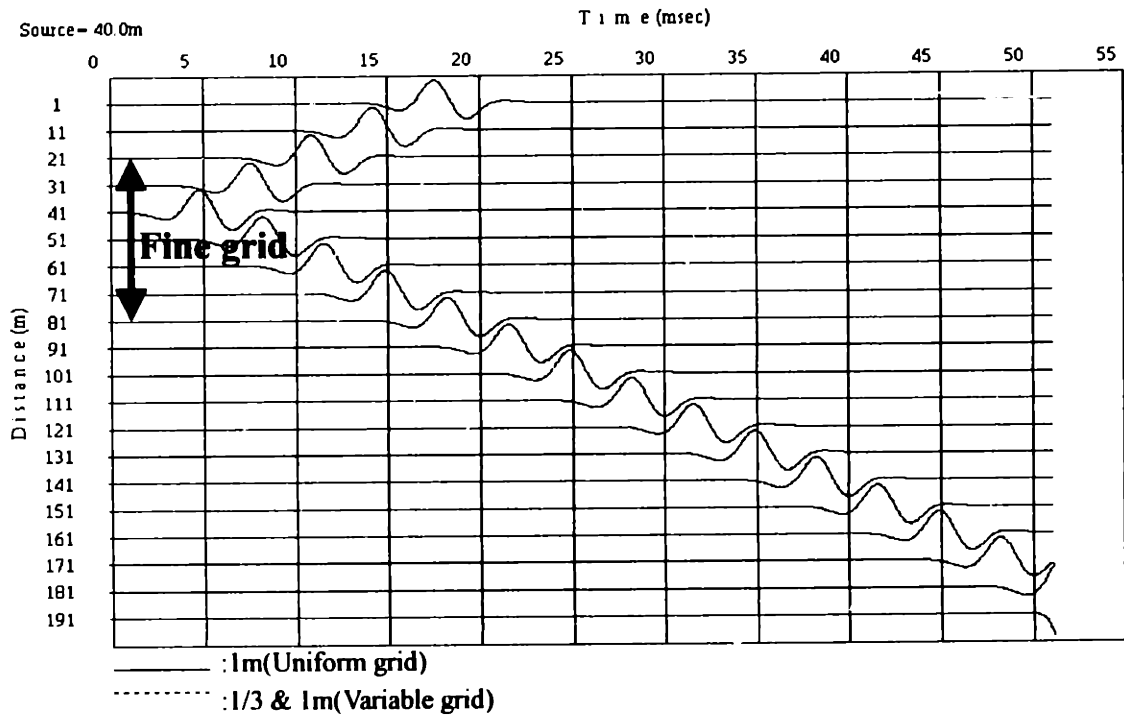
a) small gain.
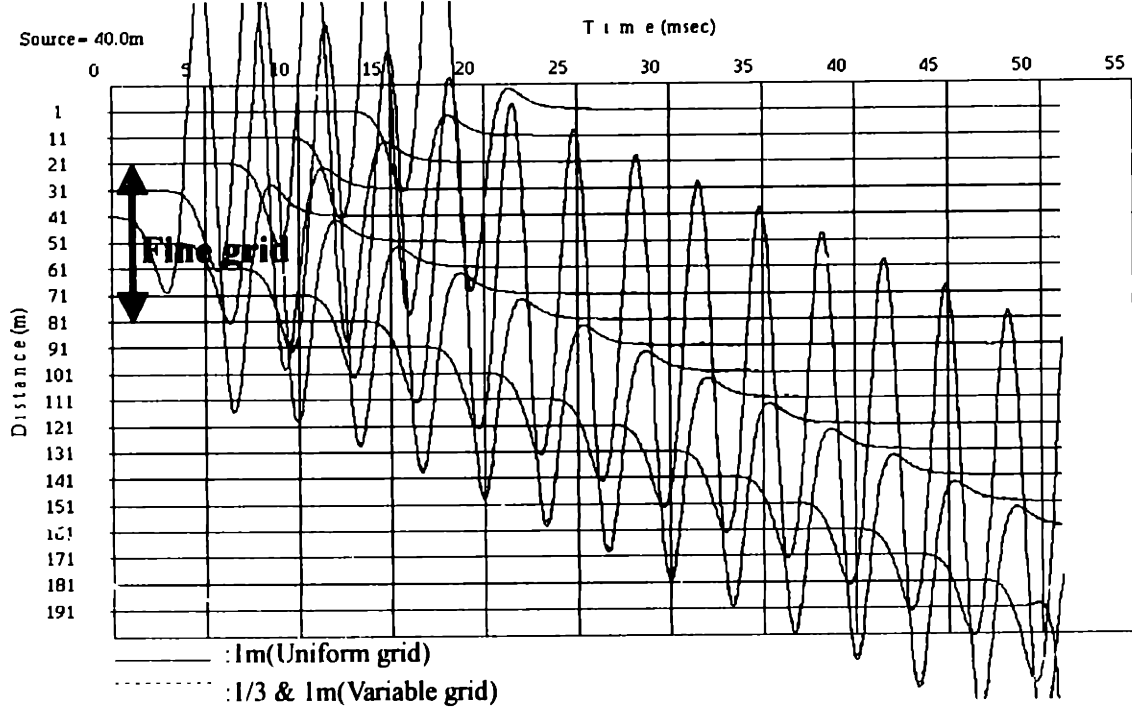
b) large gain.

Figure 4.18: Simulation with the source of 40m. Pressure collected at the receivers is plotted. a) small gain. b) large gain. Solid line: uniform grid of 1m. Dashed line: variable grid of 1/3 and 1m.
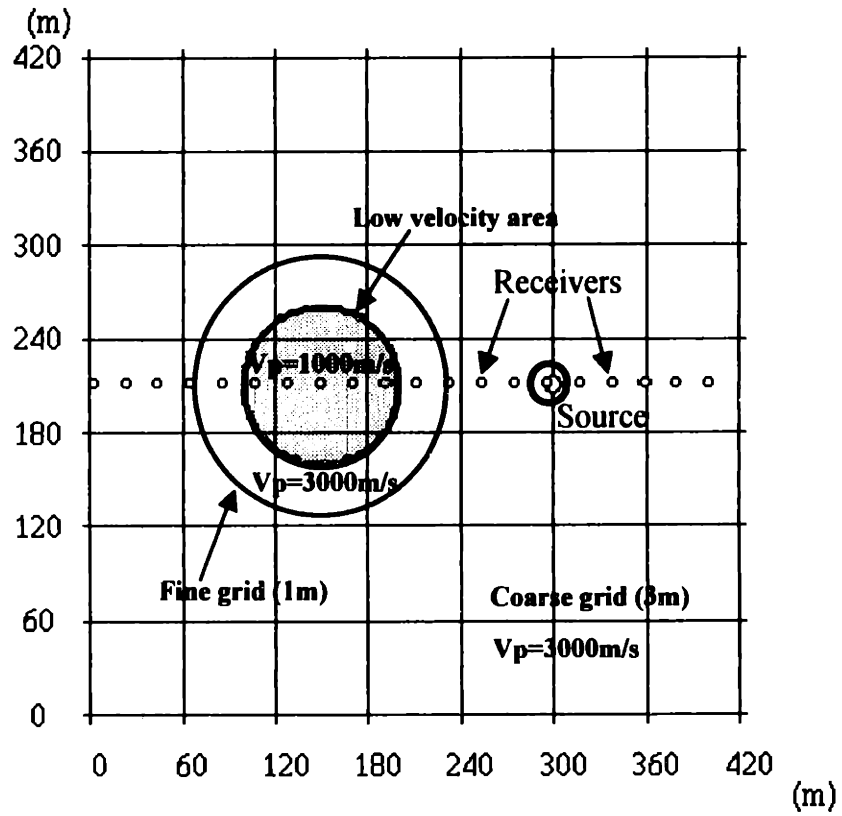
Figure 4.19: Velocity model and the location of a source and receivers. The low velocity area (a inner circle) is covered by the fine grid (a outer circle). The source is a P-wave source with a 50Hz Ricker wavelet. Velocities, densities and corresponding wave lengths are listed in Table 4.3.

a) Uniform grid of 3m

b) Variable grid
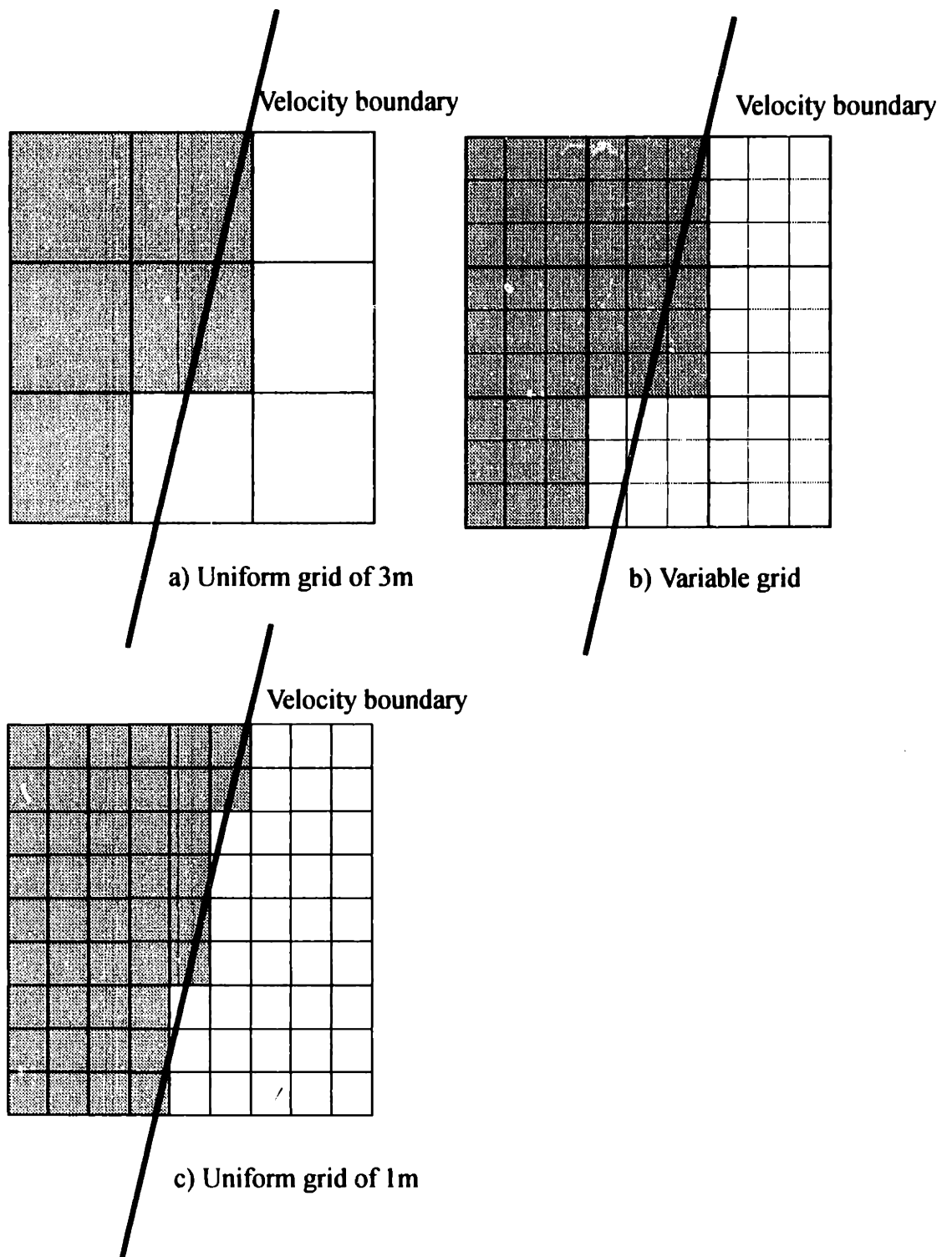
c) Uniform grid of 1m

Figure 4.20: The different discretization of velocity model.

Uniform grid of 3m.
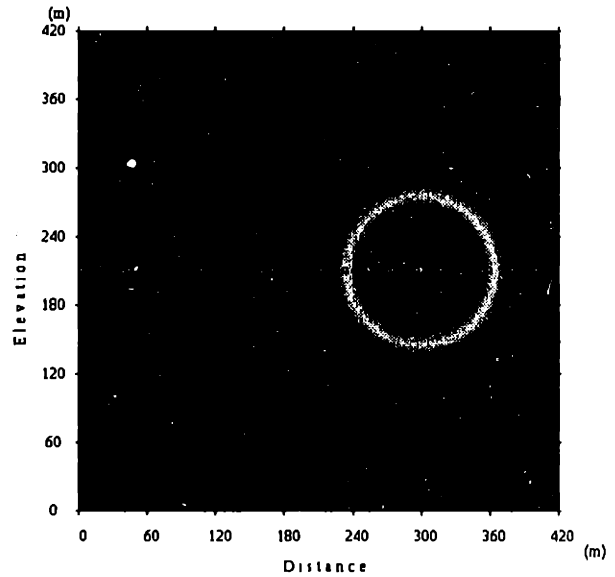
Variable grid.

Grid size is 3m in the coarse grid region and 1m in the fine grid region.
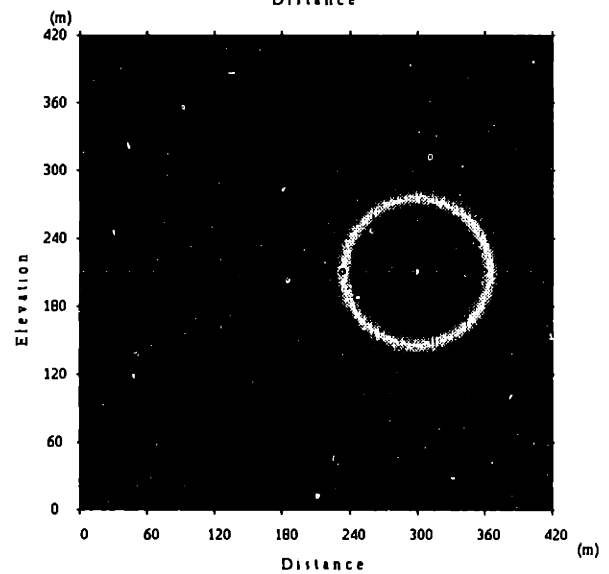
Uniform grid of 1m.
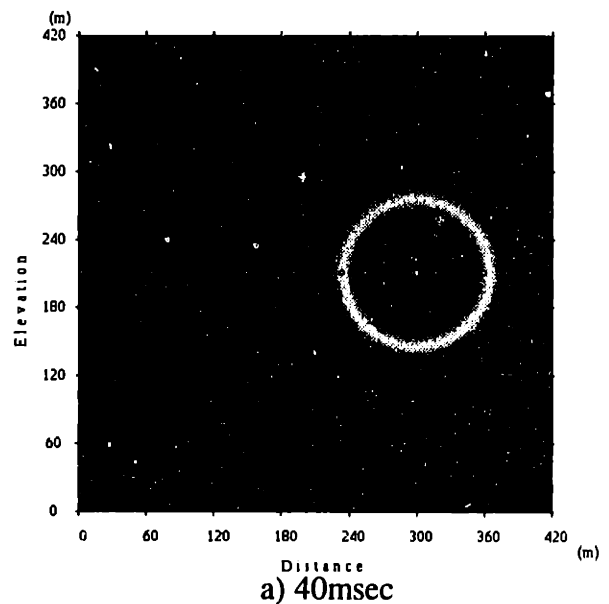
Figure 4.21: Wavefield snapshots (pressure) across a variable grid area and a low velocity area. The model is shown in Figure 4.19.

a) 40msec

110
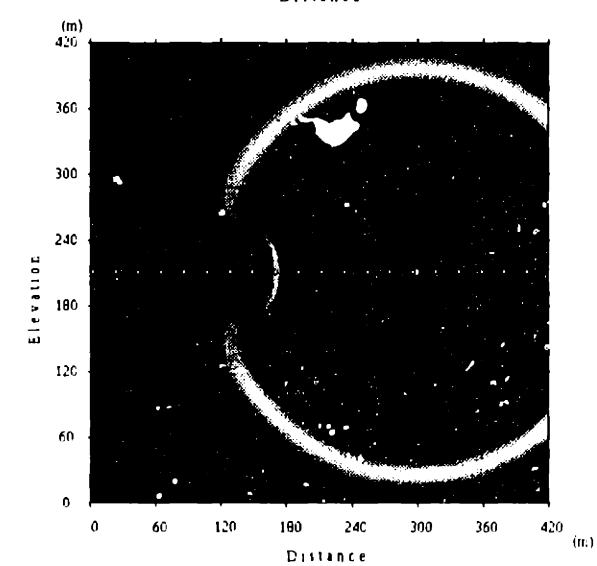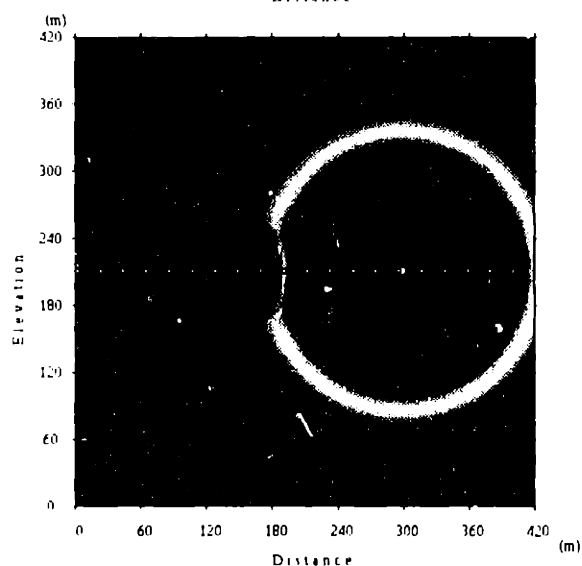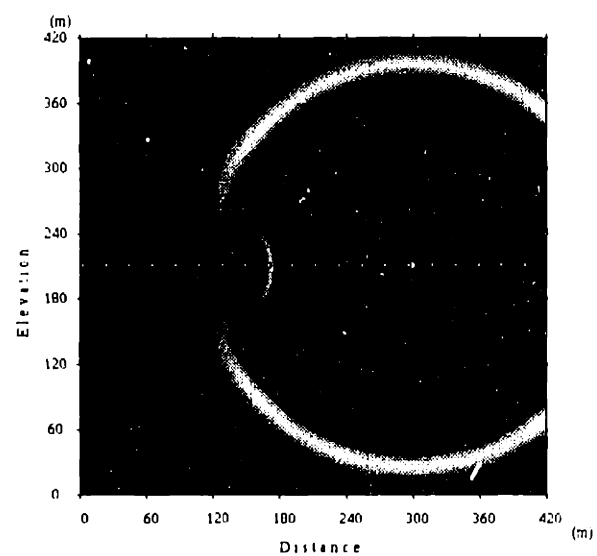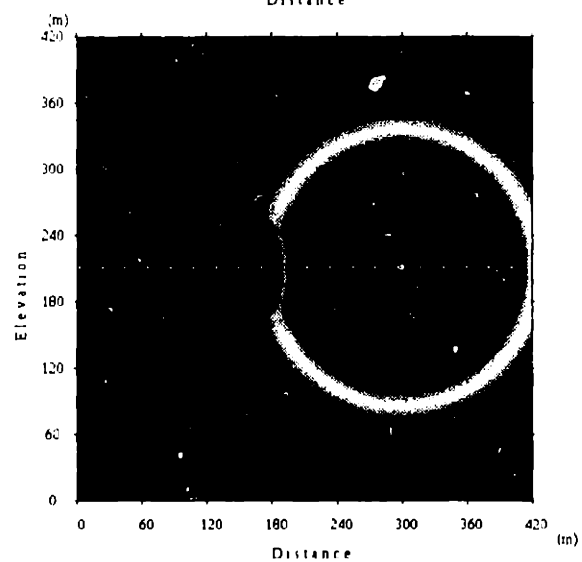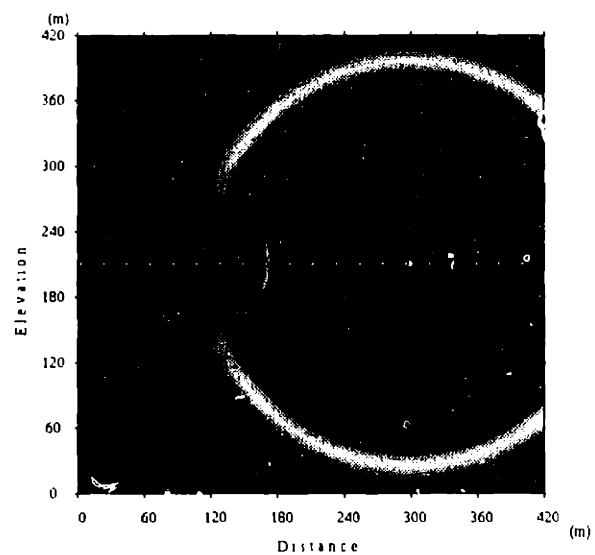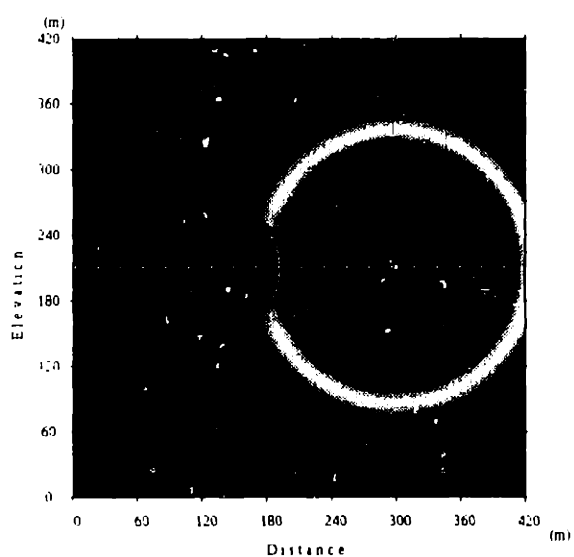
b) 60msec

c) 80msec

Figure 4.21, continued.

111
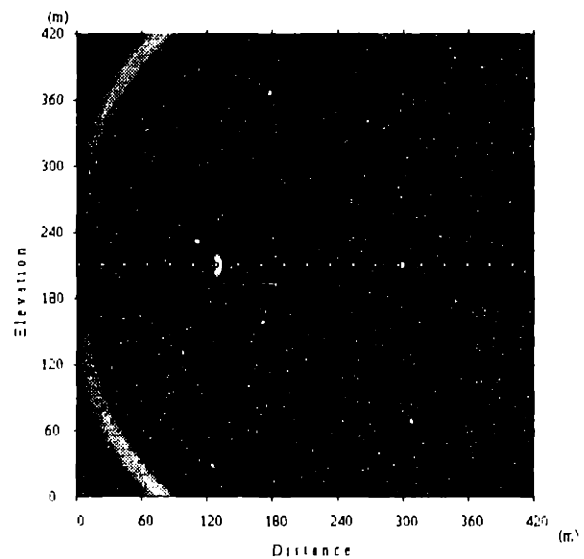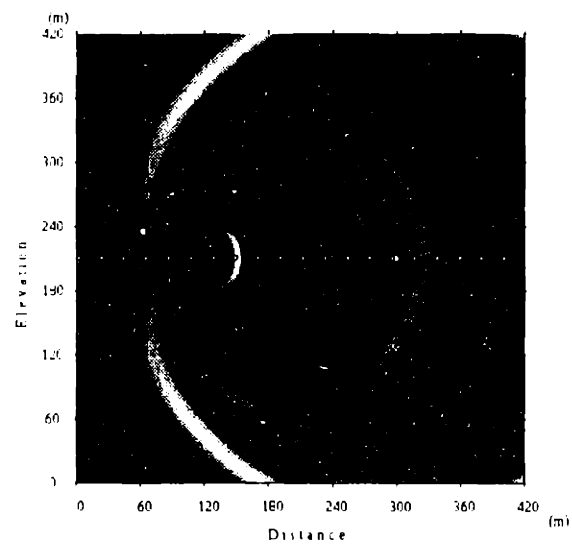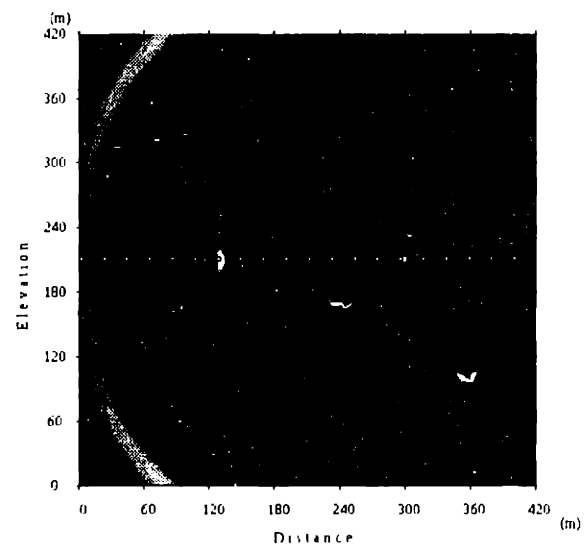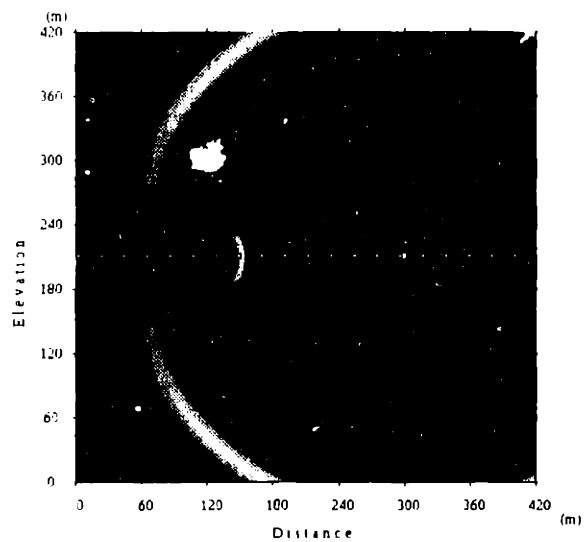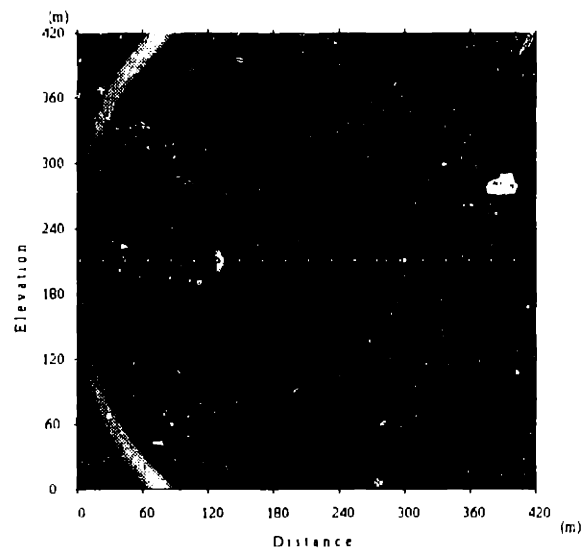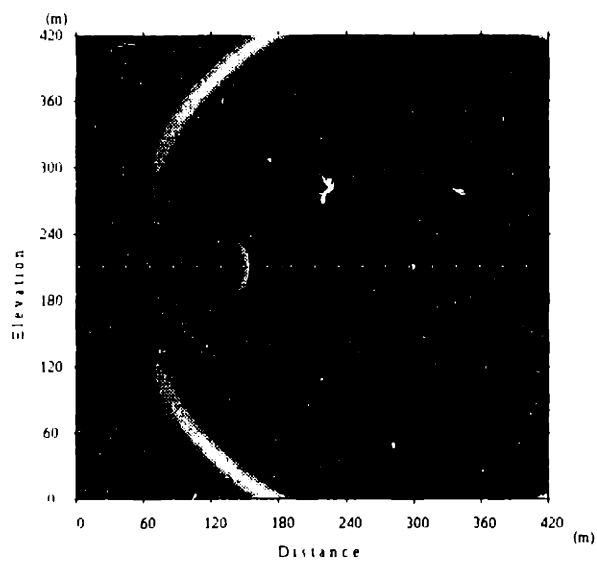
d) 100msec   e) 120msec

Figure 4.21, continued.

112
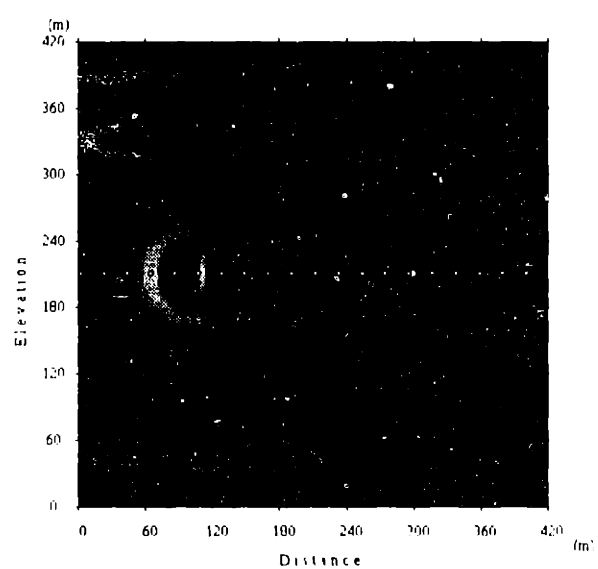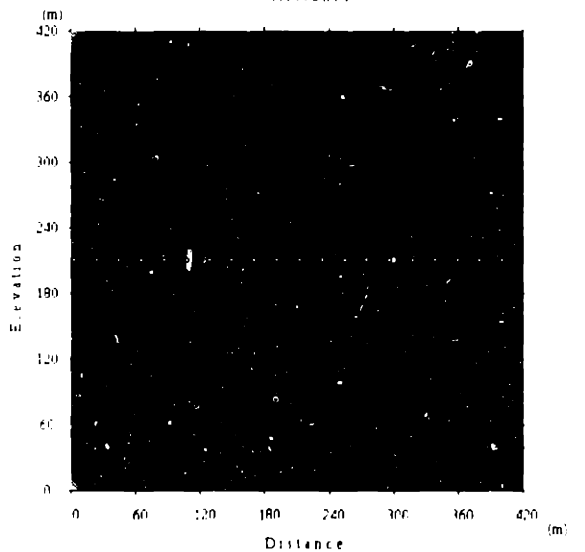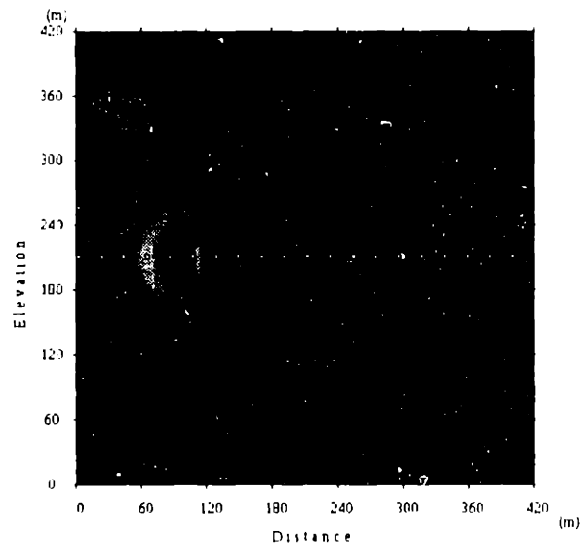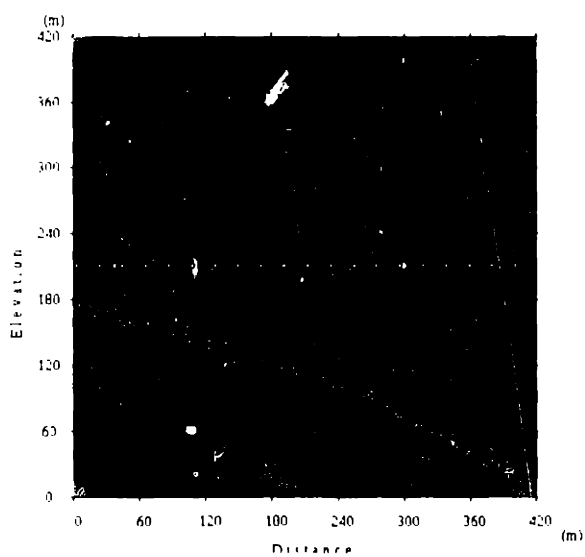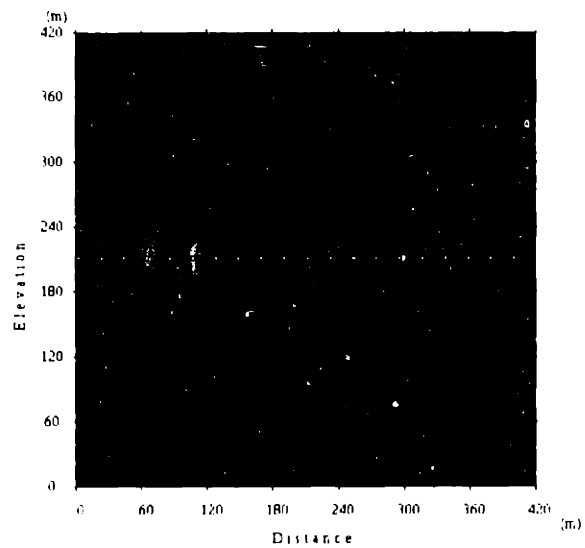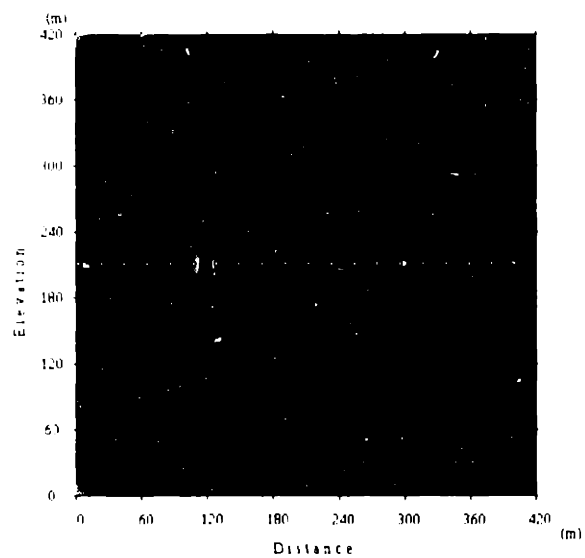
f) 140msec

g) 160msec

Figure 4.21, continued.

113
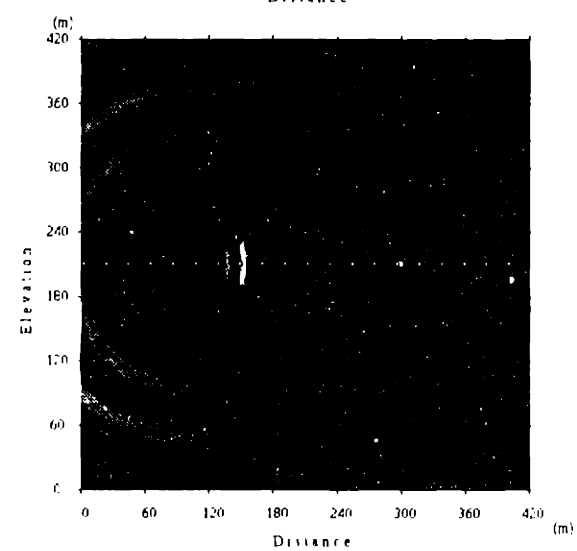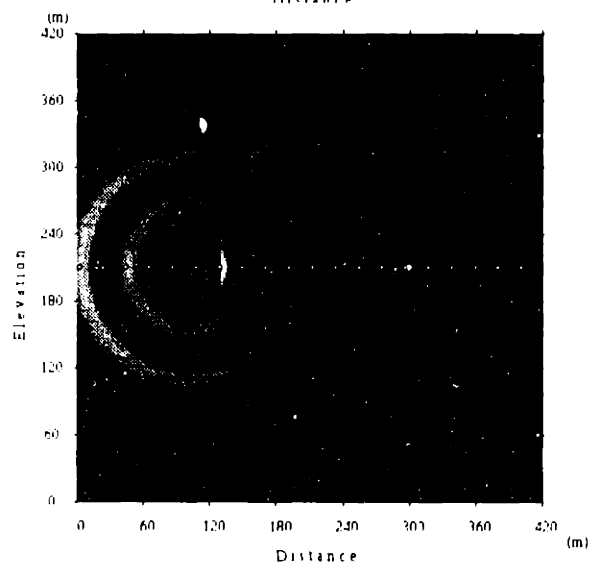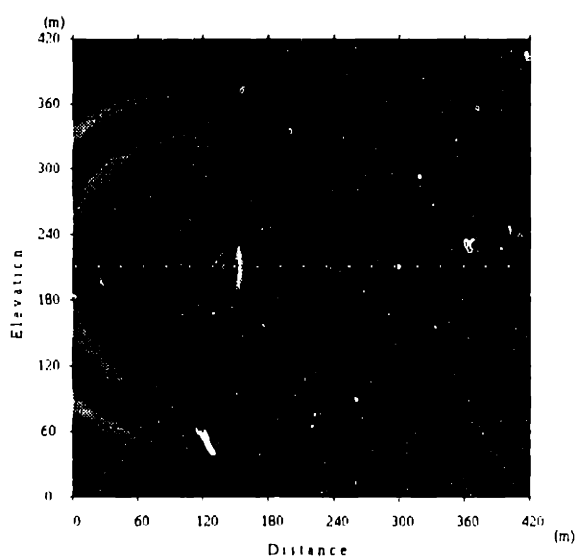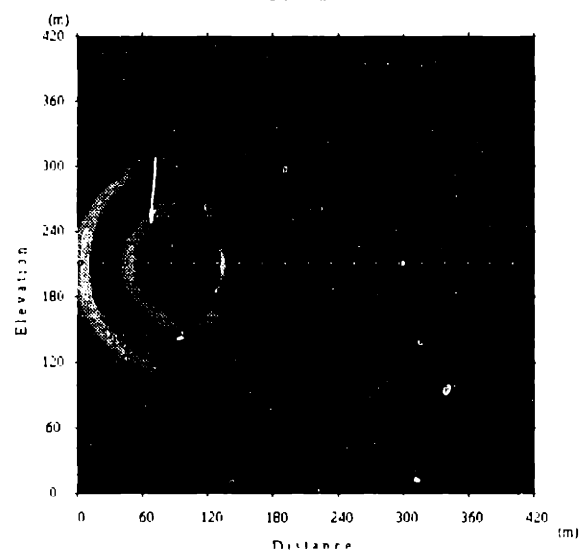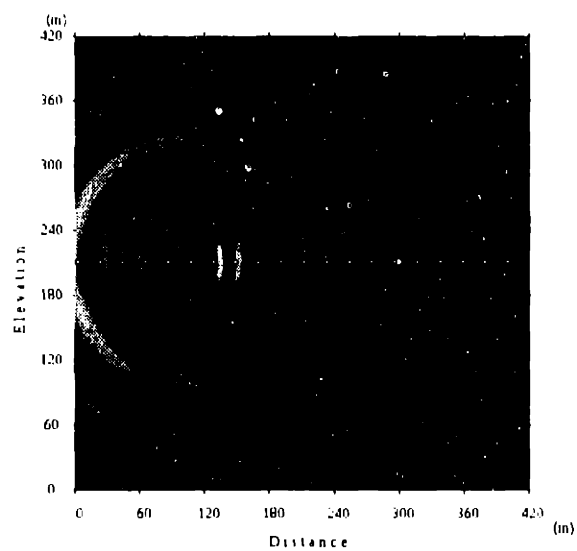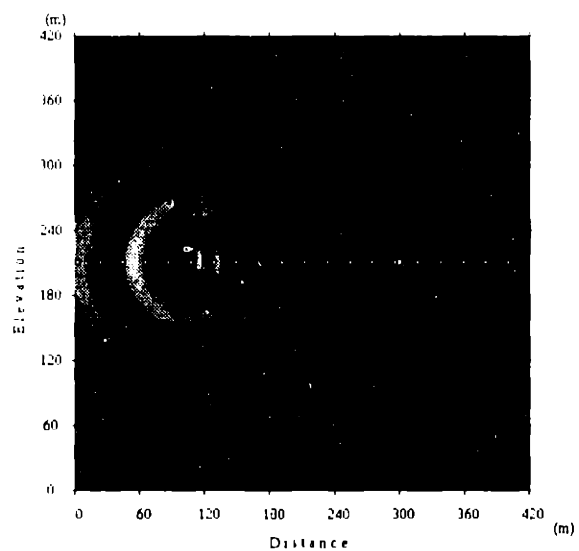
h) 180msec

i) 200msec

Figure 4.21, continued.

114

Source=300.0m   T i m e (msec)

——— :1 & 3m(Variable grid)
--------- :3m(Uniform grid)

a) Solid line: variable grid of 1m and 3m. Dashed line: uniform grid of 3m.

Source=300.0m   T i m e (msec)
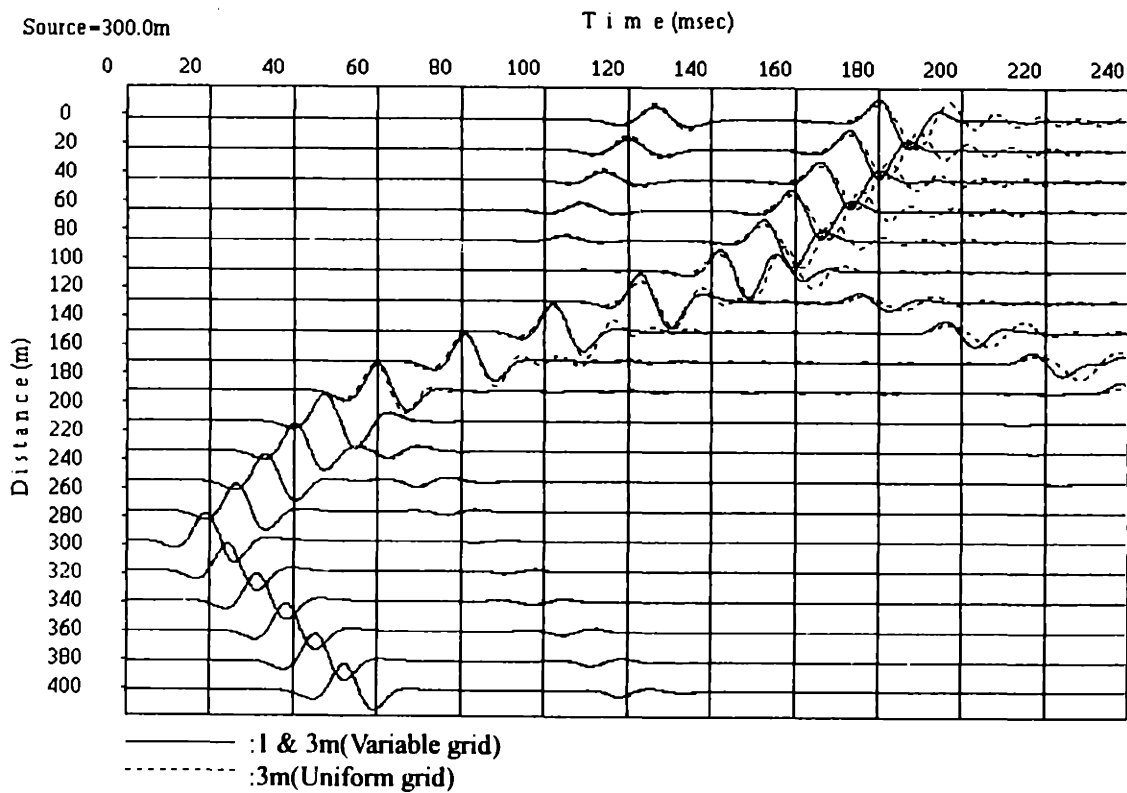
——— :1 & 3m(Variable grid)
--------- :1m(Uniform grid)
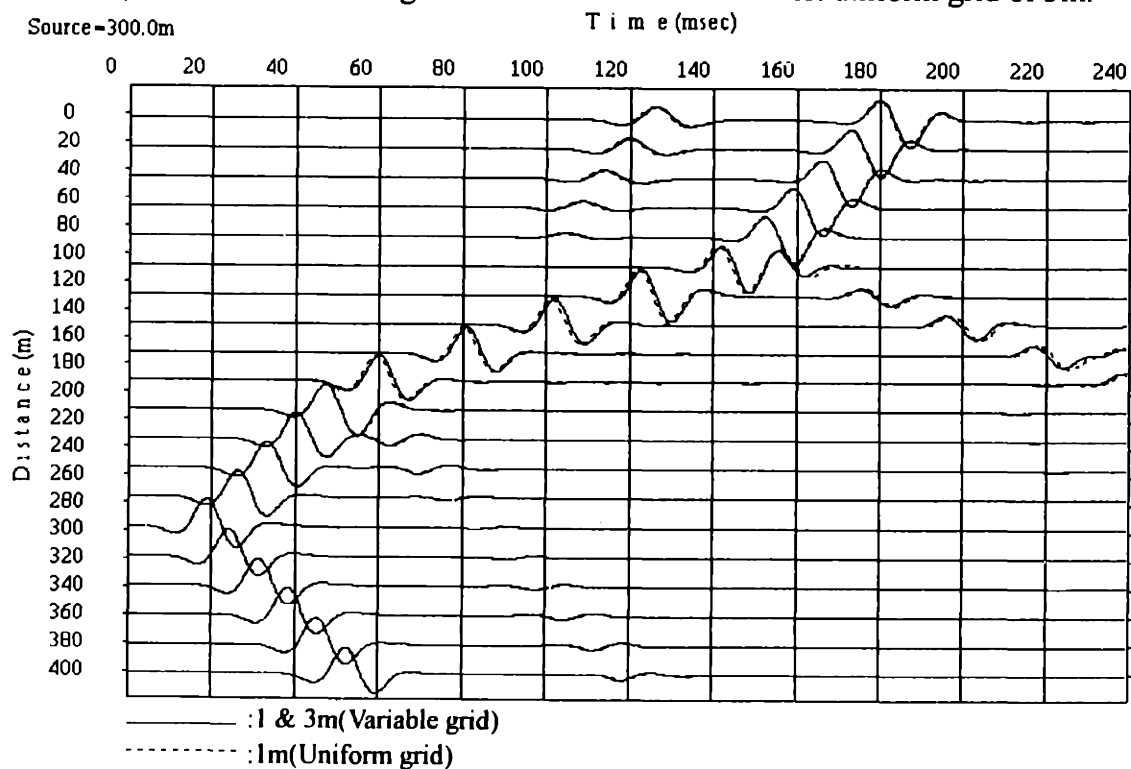
b) Solid line: variable grid of 1m and 3m. Dashed line: uniform grid of 1m.

Figure 4.22: Pressure collected at the receivers. a) The variable grid of 1m and 3m and the uniform grid of 3m. b) The variable grid of 1m and 3m, and the uniform grid of 1m.

115
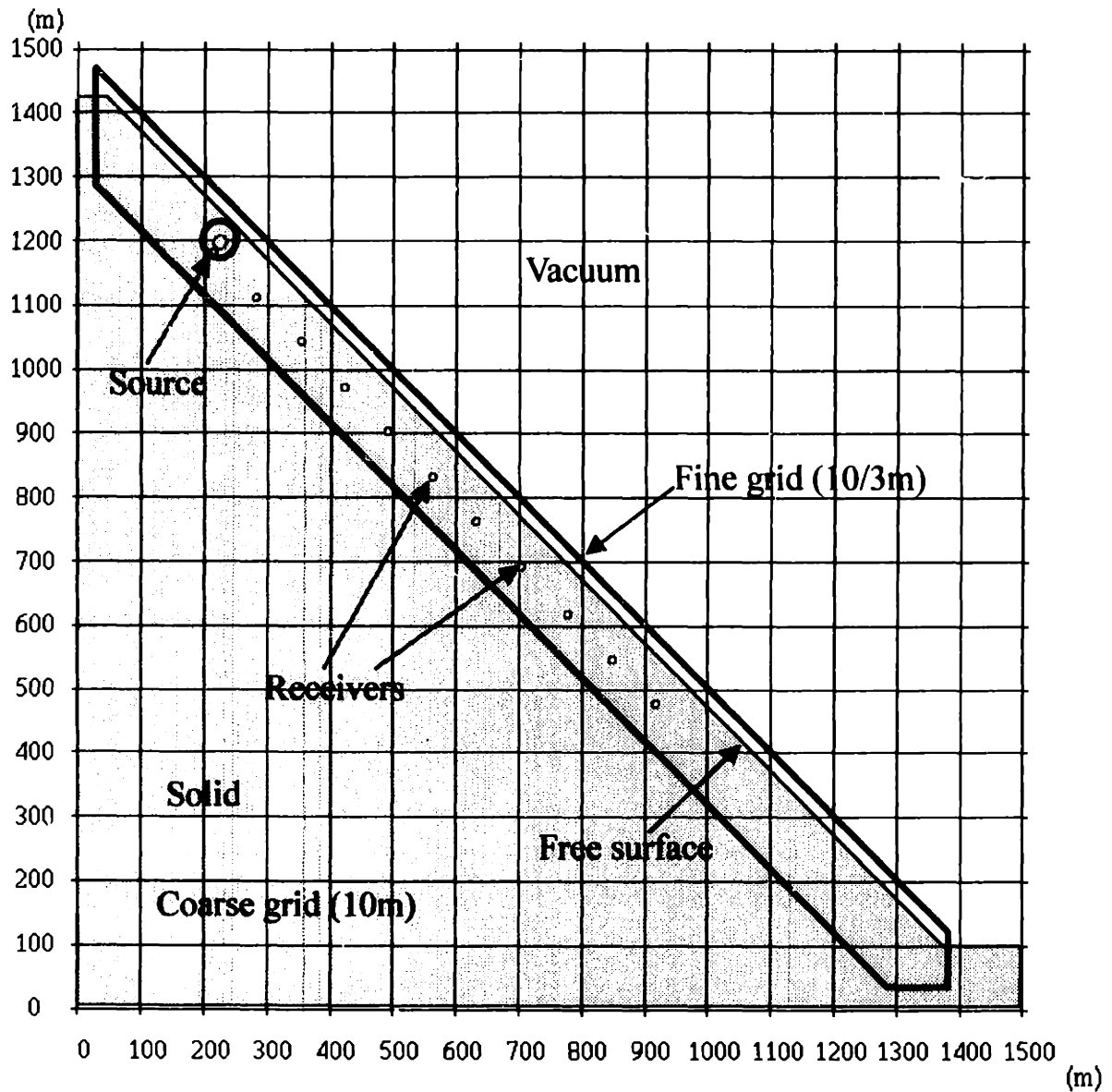
Figure 4.23: Fine grid area, and a source and receivers locations. The model is a Poisson solid with P- and S-velocities of 3000 and 1730m/s, respectively, and a density of 2500kg/m³. A P-wave source (15Hz Ricker wavelet) located 30 m below the surface is employed. Receivers are located 50 m below the surface.
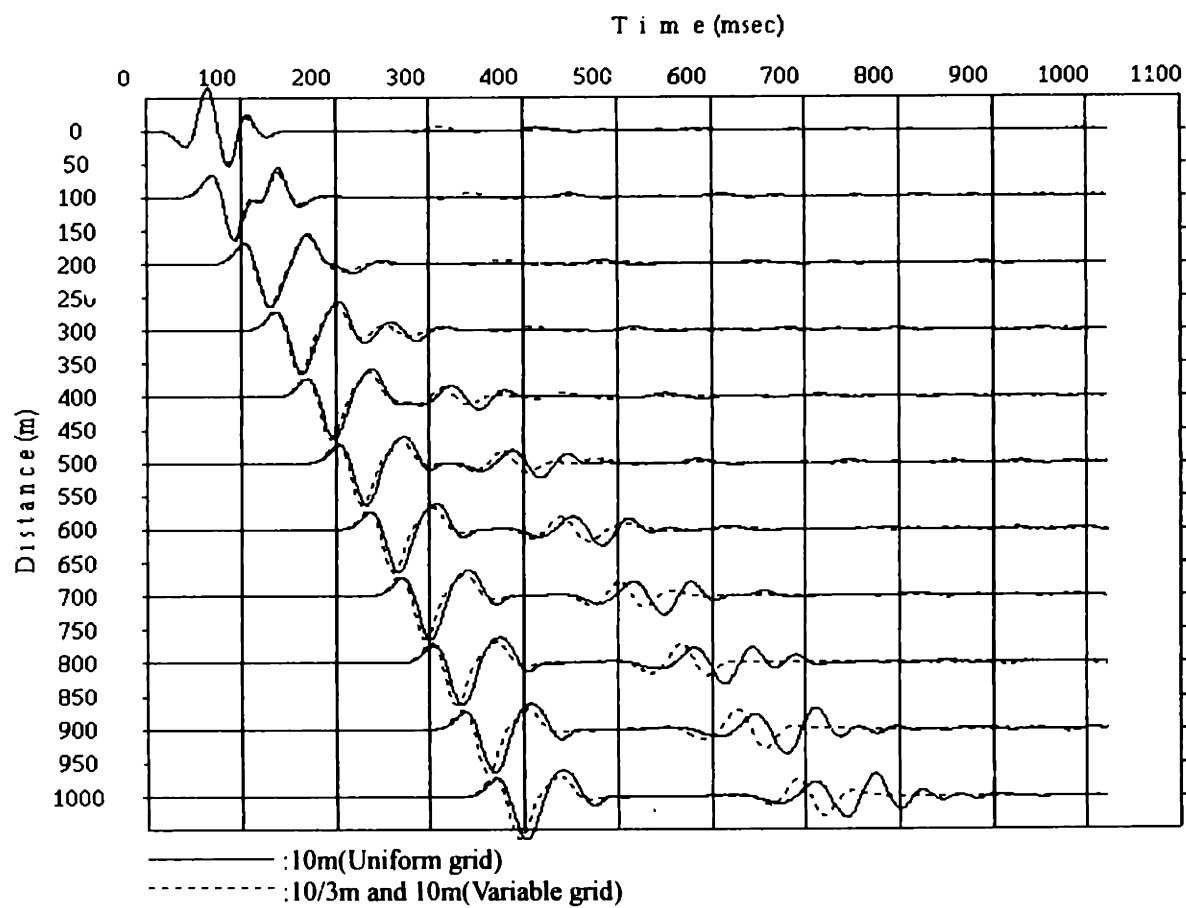
Figure 4.24: Comparison of the uniform grid of 10m with the variable grid in which the coarse grid of 10m and the fine grid of 10/3m are used. Plotted waveforms are particle velocity parallel to the surface.
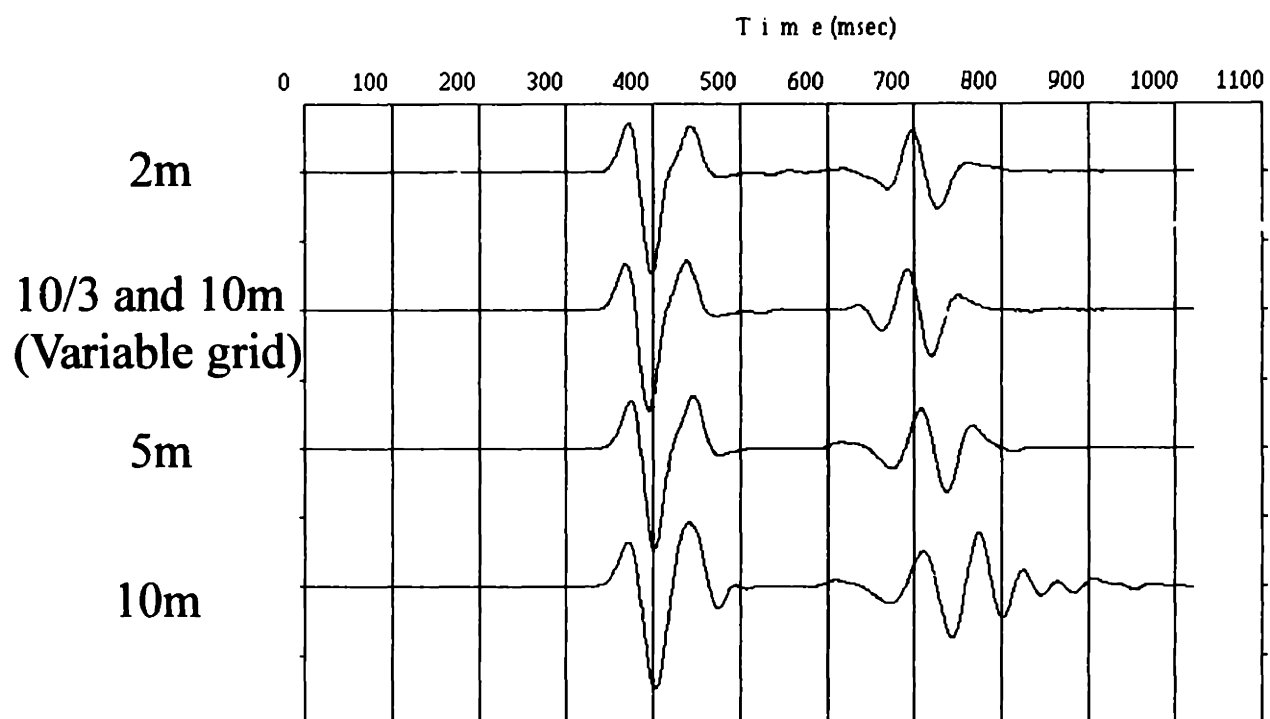
Figure 4.25: Waveforms collected at 1000m source receiver offset with the various grid sizes.

118
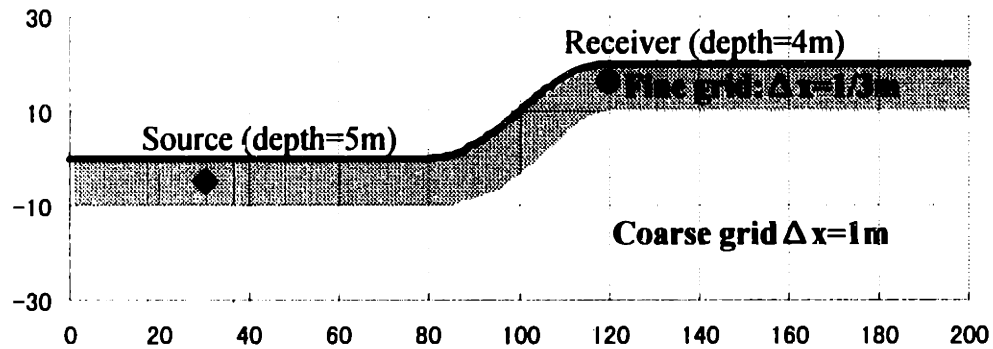
Figure 4.26: The area of the fine grid. The grid size is 1/3m in the fine grid, and 1m in the coarse grid. The model is a elastic Poisson solid with P- and S-velocities of 2000 and 1155m/s, respectively, and a density of 1000kg/m³. A P-wave source (110Hz Ricker wavelet) located at a distance of 30m and 5m below the surface is employed.
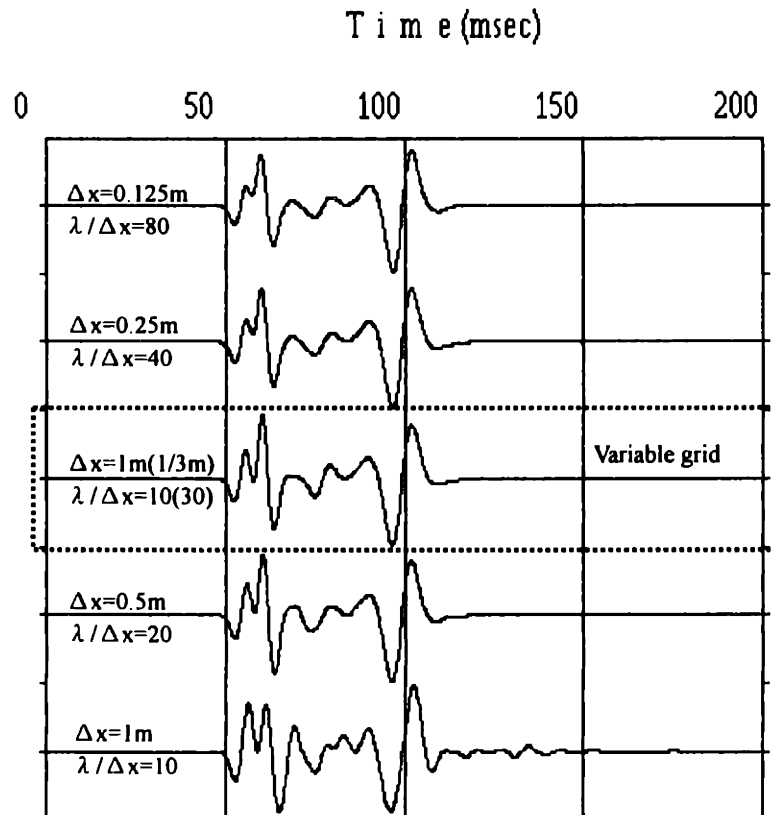
Figure 4.27: A comparison of waveforms with the various grid sizes. Particle velocity (vertical component) is plotted.

Chapter 5

Wave Propagation in Near Surface Region

5.1 Introduction

The wave propagation in the near surface region is complicated by many factors, such as large velocity contrasts, strong heterogeneity, topographic relief and large attenuation. In some cases, such complications can contaminate the seismic data in shallow seismic surveys. With careful analysis and interpretation, these complications can provide valuable information of the near surface region. The surface seismic methods can be classified into three main groups; the reflection method, the refraction method and the methods using surface waves. The effect of a complicated near surface structure on these methods are different as summarized below.

When seismic reflection method is applied to great depths, such as those in the exploration of petroleum, the contamination of data from near surface scattering can be removed by using the differences between the data character (such as frequency, apparent velocity, etc.) of the signal and the noise contaminant. In the shallow seismic reflection, it is difficult to remove this contamination, since the structures of interest are close to the structures that cause the contamination (Figure 5.1). Furthermore, wavelengths in the shallow reflection seismic method are relatively long compared to the structures of interest. This character strongly complicates the analysis of the shallow reflection data compared with the seismic data used in petroleum exploration. In spite of the significant differences between the shallow reflection and the petroleum exploration methods, analysis methods used for petroleum exploration are applied to the shallow reflection data. This inappropriate

approach may result in the poor accuracy and reliability. For example, Steeples and Miller (1998) referred to this difficulty and pointed out some pitfalls in the shallow reflection method.

The seismic refraction method may be applied to delineation of shallow subsurface structures better than the reflection method, since it only concerns with first arrival traveltimes. The recent application of tomographic reconstruction technique to refraction analysis has greatly improved the accuracy and reliability of the method (Hayashi and Saito, 1996; Lanz et al. 1998; Zhang and Toksöz, 1998; Hayashi, 1999). The obvious limitation in the seismic refraction method is the non-uniqueness of its analysis. Lay and Wallace (1995) shows the difficulty in a traveltime inversion (Figure 5.2). A velocity model that has clear layer boundaries and a model in which velocity increases smoothly, can yield the same traveltime curves. As long as we only use the first arrival traveltimes, the non-uniqueness can not be resolved. However, waveforms should have some differences between a layered model and a smooth model.

In the early 1980s, a spectral analysis of surface waves (so called SASW) was introduced (Nazarian et al. 1983). Park et al (1999a, b) improve the SASW to the multi-channel analysis of surface waves (MASW) and Xia et al. (1999a) generated two-dimensional S-wave velocity map by MASW. The SASW or MASW can estimate S-wave velocity structures that are extremely valuable in geotechnical work (Imai and Tonouchi, 1982). Therefore, the SASW (MASW) has been increasingly used in various civil engineering investigation. The SASW (MASW) uses the dispersive character of Rayleigh waves. Body waves can contaminate the data in the SASW (MASW), and the separation of the surface waves and the body waves may be one of the difficulties in the SASW (MASW) analysis. The SASW (MASW) analysis relies on an one-dimensional analysis of dispersion curves (Xia et al., 1999b). However, the analysis of dispersion curves may have the non-uniqueness that is similar to that of the refraction method. The number of theoretical studies about surface wave propagation in the heterogeneous near-surface region is relatively small.

For example, the effect of two and three-dimensional structures on the method has not been investigated.

In order to improve the accuracy and reliability of the shallow seismic methods, we have to understand the fundamental wave propagation in the near surface region, and establish a new analysis approach optimized for the shallow seismic methods. I believe that finite-difference modeling can be a valuable tool for this objective. In this chapter, I will perform several numerical simulations to show the wave propagation characters in a near surface region. Then, I will compare observed waveform data with theoretical waveforms calculated by the finite-difference method.

5.2   Near Surface Modeling

A viscoelastic two-layer structure is chosen as the model for numerical simulations. The objective of the simulations is to evaluate the effect of the following parameters on surface seismic data.

* Thickness of the first layer (low velocity layer).
* Attenuation of the first layer.
* Presence of velocity gradient.
* Presence of a step on the surface.
* Presence of a step on the layer boundary.

Figure 5.3 shows the model. Velocities, densities and Q are listed in Table 5.1.

Table 5.1   Velocities, density and Q of model

	P-velocity (m/sec)	S-velocity (m/sec)	Density (kg/m^3)	Q_p and Q_s	Wavelength(m)	
					P-waves	S-waves
First layer	1000	500	1500	10 or 10000	10	5
Second layer	3000	1500	2000	10000	30	15

A P-wave source with a 100Hz Ricker wavelet is placed at the distance of 7.5m and the depth of 2m. It is obvious that the effect of near surface structures on the surface seismic record is frequency dependent. I will use a particular frequency, 100Hz, that is a common frequency in the shallow seismic methods. Receivers are placed on the surface between the distance of 10 to 95m at 5m distance intervals. In all the following figures, the vertical component of particle velocity collected at the receivers will be plotted, and waveforms will be normalized by each trace as long as no particular notes.

Figure 5.4 shows the waveforms for the homogeneous model with a flat surface and Q_p and Q_s of 10000. The first arrival is the body waves (P-waves) and the second arrival is the surface waves (Rayleigh waves). It should be noted that the surface seismic data is simple if the model is homogeneous half space.

5.2.1 Thickness of the First Layer

The first example is an investigation about the change of waveforms due to the thickness of the low velocity first layer. In this example, the Q_p and Q_s of the first layer are set to 10000, and it can be considered an elastic case. The surface topography and the subsurface layer boundary are flat. Figure 5.5 shows the wave forms with various thicknesses. The thickness of the first layer was set to 2.5m, 5.0m, 10.0m, 20.0m and 30.0m.

For the thickness of 2.5m, we can see clear dispersive waves. However, for the thickness of 5.0m, the appearance of waveforms change drastically. The coherent dispersive waves disappear and scattered waves dominate. For the thickness of 10.0m, multiple reflection or refraction starts to dominate waveforms. For the thickness of 20.0m, we can recognize reflected waves clearly. For the thickness of 30.0m, we can see the primary reflection and two multiple reflections. In the large source-receiver offset (more than a distance of 30m), we can recognize clear P-S_v converted waves. It should be noted that the amplitude of P-S_v

reflections are larger than the P-P reflections.

5.2.2 Attenuation of the First Layer

Low velocity layers just below the surface generally have high attenuation. In this example, I use the same model as the first example but set the Q_p and Q_s of the first layer to 10. Figure 5.6 shows the waveforms with various thickness in comparison to the first example (where Q_p and Q_s of the first layer are 10,000). For the thicknesses of 2.5m and 5.0m, the appearance of waveforms changes drastically from the first example. For the thickness of 2.5m, low velocity surface waves disappear and multiple reflections and refraction dominate. For the thickness of 5.0m, scattered waves decrease amplitude and frequency. As the thickness increases, the difference between two simulations decreases. However, for the thickness of 30m, the effect of attenuation is still large. This example clearly shows the effect of the anelastic attenuation on the surface seismic data.

5.2.3 Presence of Velocity Gradient

Generally, seismic velocities in the near surface region increase with depth. In some sites, velocities increase with velocity boundaries and layers, but in other sites, velocities smoothly increase with depth. However, surface seismic methods, such as the refraction and reflection methods, can not be easily applied to both structures as mentioned before. The conventional refraction method that assume discrete refractors, faces difficulties in the presence of a velocity gradient. Likewise, the reflection method needs reflectors. In the near-surface seismic surveys, sites that have no clear layer boundaries fall difficulties with both the refraction and reflection methods.

In order to overcome these difficulties, we need to investigate wave propagation with a velocity gradient. As a preliminary study, I show several simulations for the models that have velocity gradients. Figure 5.7 defines the thicknesses of the first layer, in the models

with velocity gradient. In the calculations, Q_p and Q_s are a constant 10000. Figure 5.8 shows the waveforms with various thickness in comparison to layered models.. We can see clear distinctions between the layered models and the smooth models. This implies that using waveforms may solve the non-uniqueness in the refraction method. For the thickness of 2.5m, we can see the typical dispersion of Rayleigh waves. As the thickness increases, dispersive Rayleigh waves converge on two waves, S-waves and Rayleigh waves.

Next, I show the transition of waveforms from a layered model to a smooth model. Figure 5.9 defines models. N is the number of layers. N=2 indicates a two-layer model and N=∞ indicates a smooth model. Figure 5.10 shows the waveforms with various N. We can only see clear reflection in the case of N=2 (two layer model). For the N=3 or N=4, the appearance of waveforms are too complicated to distinguish the reflections from layer boundaries. For N grater than 6, the appearance of waveforms looks like the waveforms from the smooth model.

5.2.4   Presence of a Step on the Surface

So far, I have been concerned with the models which have a flat surface and a layer boundary. Next, I will show the effect of an irregular surface on a seismic record. To avoid complexities, I limit the study to one small step on the surface (Figure 5.3). At first, I show the simulation with an elastic homogeneous model (V_p of 3000m/sec and V_s of 1500m/sec). Figure 5.11 shows the waveforms with various step sizes. We can see Rayleigh waves scattered from the step, and converted from the body waves at the step. As the step size increases, the amplitude of scattered waves increases. However, the magnitude of scattered waves in the step size of 10m and 20m, is almost the same. In this calculation, the wavelength is approximately 30m for P-waves and 15m for Rayleigh waves. It seems that if the step size is larger than the wavelength, the step size no longer affects the amplitude of scattered waves.

Next, I show the simulation for a two-layer model. Figure 5.12 shows the waveforms for the two-layer model together with the homogeneous case. The model has only the low velocity layer behind the step. We can see that the appearance of waveforms changes drastically at the step. Figure 5.13 shows the waveforms with various thicknesses of the first layer. The step size is fixed at 10m. We can see that the appearance of waveforms changes drastically with the thickness of the first layer. The result implies that the effect of the thickness of the low velocity first layer is much larger than the effect of the step on the surface.

5.2.5 Presence of a Step on the Layer Boundary

Here, I will show the effect of an irregular layer boundary on a surface seismic record. Figure 5.14 shows the waveforms from the simulation for the flat surface model with the low velocity layer. The low velocity layer is placed only in the left half of the model. The dispersive surface waves due to the thin low velocity layer are clearly blocked at the edge of the low velocity layer. Figure 5.15 shows the waveforms from the step model on the layer boundary together with the previous one. This model is almost the same as the previous model, but the low velocity layer continues to the right side of the model. We can see that the surface waves are not blocked as in the previous calculation. This example clearly shows the significant effect of a thin low velocity layer on the surface seismic record.

Next, I will show the effect of the step shape on the layer boundary. Figure 5.16 shows models used in the simulations and corresponding waveforms. We can see the change of the appearance of waveforms due to the step shape. However, this change is relatively small in comparison to the effect of the first layer thickness (see Figure 5.11 to 5.15). The results imply that in the surface seismic methods applied to near surface region, the effect of the low velocity layer thickness is much larger than the effect of the step shape on the layer boundary.

5.2.6 Application of the Reflection Method to Active Faults Survey

Finally, I show the calculations that simulate the reflection method applied to an active faults survey. Figure 5.17 shows the velocity models used in the simulations together with the source locations. Material properties, the receiver locations and a source wavelet are identical to the previous simulations. Two models are used in the simulation as shown in Figure 5.17. The first model has a flat surface and the second model has a step on the surface. The deformation of bed rock (second layer) is 10m. The finite-difference calculation is performed for four different sources 7.5m, 37.5m, 67.5m and 97.5m. The fault is located at a distance of 52.5m in the flat model and 50.0m in the step model.

Figure 5.18 shows the waveforms from the simulation for the first model (flat surface model). In this calculation the Q_p and Q_s of the first layer are set to 10000. We can compare Figure 5.18 with Figure 5.5 showing the waveforms from the flat layer boundary models. Using a source of 7.5m, we can see the obvious complication due to the fault, at the larger distances (60 to 95m). However, it is difficult to detect the presence of the fault from the waveforms. Using a source of 37.5m, we can see the obvious discontinuity of the reflected waves behind the fault (distance of 60m). It is possible to detect the presence of the fault from the waveforms. The sources at the distance of 67.5m and 97.5m are located at the upper side of the fault. It is difficult to detect the presence of the fault from the waveforms of these two sources.

Figure 5.19 shows the waveforms from the second model simulation (a step on the surface). The figures above show the simulations in which the Q_p and Q_s of the first layer are set to 10000. The figures below show the simulations in which the Q_p and Q_s of the first layer are set to 10. The waveforms in Figure 5.19 are more complicated in comparison to the flat surface case (Figure 5.18). In the flat surface case, we can detect the fault presence in the seismic record of 37.5m. It is more difficult to detect the fault presence from the waveforms

in Figure 5.19. In particular, it is difficult to detect the fault from the simulation for the anelastic case. It is obvious that the real subsurface structures are more complicated, and the real surface seismic record is more complicated. Detecting the subsurface structure from the field record is sometimes difficult in the actual reflection surveys.

5.2.7 Conclusions from simulation

As the result of the simulations, the effects of the five subsurface condition on the surface seismic records may be ordered (from significant to slight) as follows:

1. Thickness of the first layer (low velocity layer).
2. Presence of velocity gradient.
3. Attenuation of the first layer.
4. Presence of a step on the surface.
5. Presence of a step on the layer boundary.

Figure 5.5 clearly shows the effect of low velocity layers just below the surface. Figure 5.8 and 5.10 show velocity gradient has large effect on the character of the surface seismic record. These results imply that reflection and surface waves can be used to obtain information about near surface structure. Figure 5.6 also shows the large effect of anelastic attenuation. Generally, the anelastic attenuation is large in the near surface region, and its effects should be considered in near surface wave propagation studies. Figure 5.16, 5.18 and 5.19 show that the layer boundary shape has a small effect on the surface seismic record in comparison to the presence of low velocity layers.

5.3 Comparison of Observed and Theoretical Data in the Refraction Method

5.3.1 2-D Seismic Refraction Data

A two-dimensional seismic refraction method was performed in the mountainous area of Japan. The dynamite, placed at the depth of about 1m, was used as source. The quantity of dynamite was approximately 100 to 200g. The waveform data were collected at the receivers placed on the surface. The velocity seismometers (geo-phone : OYO SMC70) that have the natural period of 28Hz were used as the receivers, and a OYO DAS-1 was used as the data acquisition system. The receivers collected the vertical component of particle velocities.

First arrival traveltimes were picked and the non-linear traveltime tomography (Hayashi and Saito, 1996) was applied to the traveltime data. The result of the tomography (P-wave velocity structure) is shown in Figure 5.20. The traveltime tomography of refraction data has non-uniqueness, and therefore, we can show several velocity models that satisfy the observed traveltime data. Figure 5.20 (a) shows a velocity model with the assumption that a velocity structure is a three-layer model. Figure 5.20 (b) shows a velocity model with the assumption that a velocity increases smoothly with depth. Figure 5.21 shows the comparison of the observed and theoretical traveltime data. We can see that both velocity models can satisfy the observed data with a smaller error than an error due to traveltime picking. We can not decide which velocity model is true, as long as we use only the first arrival travel times.

In the previous section, I showed the large difference of waveforms between layered and smooth models based on my simulations. In this section, I will calculate the theoretical waveforms for both layered and smooth velocity models, and compare the theoretical and observed waveforms.

129

5.3.2 Model Building for Viscoelastic Finite-difference Calculation

Since I have a only P-velocity model, I have to assume other material properties. S-velocity is assumed to be the $1/\sqrt{3}$ of P-velocity (Poisson solid). A density is assumed to be constant $2000 kg/m^3$. P-wave sources are placed at the depth of 1m, and a 50Hz Ricker wavelet is used as a source wavelet. The center frequency of the source wavelet is chosen from the frequency of the observed data. The simulations are performed for two cases. The first simulation uses a model in which the Q_p and Q_s are set to constant 10000. The second simulation uses a model in which the Q_p and Q_s are set to 5 in the region where the P-velocity is slower than 2000m/sec, and 100 in the region where the P-velocity is faster than 2000m/sec. The Q is generally very small in the near surface region of a mountainous area, and the later model is more realistic than the first model.

In the smooth model, velocity model is represented by 30 by 15 (horizontal by vertical) arbitrary quadrilateral cells. In the finite-difference calculations, the grid size of 0.125m is used and the model (150m by 100m) is gridded into 1200 by 800 grids. The variable grid method is not used in this simulation.

Since the absolute amplitude of waveforms highly depends on the coupling of geo-phones and the ground, I will not be concerned with absolute amplitude of waveforms in this comparison, but will be concerned only with the general appearance.

5.3.3 Comparison of Layered and Smooth Models Using the Source of 122.5m

First, I will compare the layered and smooth models. Figure 5.22 shows the observed common source data with the source at the distance of 122.5m. In Figure 5.22, waveforms are normalized by each trace. We can clearly see first arrival (P-waves) and the later low

frequency arrivals. The continuity of the later arrival implies that the model has no sharp layer boundary. Figure 5.23 shows theoretical waveforms for the layered model. Regardless of the attenuation, the appearance of waveforms differs from the observed data. The theoretical waveforms are much scattered in comparison to the observed data. Figure 5.24 shows the theoretical waveforms for the smooth model. The waveforms for a small Q model (c) are more similar to the observed data in comparison to those of the layered model. This result strongly suggests that the true model is a smooth one. We can see several obvious characters in the observed data, such as the first arrival traveltimes, the frequency difference between the first arrival and the later arrival, the amplitude ratio of the first arrival and the later arrival, the apparent velocity of the later arrival, and complicated wavefoims at smaller distances (0 to 40 m). We can see that the theoretical waveforms of the smooth model with small Q have similar characters.

5.3.4 Comparison of Observed and Theoretical Data for Other Sources

Next, I calculated theoretical waveforms for different source locations. The source locations are shown in Figure 5.25 together with the P-velocity model (identical with Figure 5.20 (b)). Based on the result of the source at the 122.5m, I use the smooth model with small Q in a low velocity area, Q_p and Q_s were set to 5 in the region where the P-velocity is slower than 2000m/sec, and 100 in the region where the P-velocity is faster than 2000m/sec. The sources are placed at the depth of 1m and a 50Hz Ricker wavelet is used as a source wavelet. Figure 5.26 shows the theoretical waveforms in comparison to the observed data. The comparison of the theoretical waveforms with observed data can be summarized as follows.

1. 3.5m (Figure 5.26 (a))
The first arrival traveltime of the theoretical waveforms agrees with the observed data. In the observed data, there is a clear first arrival and a relatively small later arrival (100 to 170msec) which shows good coherency and the same amplitude as the first arrival. In the

131

theoretical waveforms, we can see the clear first arrival. The later arrival is not clear in comparison to the observed data.

2. 27.5m (Figure 5.26 (b))

The observed data shows a obvious later arrival that has a larger amplitude than the first arrival. The theoretical data also shows the obvious later arrival with a large amplitude. A different appearance may somewhat be due to the difference of source frequency. The first arrival traveltime of the theoretical waveforms agrees with the observed data.

3. 57.0m (Figure 5.26 (c))

There is a clear later arrival that shows large amplitude and good coherency in the observed data. The coherency of the later arrival is better in the large distance than in the small distance. We can see that the theoretical waves have similar characters. A different appearance may somewhat be due to the difference of source frequency. The first arrival traveltime of the theoretical waveforms agrees with the observed data.

4. 77.5m (Figure 5.26 (d))

In the observed data, the later arrival is not clear and coherent in comparison to the other sources. The theoretical waveforms show a similar character. The first arrival traveltime of the theoretical waveforms agrees with the observed data.

5. 102.5m (Figure 5.26 (e))

There is a clear later arrival that shows large amplitude and good coherency in the observed data. Theoretical waveforms also show the clear later arrival that has large amplitude in comparison to the first arrival. The frequency of the later arrival in the theoretical waveforms is higher than the observed data. The first arrival traveltime of the theoretical waveforms agrees with the observed data.

6. 147.5m (Figure 5.26 (f))

We can see a clear first arrival and low frequency later arrival in the observed data. Theoretical waveforms also show the clear first arrival and the later arrival. The frequency and apparent velocity of the later arrival have a clear difference between the theoretical and observed data. The first arrival traveltime of the theoretical waveforms agrees with the observed data.

5.3.5 Discussion

With my modeling, it was possible to obtaine synthetic seismograms that were close to observe field data. We can say that the model used in the simulation was not far from the true structure. However, the theoretical waveforms did not completely agree with the observed data. The reason for this disagreement may be due to following factors:

1. Q and S-velocity structures

Since a P-velocity model was constructed by traveltime tomography, the accuracy and reliability of the P-velocity model are relatively high. However, Q and S-velocity models were assumed to be simple models based on the P-velocity model. The quantity of Q and Poisson's ratio were also assumed. A real structure should be more complicated. In order to perform a complete simulation, we have to obtain the Q, S-velocity and density models by based on observation.

2. Source wavelet

I used the Ricker wavelet as a source wavelet. It is obvious that a real source wavelet is more complicated. I also used a 50Hz Ricker wavelet for all sources. It is clear that each source has a different wavelet and frequency in the observed data. Furthermore, I assumed that the sources are isotropic. However, the emission of energy from real sources may not be isotropic.

3. Three-dimensional structure

Although the survey line is almost perpendicular to topography and geological structure, a three-dimensional structure may have an effect on the seismic record. In order to perform a complete simulation, we have to build a three-dimensional model and apply a three-dimensional calculation.

This simulation should be considered as a preliminary step. In order to perform complete modeling, we need to avoid the assumptions, build a three-dimensional model, and calculate three-dimensional wave propagation. Such a complete modeling is possible, but extremely expensive and time consuming at this time. However, the comparison of the waveforms for the layered model with the smooth model shows that the finite-difference modeling could be a strong analysis tool for shallow seismic methods, in spite of the assumptions.

Exploration of petroleum   Shallow seismic methods
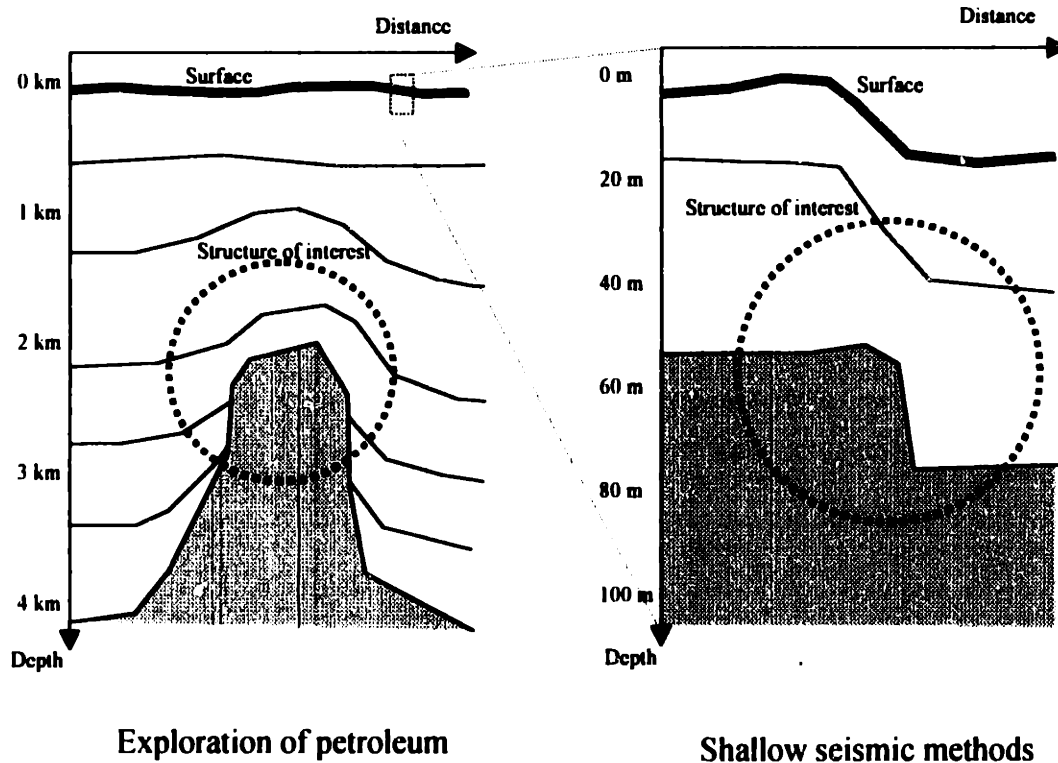
Figure 5.1.   The comparison of the exploration of petroleum and the shallow seismic methods
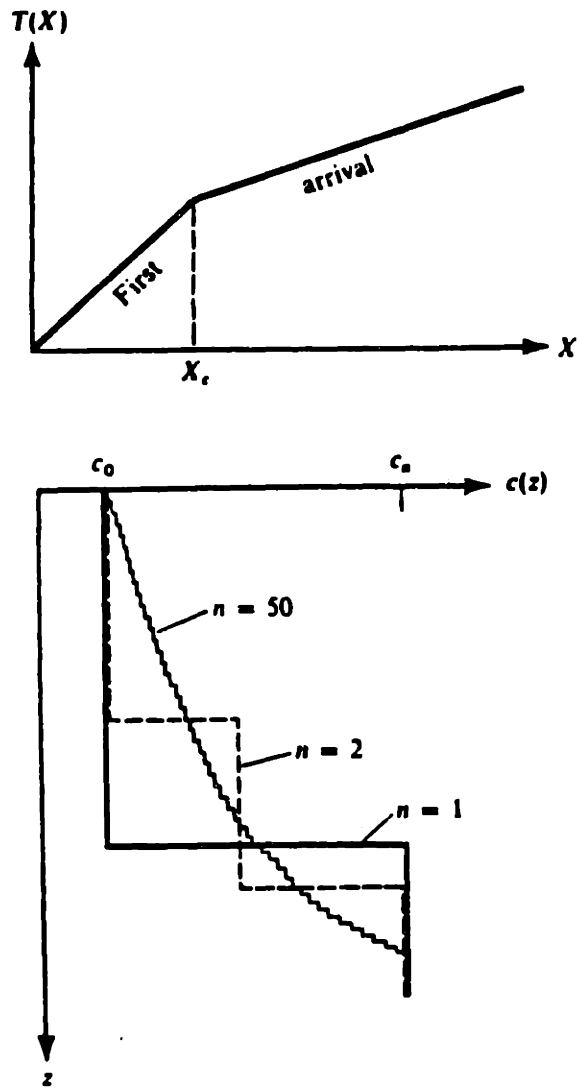
Figure 5.2: First-arrival traveltime curve that is exactly matched by the three velocity profiles shown below. (from Lay and Wallace (1995))
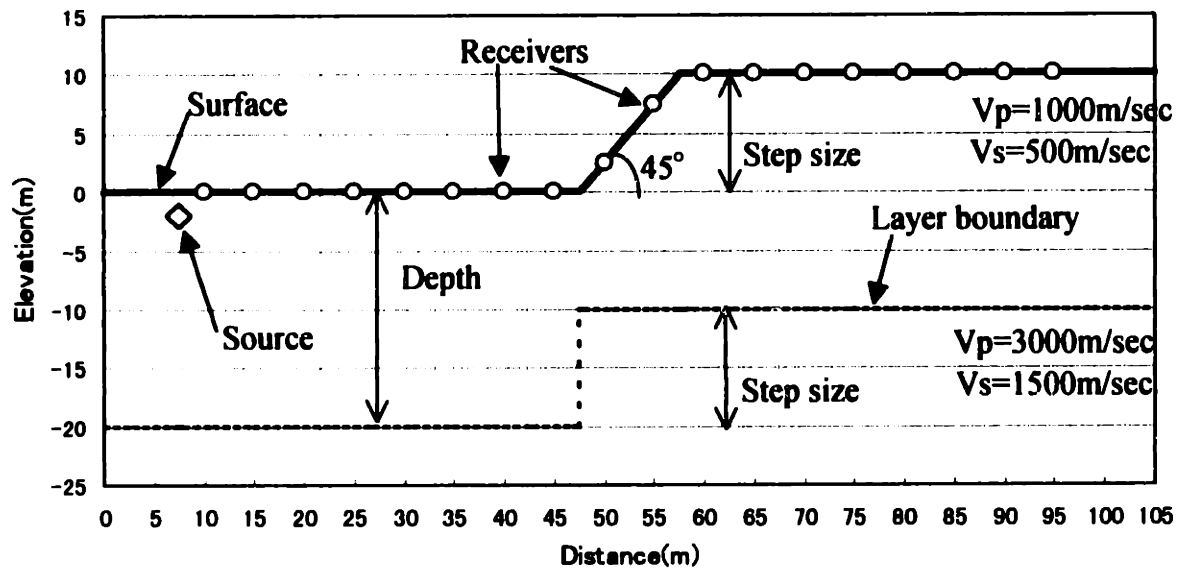
Figure 5.3: Description of the near surface model
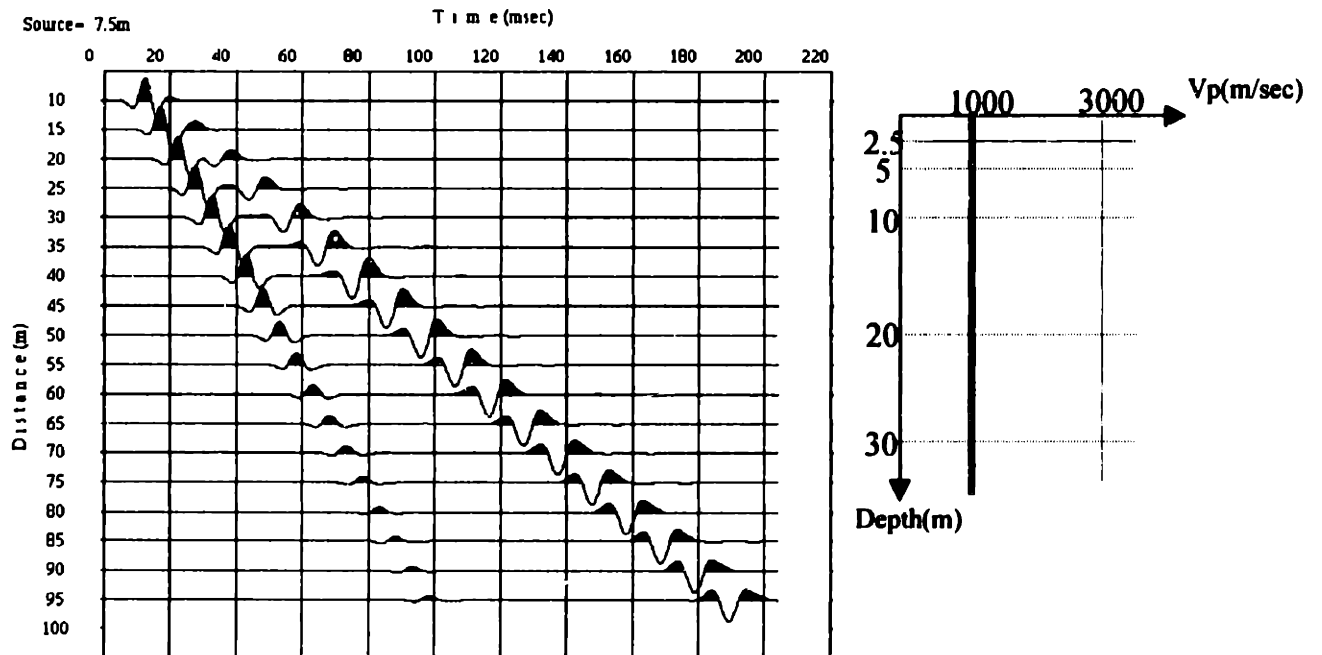
a) Vp=1000, Vs=500.
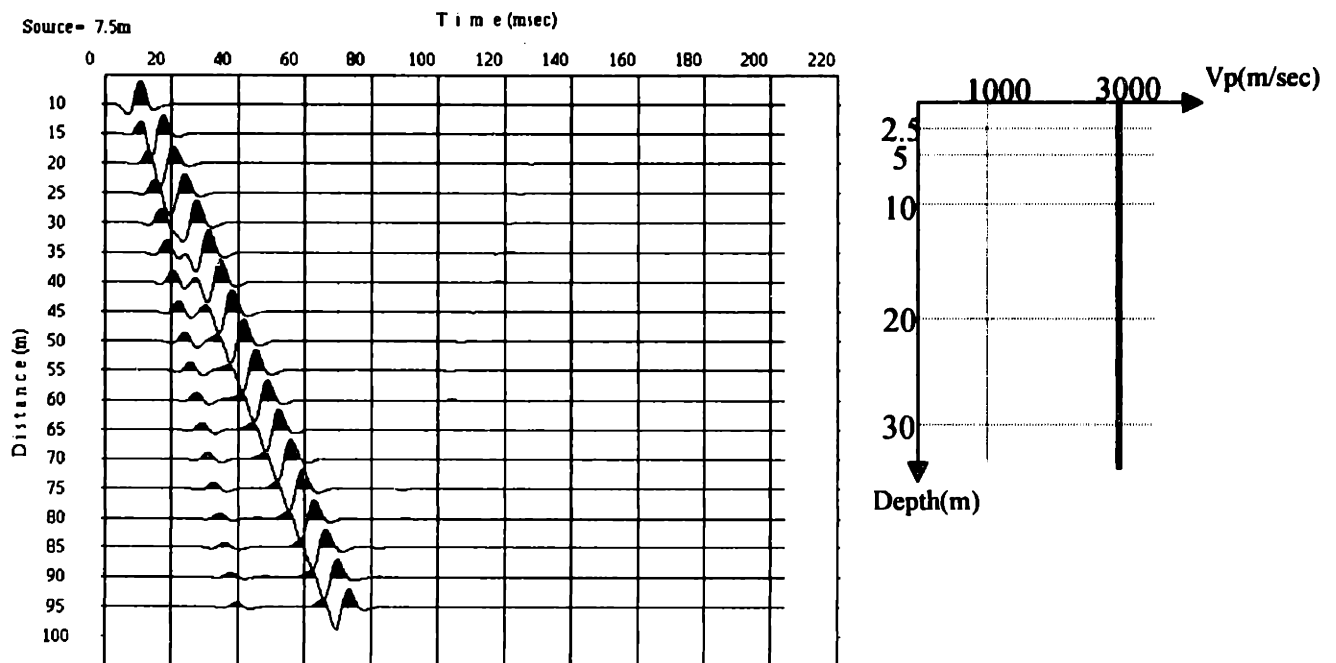
b) Vp=3000, Vs=1500.

Figure 5.4: Waveforms for the homogeneous model with flat surface and Q_p and Q_s of 10000.
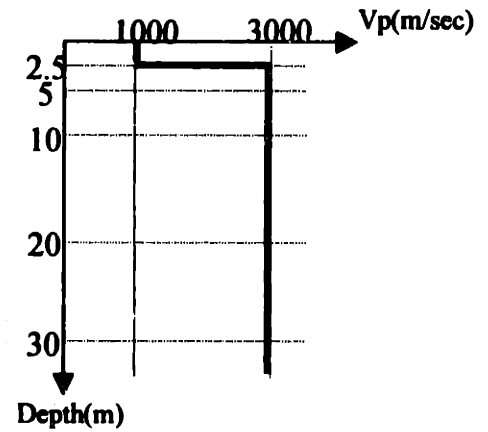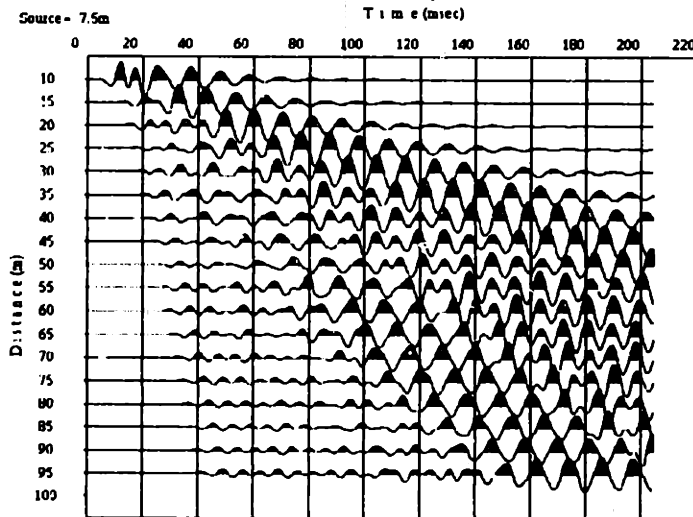
a) Thickness of the first layer is 2.5m.
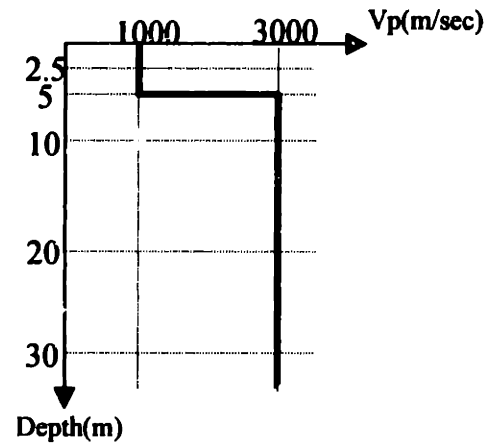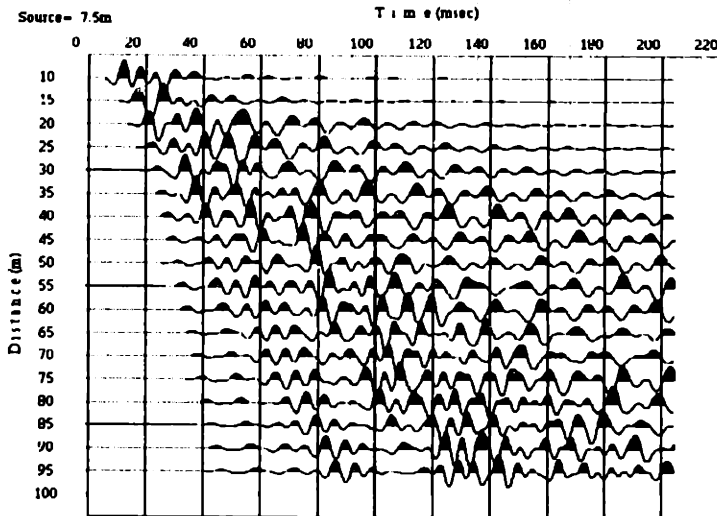
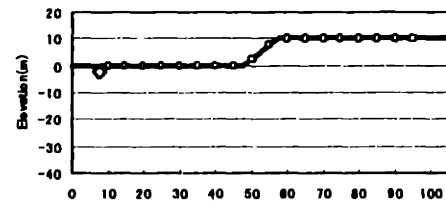b) Thickness of the first layer is 5m.
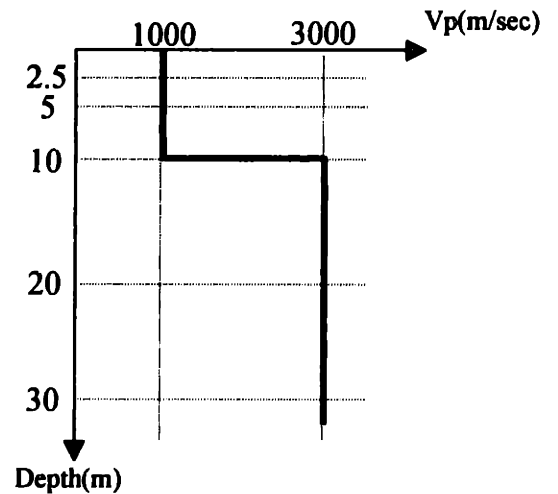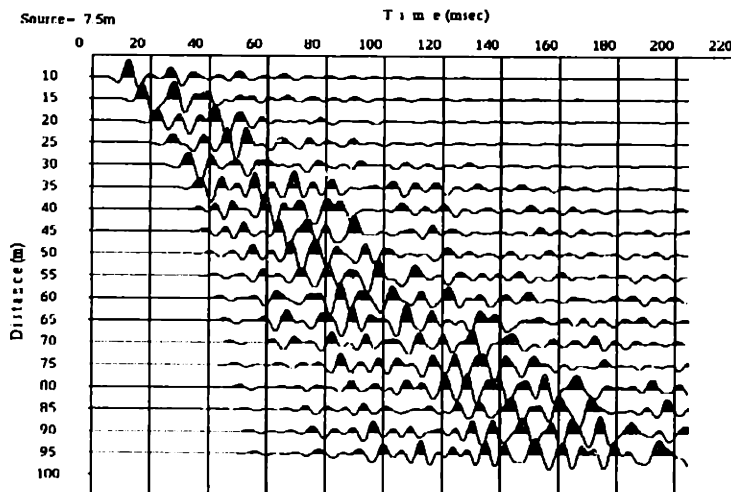
c) Thickness of the first layer is 10m.

Figure 5.5: Waveforms with various thicknesses. Q_p and Q_s of the first layer are set to 10000.

139
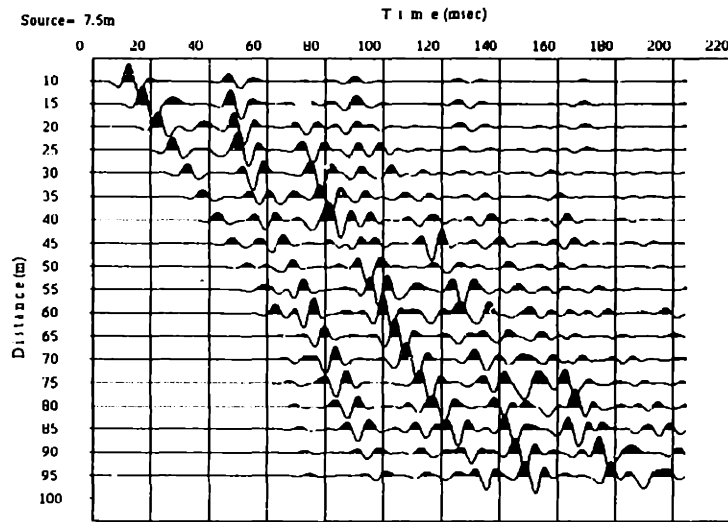
d) Thickness of the first layer is 20m.
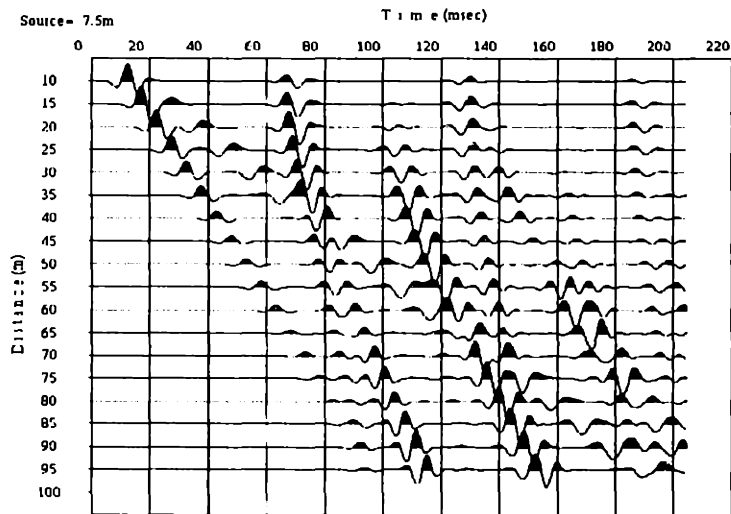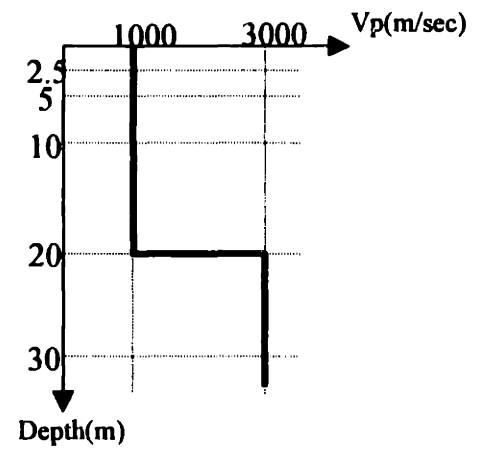
e) Thickness of the first layer is 30m.
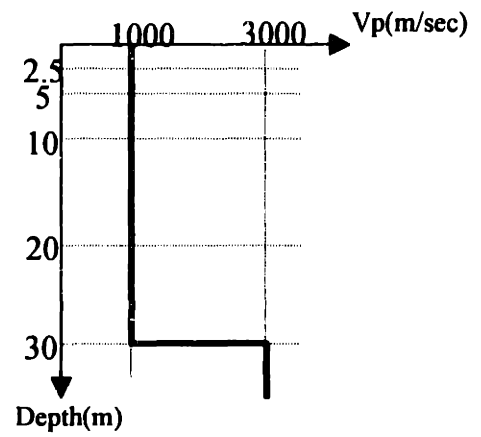
Figure 5.5, continued:

140

	Qp	Qs
1st layer	10000	10000
2nd layer	10000	10000

a) Thickness of the first layer is 5m. Q_p and Q_s of the first layer are 10000.
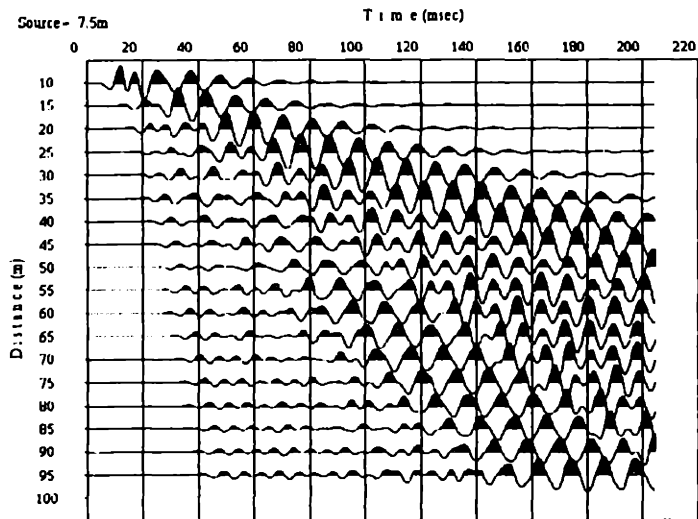
	Qp	Qs
1st layer	10	10
2nd layer	10000	10000
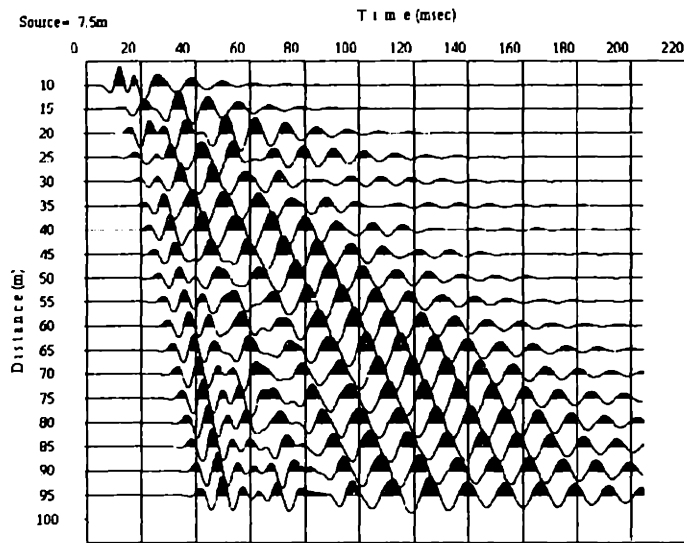
b) Thickness of the first layer is 2.5m. Q_p and Q_s of the first layer are 10.

Figure 5.6: Comparison of elastic models with varying Q values. Q_p and Q_s of the first layer are set to 10000. Thickness of the first layer is 2.5m.
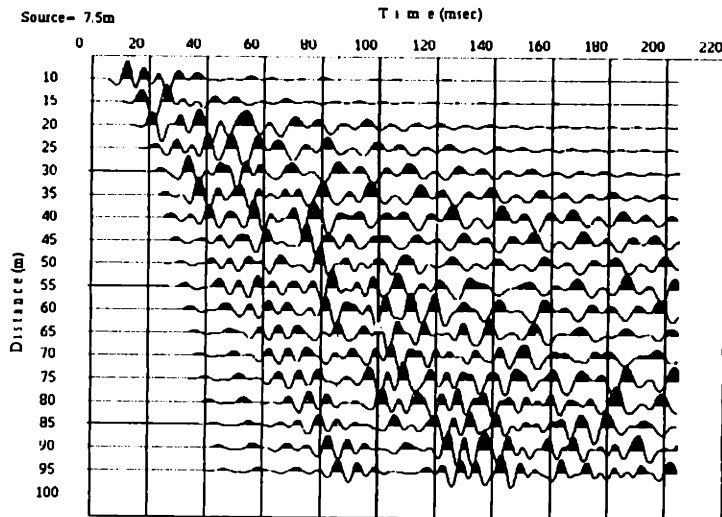
141

Source- 7.5m

c) Thickness of the first layer is 5m. Q_p and Q_s of the first layer are 10000.
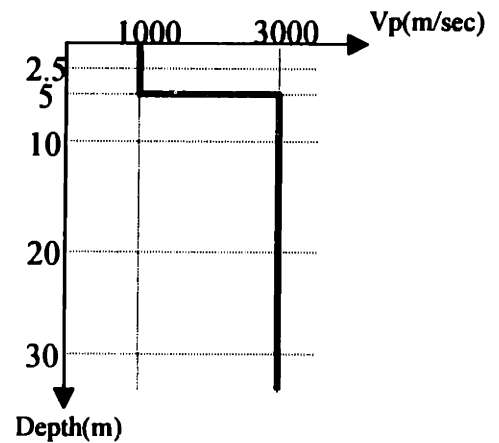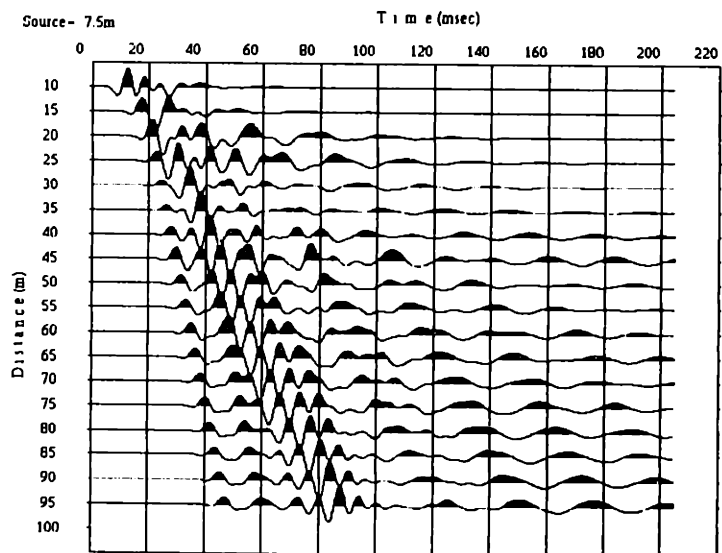
	Qp	Qs
1st layer	10000	10000
2nd layer	10000	10000

d) Thickness of the first layer is 5m. Q_p and Q_s of the first layer are 10.

	Qp	Qs
1st layer	10	10
2nd layer	10000	10000

Figure 5.6, continued: Thickness of the first layer is 5m.

142
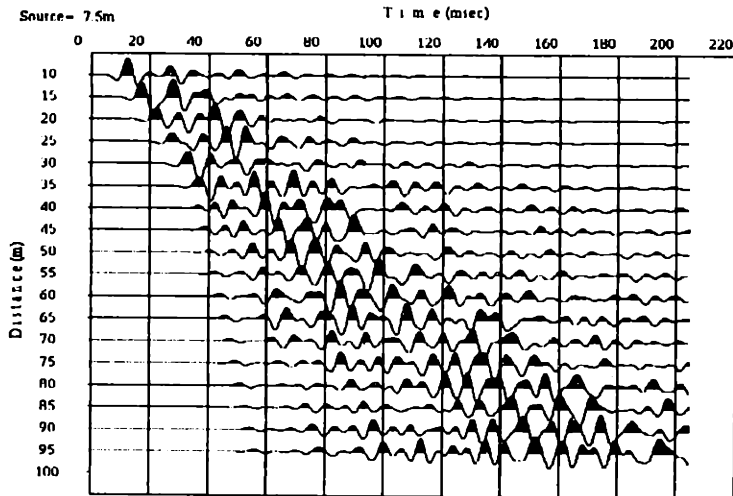
e) Thickness of the first layer is 10m. Q_p and Q_s of the first layer are 10000.

	Qp	Qs
1st layer	10000	10000
2nd layer	10000	10000
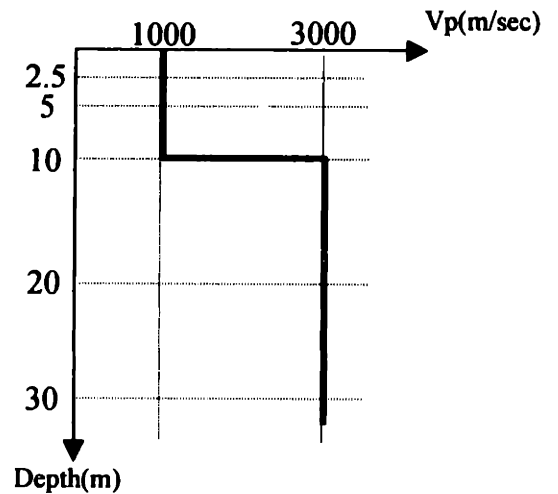
	Qp	Qs
1st layer	10	10
2nd layer	10000	10000
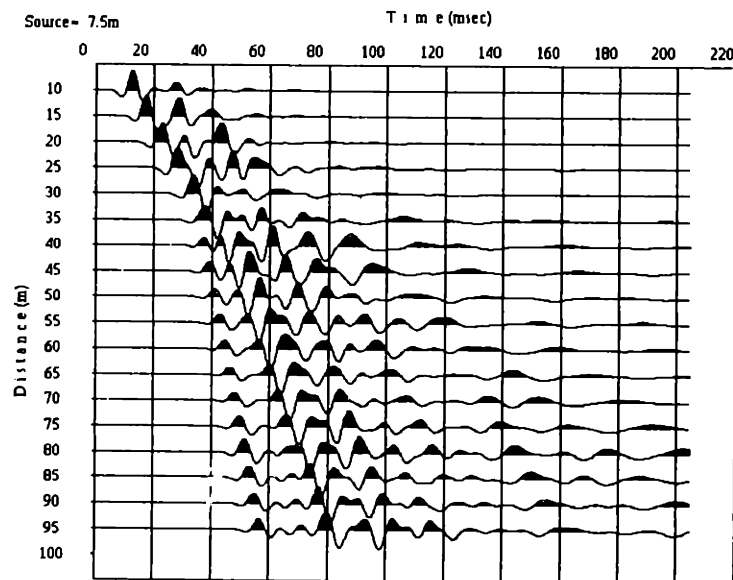
f) Thickness of the first layer is 10m. Q_p and Q_s of the first layer are 10.

Figure 5.6, continued: Thickness of the first layer is 10m.
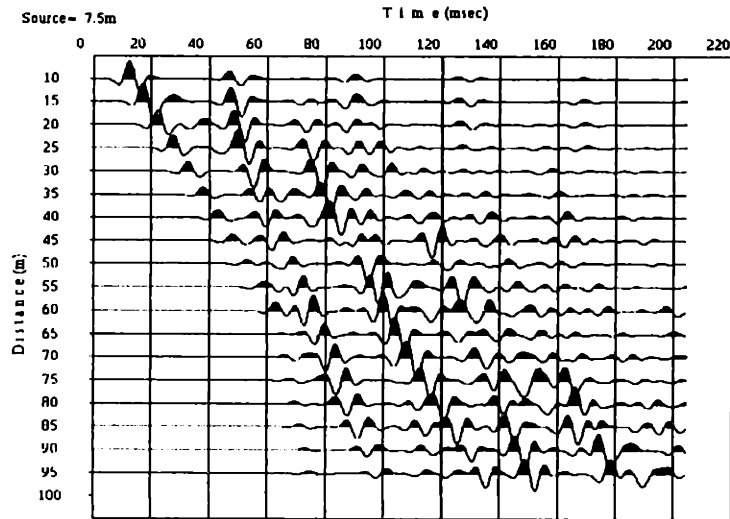
g) Thickness of the first layer is 20m. Q_p and Q_s of the first layer are 10000.
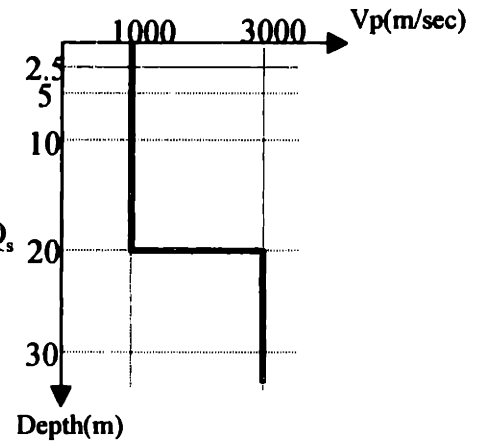
	Qp	Qs
1st layer	10000	10000
2nd layer	10000	10000
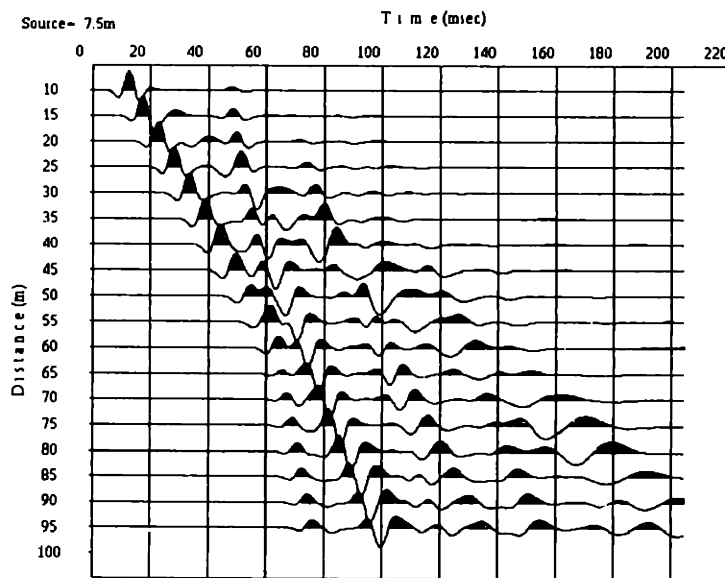
	Qp	Qs
1st layer	10	10
2nd layer	10000	10000

h) Thickness of the first layer is 20m. Q_p and Q_s of the first layer are 10.

Figure 5.6, continued: Thickness of the first layer is 20m.

144

Source= 7.5m   T i m e (msec)
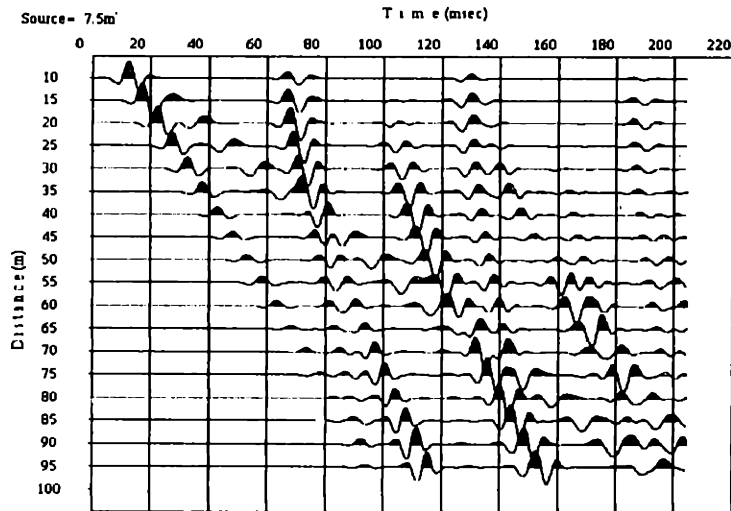
	Qp	Qs
1st layer	10000	10000
2nd layer	10000	10000
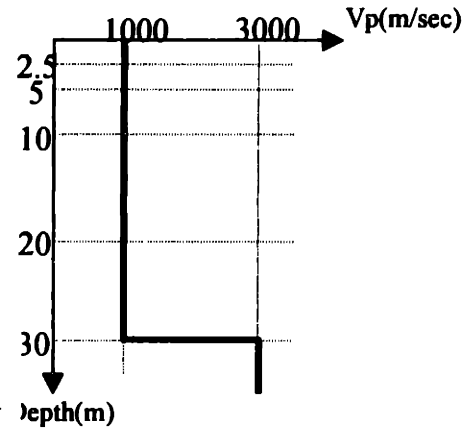
i) Thickness of the first layer is 30m. Q_p and Q_s of the first layer are 10000.
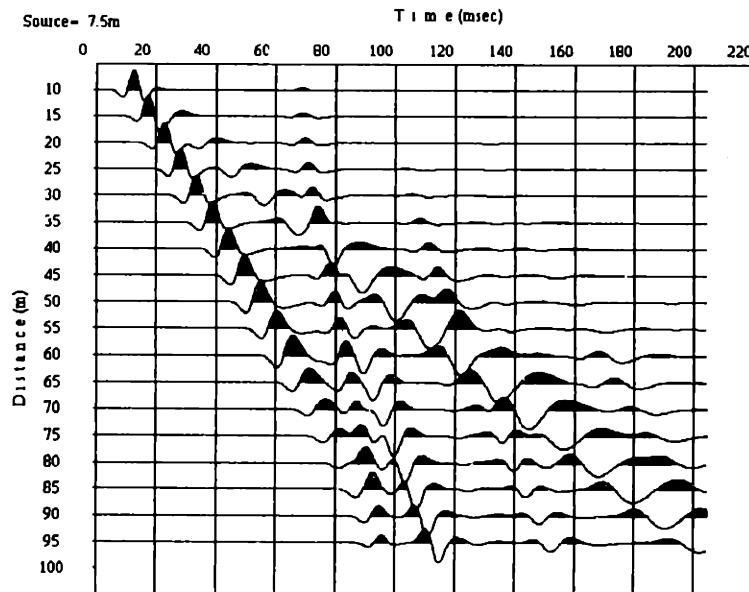
	Qp	Qs
1st layer	10	10
2nd layer	10000	10000

j) Thickness of the first layer is 30m. Q_p and Q_s of the first layer are 10.

Figure 5.6, continued: Thickness of the first layer is 30m.

Vp=1000m/sec
Vs=500m/sec

Vp=3000m/sec
Vs=1500m/sec

Velocity

Depth
(thickness)

Depth × 2

Layered model

Smooth model

Depth
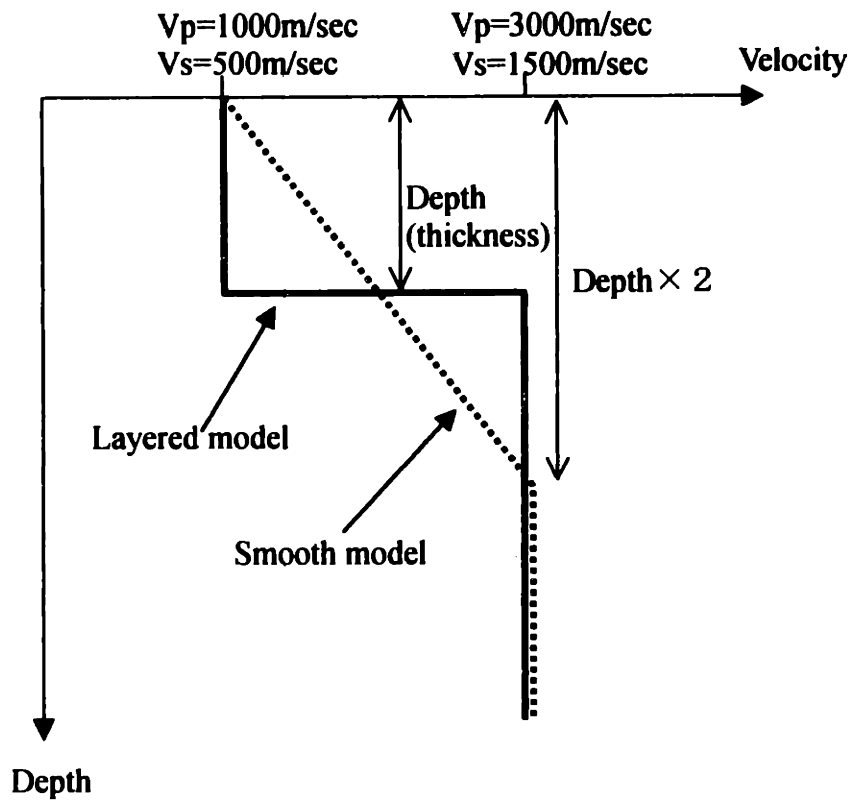
Figure 5.7 Description of thickness of first layer for the layered model and the smooth model.
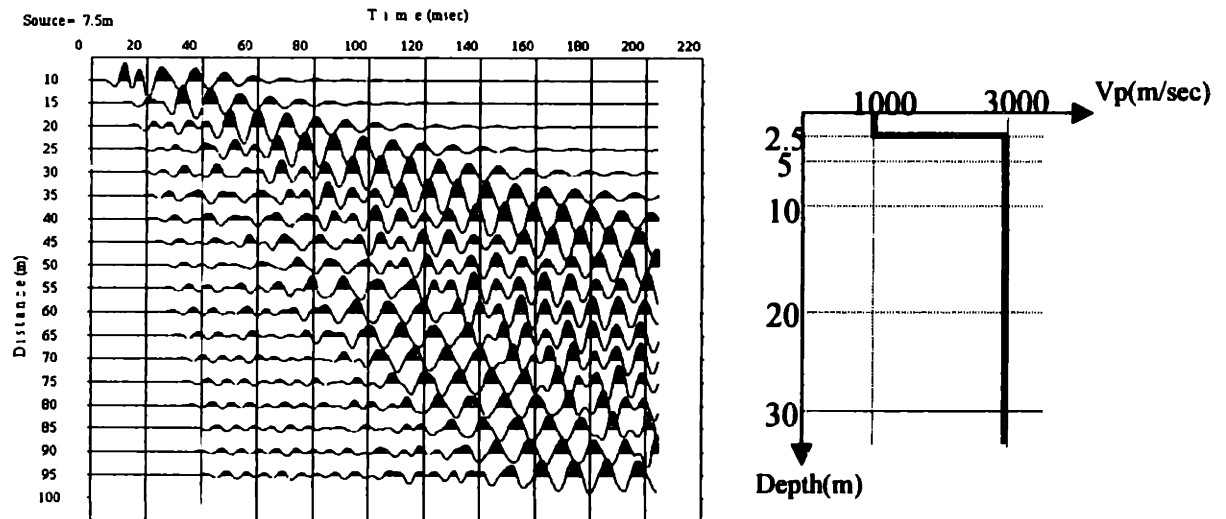
a) Layered model. Thickness of the first layer is 2.5m.
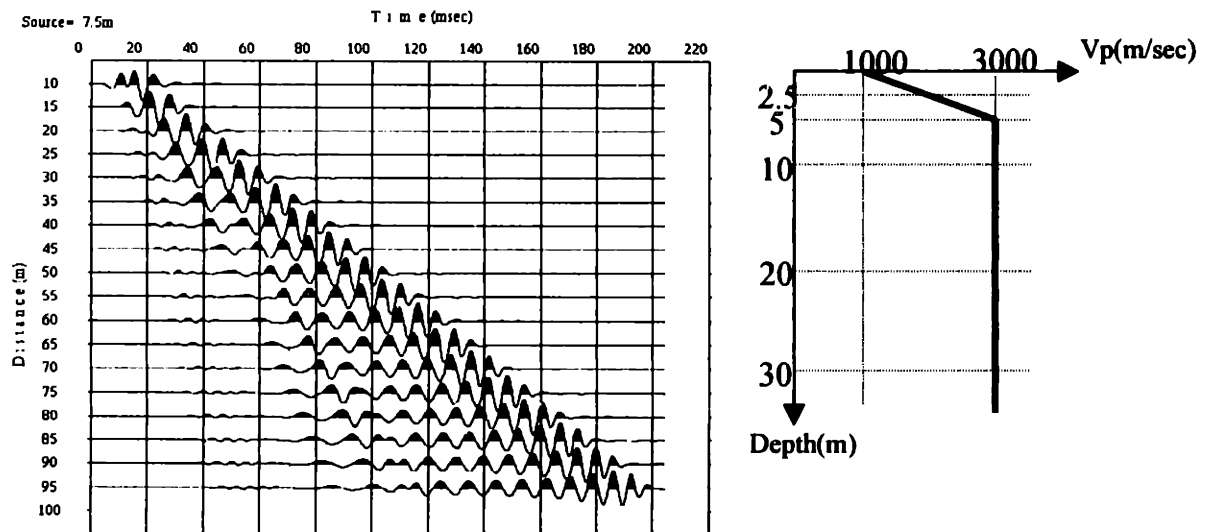
b) Smooth model. Thickness of the first layer is 2.5m.

Figure 5.8: Comparison of a layered model and a smooth model. Thickness of the first layer is 2.5m
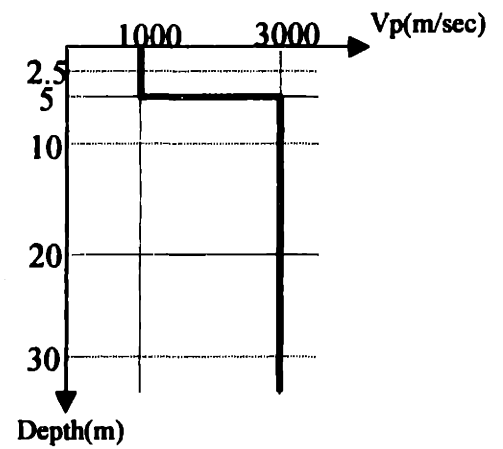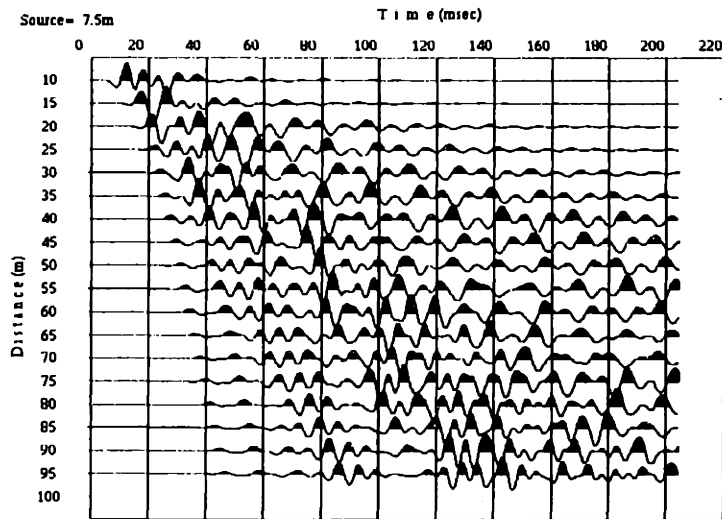
c) Layered model. Thickness of the first layer is 5m.
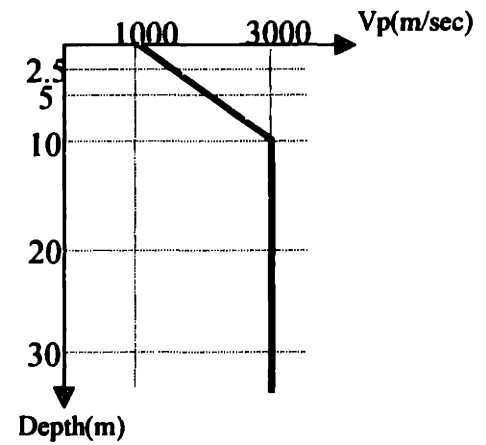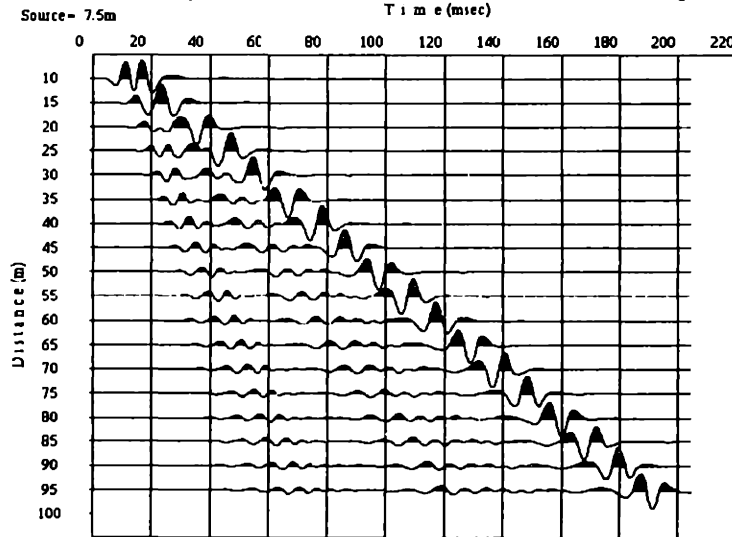
d) Smooth model. Thickness of the first layer is 5m.

Figure 5.8, continued: Thickness of the first layer is 5m

148
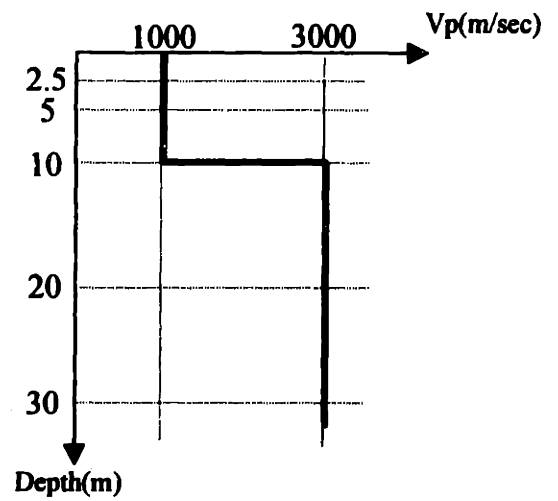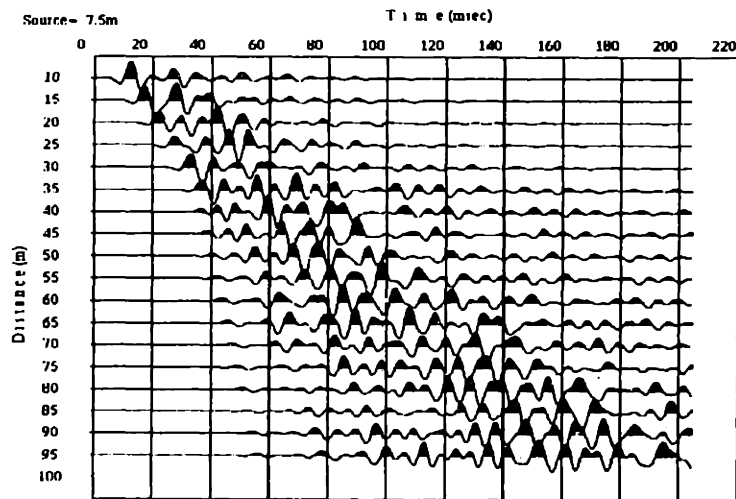
e) Layered model. Thickness of the first layer is 10m.
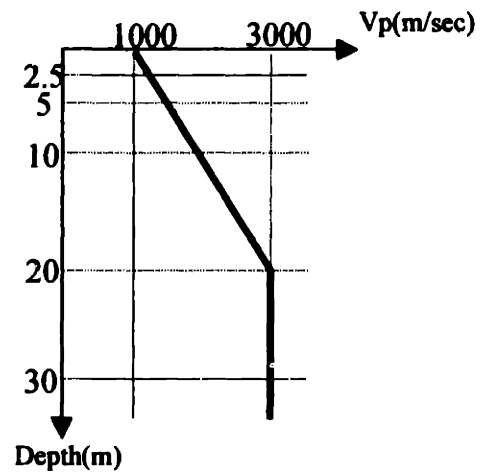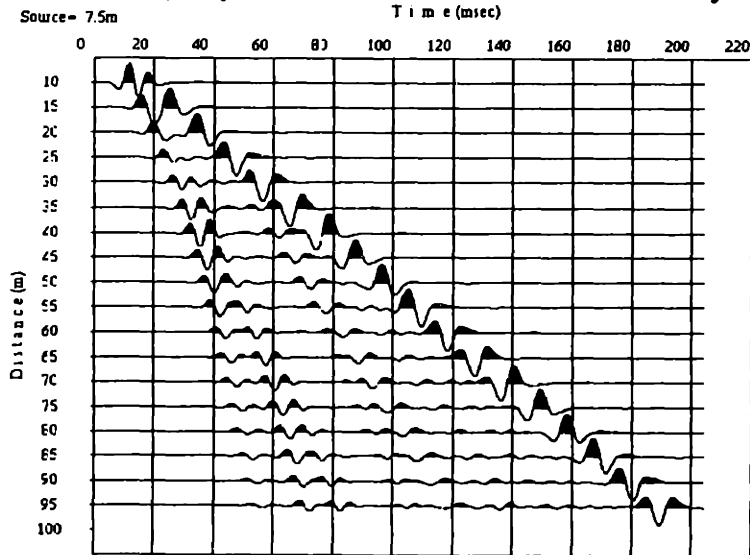
f) Smooth model. Thickness of the first layer is 10m.

Figure 5.8, continued: Thickness of the first layer is 10m

149
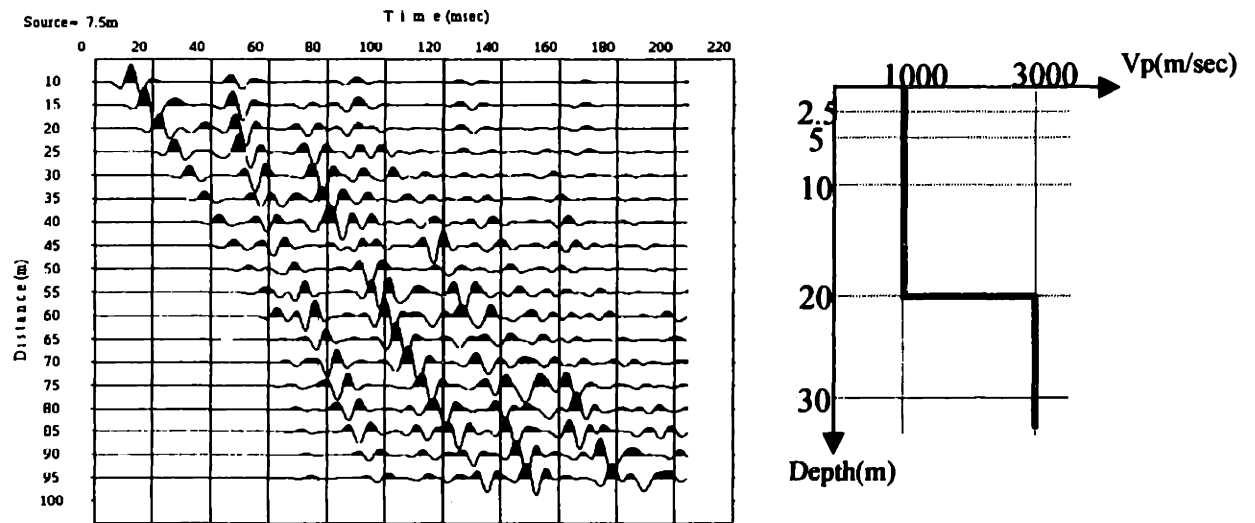
g) Layered model. Thickness of the first layer is 20m.
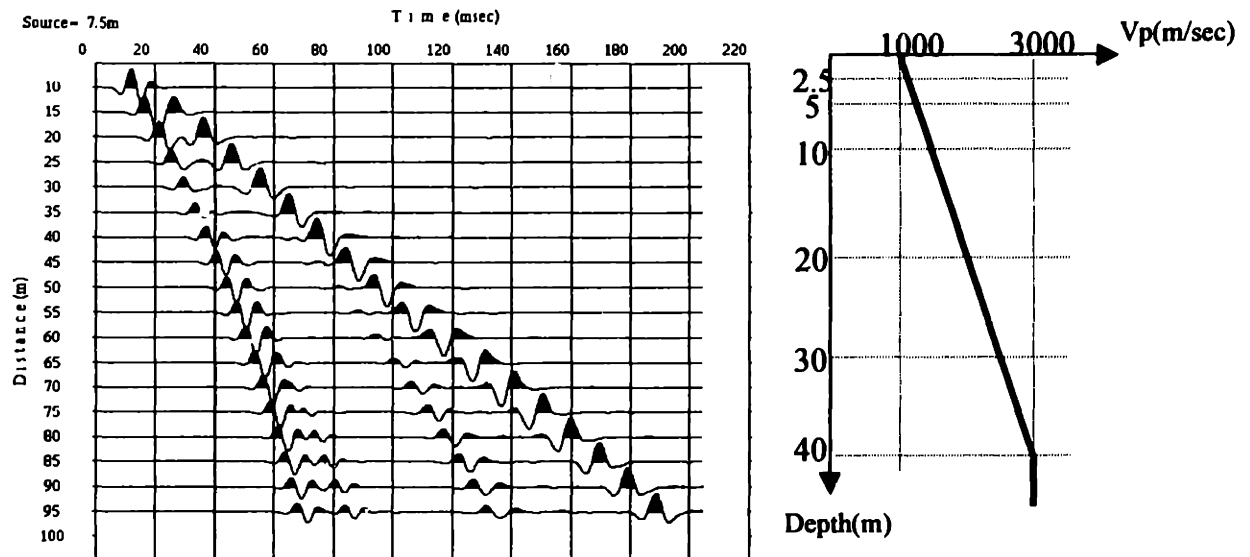
h) Smooth model. Thickness of the first layer is 20m.

Figure 5.8, continued: Thickness of the first layer is 20m

150
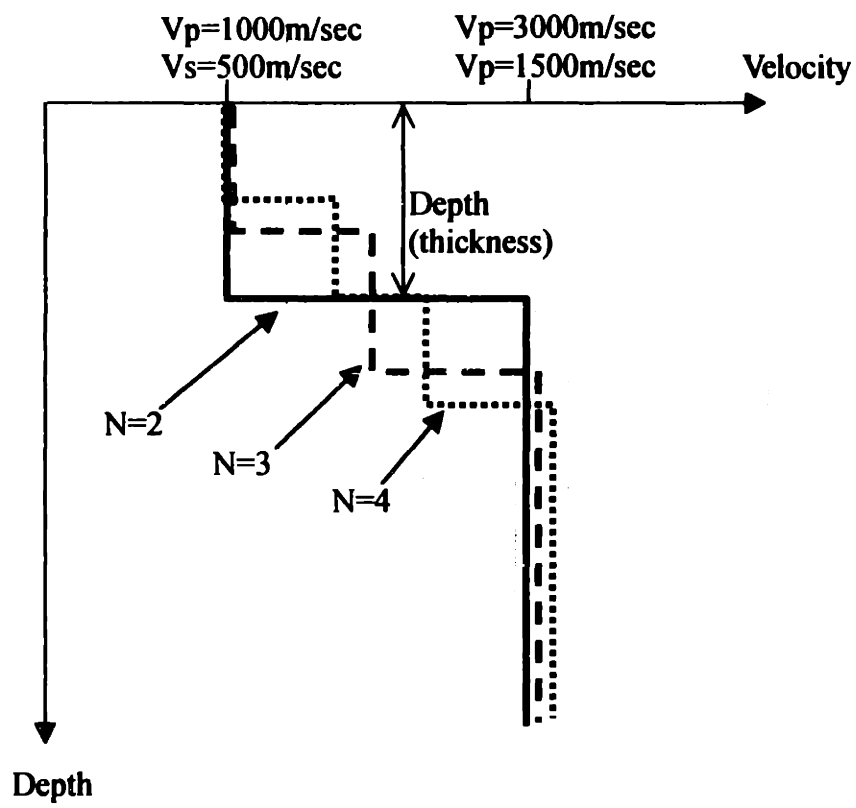
Figure 5.9: Description of N.
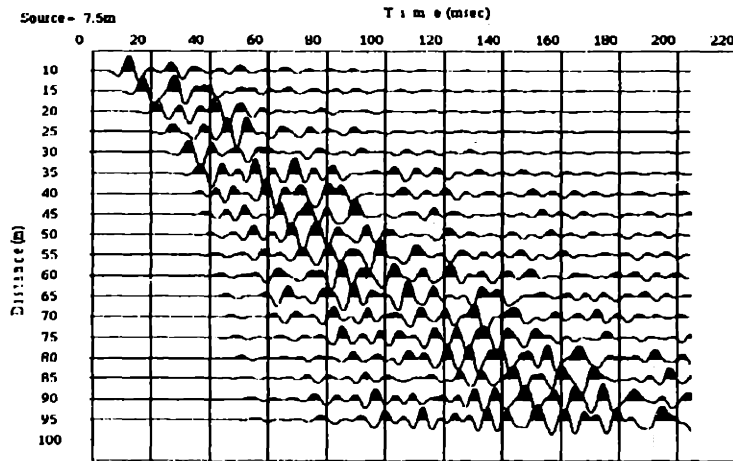
a) N=2.
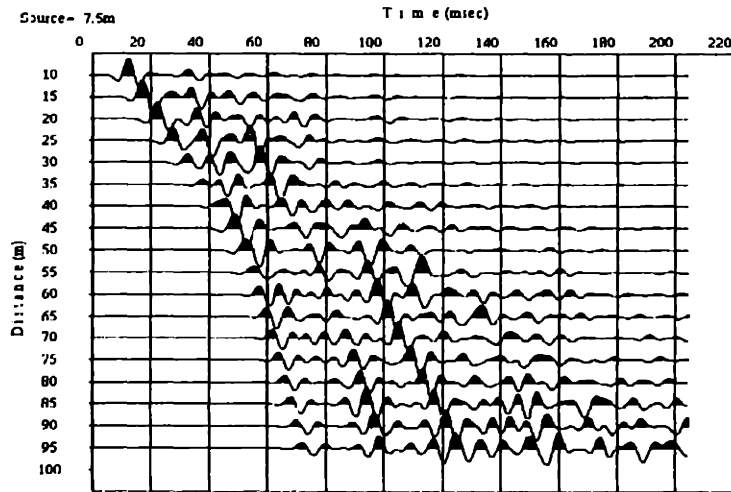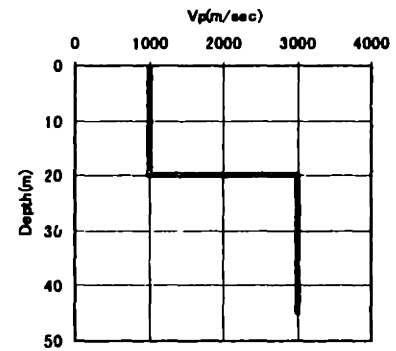
b) N=3.
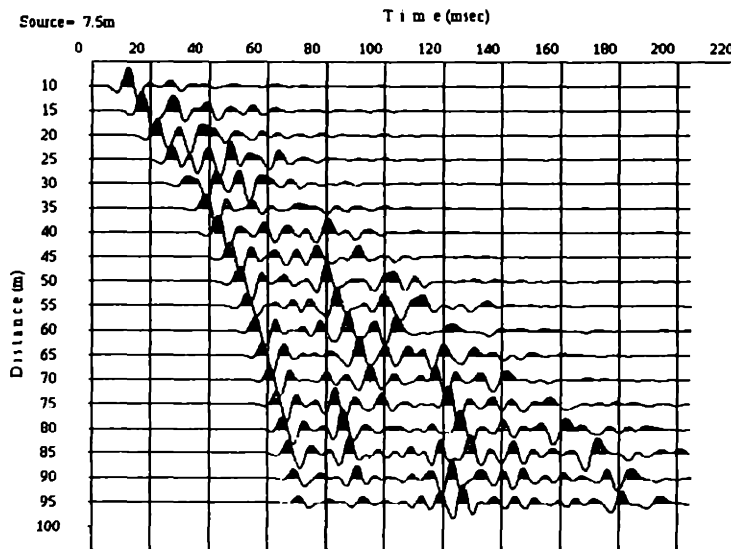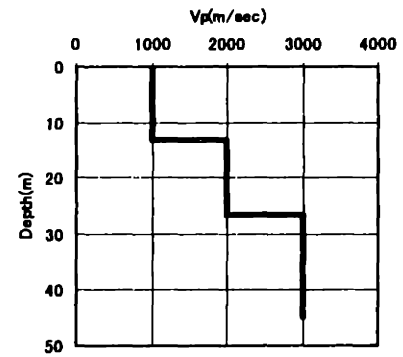
c) N=4.
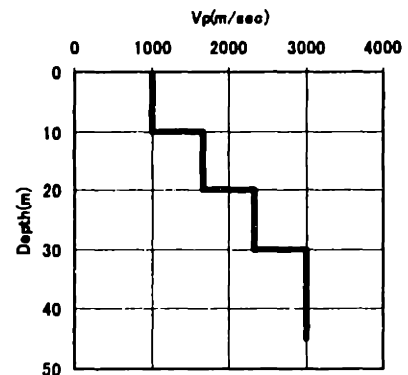
Figure 5.10: Waveforms from a layered model to smooth a model.
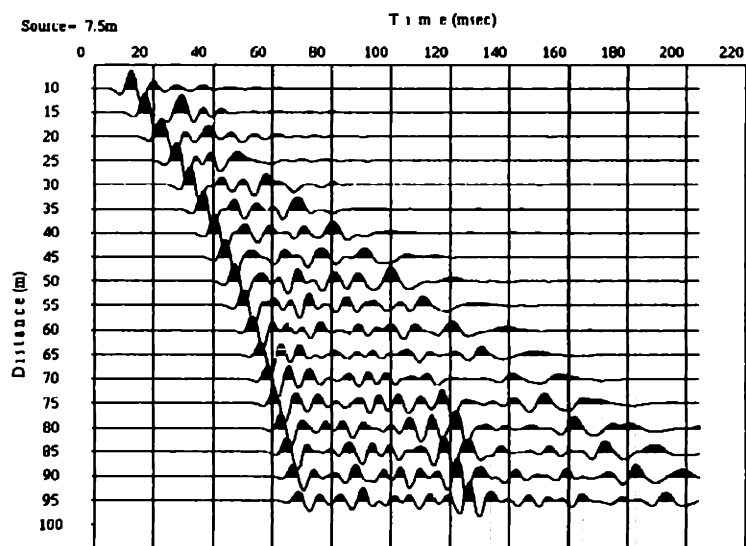
d) N=6.
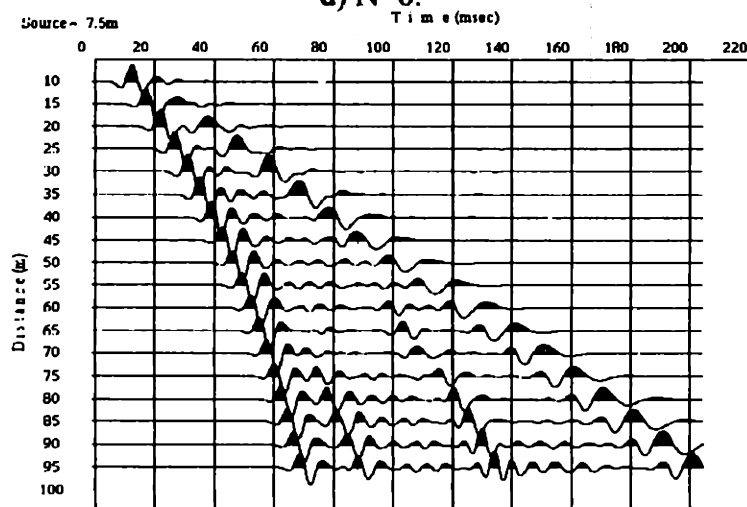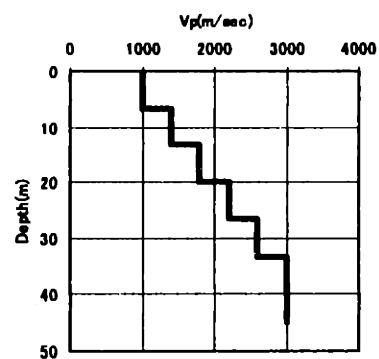
e) N=10.
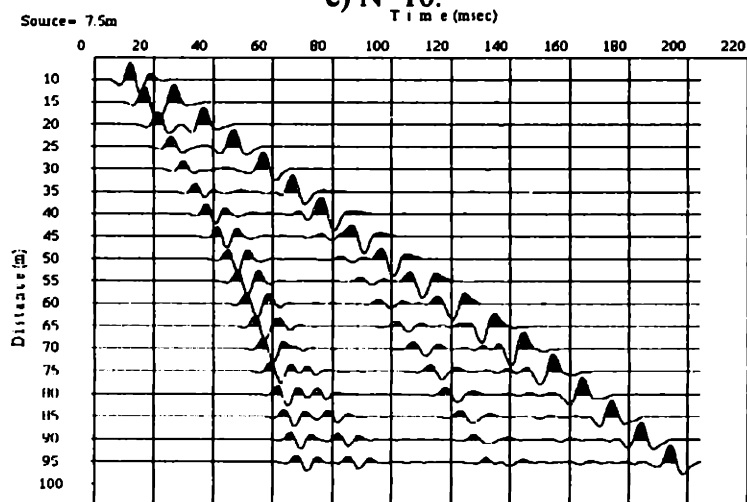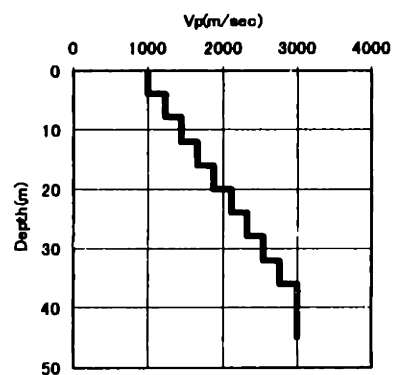
f) N=20.
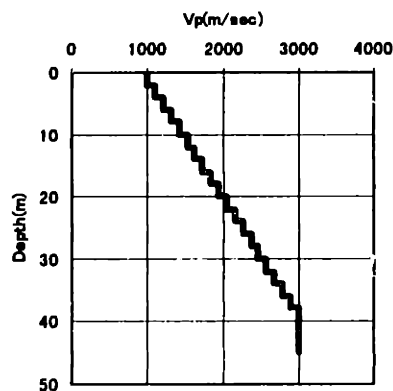
Figure 5.10, continued:

153
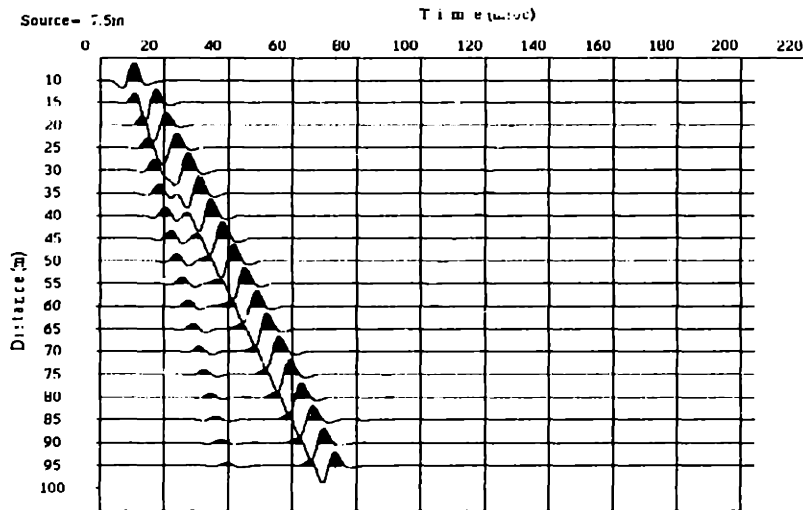
a) flat surface.
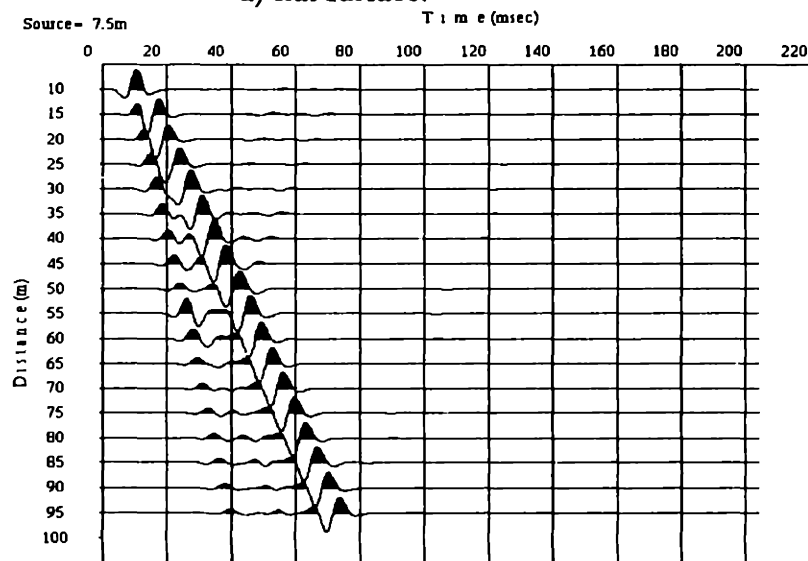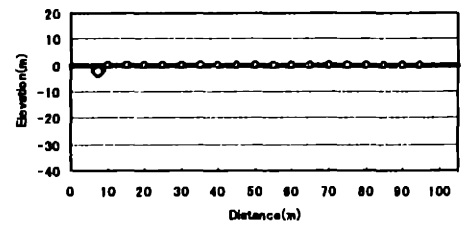
b) step size=2.5m.
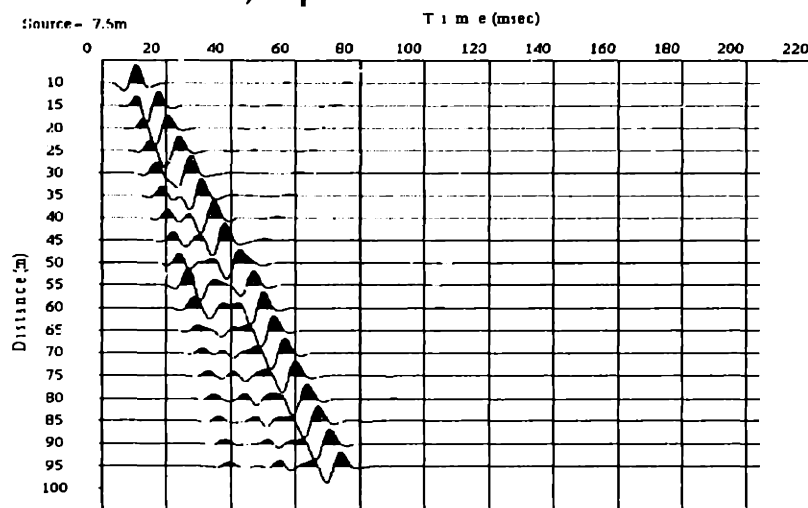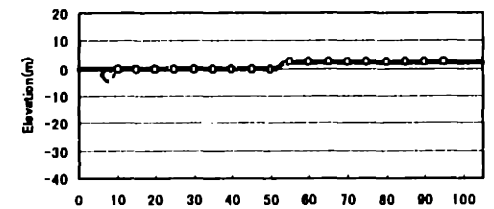
c) step size=5m.
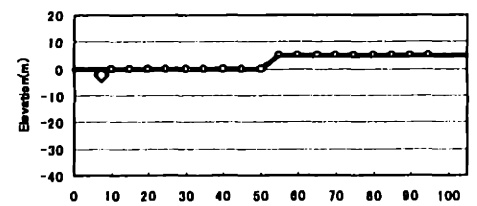
Figure 5.11: Waveforms with various step sizes.

154
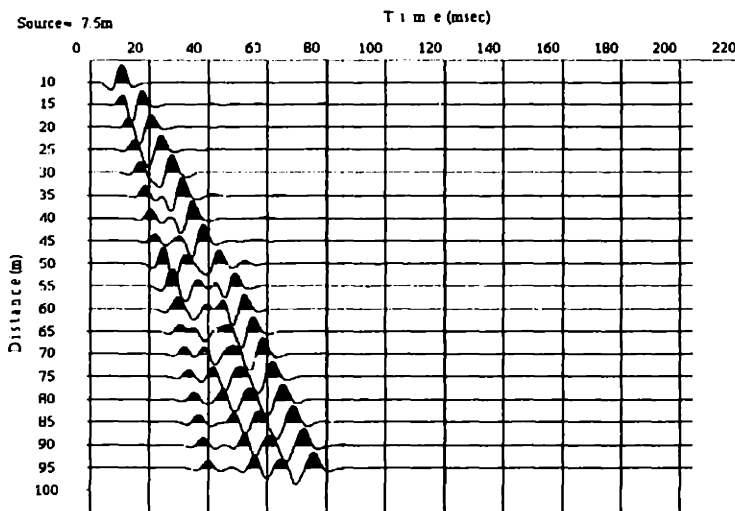
d) step size=10m.
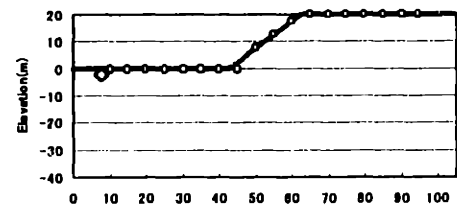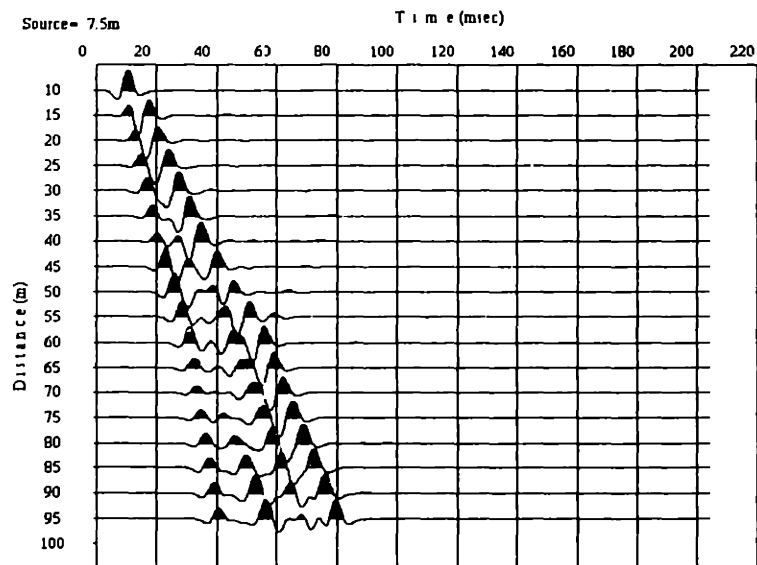
e) step size=20m.

Figure 5.11, continued:

155
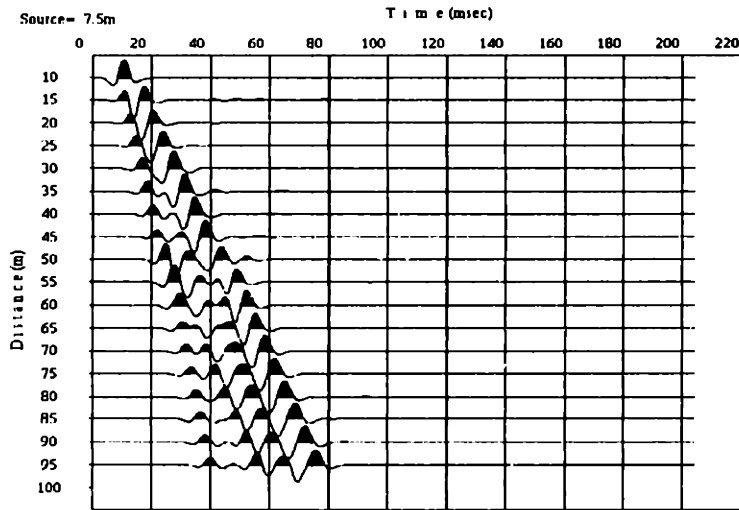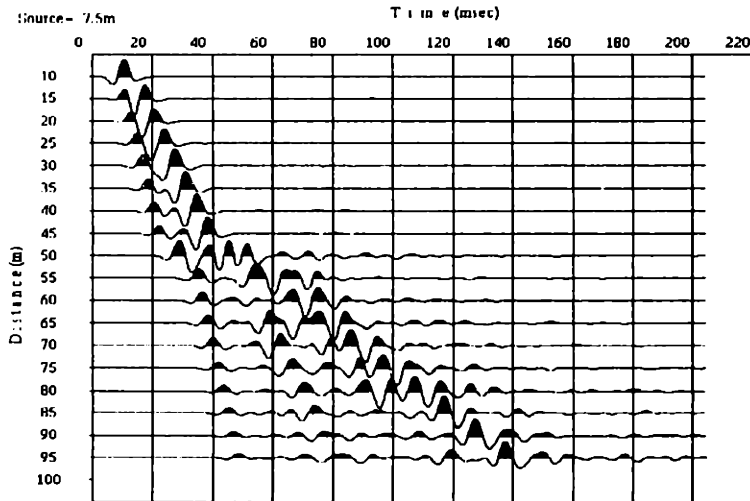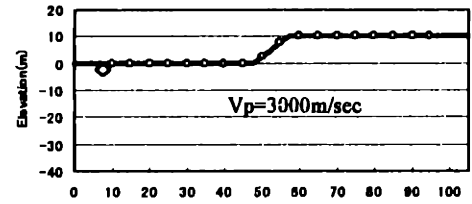
a) Two-layer model.

b) Two-layer model.
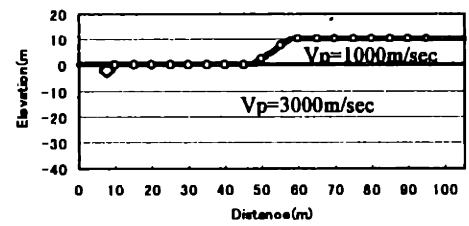
Figure 5.12: Comparison of a homogeneous model and a two-layer model with the presence of a step.

156
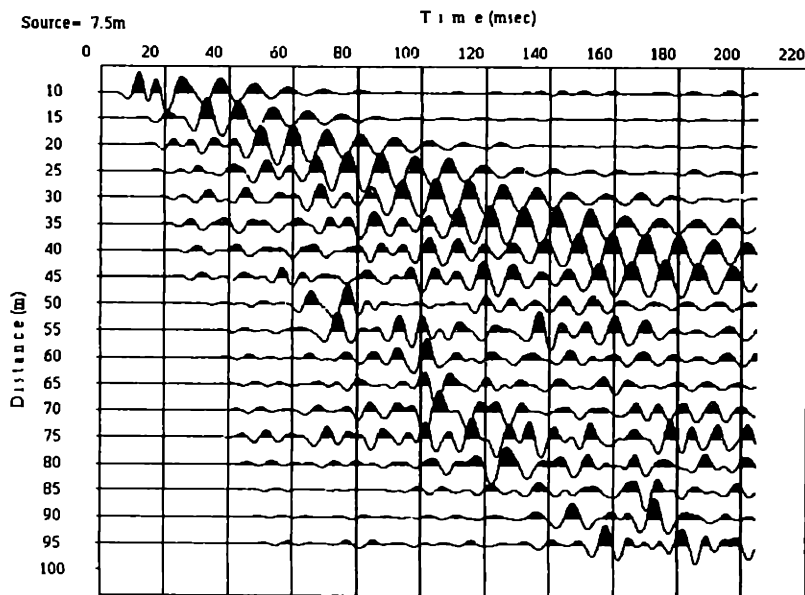
a) Thickness of the first layer is 2.5m.
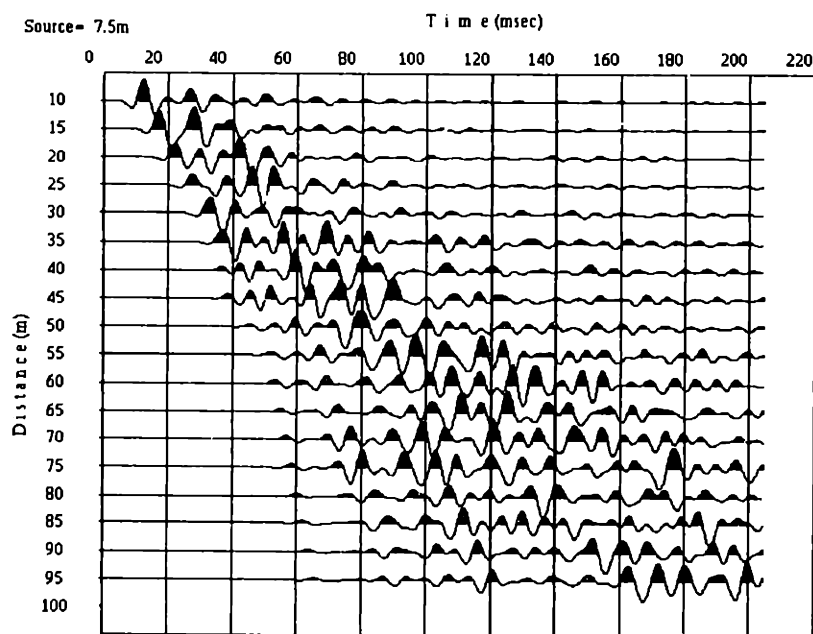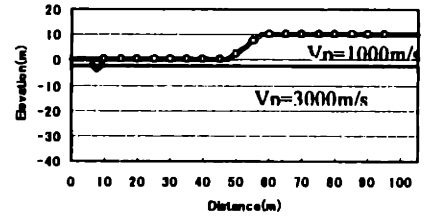
b) Thickness of the first layer is 10m.
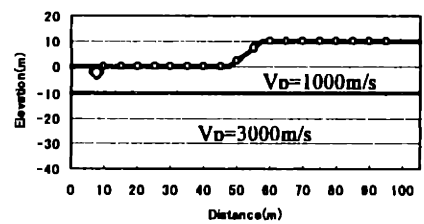
Figure 5.13: Waveforms for a two-layer model with the presence of a step.

157
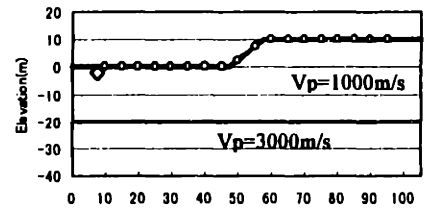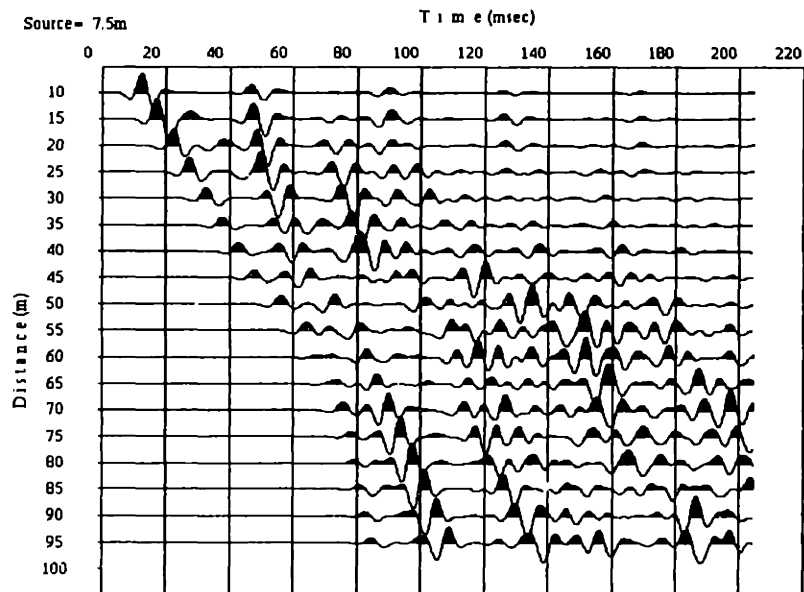
c) Thickness of the first layer is 20m.
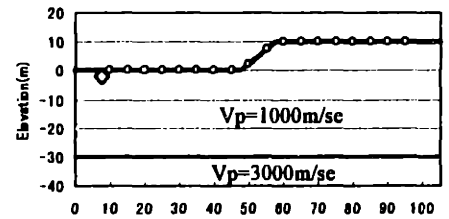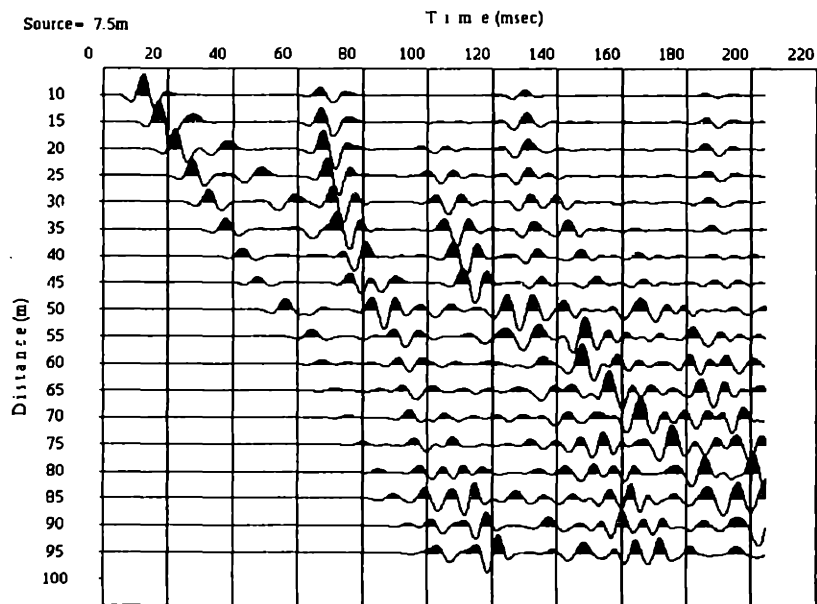
d) Thickness of the first layer is 30m.

Figure 5.13, continued:
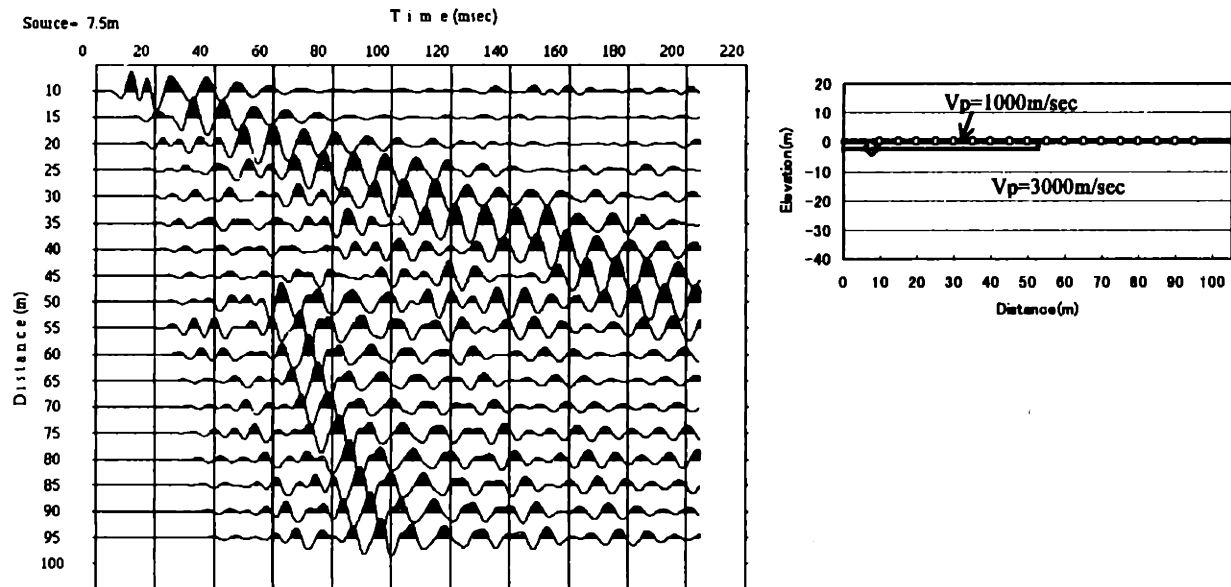
a) Normalized by each trace.
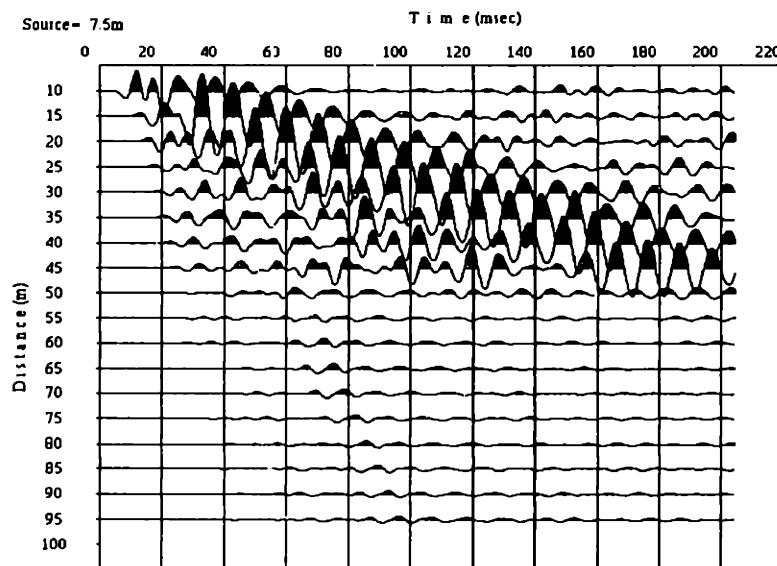
b) No normalized.

Figure 5.14: Waveforms for a two-layer model with the low velocity layer which placed only in the left half of the model.
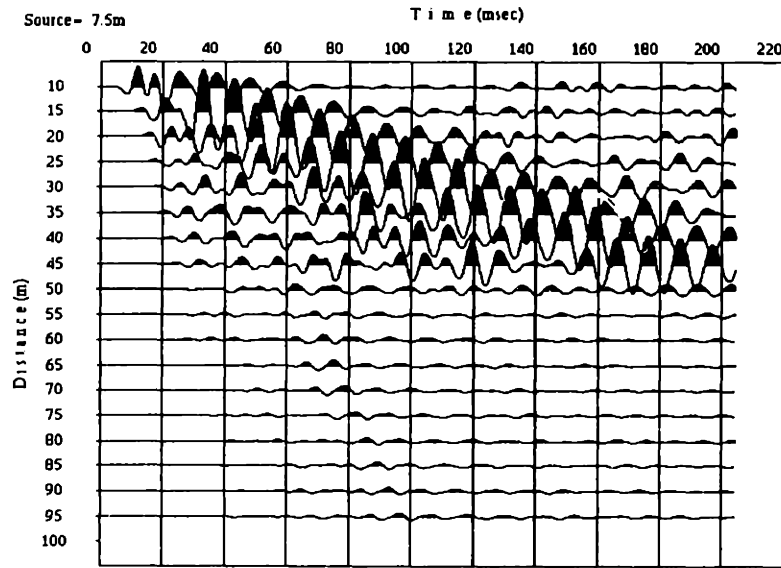
a) Low velocity layer is placed only in the left half of the model.
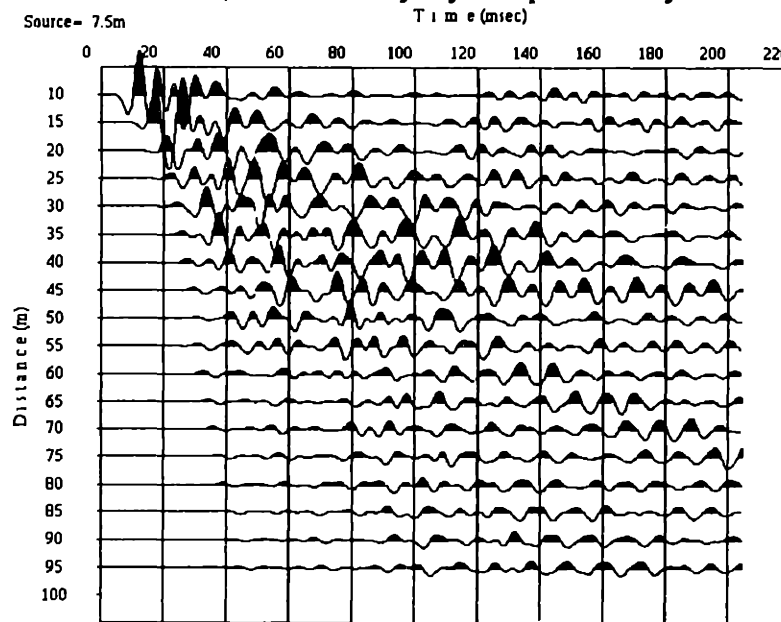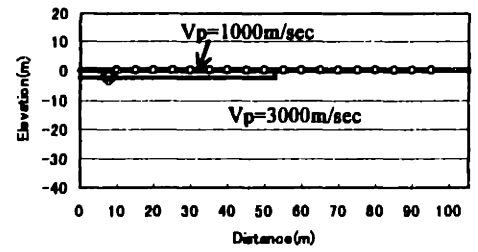
b) Low velocity layer continues to right side of the model.
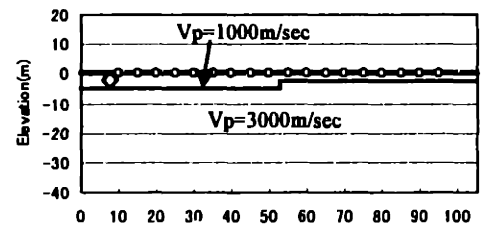
Figure 5.15: Waveforms for a two-layer model with the low velocity layer which has a step on the boundary. The waveforms are normalized by each trace.
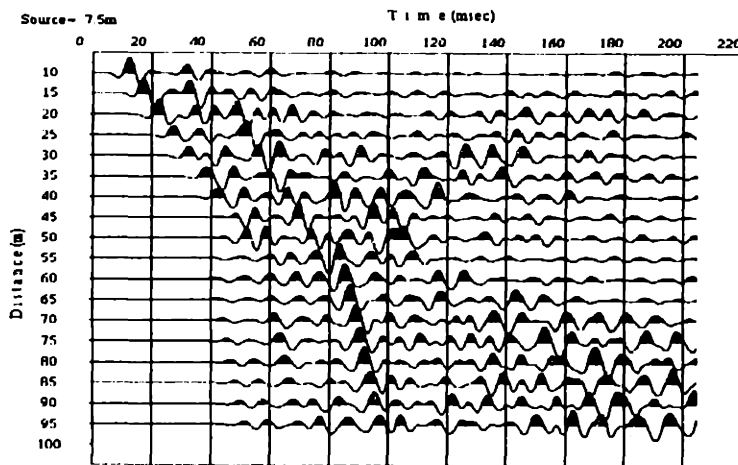
160
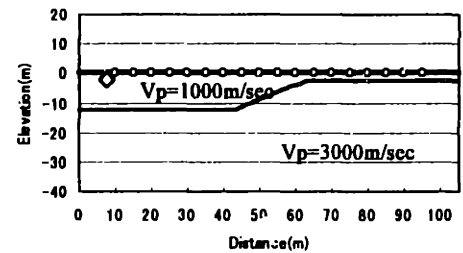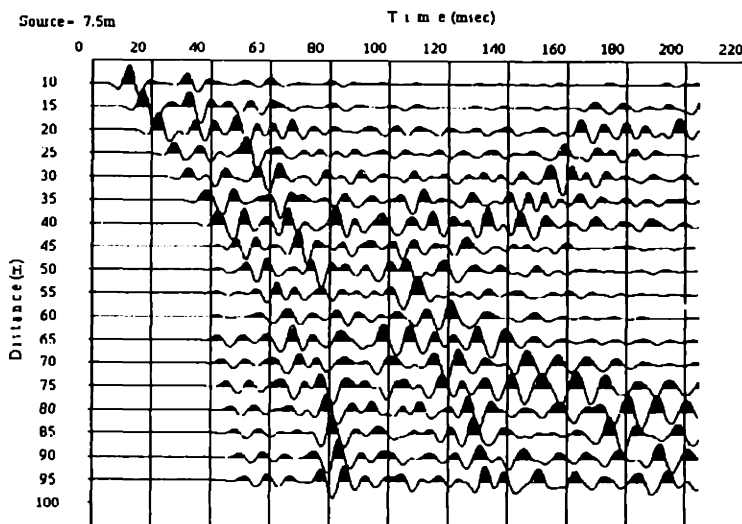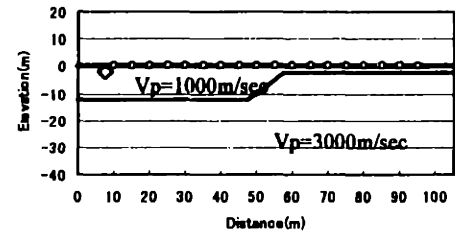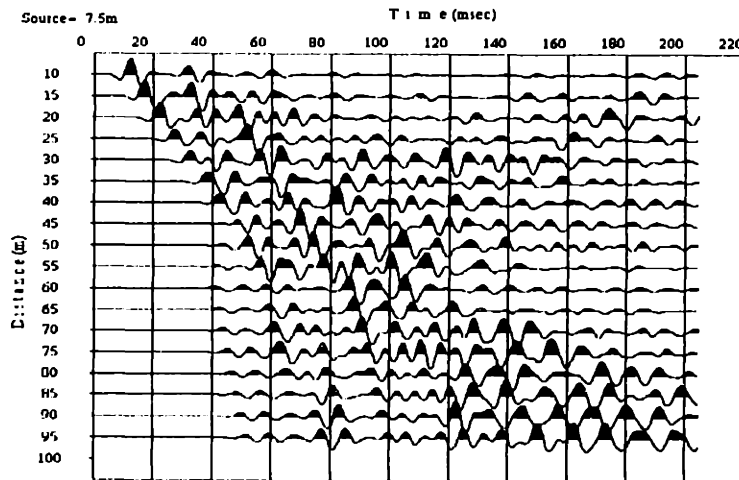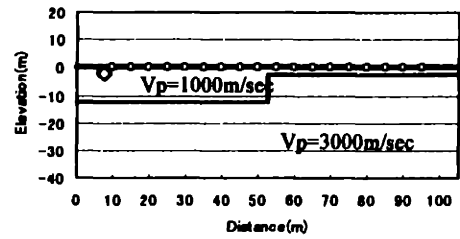
Figure5.16: Waveforms from the simulation with various step shapes.
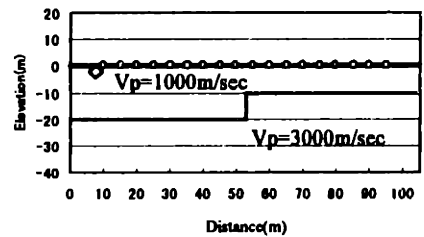
Figure5.16: continued
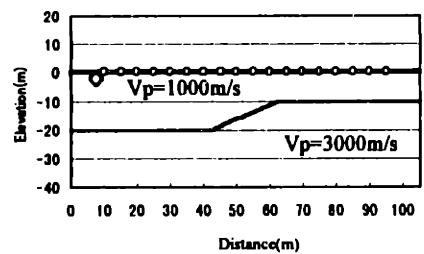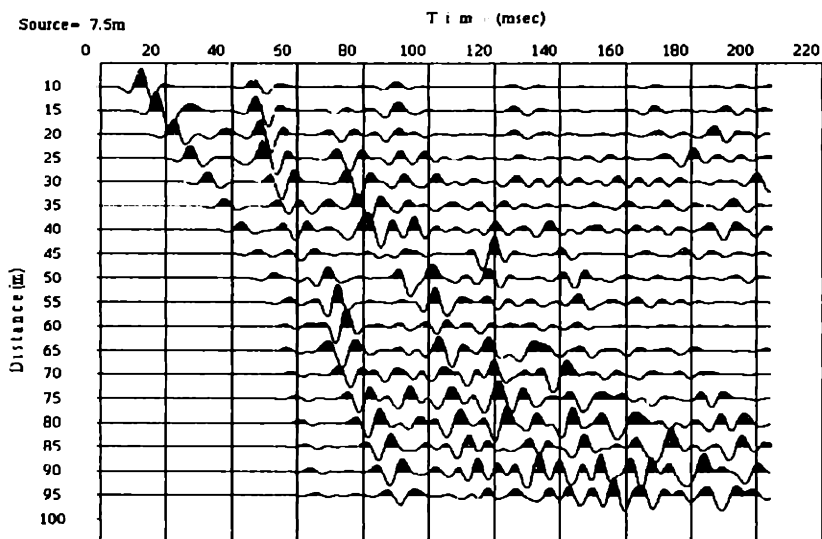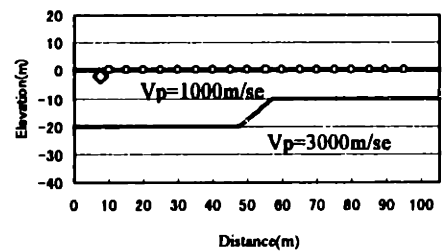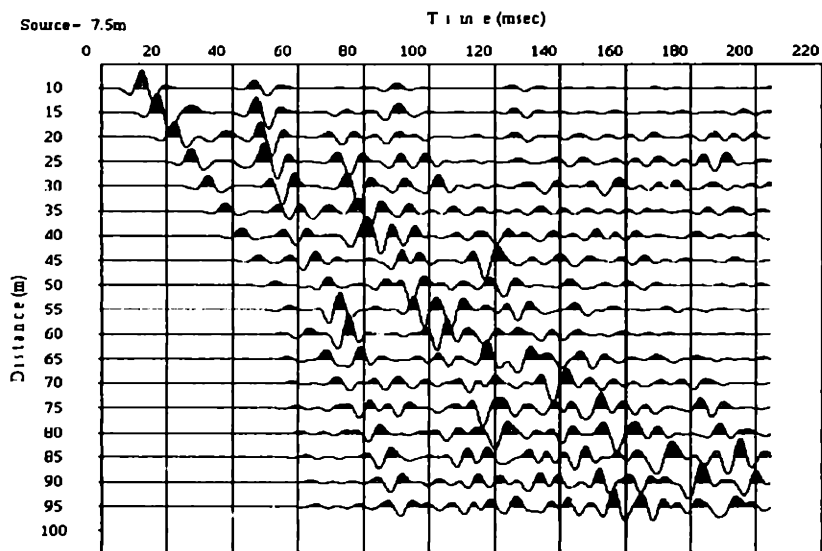
162

a) Flat surface model. The fault is located at a distance of 52.5m.
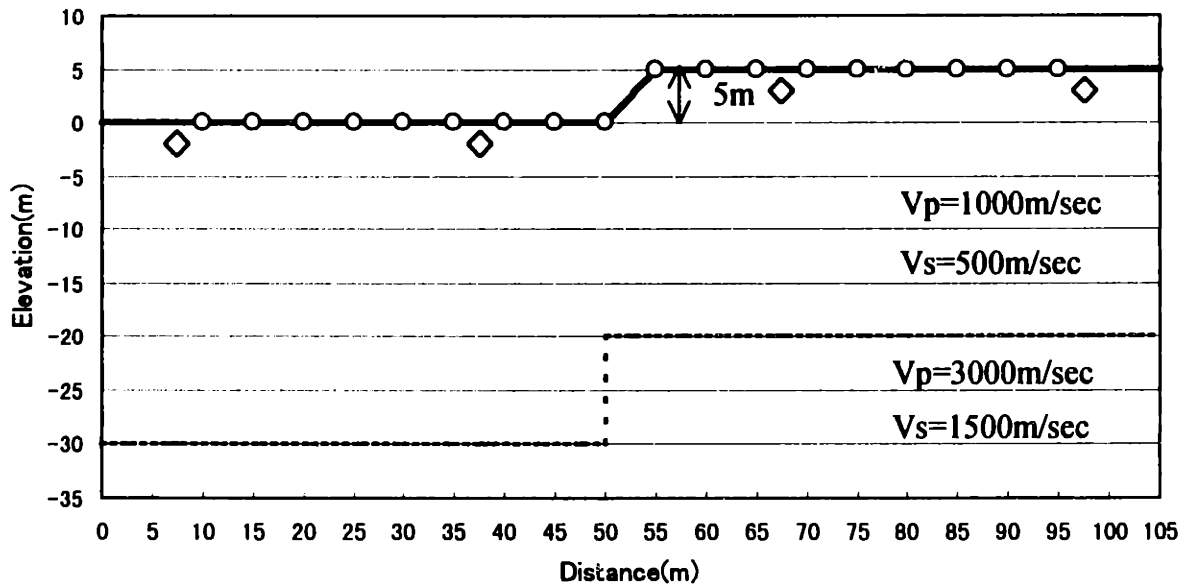
b) Step model. The fault is located at a distance of 50.0m.

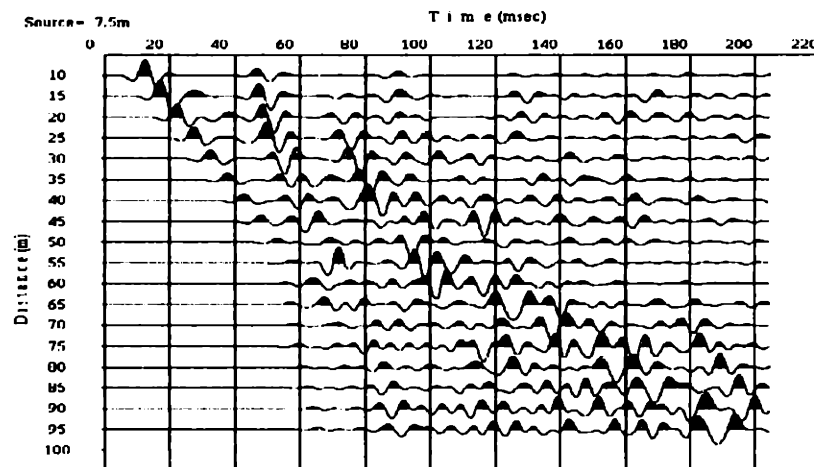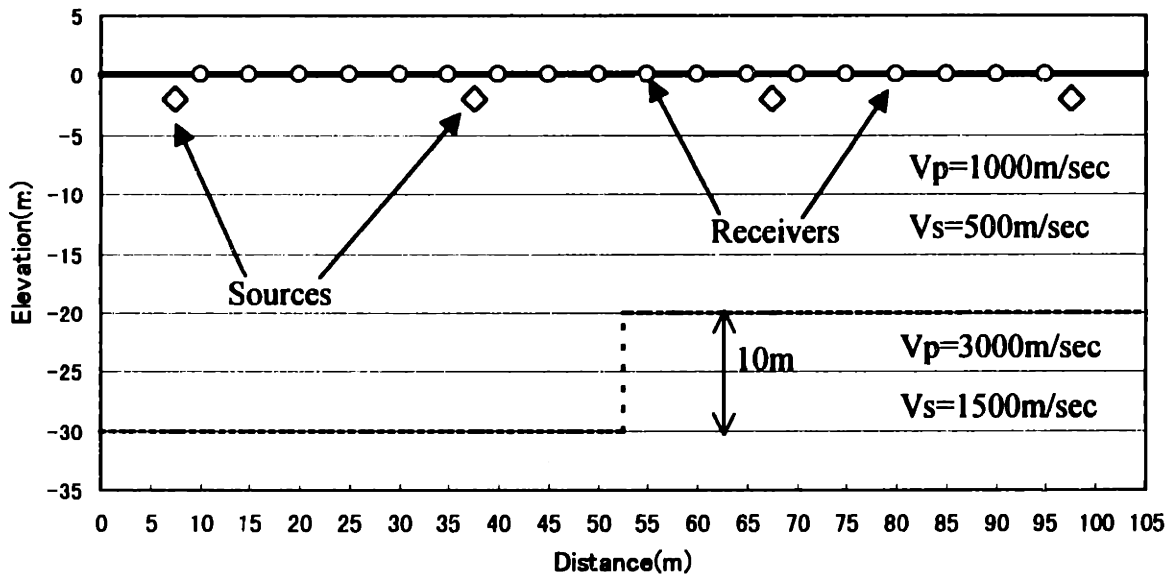Figure 5.17: Active fault models. The first model (a) has a flat surface and the second model (b) has a step on the surface. The deformation of bed rock (second layer) is 10m. The finite-difference calculation is performed for four different sources 7.5m, 37.5m, 67.5m and 97.5m. The fault is located at a distance of 52.5m in the flat model and 50.0m in the step model.
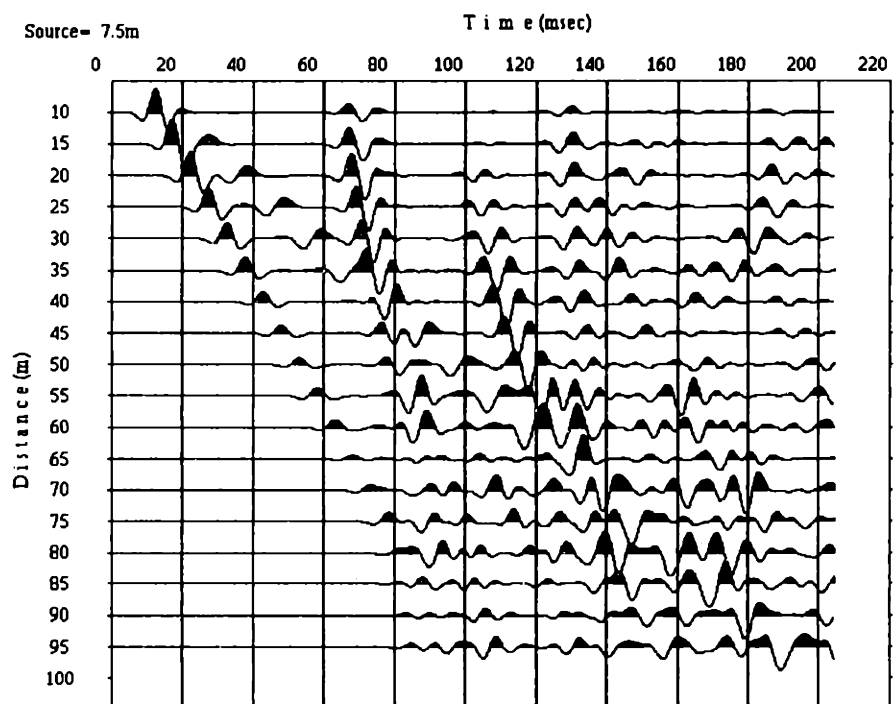
a) source=7.5m.
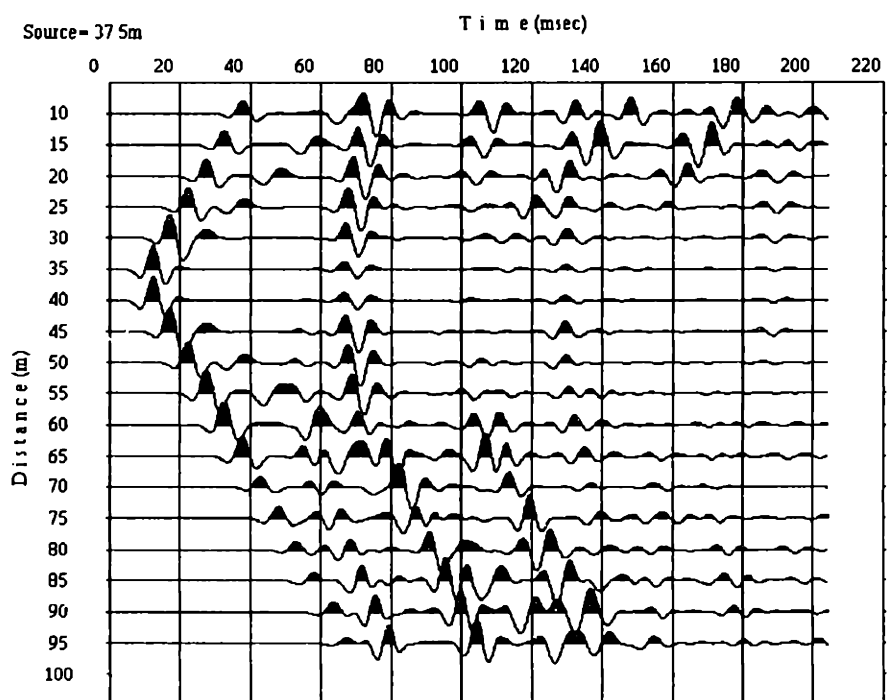
b) source=37.5m.

Figure 5.18: Waveforms from the flat surface model.

164
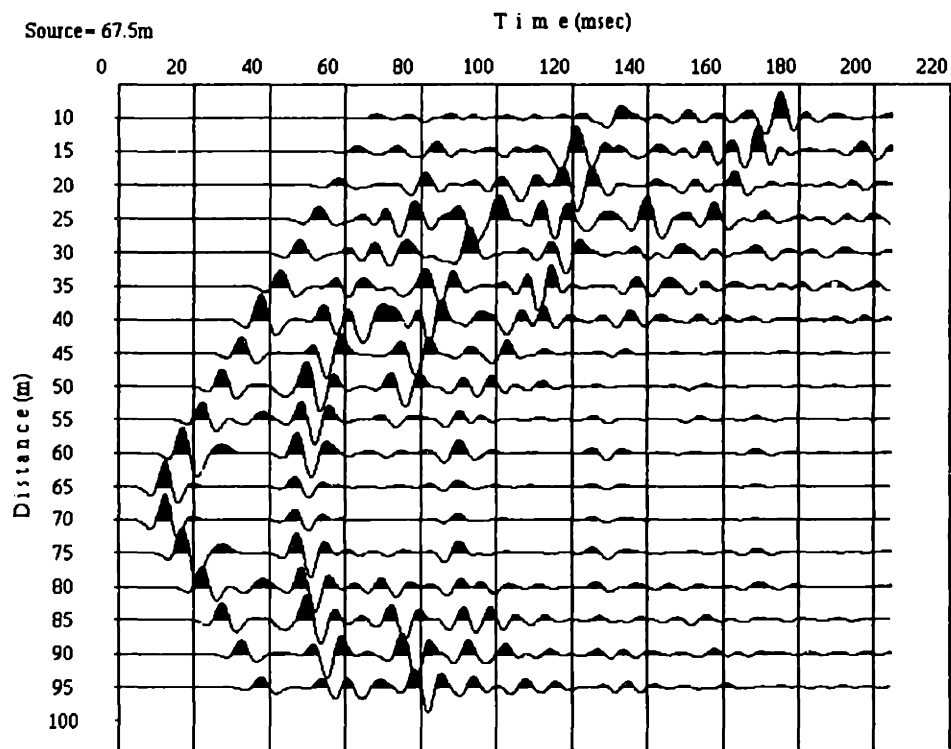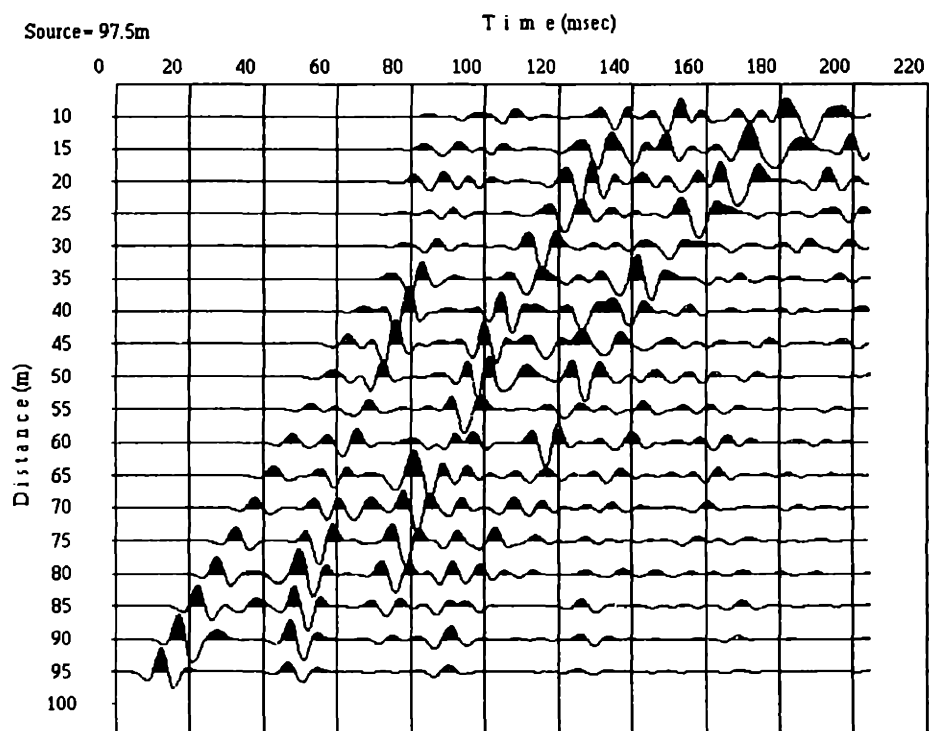
c) source=97.5m.

d) source=97.5m.

Figure 5.18, continued:

165
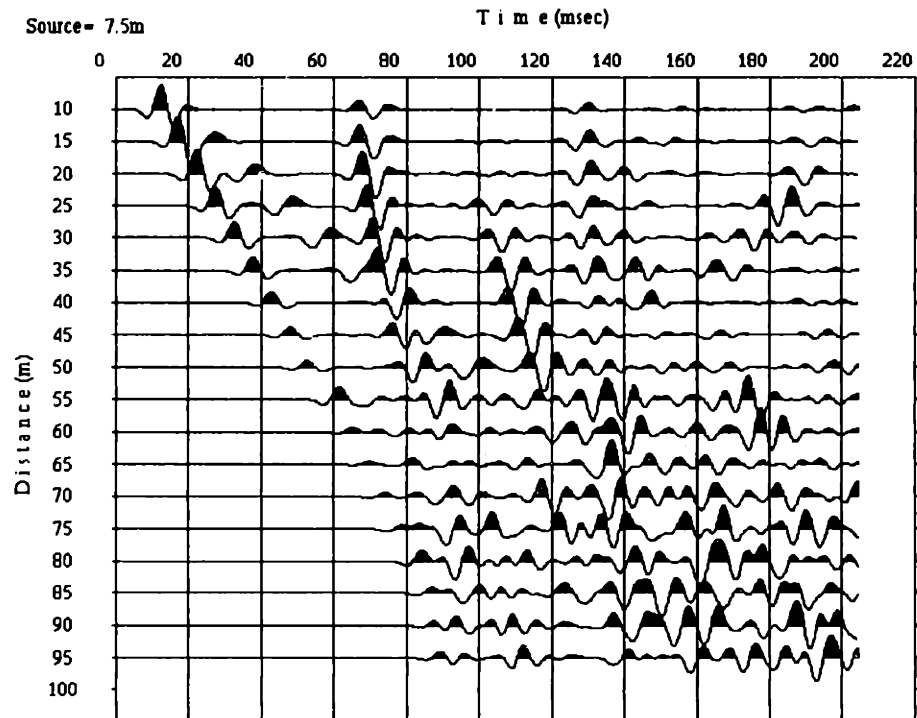
a) elastic model. source=7.5m.
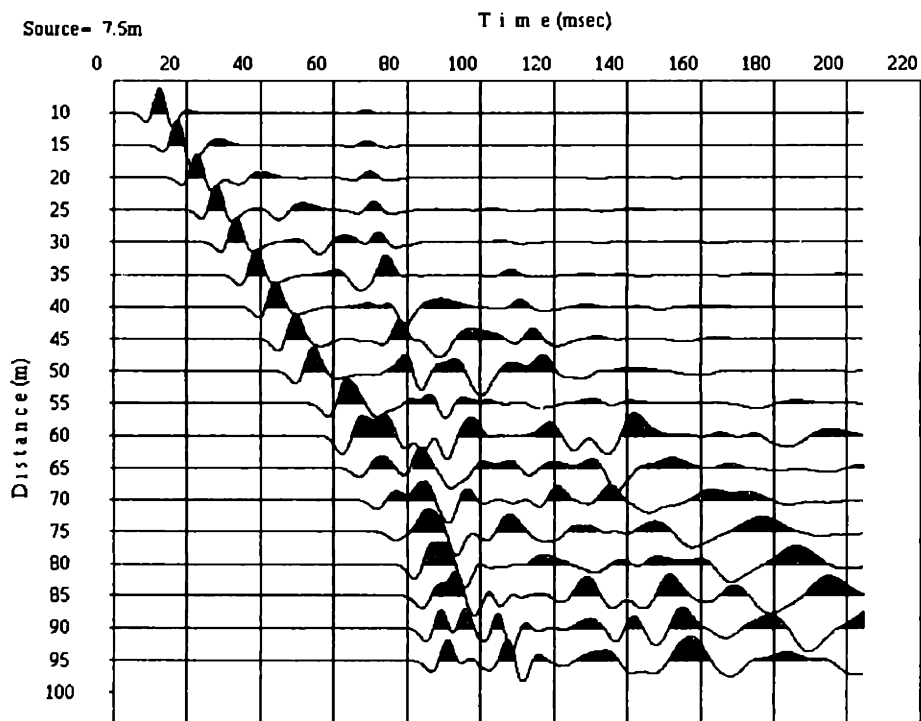
b) small Q model. source=7.5m.

Figure 5.19: Waveforms from the step model. Source =7.5m

166
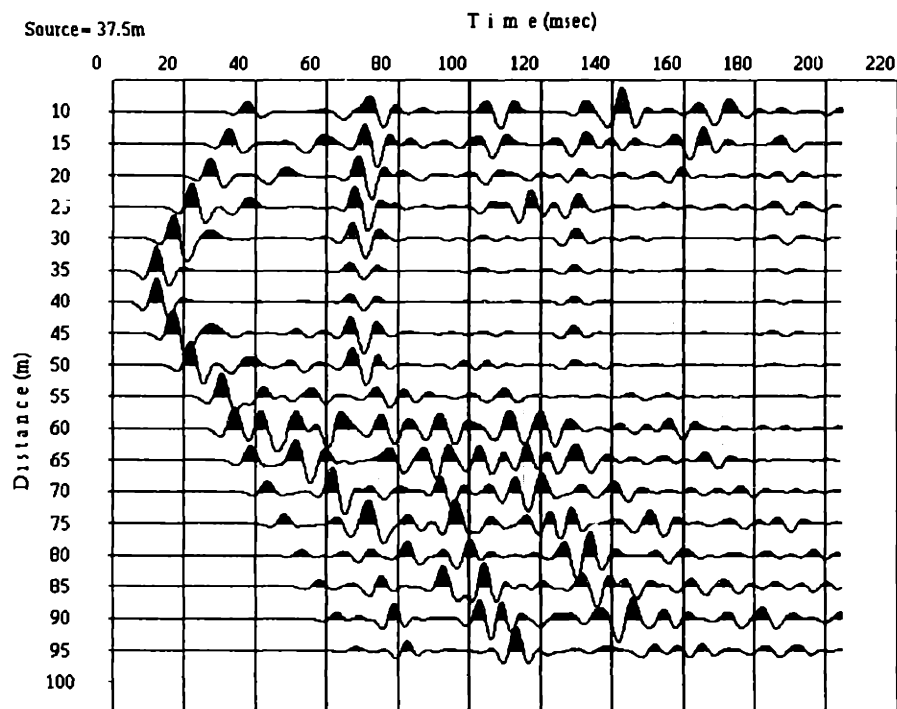
c) elastic model. source=37.5m.
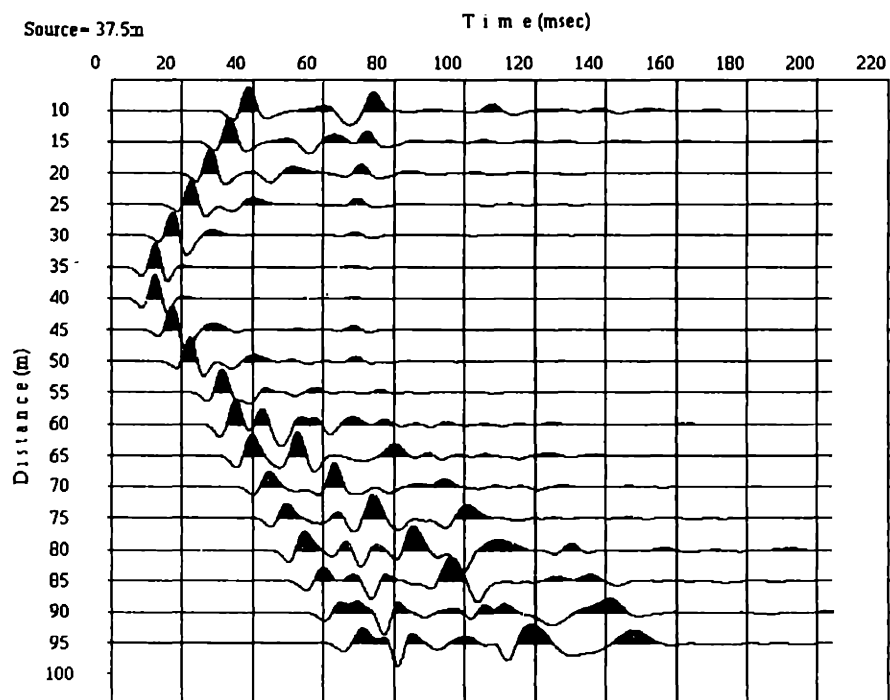
d) small Q model. source=37.5m.

Figure 5.19, continued: Source =37.5m

167
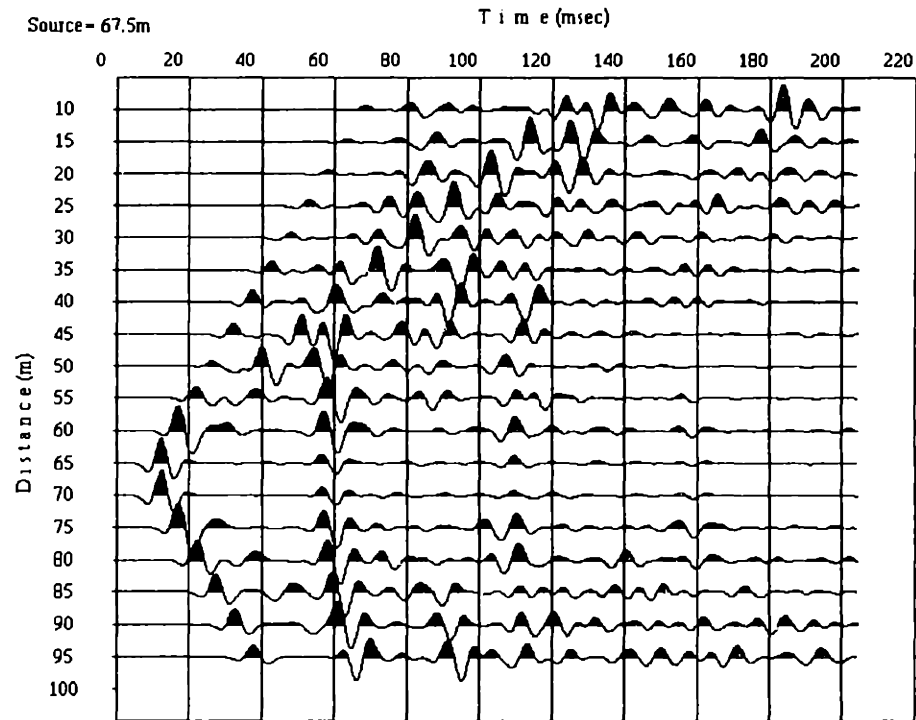
e) elastic model. source=67.5m.
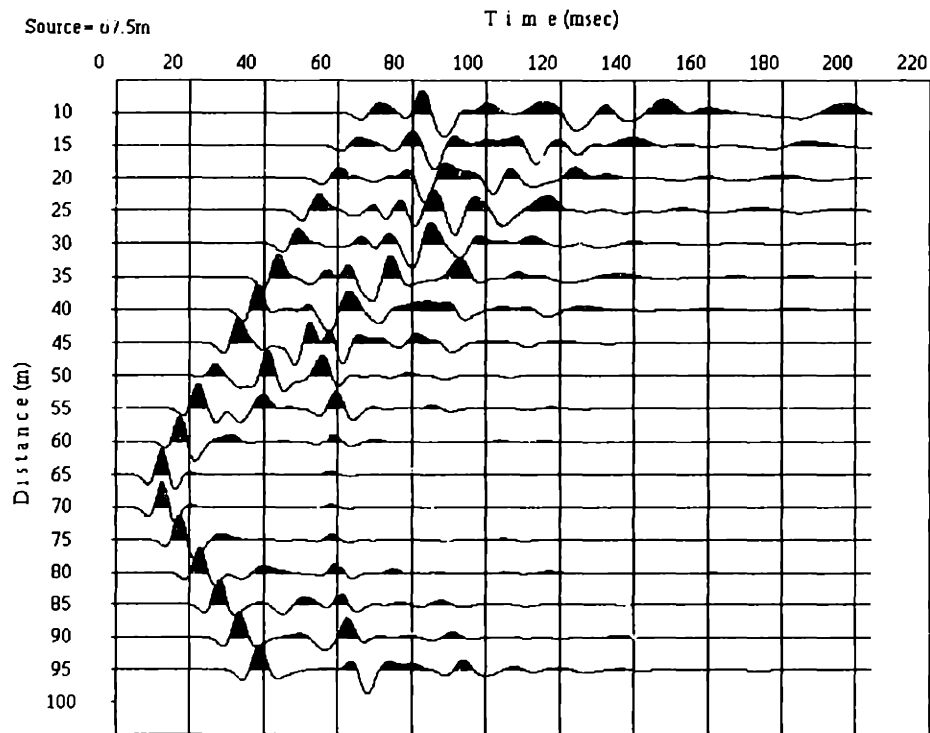
f) small Q model. source=67.5m.

Figure 5.19, continued: Source =67.5m

168
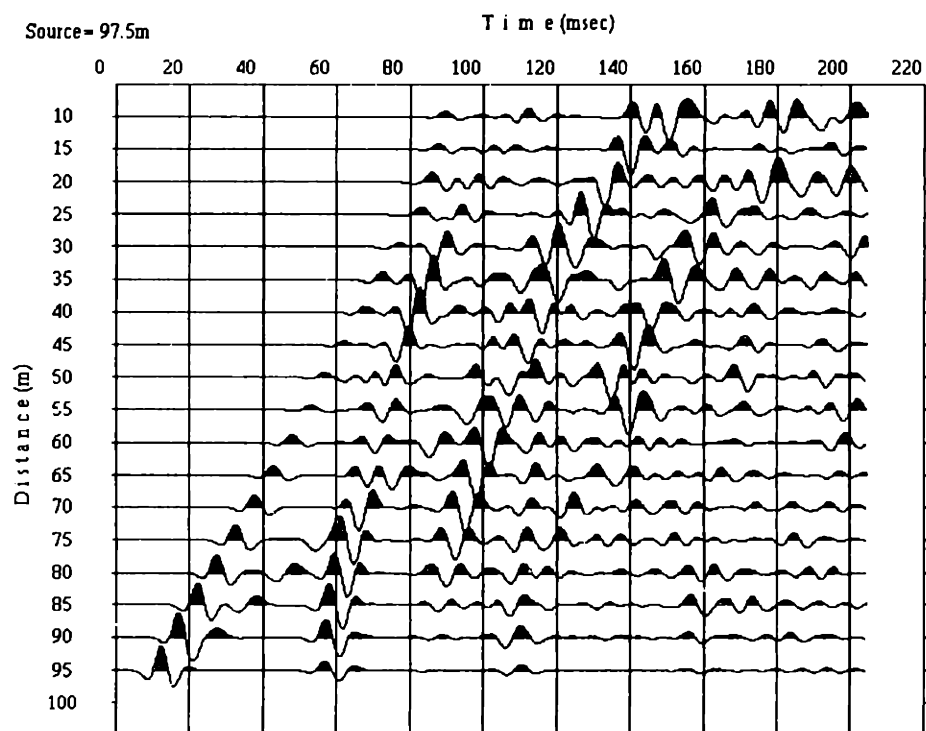
g) elastic model. source=97.5m.
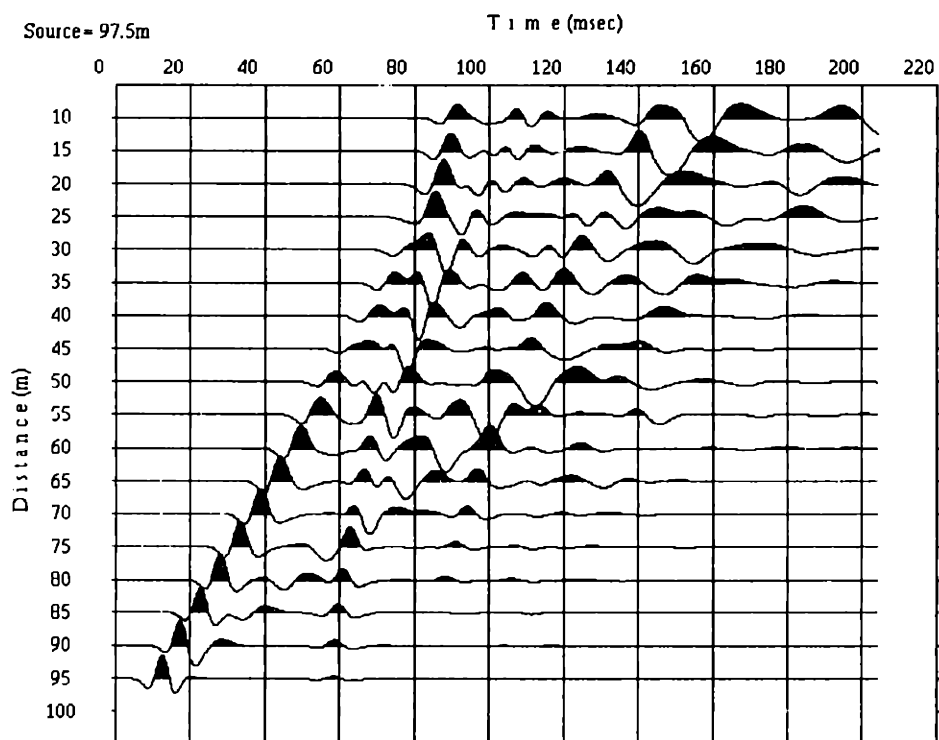
h) small Q model. source=97.5m.

Figure 5.19, continued: Source =97.5m

169
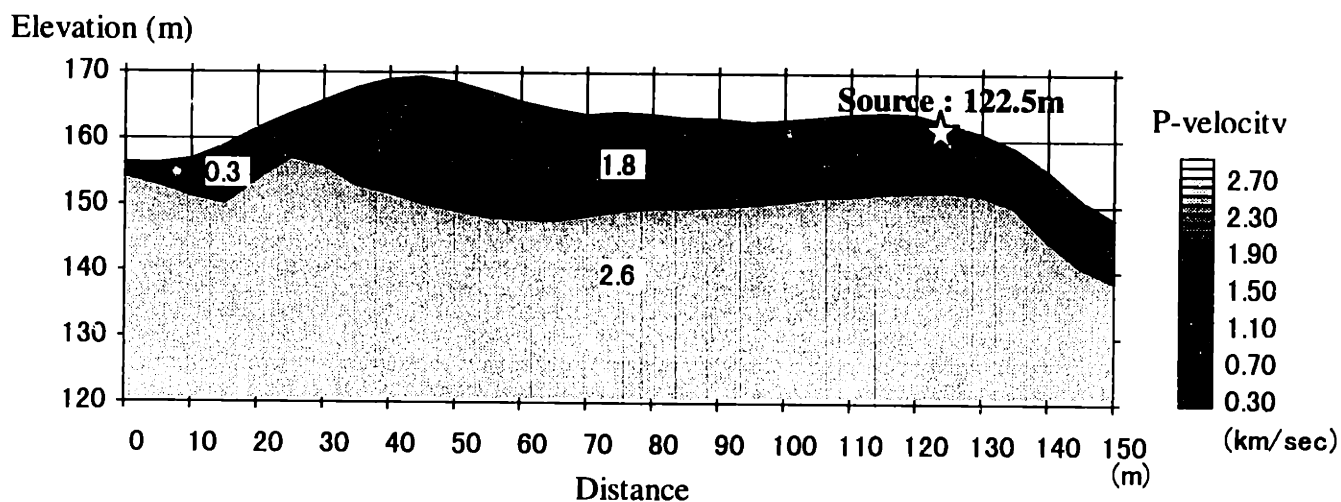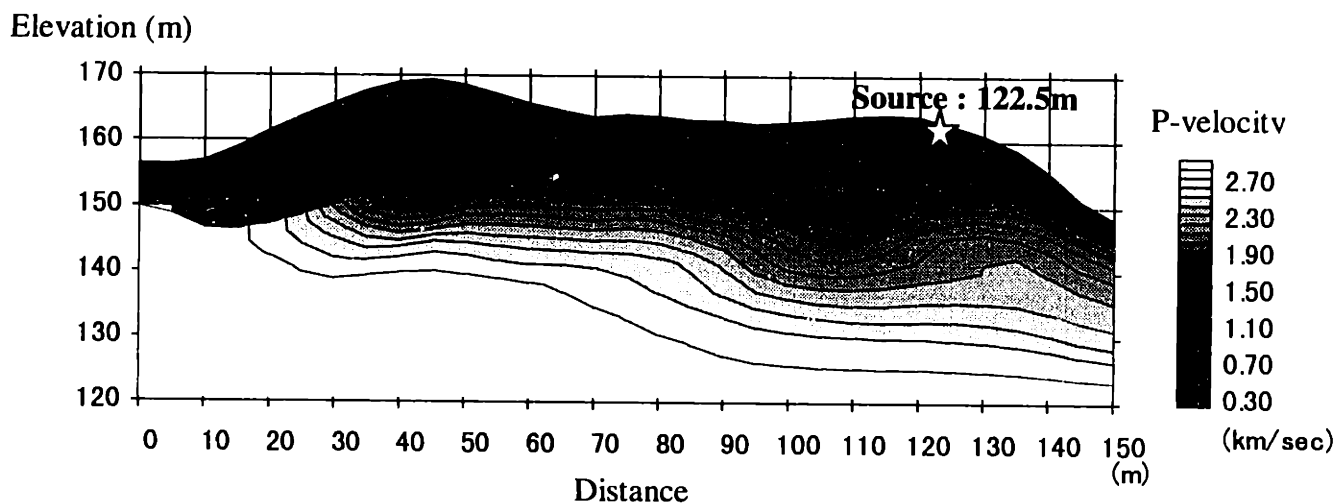
a) Three-layer model

b) Smooth model

Figure 5.20 : P-velocity tomogram obtained by the refraction traveltime tomography. a) A velocity model with the assumption that the velocity structure is a three-layer model. b) A velocity model with the assumption that the velocity is increasing with depth smoothly.
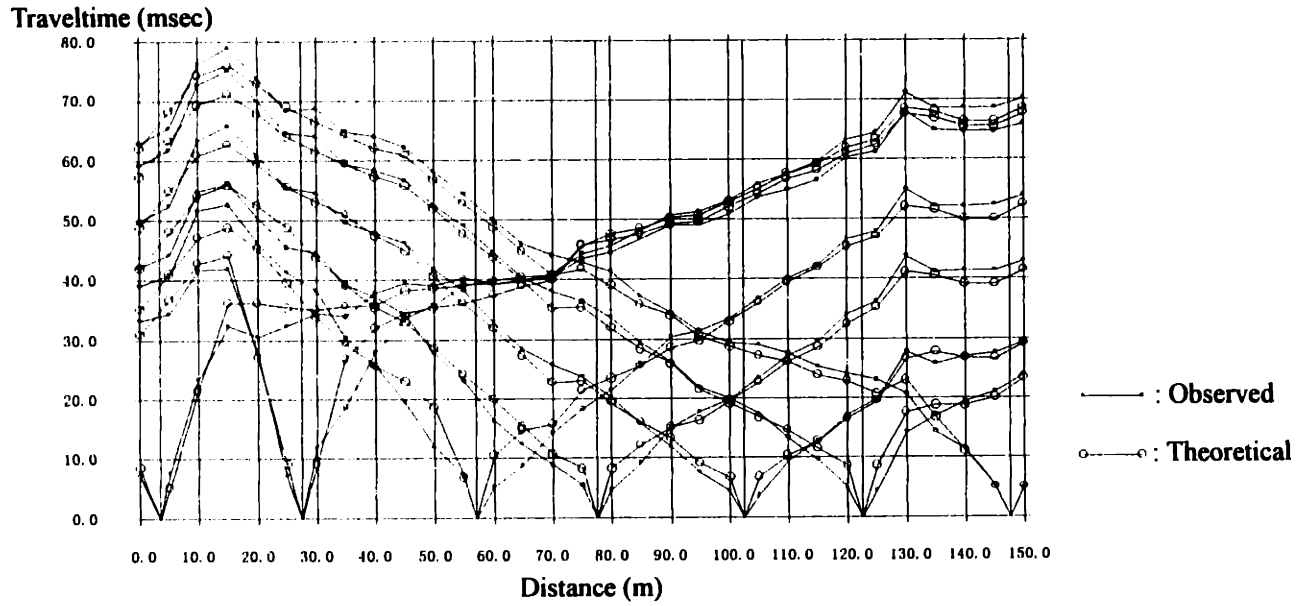
a) Three-layer model (Figure 5.20 a)
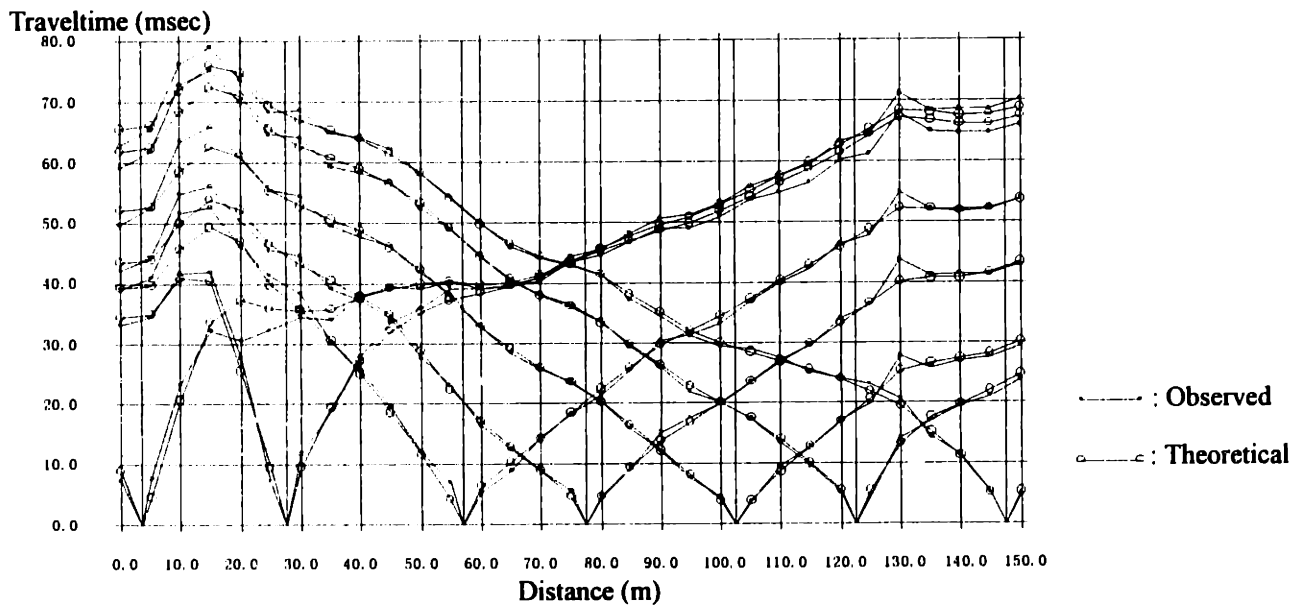
b) Smooth model (Figure 5.20 b)

Figure 5.21: Comparison of the observe and theoretical traveltime data.
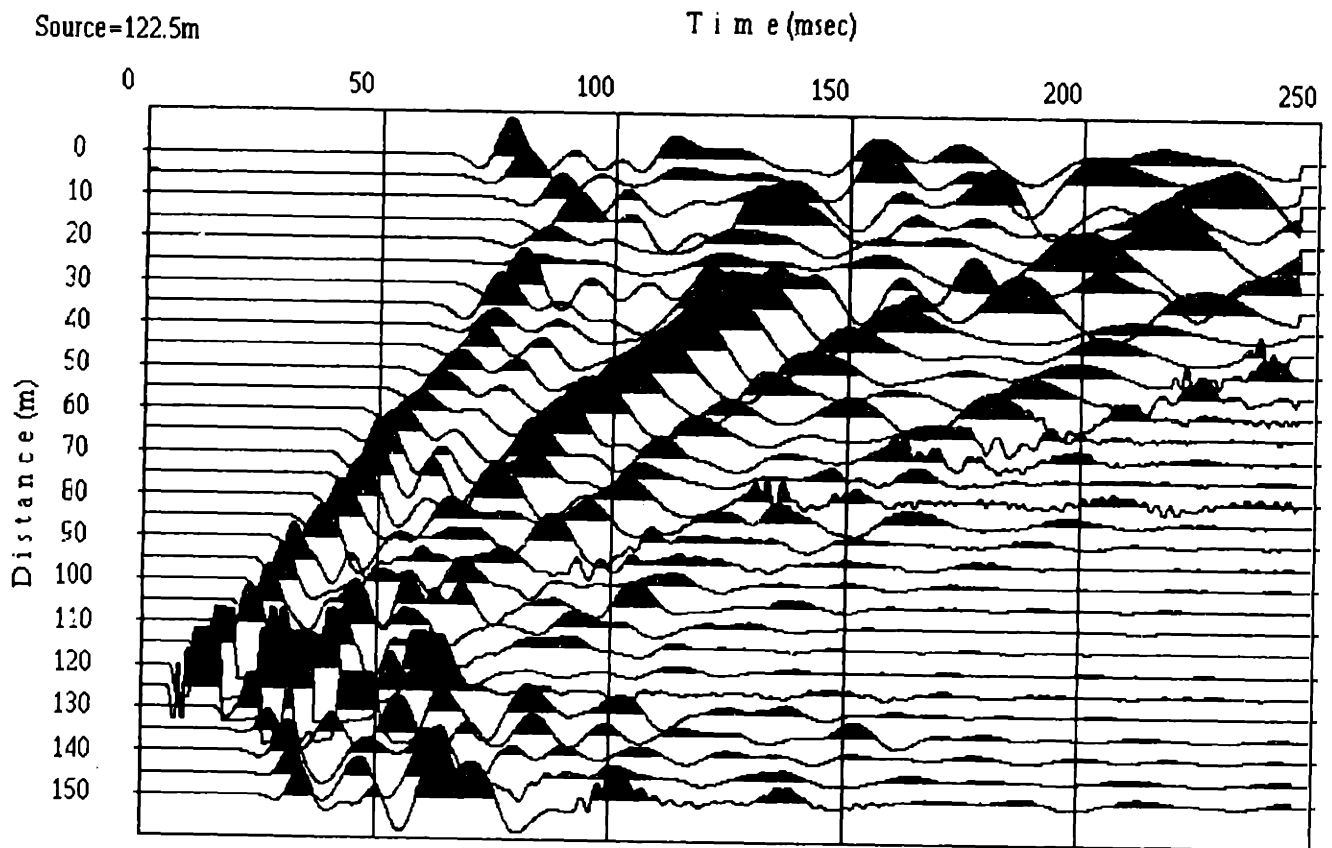
Figure 5.22: Example of observed common source data. A source location is 122.5m. A source depth is about 1m. The quantity of is 100g. A particle velocity (vertical component) is plotted.

Source=122.5m

T i m e (msec)

a) Observed data

Source=122.5m

T i m e (msec)

b) Q=10000

Source=122.5m

T i m e (msec)

c) Q=5 (Vp < 2000m/sec) and Q=100 (Vp ≥ 2000m/sec)

Figure 5.23 Comparison of theoretical data with observed data (layered model)
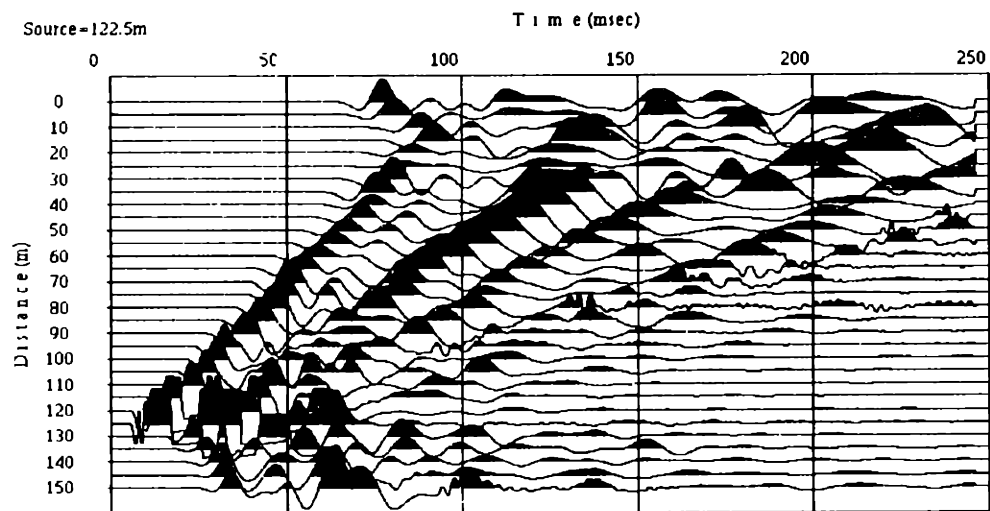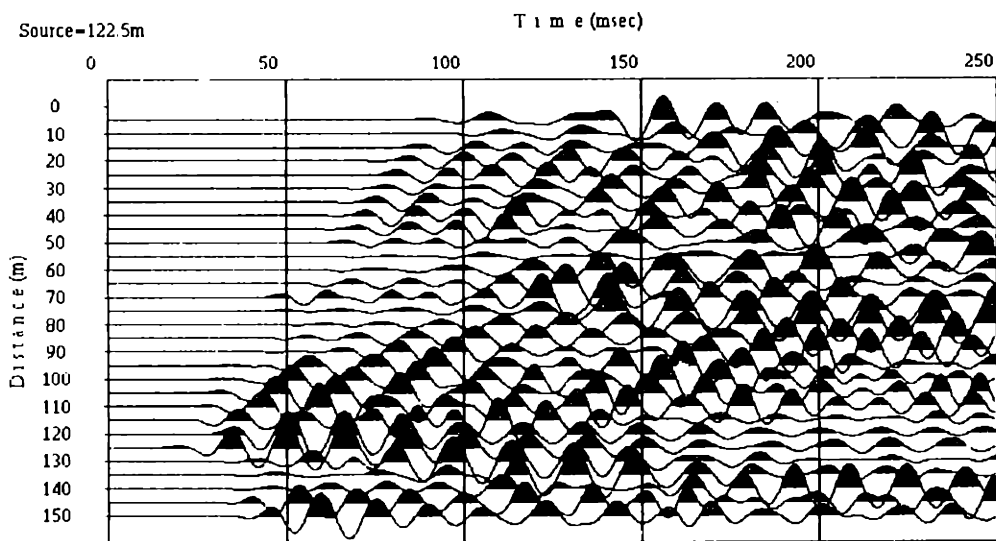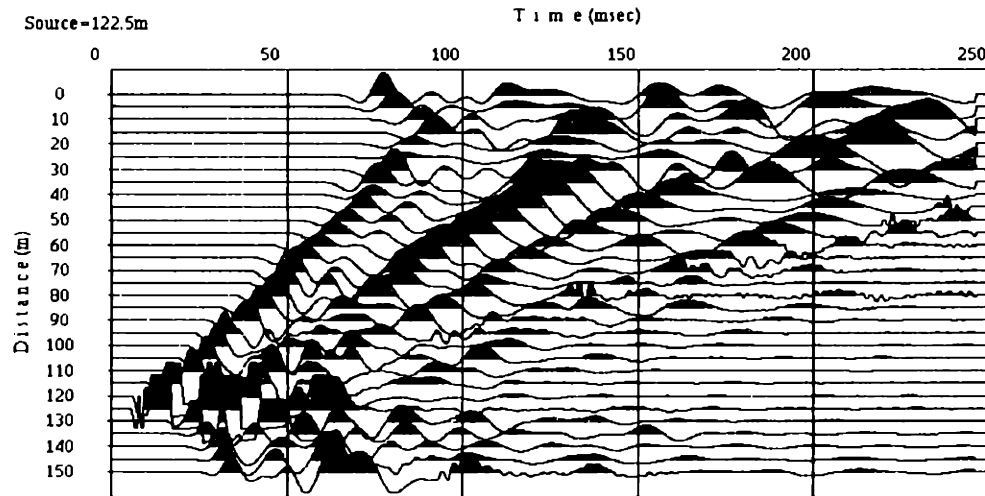
a) Observed data
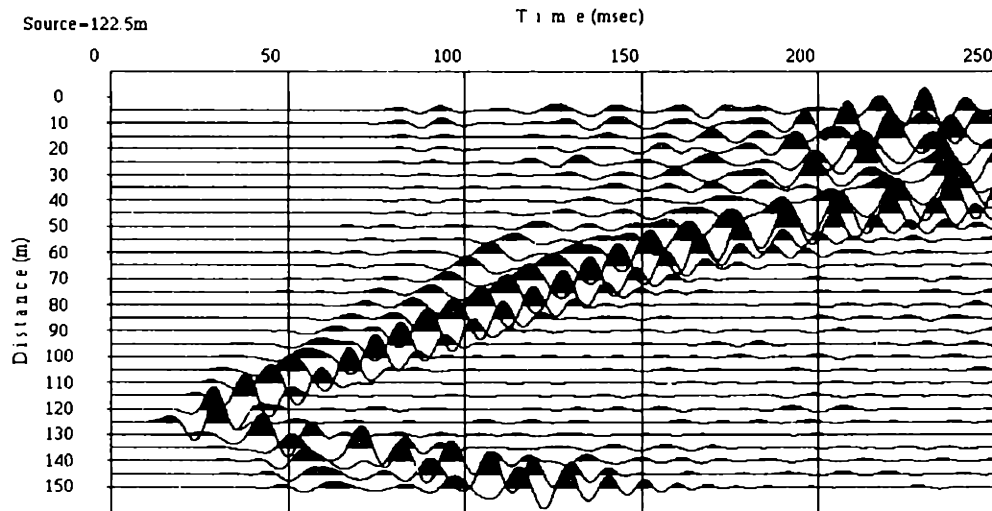
b) Q=10000
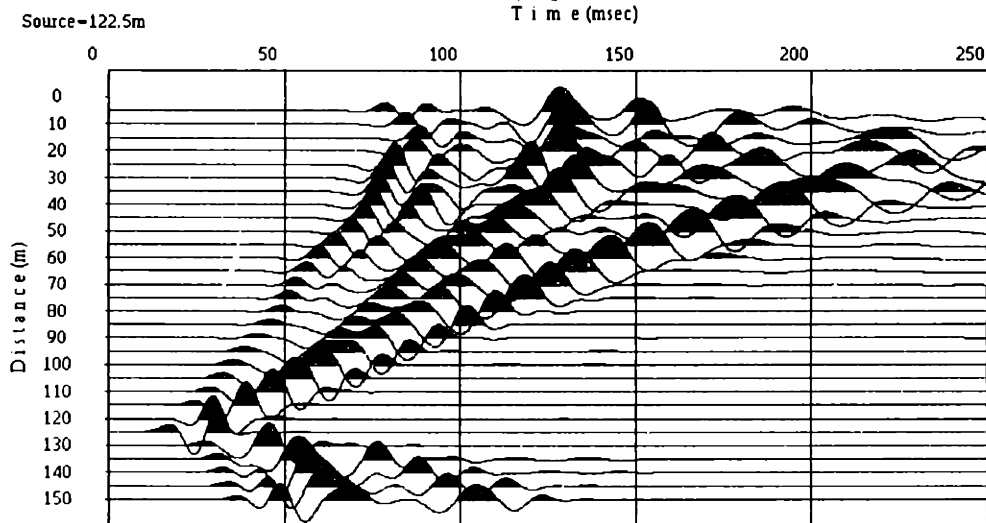
c) Q=5 (Vp < 2000m/sec) and Q=100 (Vp ≧ 2000m/sec)

Figure 5.24 Comparison of theoretical data with observed data (smooth model)

174
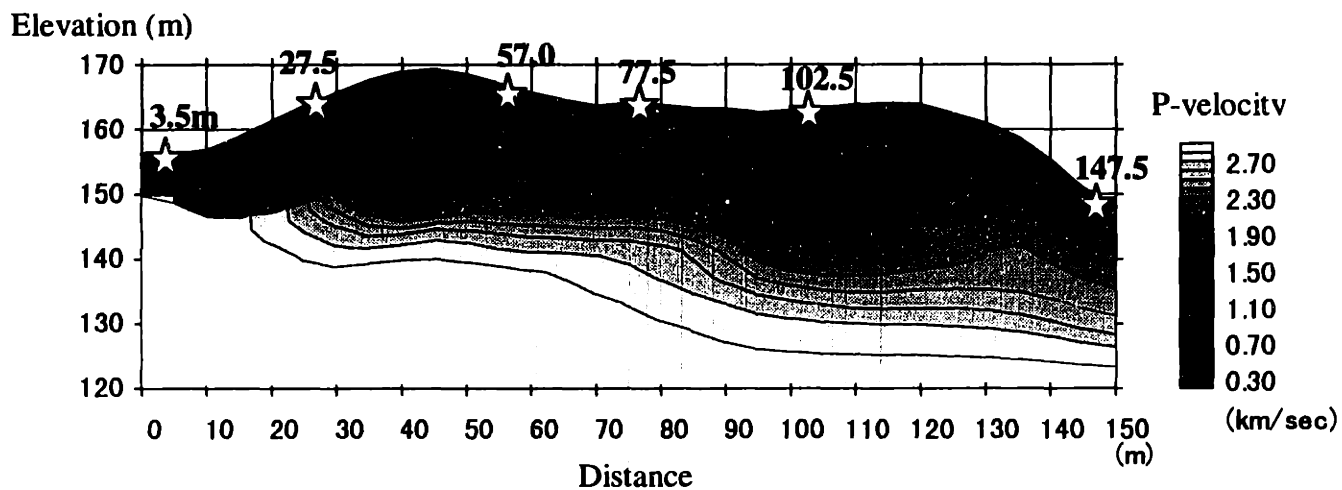
Figure 5.25: Source locations and P-velocity model. The sources are placed at the depth of 1m and a 50Hz Ricker wavelet is used as a source wavelet.
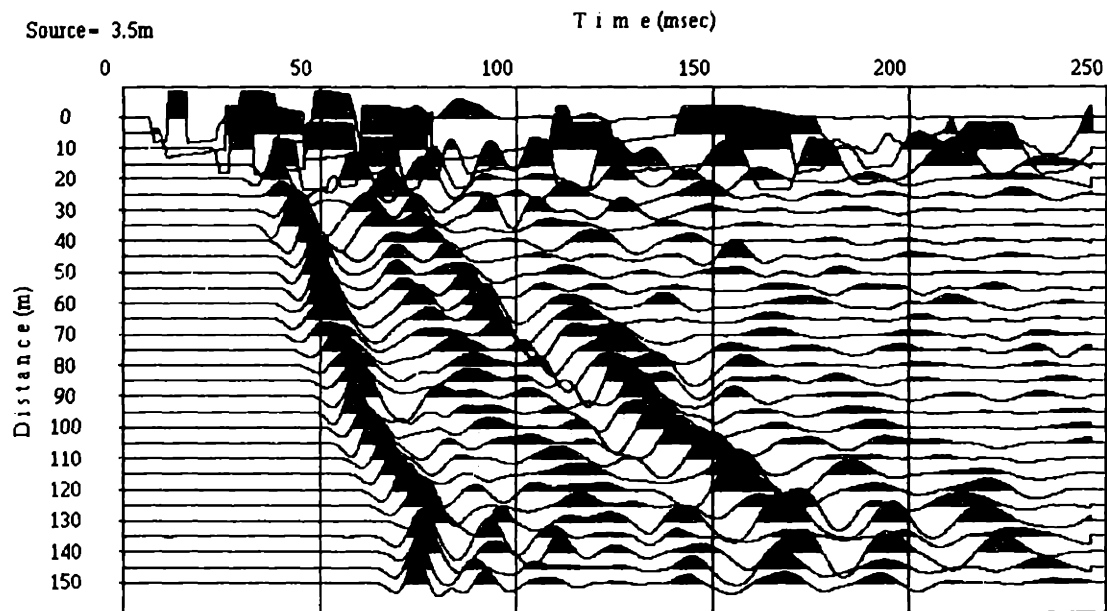
a) Observed data (Source=3.5m)
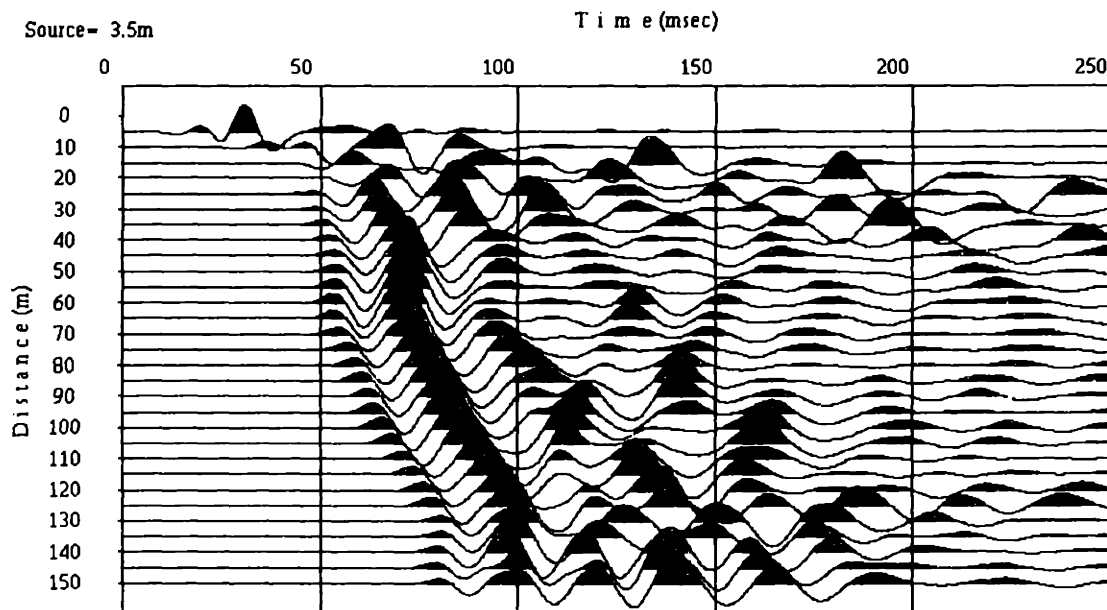
b) Theoretical data (Source=3.5m)

Figure 5.26: Comparison of observed data and theoretical data.
(Source=3.5m)

T i m e (msec)
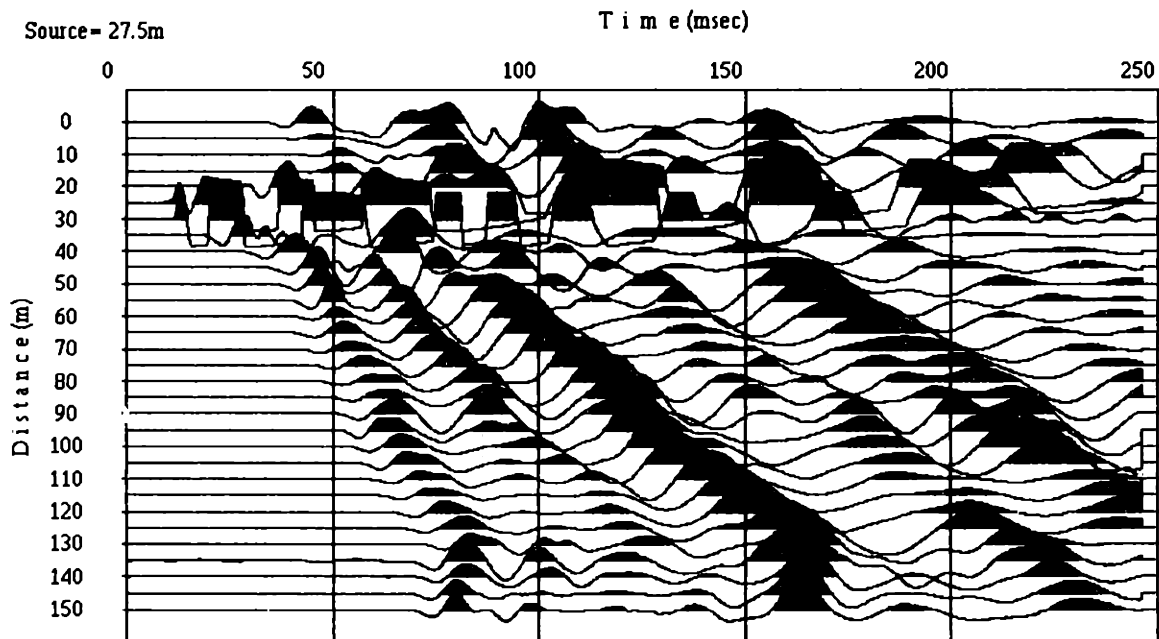
c) Observed data (Source=27.5m)

T i m e (msec)
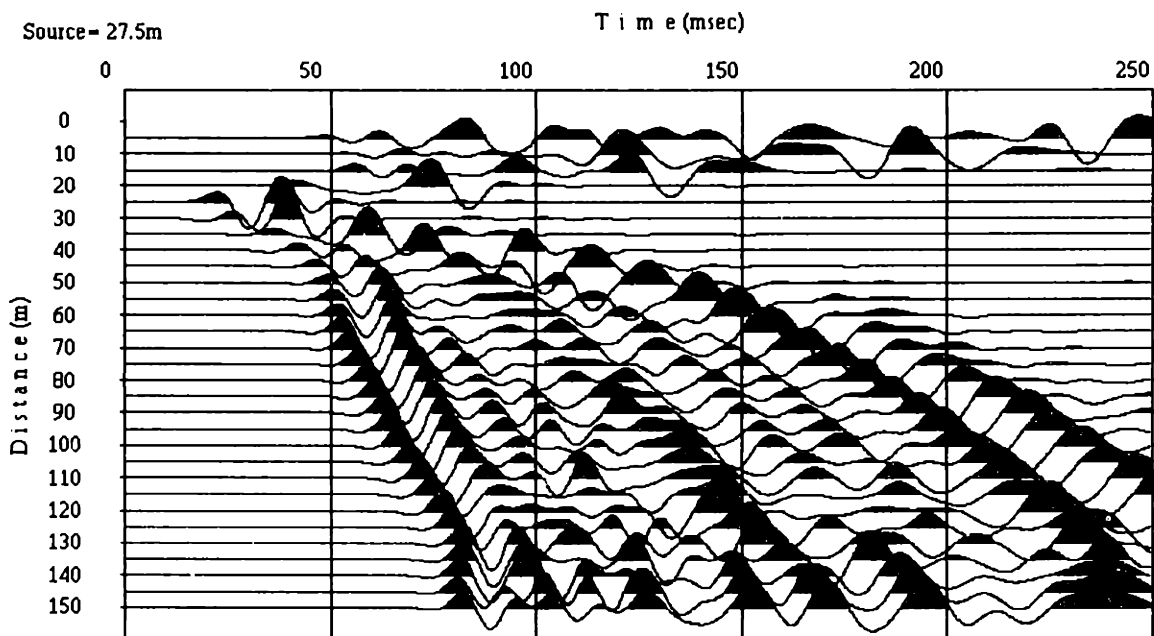
d) Theoretical data (Source=27.5m)

Figure 5.26 continued: Comparison of observed data and theoretical data.
(Source=27.5m)

Source= 57.0m

T i m e (msec)
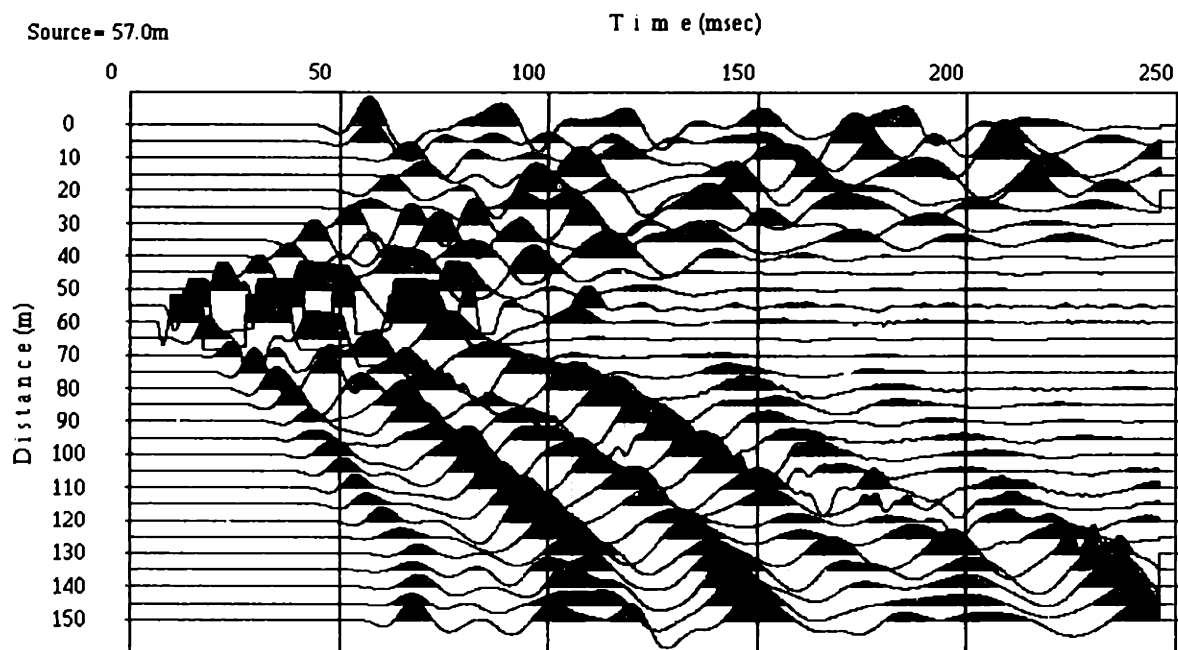
e) Observed data (Source=57.0m)

Source= 57.0m

T i m e (msec)
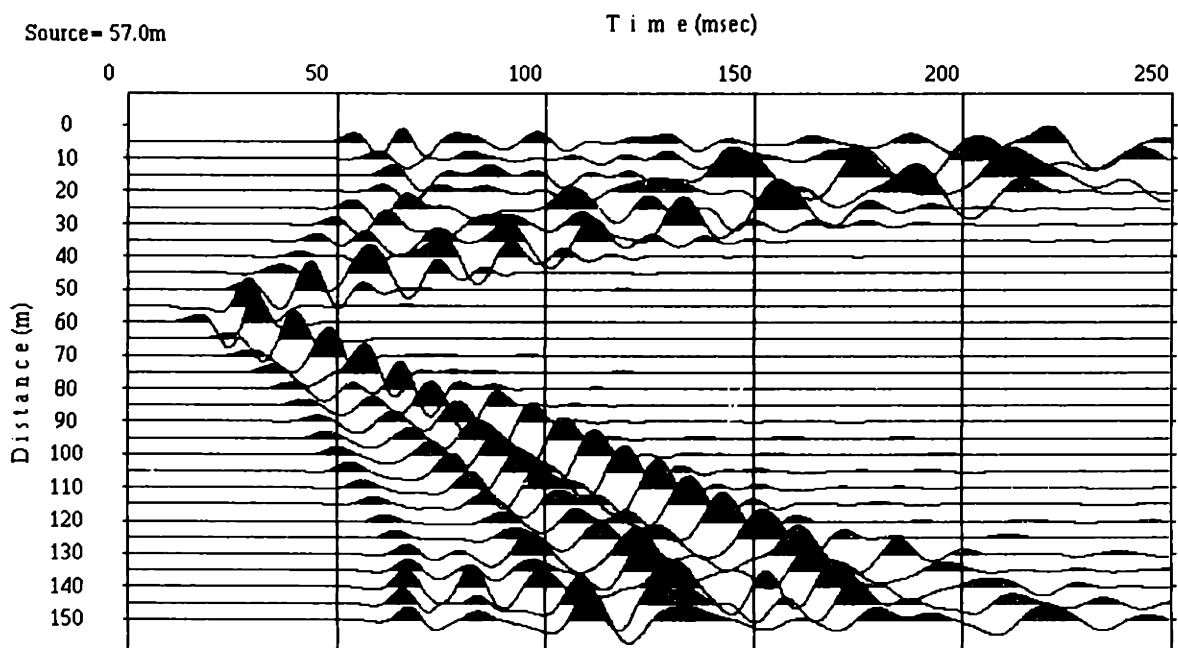
f) Theoretical data (Source=57.0m)

Figure 5.26 continued: Comparison of observed data and theoretical data.
(Source=57.0m)

178
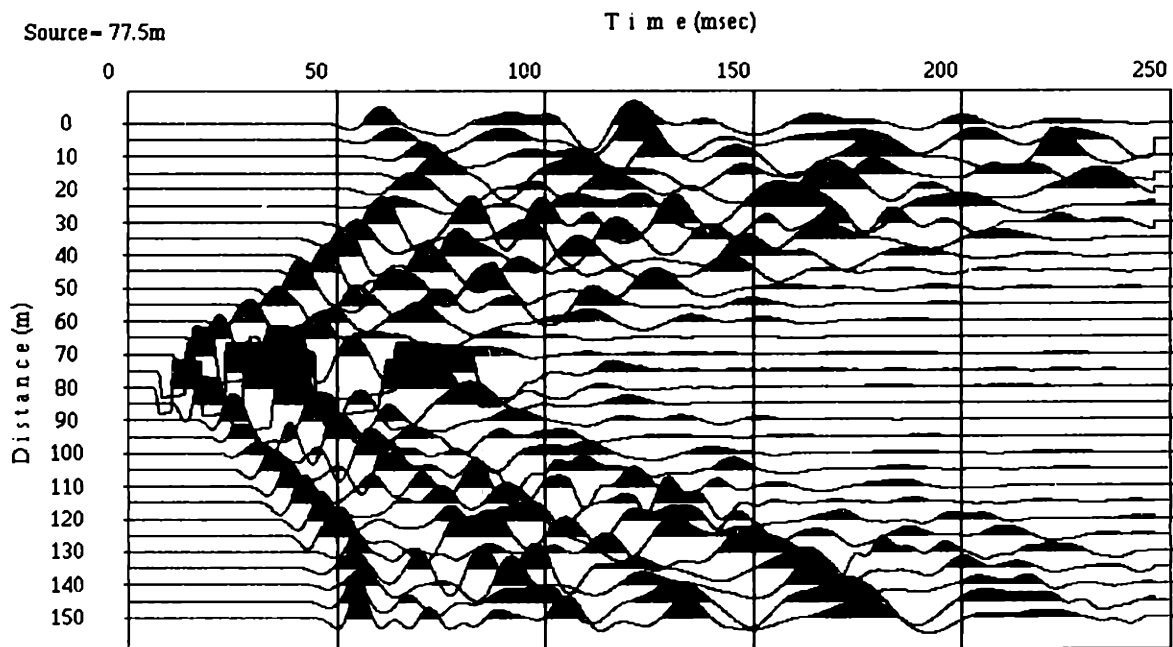
g) Observed data (Source=77.5m)
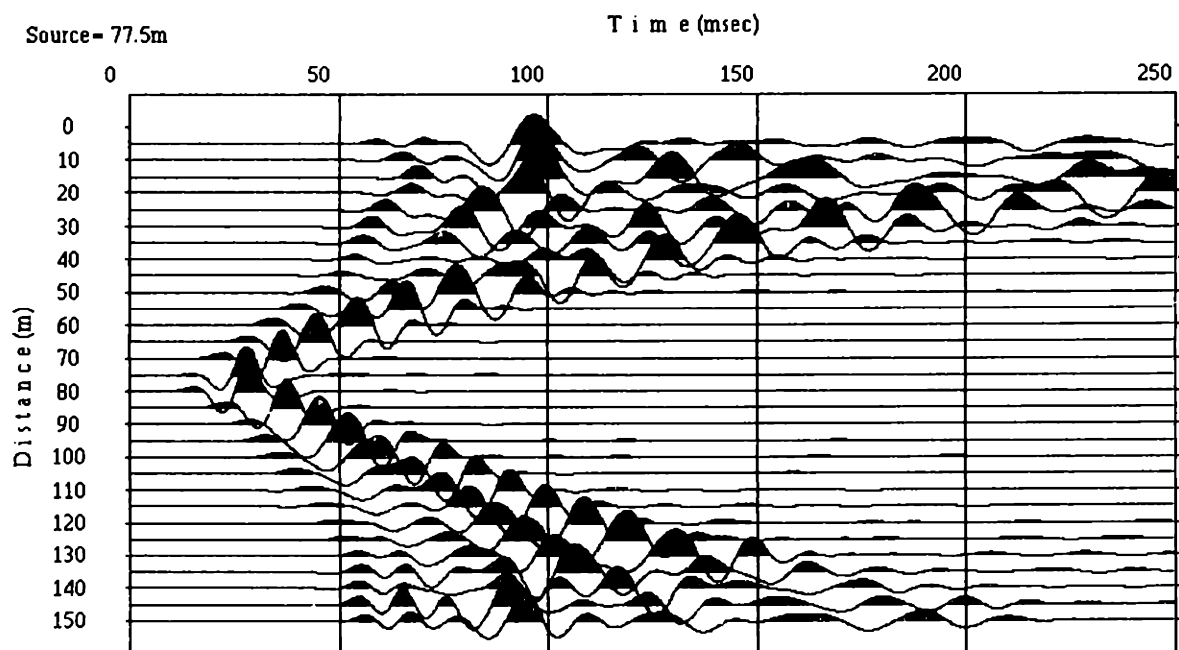
h) Theoretical data (Source=77.5m)

Figure 5.26 continued: Comparison of observed data and theoretical data.
(Source=77.5m)

179
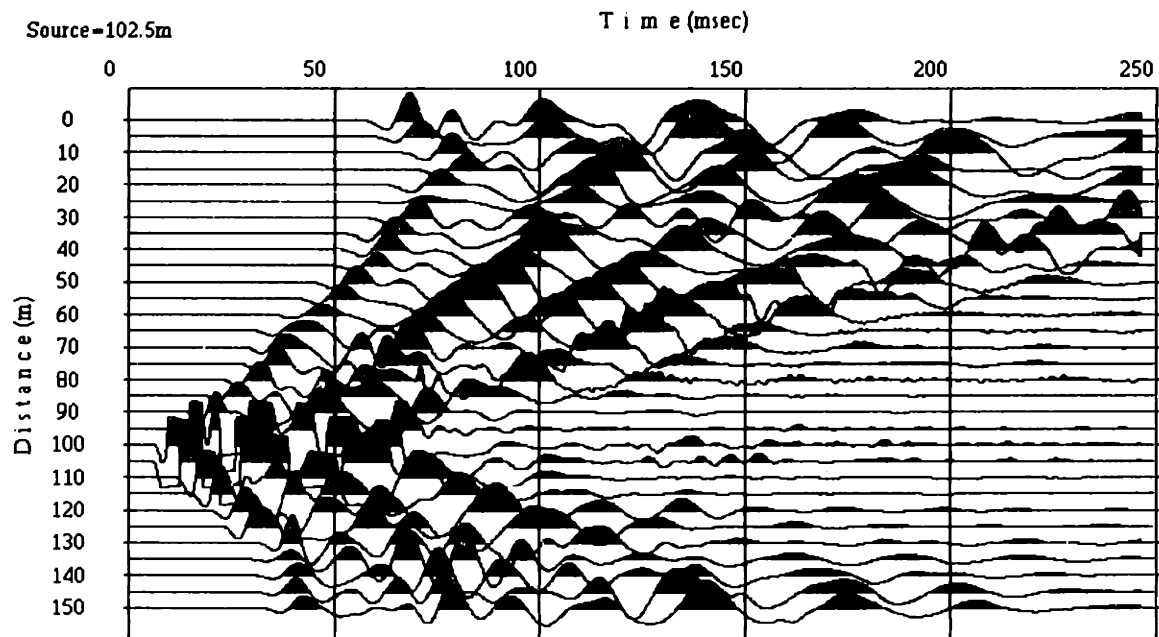
i) Observed data (Source=102.5m)
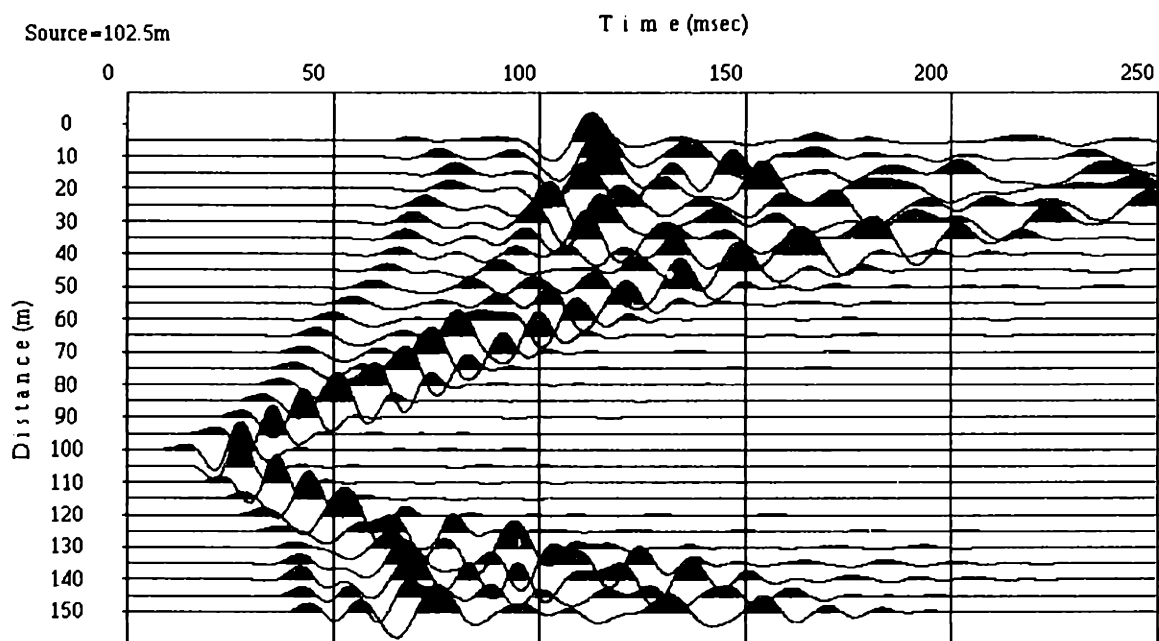
j) Theoretical data (Source=102.5m)

Figure 5.26 continued: Comparison of observed data and theoretical data.
(Source=102.5m)

180
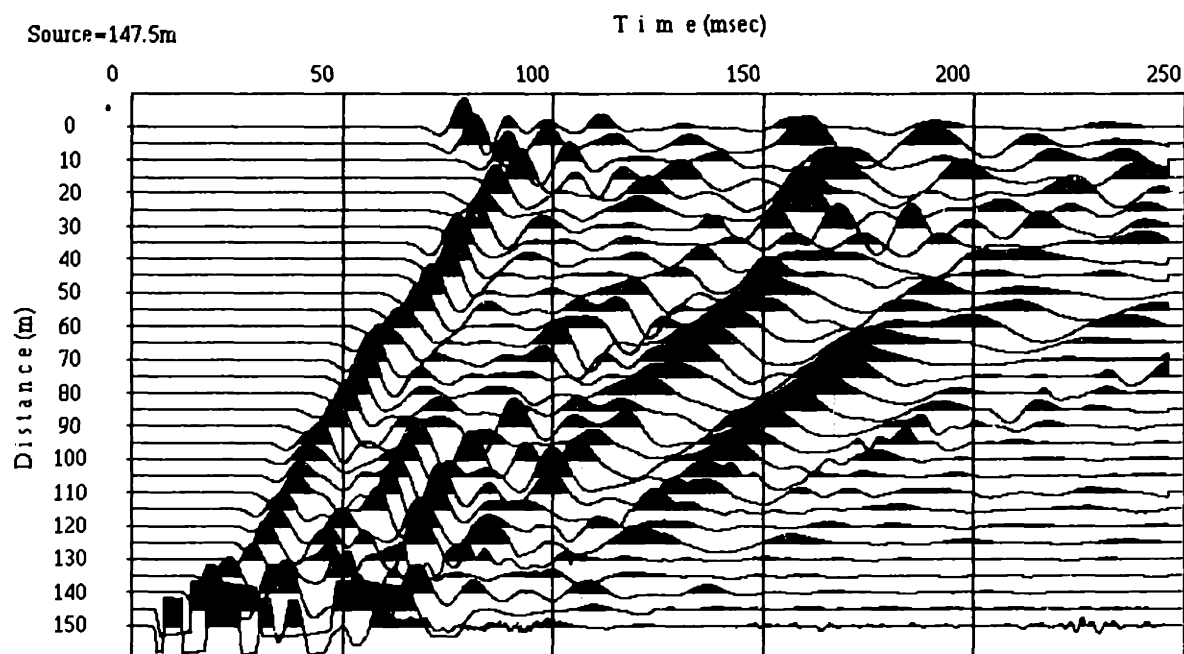
k) Observed data (Source=147.5m)
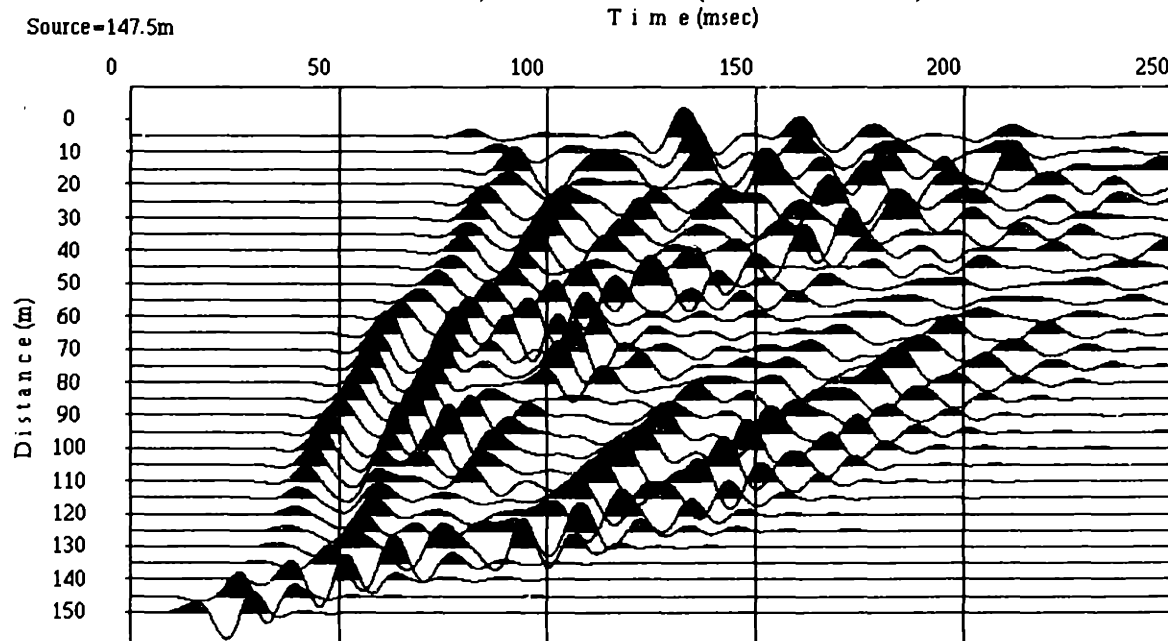
l) Theoretical data (Source=147.5m)

Figure 5.26 continued: Comparison of observed data and theoretical data.
(Source=147.5m)

Chapter 6

Conclusions

In this thesis, a variable grid, viscoelastic, 2-D finite-difference method is developed for supporting shallow seismic field survey. The new method is simple to implement for staggered grid finite-difference schemes, is computationally efficient, and enables modeling of highly irregular topography.

In order to demonstrate the accuracy and reliability of the code, benchmark tests were performed using simple models. The results confirm that the second-order approximation requires 20 grid-points per wavelength, and the fourth-order approximation requires 10 grid-points per wavelength.

An accurate free-surface boundary condition for irregular topography, and a stable and efficient variable grid implementation were presented. The results of numerical tests imply that the method presented in this thesis requires at least 30 grid-points per wavelength. In particular, relatively gentle slopes require a large number of grid-points per wavelength. Implementation of variable grid, with high grid density near the surface and low velocity zone, ensures accuracy in the calculation with improved computational efficiency. The method allows us to handle complex structures in finite-difference modeling. Although the method was implemented in 2-D, it can be easily extended to 3-D wave propagation problems.

Several numerical simulations were performed to show the characters of wave propagation in the near surface region. The simulations show that the low velocity thin layers just below the surface and anelastic attenuation have a significant effect on the surface seismic record.

The algorithm was also applied to 2-D modeling of a near surface structure beneath a 2-D refraction survey line. The characters in the observed data can be explained by a subsurface model constructed by P-velocity traveltime tomography.

There are several improvements needed for the finite-difference method developed in this thesis for broader applications. The inclusion of anisotropy is an important extension. We used the grid size ratio of three. The development of a stable calculation using a larger grid size ratio is another task. The most important improvement is the development of a three-dimensional code. It is currently possible to apply realistic three-dimensional modeling that includes attenuation and irregular free surface topography to practical problems. This extension also requires overcoming difficulties of generating 3-D earth model. The finite-difference method can be used as a forward modeling method for full wave tomography. The development of practical full wave tomography is one of our ultimate goals in near surface seismic studies.

Appendix A

Derivation of the 2-D and 3-D Viscoelastic Wave Equation

The constitutive relation for a linear viscoelastic 2-D (i,j,k = x,y) or 3-D (i,j,k = x,y,z) homogeneous isotropic solid is,

$$\sigma_{ij} = \dot{\Lambda} * \delta_{ij}\varepsilon_{kk} + 2\dot{M} * \varepsilon_{ij}, \tag{A-1}$$

according to Christensen (1982). It is possible to express the time derivative of ε_{ij} as,

$$\dot{\varepsilon}_{ij} = \frac{1}{2}\left(\partial_i\upsilon_j + \partial_j\upsilon_i\right). \tag{A-2}$$

Let us define

$$\Pi = \Lambda + 2M \tag{A-3}$$

and use the standard linear solid model for Π and M, i.e.,

$$\Pi = \pi\left(1 - \sum_{l=1}^{L}\left(1 - \frac{\tau_{\varepsilon l}^p}{\tau_{\sigma l}}\right)e^{\frac{-t}{\tau_{\sigma l}}}\right)\theta(t) \tag{A-4}$$

and

$$M = \mu\left(1 - \sum_{l=1}^{L}\left(1 - \frac{\tau_{\varepsilon l}^s}{\tau_{\sigma l}}\right)e^{\frac{-t}{\tau_{\sigma l}}}\right)\theta(t). \tag{A-5}$$

The definition of Π allows us to define Q independently for P-waves and S-waves through the $\tau_{\varepsilon l}^p$ (P-waves) and $\tau_{\varepsilon l}^s$ (S-waves). Using equations (A-1) through (A-3), we find for a diagonal element of $\dot{\sigma}_{ij}$, (i=j),

$$\dot{\sigma}_{ij} = \left(\dot{\Pi} - 2\dot{M}\right) * \partial_k\upsilon_k + 2\dot{M} * \partial_i\upsilon_j \tag{A-6}$$

and for an off-diagonal element (i ≠ j)

$$\dot{\sigma}_{ij} = \dot{M} * \left(\partial_i\upsilon_j + \partial_j\upsilon_i\right). \tag{A-7}$$

184

By evaluating parts of convolution and defining the memory variables r_{ijl}, we can write equation (A-6) as

$$\dot{\sigma}_{ij} = \left(\pi \left(1 - \sum_{l=1}^{L} \left(1 - \frac{\tau_{\varepsilon l}^{p}}{\tau_{\sigma l}} \right) \right) - 2\mu \left(1 - \sum_{l=1}^{L} \left(1 - \frac{\tau_{\varepsilon l}^{s}}{\tau_{\sigma l}} \right) \right) \right) \partial_{k} \upsilon_{k}$$

$$+ 2\mu \left(1 - \sum_{l=1}^{L} \left(1 - \frac{\tau_{\varepsilon l}^{s}}{\tau_{\sigma l}} \right) \right) \partial_{i} \upsilon_{j} + \sum_{l=1}^{L} r_{ijl} \qquad (A\text{-}8)$$

and equation (A-7) as

$$\dot{\sigma}_{ij} = \mu \left(1 - \sum_{l=1}^{L} \left(1 - \frac{\tau_{\varepsilon l}^{s}}{\tau_{\sigma l}} \right) \right) \left(\partial_{i} \upsilon_{j} + \partial_{j} \upsilon_{i} \right) + \sum_{l=1}^{L} r_{ijl} \qquad (A\text{-}9)$$

Applying the same technique as was used to derive equation (2.2.25) from equation (2.2.23) yields for diagonal r_{ijl} (i=j)

$$\dot{r}_{ijl} = -\frac{1}{\tau_{\sigma l}} \left(r_{ijl} + \left(\pi \left(\frac{\tau_{\varepsilon l}^{p}}{\tau_{\sigma l}} \right) - 2\mu \left(\frac{\tau_{\varepsilon l}^{s}}{\tau_{\sigma l}} \right) \right) \partial_{k} \upsilon_{k} + 2\mu \left(\frac{\tau_{\varepsilon l}^{s}}{\tau_{\sigma l}} \right) \partial_{i} \upsilon_{j} \right)$$

$$1 \le l \le L . \qquad (A\text{-}10)$$

and off-diagonal (i≠j)

$$\dot{r}_{ijl} = -\frac{1}{\tau_{\sigma l}} \left(r_{ijl} + \mu \left(\frac{\tau_{\varepsilon l}^{s}}{\tau_{\sigma l}} \right) \left(\partial_{i} \upsilon_{j} + \partial_{j} \upsilon_{i} \right) \right) \quad 1 \le l \le L . \qquad (A\text{-}11)$$

Adding Newton's second law,

$$\upsilon_{i} = \frac{1}{\rho} \partial_{j} \sigma_{ij} , \qquad (A\text{-}12)$$

yields the viscoelastic wave equation. Specializing to two dimensions (i,j,k =x,y) and one standard linear solid (L=1) results in equations (2.2.31) to (2.2.38).

185

Appendix B

2-D Finite-difference Equations

I show the finite-differential equations derived from equations (2.2.31) to (2.2.38). For the sake of simplicity, Clank-Nicolson scheme is not employed in the following finite-differential equations.

Equations governing stress:

$$\sigma_{xx,i,j}^{n+1} = \sigma_{xx,i,j}^{n} + \frac{\Delta t}{\Delta x}\left(\frac{\pi \tau_{\varepsilon,i,j}^{P}}{\tau_{\sigma}}\left(c_1\left(\upsilon_{x,i+3/2,j}^{n} - \upsilon_{x,i-3/2,j}^{n}\right) + c_2\left(\upsilon_{x,i+1/2,j}^{n} - \upsilon_{x,i-1/2,j}^{n}\right)\right)\right.$$

$$+ \frac{1}{\tau_{\sigma}}\left(\pi\tau_{\varepsilon,i,j}^{P} - 2\mu\tau_{\varepsilon,i,j}^{s}\right)\left(c_1\left(\upsilon_{z,i,j+3/2}^{n} - \upsilon_{z,i,j-3/2}^{n}\right) + c_2\left(\upsilon_{z,i,j+1/2}^{n} - \upsilon_{z,i,j-1/2}^{n}\right)\right)\right)$$

$$+ \frac{\Delta t}{2}\left(r_{xx,i,j}^{n+1} + r_{xx,i,j}^{n}\right) \tag{B-1}$$

$$\sigma_{zz,i,j}^{n+1} = \sigma_{zz,i,j}^{n} + \frac{\Delta t}{\Delta x}\left(\frac{\pi\tau_{\varepsilon,i,j}^{P}}{\tau_{\sigma}}\left(c_1\left(\upsilon_{z,i,j+3/2}^{n} - \upsilon_{z,i,j-3/2}^{n}\right) + c_2\left(\upsilon_{z,i,j+1/2}^{n} - \upsilon_{z,i,j-1/2}^{n}\right)\right)\right.$$

$$+ \frac{1}{\tau_{\sigma}}\left(\pi\tau_{\varepsilon,i,j}^{P} - 2\mu\tau_{\varepsilon,i,j}^{s}\right)\left(c_1\left(\upsilon_{x,i+3/2,j}^{n} - \upsilon_{x,i-3/2,j}^{n}\right) + c_2\left(\upsilon_{x,i+1/2,j}^{n} - \upsilon_{x,i-1/2,j}^{n}\right)\right)\right)$$

$$+ \frac{\Delta t}{2}\left(r_{zz,i,j}^{n+1} + r_{zz,i,j}^{n}\right) \tag{B-2}$$

$$\sigma_{xz,i,j}^{n+1} = \sigma_{xz,i,j}^{n} + \mu\frac{\Delta t \tau_{\varepsilon,i,j}^{s}}{\Delta x \tau_{\sigma}}\left(c_1\left(\upsilon_{x,i,j+3/2}^{n} - \upsilon_{x,i,j-3/2}^{n}\right) + c_2\left(\upsilon_{x,i,j+1/2}^{n} - \upsilon_{x,i,j-1/2}^{n}\right)\right.$$

$$+ c_1\left(\upsilon_{z,i+3/2,j}^{n} - \upsilon_{z,i-3/2,j}^{n}\right) + c_2\left(\upsilon_{z,i+1/2,j}^{n} - \upsilon_{z,i-1/2,j}^{n}\right)\right)$$

$$+ \frac{\Delta t}{2}\left(r_{xz,i,j}^{n+1} + r_{xz,i,j}^{n}\right) \tag{B-3}$$

Equations governing particle velocities:

$$\upsilon_{x,i,j}^{n+1} = \upsilon_{x,i,j}^{n} + \rho\frac{\Delta t}{\Delta x}\left(c_1\left(\sigma_{xx,i+3/2,j}^{n} - \sigma_{xx,i-3/2,j}^{n}\right) + c_2\left(\sigma_{xx,i+1/2,j}^{n} - \sigma_{xx,i-1/2,j}^{n}\right)\right.$$

$$+ c_1\left(\sigma_{xz,i,j+3/2}^{n} - \sigma_{xz,i,j-3/2}^{n}\right) + c_2\left(\sigma_{xz,i,j+1/2}^{n} - \sigma_{xz,i,j-1/2}^{n}\right)\right) \tag{B-4}$$

$$\upsilon_{z,i,j}^{n+1} = \upsilon_{z,i,j}^{n} + \rho\frac{\Delta t}{\Delta x}\left(c_1\left(\sigma_{zz,i+3/2,j}^{n} - \sigma_{zz,i-3/2,j}^{n}\right) + c_2\left(\sigma_{zz,i+1/2,j}^{n} - \sigma_{zz,i-1/2,j}^{n}\right)\right.$$

$$+ c_1\left(\sigma^n_{zz,i,j+3/2} - \sigma^n_{zz,i,j-3/2}\right) + c_2\left(\sigma^n_{zz,i,j+1/2} - \sigma^n_{zz,i,j-1/2}\right)\big)\big) \qquad \text{(B-5)}$$

Equations governing memory variables:

$$r^{n+1}_{xx,i,j} = r^n_{xx,i,j} - \frac{\Delta t}{\tau_\sigma}\left(r^n_{xx,i,j} + \frac{\pi}{\Delta x}\left(\frac{\tau^p_{\varepsilon,i,j}}{\tau_\sigma}-1\right)\left(c_1\left(v^n_{x,i+3/2,j} - v^n_{x,i-3/2,j}\right) + c_2\left(v^n_{x,i+1/2,j} - v^n_{x,i-1/2,j}\right)\right)\right.$$

$$\left. + \frac{1}{\Delta x}\left(\pi\left(\frac{\tau^p_{\varepsilon,i,j}}{\tau_\sigma}-1\right) - 2\mu\left(\frac{\tau^s_{\varepsilon,i,j}}{\tau_\sigma}-1\right)\right)\left(c_1\left(v^n_{z,i,j+3/2} - v^n_{z,i,j-3/2}\right) + c_2\left(v^n_{z,i,j+1/2} - v^n_{z,i,j-1/2}\right)\right)\right)$$

$$\text{(B-6)}$$

$$r^{n+1}_{zz,i,j} = r^n_{zz,i,j} - \frac{\Delta t}{\tau_\sigma}\left(r^n_{zz,i,j} + \frac{\pi}{\Delta x}\left(\frac{\tau^p_{\varepsilon,i,j}}{\tau_\sigma}-1\right)\left(c_1\left(v^n_{z,i,j+3/2} - v^n_{z,i,j-3/2}\right) + c_2\left(v^n_{z,i,j+1/2} - v^n_{z,i,j-1/2}\right)\right)\right.$$

$$\left. + \frac{1}{\Delta x}\left(\pi\left(\frac{\tau^p_{\varepsilon,i,j}}{\tau_\sigma}-1\right) - 2\mu\left(\frac{\tau^s_{\varepsilon,i,j}}{\tau_\sigma}-1\right)\right)\left(c_1\left(v^n_{x,i+3/2,j} - v^n_{x,i-3/2,j}\right) + c_2\left(v^n_{x,i+1/2,j} - v^n_{x,i-1/2,j}\right)\right)\right)$$

$$\text{(B-7)}$$

$$r^{n+1}_{xz,i,j} = r^n_{xz,i,j} - \frac{\Delta t}{\tau_\sigma}\left(r^n_{xz,i,j} + \frac{\mu}{\Delta x}\left(\frac{\tau^s_{\varepsilon,i,j}}{\tau_\sigma}-1\right)\left(c_1\left(v^n_{x,i,j+3/2} - v^n_{x,i,j-3/2}\right) + c_2\left(v^n_{x,i,j+1/2} - v^n_{x,i,j-1/2}\right)\right)\right.$$

$$\left. + c_1\left(v^n_{z,i+3/2,j} - v^n_{z,i-3/2,j}\right) + c_2\left(v^n_{z,i+1/2,j} - v^n_{z,i-1/2,j}\right)\right)\big) \qquad \text{(B-8)}$$

i : x-axes discretization.
j : y-axes discretization.
n : time discretization.
Δt : time step (sec).
Δx : grid size(m).

$\sigma_{xx}, \sigma_{zz}, \sigma_{xz}$: the symmetric stress tensor.

v_x, v_z : the particle velocities.

r_{xx}, r_{zz}, r_{xz} : the memory variables.

$\tau^p_\varepsilon, \tau^s_\varepsilon$: the viscoelastic strain relaxation times for P- and SV-waves, respectively.

τ_σ :the viscoelastic stress relaxation time for both the P- and SV waves.

μ : the relaxation modulus corresponding to SV-waves, $\mu = \rho\beta^2$.

π : the relaxation modulus corresponding to P-wave, $\pi = \lambda + 2\mu = \rho\alpha^2$.

ρ : the density (kg/m³).
α : P-velocity (m/sec).
β : S-velocity (m/sec).
c1 : -1/24.
c2 : 9/8.

References

Alterman, Z. and Karal, F. C., 1968, Propagation of elastic waves in layered media by finite difference methods, Bull. Seism. Soc. Am., 58, 367-398.

Alterman, Z. and Kornfull, P., 1968, Finite didifference solution for pulse propagation in a shere, Israel J. of Technology 6, 138-149.

Blanch, J. O., Robertsson, J. O., Symes, W. W., 1993, Viscoelastic finite-difference modeling, Tech. Rep. 93-04, Department of Computational and Applied Mathematics, Rice University.

Blanch, J. O., Robertsson, J. O., Symes, W. W., 1995, Modeling of a constant Q: Methodology and algorithm for an efficient and optimally inexpensive viscoelastic technique, Geophysics, 60, 176-184.

Boore, D. M., 1972, Finite difference methods for seismic wave propagation in heterogeneouss materials, in Methods in Computatioal Physics, 11. B. A. Bolt, Ed., Academic Press.

Carcione, J. M., Kosloff, D., and Kosloff, R., 1988, Wave propagation simulation in a linear viscoelastic medium, Geophys. J. Roy. Astr. Soc., 93, 393-407.

Carcione, J. M., 1993, Seismic modeling in viscoelastic media, Geophysics, 58, 110-120.

Christensen, R. M., 1982, Theory of viscoelasticity -An introduction: Academic Press, Inc.

Day, S. M., and Minster, J. B., 1984, Numerical simulation of attenuated wavefields using a Pade approximant method, Geophys. J. Roy. Astr. Soc., 78, 105-118.

De Lilla, A., 1997, Finite difference seismic wave propagation using variable grid sizes, M.Sc. Thesis, Massachusetts Institute of Technology.

Falk, J., Tessmer, E., and Gajewski, D., 1995, Tube wave modeling by the finite-difference method with varying grid spacing, Technical report, Institute fur Geophysik, Universitat Hamburg, Internal report.

Fuyuki, M., and Matsumoto, Y., 1980, Finite-difference analysis of Rayleigh wave scattering at a trench, Bulletin of Seismological Society of America, 86, 1091-1106.

Graves, R. W., 1996, Simulating seismic wave propagation in 3D elastic media using staggered-grid finite differences, Bulletin of Seismological Society of America, 86, 1091-1106

Hayashi, K. and Saito, H., 1996, Automatic correction of velocity structures in seismic refraction prospecting, 66th Annual International Meeting, Soc. Expl. Geophys., Expanded Abstracts, 1658-1661.

Hayashi, K., 1999, Application of high resolution seismic refraction method to civil engineering investigations, 61st EAGE Conference & Technical Exhibition, Extended Abstracts, 4-46.

Hestholm, S. O., and Ruud, B. O., 1994, 2D finite-difference elastic wave modeling including surface topography, Geophysics Prospecting, 42, 371-390.

Higdon, R. L. 1986, Absorbing boundary conditions for difference approximations to the multi-dimensional wave equation, Mathematics of computation 47, 437-459.

Higdon, R. L. 1987, Numerical absorbing boundary conditions for the wave equation, Mathematics of computation, 49, 65-90.

Higdon, R. L. 1990, Radiation boundary conditions for elastic wave equation, SIAM J. Numer. Amal. 27, 831-870.

Imai, T., and Tonouchi, K., 1982, Correlation of N-value with S-wave velocity, Proc. of 2nd Europ. Sympo. On Penetration Testing, 67-72.

Jih, R. S., McLaughlin, K. R., and Der, Z. A., 1988, Free-boundary conditions of arbitrary polygonal topography in a two-dimensional explicit elastic finite-difference scheme, Geophysics, 53, 1045-1055.

Kerry, K. R., Ward, R. W., Treitel, S., and Alford, R. M., 1976, Synthetic seismograms: A finite-difference approach, Geophysics, 41, 2-27.

Lanz, E., Maurer, H., and Green, A. G., 1998, Refraction tomography over a buried waste disposal site, Geophysics, 63, 1414-1433.

Lay, T. and Wallace, T. C.,1995, Modern Global Seismology, Academic Press.

Levader, A. R., 1988, Fourth-order finite-difference P-SV seismograms, Geophysics, 53, 1425-1436.

Liu, H. P., Anderson, D. L., Kanamori, H., 1976, Velocity dispersion due to anelasticity; implications for seis,ology and mantle composition, Geophys. J. R. astr. Soc., 47, 41-58.

McLaughlin, K. L., and Day, S. M., 1994, 3d elastic finite-difference seismic-wave simulations, Computers in Physics, 8, 656-664.

Nazarian, S., Stoke, K. H., II, and Hudson, W. R., 1983, Use of spectral analysis of surface waves method for determination of moduli and thickness of pavement system, Transport. Res. Record, 930, 38-45.

Peng, C., and Toksöz, M. N., 1995, An optimal absorbing boundary condition for elastic wave modeling, Geophysics, 60, 296-301.

Park, C. B., Miller, R. D., and Xia, J., 1999a, Multimodal analysis of high frequency surface waves, Proceedings of the symposium on the application of geophysics to engineering and environmental problems '99, 115-121.

Park, C. B., Miller, R. D., and Xia, J., 1999b, Multichannel analysis of surface waves, Geophysics, 64, 800-808.

Pipkin, A. C., 1986, Lectures on viscoelasticity theory, Springer Verlag, New York, Inc.

Robertsson, J. O. A., Blanch, J. O., and Symes, W. W., 1994, Viscoelastic finite-difference modeling, Geophysics, 59, 1444-1456.

Robertsson, J. O. A., 1996, A numerical free-surface condition for elastic/viscoelastic finite-difference modeling in the presence of topography, Geophysics, 61, 1921-1934.

Robertsson, J. O. A., 1997,

Steeples, D. W., 1998, Shallow seismic reflection section, Geophysics, 63, 1210-1212.

Steeples, D. W. and Miller, R. D., 1998, Avoiding pitfalls in shallow seismic reflection surveys, Geophysics, 63, 1213-1224.

Strang, G., 1986, Introduction to applied mathematics, Wellweley-Cambridge Press.

Tessmer, E., Kosloff, D., and Behle, A., 1992, Elastic wave propagation simulation in the presence of surface topography, Geophys. J. Int.,108 621-632.

Virieux, J. 1986, P-SV wave propagation in heterogeneous media: Velocity-stress finite difference method, Geophysics, 51, 889-901.

Xia, J., Miller, R. D., and Park, C. B., 1999a, Configuration of near surface shear wave velocity by inverting surface wave, Proceedings of the symposium on the application of geophysics to engineering and environmental problems '99, 95-104

Xia, J., Miller, R. D., and Park, C. B., 1999b, Estimation of near-surface shear-wave velocity by inversion of Rayleigh waves, Geophysics, 64, 691-700.

Xu, T., and McMechan, G. A., 1998, Efficient 3-D viscoelastic modeling with application to near-surface land seismic data, Geophysics, 63, 601-612.

Zhang, J., and Toksöz, M. N., 1998, Nonlinear refraction traveltime tomography, Geophysics, 63, 1726-1737.